

EFFECT OF MOUNTING MISALIGNMENTS ON THE TRIBOLOGICAL BEHAVIOUR OF ELASTOMERIC SEALS: ANALYTICAL PREDICTIVE MODELS AND EXPERIMENTAL VALIDATION

PhD THESIS

Presented by

Bihotz Pinedo Araukua

Supervisors:

Dr. Josu Aguirrebeitia

Dr. Marcello Conte

July 2016

Nere bizitzako pertsona garrantzitsuenei:

Ama, aita, Eider eta Constan.

“Research is creating new knowledge”

-Neil Armstrong-

Acknowledgements

Primeramente, me gustaría dar las gracias a mis directores de tesis, Josu y Marcello, por haberme apoyado, guiado y dado esos consejos tan útiles durante todo este trayecto. En especial, mi más profundo agradecimiento a ti, Marcello, porque he disfrutado mucho trabajando mano a mano contigo durante unos años y, sobre todo, por haberme animado y apoyado cada día.

Fundación Centros Tecnológicos-Iñaki Goenaga fundazioari eta IK4-Teknikerreri ere eskertu nahi deusiet doktoretza zentru teknologiko batean egiteko emondako aukera. Halako ekimenik izan ezean tesi hau gauzatzea ez litzateke posible izango. Era berean, eskerrak emon nahiko neuskioz Bilboko Ingenieritza Eskolako Mekanika Departamenduari tesia bertan egiteko emondako aukeragaitik.

I also would like to express my most sincere gratitude to Bournemouth University, in particular to Mark Hadfield and Mayank Anand, for their help and hospitality during my stay. I would also like to thank Iakovos Tzanakis, for the time he devoted to assist me on the use of thermal cameras as well as for the interesting discussions we had about the frictional heating in polymers. My stay in Bournemouth was a wonderful experience!

I cannot fail to express my gratitude to the EPSRC Engineering Instrument Pool in the UK for the loan of instrumentation to carry out my research. This thesis would have not been possible without your contribution.

Además, no quiero perder la oportunidad de dar las gracias a la empresa Azol-Gas S.L. por diseñar y fabricar un resorte de gas a medida para que pudiera llevar a cabo mi investigación. Sin vuestra aportación, esta tesis no hubiera sido posible. También me gustaría dar las gracias a la empresa Productos Salinas S.A. por facilitarme el material para llevar a cabo parte de los ensayos.

Asimismo, me gustaría dar las gracias a mi compañero Peio Orbea, por haberme ayudado y acogido tan bien en Metrología mientras realizaba ensayos, y sobre todo, gracias por tu sentido del humor. Te vamos a echar de menos. También quiero agradecer a mis compañeros Juan Carlos Rodríguez y Andoni Delgado por haberme ayudado a diseñar utillajes específicos para mi tesis, así como a Ana Aranzabe y Amaya Igartua, por su apoyo y gran ayuda.

Orokorrean, eskerrik asko IK4-Teknikerreko nire kide guztiei! Bereziki, Tribologia, Gainazalen Fisika eta Diseinu, Fabrikazio eta Muntaia Unitateei, eurekin pasatako momentu ahaztezin guztiengaitik. Baita zuri ere, Edurne, zeure sostengu eta adiskidetasunagaitik.

Azkenik, eskerrik beroenak emon nahiko neuskiez nire senideei eta bereziki nire gurasoei, nigan izandako konfidantza eta baldintzarik gabeko laguntzagatik. Ama, aita eta Eidertxo, eskerrik asko, neure euskarria zarie! Tesi hau zuena bezain nirea da. Nire esker onak zeuri ere Constan, dana errezagoa izatea egiten baitozu.

SUMMARY

The main objective of this thesis is to investigate the effects of mounting eccentricities or shaft to bore misalignments on the tribological behaviour of elastomeric seals in an attempt to contribute to the lack of studies related to the life expectancy of seals. To this aim, this work deals with the study of the effect of rod eccentricities on the contact pressure distribution on seals, the friction generated, the volume loss and the contact temperature distribution along elastomeric seals during operation combining analytical, numerical and experimental methods.

Mounting misalignments are unavoidable and their nature may be very diverse. Among the different sources of mounting misalignments are mounting errors and incorrect design or manufacturing tolerances. Furthermore, in most cases, misalignments result from the combination of all these factors.

The main effect of rod mounting eccentricities is a non-uniform contact force distribution along the seal. As a consequence, some sections of the seal will be subjected to an excessive contact pressure (radial overload) whereas in other sections, the contact between parts may be lost. In the latter case, the immediate consequence is the leakage of the seal. In the former case, radial overloads will lead to a reduced service life of the seal due to the breaking down of the lubricant film and therefore to a temperature rise that may cause thermal degradation and abrupt wear. Hence, immediate consequence of an incorrect seal mounting is a premature seal failure due to radial overloads. Nevertheless, even if mounting eccentricities affect considerably the life

Summary

expectancy of seals, their effect on the tribological performance of seals has not been studied in detail up to now. Hence the present work is mainly motivated by the need to understand how the inevitable mounting misalignments alter the performance of seals. The main objectives of the thesis and the structure of the research work are presented in Chapter 1. Moreover, although this research work is focused on the study of the effects of rod mounting misalignments on seals, a failure guide of the most common elastomeric seal failures as well as their main causes are also presented within this chapter.

In an attempt to meet the challenge of measuring experimentally the contact pressure distribution between a specific seal and the rod under certain mounting conditions, in this thesis a novel analytical method has been developed. In particular, a procedure to build an analytical tri-dimensional eccentricity model of seals that enables calculating the contact force distribution along a complete seal as a function of radial mounting eccentricities is herein proposed and presented in Chapter 2. The model was completed and adjusted by means of numerical results. In order to complete and validate the model, experimental misalignment tests were carried out in a specific test rig designed to this aim. The proposed methodology may be a useful tool for design purposes in order to avoid the high computational costs associated with long computational times of simulations carried out on numerical 3D models. Moreover, the procedure may be also very useful for the industry since knowing the contact forces between the seals and the counterparts is of great interest and the base for further friction, wear and temperature predictions as demonstrated in this work.

With the aim of investigating the effect of radial overloads on the service life of seals under actual operating conditions, experimental tests were carried out on seals under both concentric and controlled eccentric mounting conditions. The test rig used for sealing system characterization and the results of the tests are presented in Chapter 3. In particular, friction and wear measurements were carried out, and volume loss vs. sliding distance curves of the tested seals were built in order to evaluate and compare the tribological performance of seals working under concentric and eccentric mounting conditions. Furthermore, wear rate and friction distribution calculations of the seal samples have been also herein addressed through the use of the eccentricity contact model developed.

Regarding the effect of radial overloads arising from mounting eccentricities on the temperature rise of seals due to frictional heating, this investigation has been carried out through the development of a specific methodology presented in Chapter 4. Radial overloads may lead to an excessive temperature rise on seals that may result in an overheating of the surfaces in certain seal sections due to frictional heating, even in lubricated contacts. Hence, knowing the temperatures reached at the contact is of great interest but also a challenge considering that seals are usually mounted in closed grooves and moving relative to their mating surfaces. The methodology herein proposed overcomes this challenge and enables estimating the contact temperature distribution on seals during operation combining analytical models, thermo-mechanical properties of the materials involved and some experimental inputs. The investigation was carried out in two stages. In a first stage, an experimental investigation on the frictional

Summary

heating phenomenon on elastomeric seals was carried out at laboratory scale. In a second stage, the knowledge gained from this basic study was extended to develop a procedure to calculate the temperatures reached at the contact between an entire seal and its mating surfaces during operation. In line with the topic of this thesis, the proposed procedure was applied to estimate and compare the contact temperature distribution on seals subjected to concentric and eccentric mountings. It is thought that the proposed methodology may be useful and of great interest for the industry, considering the lack of applicable experimental techniques and given the low thermal resistance of elastomers.

At the end of this thesis, in Chapter 5, the main conclusions of the work carried as well as future possible research in line with this thesis are presented.

RESUMEN

El principal objetivo de esta tesis es investigar los efectos que producen las excentricidades de montaje en el comportamiento tribológico de las juntas elastoméricas de cara a contribuir a la falta de estudios existentes relacionados con la expectativa de vida en servicio de éstas. Con este fin, este trabajo aborda el estudio del efecto de posibles desalineamientos radiales del eje en la distribución de la presión de contacto de las juntas, en la fricción generada, en el desgaste producido y en la distribución de la temperatura en el contacto, mediante la combinación de técnicas analíticas, numéricas y experimentales.

La presencia de excentricidades en elementos de máquina es inevitable y su naturaleza puede ser muy diversa. Los errores de montaje, y de tolerancias de diseño o de fabricación, son algunas de las fuentes más frecuentes de excentricidades. Es más, en la mayoría de los casos, son el resultado de una combinación de varios de estos factores.

El principal efecto de las excentricidades de eje es una distribución no-uniforme de la fuerza de contacto a lo largo de la junta. Como consecuencia, algunas secciones de la junta estarán sometidas a una excesiva fuerza de contacto (sobrecarga radial), mientras que en otras secciones podría llegar a perderse el contacto entre la junta y su contra-superficie. En este último caso, la consecuencia inmediata será la pérdida de sellado y, por lo tanto, la fuga del fluido a sellar. En el primer caso, las sobrecargas radiales darán lugar a una reducción de la vida de servicio de la junta debido a la rotura de la película de lubricante y,

como consecuencia, a un aumento de temperatura en el contacto, lo que acelerará el proceso de desgaste de la junta pudiendo incluso degenerar en la degradación térmica de ésta. En definitiva, el efecto inmediato de un montaje incorrecto de las juntas es un fallo prematuro de las mismas, debido a sobrecargas radiales. Si bien las excentricidades afectan considerablemente a la vida útil de las juntas, su efecto en el comportamiento tribológico de las mismas no se ha estudiado en detalle hasta ahora. Por ello, la principal motivación del presente trabajo ha sido la necesidad de investigar en detalle y entender la manera en que afectan las excentricidades de montaje al funcionamiento y vida en servicio de las juntas elastoméricas. Los principales objetivos y la estructura del presente trabajo de investigación se presentan en el Capítulo 1. Este capítulo también recoge un listado de los fallos más comunes de las juntas elastoméricas, así como principales causas.

Con objeto de superar el reto que supone la medición experimental de la distribución de la presión de contacto entre una determinada junta y su vástago bajo unas condiciones de montaje específicas, en este trabajo de tesis se ha desarrollado un modelo analítico novedoso. En particular, en esta investigación se ha propuesto un procedimiento para desarrollar modelos analíticos tri-dimensionales de excentricidad de juntas que permiten calcular la distribución de la fuerza de contacto a lo largo de éstas en función del desalineamiento. Este procedimiento se recoge en el Capítulo 2. El modelo se ha completado y ajustado mediante resultados numéricos. La validación del modelo se ha llevado a cabo mediante ensayos experimentales en un banco de ensayos diseñado y fabricado para esta finalidad. La metodología propuesta en

este trabajo puede ser una herramienta útil para fines de diseño de cara a evitar los grandes costes computacionales asociados a las simulaciones numéricas 3D. A su vez, la metodología también puede resultar de gran utilidad para la industria ya que conocer la distribución de la fuerza en el contacto resulta indispensable de cara a realizar posteriormente predicciones sobre la fricción, desgaste y distribución de temperatura en las juntas, tal y como se ha demostrado en este trabajo.

Con objeto de investigar sobre el efecto de las sobrecargas radiales en la vida en servicio de las juntas elastoméricas, en este trabajo se ha llevado a cabo una campaña de ensayos en juntas sometidas a montajes concéntricos y de excentricidad controlada bajo condiciones operativas reales. Tanto el banco de ensayos empleado para la caracterización tribológica de las juntas como los resultados de los ensayos llevados a cabo, se recogen en el Capítulo 3. En particular, se realizaron medidas de fricción y desgaste, y se construyeron curvas de desgaste vs. distancia recorrida por las juntas, a fin de evaluar y comparar el comportamiento tribológico de juntas sometidas a un montaje concéntrico y excéntrico. Además, en este trabajo también se ha abordado el cálculo de la tasa de desgaste y de la distribución de la fricción a lo largo de las juntas mediante el uso del modelo tri-dimensional de contacto desarrollado.

En lo que respecta al incremento de la temperatura en la junta debido al calentamiento por fricción, y originado por la presencia de sobrecargas radiales en la misma, en esta tesis se ha desarrollado una metodología específica que se presenta en el Capítulo 4 para estimar la temperatura en el contacto entre la junta y su contra-superficie, bajo condiciones

operativas. En efecto, las sobrecargas radiales pueden dar lugar a un aumento excesivo de temperatura en secciones específicas de las juntas debido al calentamiento por fricción, incluso en condiciones lubricadas. Por ello, conocer las temperaturas alcanzadas en el contacto suscita un gran interés que representa además un gran desafío, puesto que las juntas están montadas en alojamientos cerrados de difícil acceso y están sometidas a un movimiento relativo con respecto a su contra-superficie. Además, cualquier técnica basada en el contacto no es aplicable, porque su uso podría alterar las mediciones. La metodología propuesta en este trabajo supera este reto y permite estimar la distribución de la temperatura en el contacto de juntas en condiciones operativas mediante una combinación de modelos analíticos, propiedades termo-mecánicas de los materiales implicados y algunos datos experimentales. La investigación se ha llevado a cabo en dos fases. En una primera fase, se ha realizado un estudio experimental a escala laboratorio del aumento de temperatura en elastómeros debido al fenómeno de calentamiento por fricción. En una segunda fase, gracias al conocimiento adquirido durante el estudio experimental se ha desarrollado un procedimiento que permite estimar la temperatura alcanzada en el contacto entre una junta y su contra-superficie en condiciones operativas. En línea con la temática de esta tesis, la metodología ha sido aplicada a fin de estimar y comparar la distribución de temperaturas en una junta sometida a un montaje concéntrico, y otra sometida a un montaje excéntrico. La metodología planteada en este trabajo puede resultar de gran interés y utilidad para la industria, teniendo en cuenta que las técnicas experimentales aplicables actualmente son muy escasas y relativamente baja la resistencia térmica de los elastómeros.

El Capítulo 5 recoge las principales conclusiones del trabajo llevado a cabo en esta tesis, así como algunas de las posibles líneas de investigación futuras en este ámbito.

LIST OF CONTENT

| | |
|---|-----------|
| Acknowledgements | i |
| SUMMARY | v |
| RESUMEN..... | ix |
| LIST OF CONTENT | xvii |
| LIST OF FIGURES..... | xxi |
| LIST OF TABLES | xxix |
| NOMENCLATURE | xxx |
| Chapter 1: Introduction, objectives and structure | 1 |
| 1.1 Introduction | 1 |
| 1.2 Objectives | 27 |
| 1.3 Beneficiaries | 30 |
| 1.4 References..... | 32 |
| Chapter 2: Tri-dimensional eccentricity model of seals | 35 |
| 2.1 Introduction | 35 |
| 2.2 Static and dynamic eccentricities..... | 40 |
| 2.3 Experimental measurements..... | 44 |
| 2.3.1 Experimental setup and specimens..... | 45 |
| 2.3.2 Experimental results..... | 50 |
| 2.4 Modelling method for seals..... | 52 |
| 2.4.1 Functional contact relation | 54 |

List of Content

| | | |
|---|---|-----------|
| 2.4.2 | Geometrical interference model | 61 |
| 2.5 | Numerical 3D model | 63 |
| 2.5.1 | Modelling | 63 |
| 2.5.2 | Numerical results | 65 |
| 2.6 | Analytical model..... | 66 |
| 2.6.1 | Frictionless contact model not including tangential forces, (Theor. (FN))..... | 68 |
| 2.6.2 | Frictionless contact model including tangential forces, (Theor. ($FN + T$))..... | 70 |
| 2.6.3 | Frictional contact model non including tangential effects, (Theor. ($FN + Ff$))..... | 72 |
| 2.6.4 | Frictional contact model including tangential forces, (Theor. ($FN + T + Ff$)) | 73 |
| 2.7 | Results | 75 |
| 2.7.1 | Model validation..... | 75 |
| 2.7.2 | Contact pressure field | 79 |
| 2.8 | Conclusions | 85 |
| 2.9 | References | 87 |
| Chapter 3: Effect of mounting eccentricity on seal performances – Experimental tests | | 91 |
| 3.1 | Introduction..... | 91 |
| 3.2 | Specimens & materials | 95 |
| 3.3 | Experimental setup | 101 |

| | | |
|--|--|------------|
| 3.3.1 | Test rig description..... | 102 |
| 3.3.2 | Mounting configurations of seals under study..... | 105 |
| 3.4 | Test conditions..... | 108 |
| 3.5 | Contact force calculation..... | 109 |
| 3.6 | Experimental results..... | 115 |
| 3.6.1 | Effect of rod to bore misalignments on friction..... | 116 |
| 3.6.2 | Effect of rod to bore misalignments on seal wear..... | 120 |
| 3.7 | Wear rate calculations..... | 128 |
| 3.8 | Friction coefficient curves and friction force distribution along seals..... | 141 |
| 3.8.1 | Approach..... | 141 |
| 3.8.2 | Friction coefficient curves..... | 143 |
| 3.8.3 | Case study: Friction force distribution along an eccentric seal..... | 144 |
| 3.9 | Conclusions..... | 148 |
| 3.10 | References..... | 150 |
| Chapter 4: Frictional heating on elastomeric seals during operation: An approach..... | | 155 |
| 4.1 | Introduction..... | 155 |
| 4.2 | Contact temperature concept..... | 161 |
| 4.3 | Experimental study of the frictional heating phenomenon on TPU and NBR elastomers..... | 166 |
| 4.3.1 | Specimens and characterization..... | 166 |

List of Content

| | | |
|--|---|------------|
| 4.3.2 | Experimental setup | 173 |
| 4.3.3 | Experimental results | 181 |
| 4.4 | Analytical calculations and comparison with experimental results | 205 |
| 4.5 | Effect of misalignments on the temperature rise of dynamic seals due to frictional heating..... | 209 |
| 4.5.1 | Procedure to estimate contact temperatures on dynamic seals during operation. General approach..... | 210 |
| 4.5.2 | Comparison of the contact temperature distribution on concentric and eccentric seals. Case study..... | 214 |
| 4.5.3 | Methodology validation | 219 |
| 4.6 | Conclusions | 222 |
| 4.7 | References | 225 |
| Chapter 5: General conclusions & Future work..... | | 229 |
| 5.1 | General conclusions | 229 |
| 5.2 | Future work..... | 234 |
| Relevant publications of the author | | 237 |
| Appendix: Relevant Journal Publications..... | | 239 |

LIST OF FIGURES

| | |
|---|----|
| Figure 1: Sealing system of an actuator. | 2 |
| Figure 2: Basic shaft seal design (Source: Trelleborg [1])..... | 4 |
| Figure 3: Typical reciprocating seal designs: (a) elastomer energized, and (b) with metallic U spring (Source: Trelleborg [2]). | 5 |
| Figure 4: Geometry examples of rod and piston seals (Source: [6])..... | 6 |
| Figure 5: Factors affecting the seal performance (Source: [3]). | 7 |
| Figure 6: Stress/strain curves of different seal materials (Source: [5]) .. | 10 |
| Figure 7: Operating temperature range of different elastomer materials (Source: Parker [8]). | 12 |
| Figure 8: Contact between sealing lips and metallic counterparts (Source: Kastas Sealing Technologies AS [7]). | 15 |
| Figure 9: Pie chart of the main seal failure causes. | 16 |
| Figure 10: Possible causes of failure for radial shaft seals (Source: Freudenberg Simrit GmbH & Co.KG [9]). | 17 |
| Figure 11: Dieseling damage on a seal (Source: [11]). | 19 |
| Figure 12: Seal damage due to an incorrect mounting (Source: IK4- Tekniker). | 20 |
| Figure 13: Extrusion damage (Source: Parker Hannifin Corporation [4]). | 21 |
| Figure 14: Fatigue damage on a seal (Source: IK4-Tekniker)..... | 25 |
| Figure 15: Typical stages of wear processes..... | 26 |

List of Figures

| | |
|--|----|
| Figure 16: Static eccentricity or shaft to bore misalignment..... | 41 |
| Figure 17: Dynamic run-out..... | 43 |
| Figure 18: Acceptable eccentricity values: (a) shaft to bore misalignment, (b) dynamic run-out. (Source: Trelleborg Sealing Solutions [28])..... | 44 |
| Figure 19: Drawing of the gas spring (Source: Azol-Gas S.L.). | 46 |
| Figure 20: Experimental setup for misalignment tests: (a) schematic view and (b) test rig assembly..... | 47 |
| Figure 21: Principal dimensions of the seal groove (in mm). | 50 |
| Figure 22: Reaction forces on the seal as a function of the applied misalignment..... | 51 |
| Figure 23: Proposed process scheme..... | 53 |
| Figure 24: Bi-dimensional model of the sealing system..... | 56 |
| Figure 25: Experimental compressive stress-strain curve of TPU. | 57 |
| Figure 26: Instron 3369 universal machine..... | 57 |
| Figure 27: Forces obtained from the differential element of seal. | 59 |
| Figure 28: Reaction and tangential forces in a seal section as a function of mounting interference or compression. | 60 |
| Figure 29: Geometrical interference model. | 62 |
| Figure 30: Possible interference configurations..... | 63 |
| Figure 31: Tri-dimensional model of the sealing system under study. ... | 64 |
| Figure 32: Simulation procedure of the seal: (a), (b) and (c) mounting, and (d) rod misalignment (d)..... | 65 |

Figure 33: Numerically obtained contact forces vs. rod misalignment...66

Figure 34: Forces acting on a differential element of seal when friction and tangential effects are ignored.69

Figure 35: Forces acting on a differential of seal when friction is ignored and tangential forces are considered.....71

Figure 36: Forces acting on a differential element of seal when tangential forces are ignored and friction between parts is considered. 72

Figure 37: Forces acting on a circumferential section of the seal.....74

Figure 38: Radial contact forces in the sealing lip as a function of circumferential position and rod eccentricity value.....76

Figure 39: Analytically (Theor.) and numerically (FEM) obtained contact forces vs. misalignment.78

Figure 40: Comparison between experimental, numerical and analytical results.79

Figure 41: Contact pressure between the seal and the rod under concentric mounting conditions ($\delta r = 0mm$).....81

Figure 42: Contact pressure between the seal and the rod for.....82

Figure 43: Comparison of the contact pressure under different contact conditions.....83

Figure 44 : Contact pressure field under ideal concentric conditions ($\delta r = 0 mm$).....84

Figure 45: Contact pressure field for a rod misalignment of $\delta r = 0.1mm$84

List of Figures

| | |
|--|-----|
| Figure 46: Contact pressure field for a rod misalignment of $\delta r = 0.2 \text{ mm}$ | 85 |
| Figure 47: Thermal stability curves of seal samples with temperature studied by means of TGA analysis. | 99 |
| Figure 48: DSC curves of the (a) TPU (seal A) and (b) NBR (seal B). | 101 |
| Figure 49: Test rig TESSA for seal characterization. | 102 |
| Figure 50: Rotatory part of the sealing test rig. | 103 |
| Figure 51: Reciprocating part of the sealing test rig. | 104 |
| Figure 52: Experimental setup for tribological tests of seals. | 106 |
| Figure 53: Test rig assembly. | 107 |
| Figure 54: 2D FEM model of seal B. | 111 |
| Figure 55: Experimental compressive stress-strain curve of the seal materials. | 112 |
| Figure 56: Reaction and tangential forces in seal B as a function of mounting interference or compression. | 113 |
| Figure 57: Friction of seals A (TPU) and B (NBR) under concentric conditions ($\delta r = 0 \text{ mm}$). | 116 |
| Figure 58: Friction of seals A (TPU) and B (NBR) under eccentric conditions ($\delta r = 0.15 \text{ mm}$). | 117 |
| Figure 59: Comparison of the friction force generated by seal A (TPU) under concentric and eccentric conditions. | 119 |
| Figure 60: Comparison of the friction force generated by seal B (NBR) under concentric and eccentric conditions. | 119 |

Figure 61: Evolution of the wear process on seals with the travelled distance under: (a) concentric conditions, $\delta r = 0mm$ and (b) eccentric conditions, $\delta r = 0.15mm$ 123

Figure 62: Volume loss (mm^3) vs. travelled distance for tests carried out under: (a) concentric and (b) eccentric ($\delta r = 0.15mm$) mounting conditions. 125

Figure 63: SEM micrographs of the A type seal samples after travelling 18 km under: (a) concentric conditions, $\delta r = 0 mm$ and (b) eccentric conditions, $\delta r = 0.15 mm$ 128

Figure 64: Relationship between the volume loss of the seal sample B (NBR) and the travelled distance. 133

Figure 65: Evolution of the wear along the sealing lip with the travelled distance D and under: (a) concentric conditions, $\delta r = 0mm$ and (b) eccentric conditions, $\delta r = 0.15mm$ 137

Figure 66: Seal/rod contact force evolution with the travelled distance under concentric conditions ($\delta r = 0mm$). 138

Figure 67: Contact force evolution of the most compressed seal section under eccentric conditions ($\delta r = 0.15mm$). 139

Figure 68: Relationship between the volume loss of the seal sample A (TPU) and the travelled distance. 140

Figure 69: Comparison of the friction coefficient curves of seal A (TPU) under concentric and eccentric conditions. 143

Figure 70: Comparison of the friction coefficient curves of seal B (NBR) under concentric and eccentric conditions. 144

List of Figures

| | |
|--|-----|
| Figure 71: Radial contact forces in the sealing lip along the whole seal A as a function of rod to bore eccentricity value. | 145 |
| Figure 72: Steady contact and friction force distribution of seal A (TPU) for a rod to bore misalignment of $\delta r = 0.15mm$ | 147 |
| Figure 73: Tribo-pair selected for the study of the frictional heating phenomenon at laboratory scale. | 167 |
| Figure 74: Thermal properties of the test samples: (a) NBR and (b) TPU. | 170 |
| Figure 75: 3D roughness of the (a) TPU and (b) NBR samples. | 172 |
| Figure 76: Optical examination of polymer surfaces before the tests: (a) TPU and (b) NBR. | 173 |
| Figure 77: Cylinder on flat assembly. | 175 |
| Figure 78: Test assembly for sliding tests in the TE77 friction machine. | 175 |
| Figure 79: Scheme of the components of an IR camera [26]. | 177 |
| Figure 80: TE77 high frequency sliding test rig (Plint tribology). | 180 |
| Figure 81: Thermal image example from the tribo-system. | 180 |
| Figure 82: Friction of Non-Chromed plated (NC) cylinders sliding against TPU. | 181 |
| Figure 83: Friction of Non-Chromed plated (NC) cylinders sliding against NBR. | 182 |
| Figure 84: Effect of the chromium-plating process on the friction of the TPU samples. | 185 |

Figure 85: Effect of the chromium-plating process on the friction of the NBR samples. 186

Figure 86: Friction and temperature curves of the TPU samples sliding against steel mating surfaces with different roughness and surface conditions at 0.1m/s. 188

Figure 87: Friction and temperature curves of NBR samples sliding against steel mating surfaces with different roughness and surface conditions at 0.1m/s. 190

Figure 88: Friction and temperature curves of the TPU samples sliding against steel mating surfaces with different roughness and surface conditions at 0.25m/s. 192

Figure 89: Friction and temperature curves of the NBR samples sliding against steel mating surfaces with different roughness and surface conditions at 0.25m/s. 193

Figure 90: Temperature measurement in the bulk of the elastomeric samples throughout the tests: (a) at 0.1m/s and (b) at 0.25m/s. 195

Figure 91: TPU surface (a) before and (b) after the tests..... 196

Figure 92: NBR surface (a) before and (b) after the tests. 197

Figure 93: Micrographs of the wear scars under different conditions. . 199

Figure 94: Frictional energy vs mass loss..... 201

Figure 95: Comparison between test results at 0.1m/s for the (a) TPU and (b) NBR samples. 202

Figure 96: Comparison between test results at 0.25 m/s for the (a) TPU and (b) NBR samples. 203

List of Figures

Figure 97: Comparison between experimental and analytical flash temperature curves at (a) 0.1m/s and (b) 0.25m/s..... 208

Figure 98: Heat flux partitioning. 212

Figure 99: (a) TGA, (b) DSC and (c) FTIR characterization results on the surface of the most compressed seal section..... 221

Figure 100: Factors affecting the service life of seals. 230

LIST OF TABLES

| | |
|---|-----|
| Table 1: Main properties of the seal under study. | 48 |
| Table 2: Main characteristics of seals under study. | 96 |
| Table 3: Mechanical properties of seals under study. | 97 |
| Table 4: Test conditions. | 108 |
| Table 5: Wear results of the tested samples. | 122 |
| Table 6: Micrographs of the worn surfaces of seal samples A. | 127 |
| Table 7: Some of the most popular abrasive wear models [42]. | 130 |
| Table 8: Contact forces between the seals and the rod before the tests. | 131 |
| Table 9: Specific wear rates for seal B (NBR). | 134 |
| Table 10: Worn volume evolution of a differential of seal tested under different mounting conditions. | 136 |
| Table 11: Specific wear rates for seal A (TPU). | 141 |
| Table 12: Resultant contact and friction forces on the seal. | 145 |
| Table 13: Main properties of the polymer samples at room temperature (+25°C). | 171 |
| Table 14: Test parameters. | 176 |
| Table 15: Measured contact widths. | 206 |
| Table 16: Analytical models for flash temperature calculations. | 207 |
| Table 17: Main data used for temperature calculations. | 215 |

NOMENCLATURE

Chapter 2

| | |
|--------------------|---|
| δ_i : | rod/seal interference at concentric position |
| δ_r : | rod radial misalignment value |
| δ_φ : | mounting interference of a differential seal section which forms an angle φ with the misalignment direction |
| φ : | polar coordinate |
| μ : | friction coefficient |
| λ : | value of φ at which the contact between the seal and the rod is lost |
| e : | nominal gap between the seal and the bore |
| r_m : | average radius |
| r_i : | average radius at concentric position |
| T : | tangential force generated in the seal |
| F_f : | friction force between the seal and the rod |
| F_N : | normal force between the seal and the rod |
| F_{md} : | contact force between the seal and the rod in the misalignment direction |
| F_r : | contact force between the seal and the rod in radial direction |

Chapter 3

| | |
|--------------|--|
| δ_i : | rod/seal interference at concentric position |
| δ_r : | rod radial misalignment value |

| | |
|--------------------------------|--|
| μ: | friction coefficient |
| μ_{con}: | friction coefficient between the seal and the rod under concentric test conditions |
| d: | rod diameter |
| D: | travelled distance |
| F_N: | normal force between the seal and the rod |
| $F_{f,con}$: | friction force generated between the seal and the rod under concentric test conditions |
| F_r: | contact force between the seal and the rod in radial direction |
| H: | indentation hardness |
| k: | specific wear rate |
| K: | wear coefficient |
| s: | sliding distance |
| T: | tangential force generated in the seal |
| V: | volume removed from the surface per unit of sliding distance |
| W: | applied normal load |

Chapter 4

| | |
|-------------------------------------|--------------------------|
| ΔT_{nom}: | nominal temperature rise |
| ΔT_f: | flash temperature rise |
| Δm: | mass loss |

Nomenclature

| | |
|-----------------------------------|--|
| <i>A</i> : | contact area |
| <i>A_s</i> : | swept contact area |
| <i>α</i> : | heat partitioning coefficient |
| <i>b</i> : | half of the contact width |
| <i>ρ</i> : | material density |
| <i>C_p</i> : | heat capacity of a material |
| <i>ε</i> : | material emissivity |
| <i>K</i> : | thermal conductivity of a material |
| <i>χ</i> : | thermal diffusivity of a material |
| <i>μ</i> : | friction coefficient |
| <i>E_w</i> : | specific wear energy |
| <i>E</i> : | energy dissipated by friction |
| <i>F_N</i> : | contact load |
| <i>h</i> : | average convective heat transfer coefficient |
| <i>l_s</i> : | cross section thickness |
| <i>Pe</i> : | Peclet number |
| <i>q</i> : | heat flux |
| <i>q_s</i> : | heat flux entering the seal |
| <i>q_c</i> : | heat flux entering the counterface |
| <i>q_{tot}</i> : | total heat flux |
| <i>Q</i> : | generated heat |
| <i>T_b</i> : | bulk temperature |
| <i>T_{b_exp}</i> : | experimental bulk temperature |

| | |
|--------------|--------------------------------|
| T_c : | contact temperature |
| T_{fave} : | average flash temperature |
| T_{fexp} : | experimental flash temperature |
| T_{fmax} : | maximum flash temperature |
| T_{surf} : | surface temperature |
| v : | sliding velocity |
| W_{obj} : | radiation of the sample |
| W_{bb} : | radiation of a blackbody |

Chapter 1: Introduction, objectives and structure

1.1 Introduction

Elastomeric seals are components mounted in most of the devices where a fluid has to be sealed. Their use is extended to a wide range of industries such as the automotive, energy, aerospace and manufacturing industries. They are critical components in engines, landing gears, flight controls, airframes, transmissions and pumps, among others. Their function is to avoid the transfer of fluid from one area of the device to another, and even to avoid the entry of dirt particles into the system.

Sealing systems usually comprise the combination of different seal types. Rod seals, piston seals, wiper seals, guide rings and static seals are usually combined in order to avoid fluid leakages and the entry of dust into the system. In Figure 1 the different configurations forming the sealing system of a pneumatic actuator are shown. The function of the rod seal is to prevent fluid leakages to the ambient side. The wiper or scraper rings prevent penetration of dirt particles into the system. Rod and wiper seals work together to protect the system keeping it free from dust, water and other contaminants. O-rings are static seals used to avoid leakages through static parts of the system. Finally, the main role

Chapter 1: Introduction, objectives and structure

of the guide or wear rings is to accommodate the side loads maintaining, to the extent possible, the concentricity of seals. In some cases, sealing systems also include back-up rings whose main role is to prevent seal extrusion.

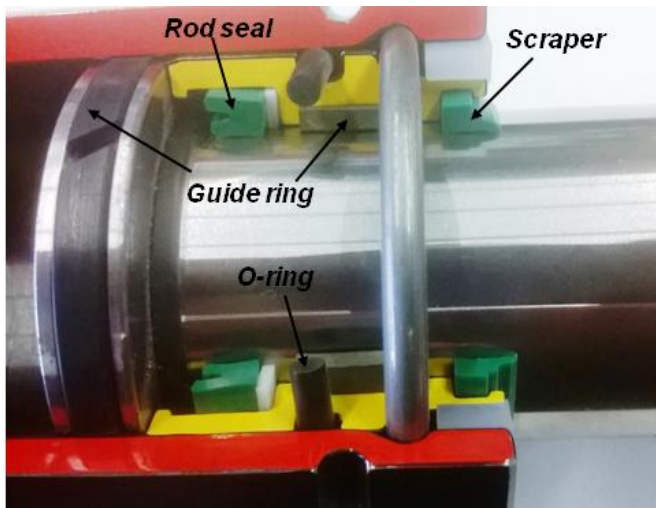


Figure 1: Sealing system of an actuator.

Seals are usually classified according to different criteria in: rod or piston seals, static or dynamic seals, and hydraulic or pneumatic seals. Whether the seal is dynamic or static, it must seal in general against two surfaces one of which is in relative motion to the other, in the former case, and stationary, in the latter case. Moreover, in both cases, a certain interference or compression is needed between sealing surfaces in order to prevent leakage. According to the type of relative motion, seals are usually classified in two main groups: rotary seals and reciprocating seals. Rotary seals are mainly used to provide adequate sealing between a rod and a bore rotating (or oscillating) one respect to

the other, while reciprocating seals are commonly used to seal two surfaces in a relative reciprocating motion.

Rotary seals, also known as “shaft seals”, could be found in a wide range of devices such as industrial pumps, couplings, gearboxes, turbines, engines, bearings, compressors and washing machines. Among all the rotary seal types, lip seals are the most used ones (in many catalogues referred as “radial oil seals”). Their geometry (Figure 2) is usually asymmetric and their main characteristic is that they have a sealing lip usually known as “dynamic lip”. Rotary seals are energized by a metallic garter spring whose main roles are: to provide a circumferential spring force, to increase their load carrying capacity and even to compensate the change in rubber properties that may occur due to temperature and chemical attacks. The spring material is usually steel SAE1074 or stainless steel AISI304 [1]. Designers adapt the stiffness of the garter spring in order to adjust the contact pressure provided by the seal to desired values. The different parts of a rotary seal are presented in Figure 2. Regarding materials, most of the rotary seals found in the industry are made from rubber materials such as: Nitrile Butadiene Rubber (NBR), Acrylic Rubber (ACM), Silicone Rubber (VQM), Fluorinated Rubber (FKM) and Hydrogenated Nitrile Rubber (HNBR). In general, the maximum operating pressure of shaft seals is about 0.5 bar and their maximum operating velocity can be up to 30m/s in many cases.

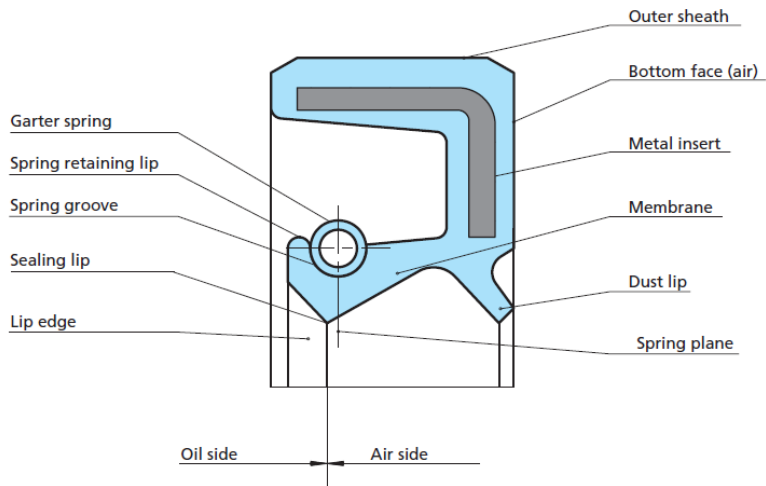


Figure 2: Basic shaft seal design (Source: Trelleborg [1]).

Reciprocating seals are usually found in devices such as pneumatic and hydraulic cylinders, injector pumps, brake cylinders, drill striker pistons, presses and injection moulding mills. Nowadays, there is a wide variety of commercial reciprocating seal geometries, dimensions and materials. Reciprocating seals are usually made from both elastomer and plastic. In the case of seals made from plastic materials, they must be energized to guarantee an adequate sealing due to their low load carrying capacity. In other words, plastic materials do not provide to the seal the necessary interference or contact pressure to seal, thus, an extra element that makes this function is needed. In particular, two energizing methods are mainly used: one method consists in introducing an elastomeric component (Figure 3a), and the other method consists in incorporating a metal spring in the U-seal or lip seal (Figure 3b). In the former case, the seal is composed of a plastic slipper seal and an energising O-ring which ensures enough interference even at low

pressures. In the latter case, the metal spring provides the primary sealing force at zero pressure, and as the pressure increases, the fluid energizes the seal.

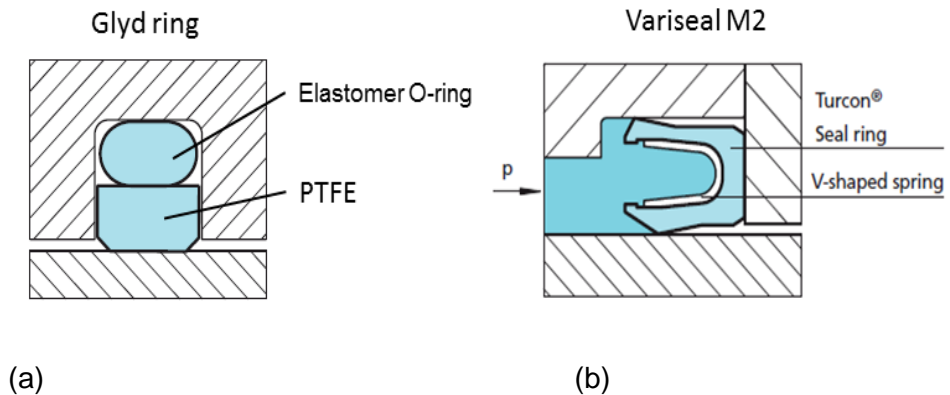


Figure 3: Typical reciprocating seal designs: (a) elastomer energized, and (b) with metallic U spring (Source: Trelleborg [2]).

The dynamic sealing mechanism of lip seals has been the subject of several studies during the last decades. Due to the geometry of the lip seal itself, as the shaft rotates, oscillates or reciprocates, a pumping mechanism is generated which originates a continuous oil film between the seal and the shaft. The pumping mechanism depends on two main factors: the asymmetric geometry of the lip seal and the texture or roughness pattern of the seal in the contact area [3]. Due to the geometric design, the inward pumping is stronger than the outward pumping and that is why the seal does not leak. Thus, a lip seal has to reach a compromise between sealing and good lubrication. Moreover, the shape of the cross-section of the seal affects its performance especially at low pressures. As the fluid pressure increases, the effect of the cross-section becomes more negligible [1].

Chapter 1: Introduction, objectives and structure

Several studies on sealing systems resulted in a wide variety of seal geometries and materials, and a better knowledge about the performance of sealing components during operation. Figure 4 presents some of the most typical rod and piston seal geometries for hydraulic actuators. In fact, the geometry of the dynamic sealing surface determines the most important sealing parameters such as the contact pressure between surfaces, friction, the film breaking ability, hydroplaning characteristics and contamination exclusion, among others [1,4].

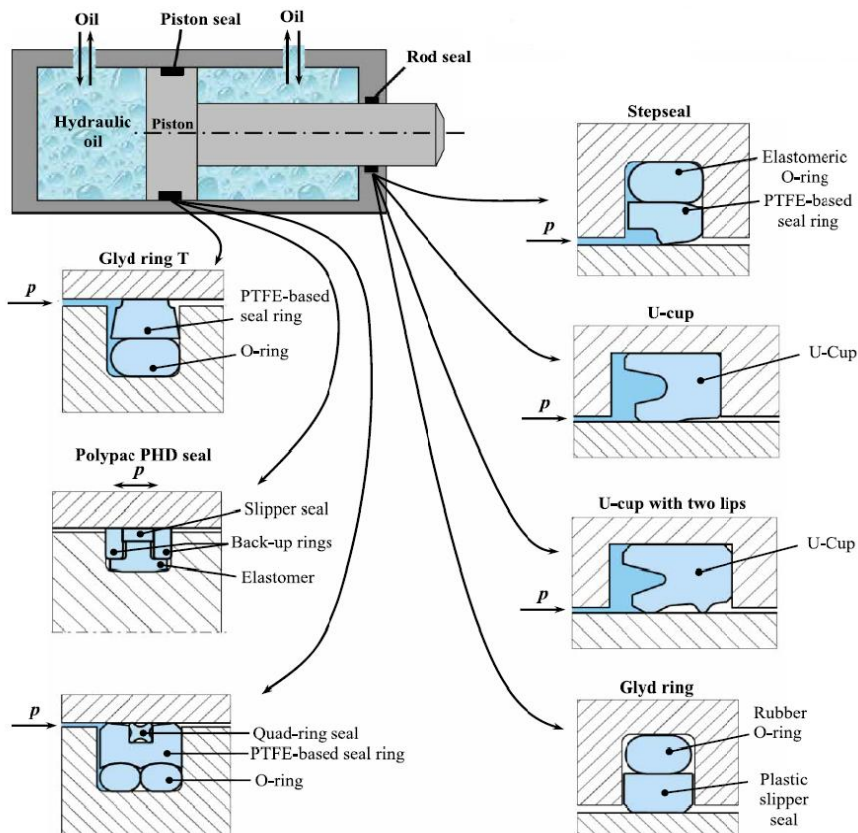


Figure 4: Geometry examples of rod and piston seals (Source: [6]).

Due to the wide range of parameters involved in every sealing operation, designing the most appropriate sealing system for a specific application is a challenge. In Figure 5 the main factors affecting sealing are illustrated. Geometry of the cross section, material and roughness of seals and its relative counterparts, sealed fluid properties, manufacturing tolerances and operating conditions of the system affect leakage rate, friction and wear of sealing components.

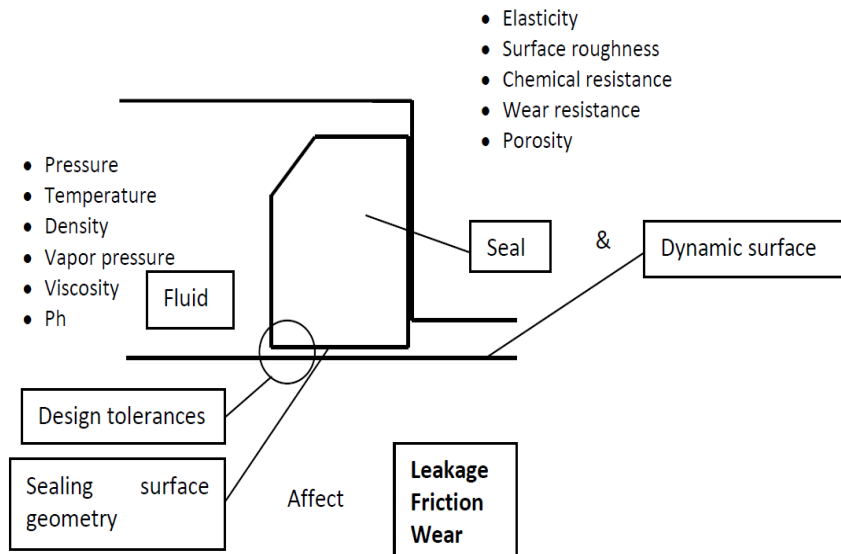


Figure 5: Factors affecting the seal performance (Source: [3]).

Selection of the best combination of seal materials and mating materials is essential in order to increase the efficiency and the service life of sealing systems. Due to the continuous demand of the market for higher and higher performance mechanical devices, continuous advances in seals and in sealing materials are needed. Low friction, low wear and low leakage are desirable properties of seals. Moreover, the costs associated with seal replacements or system downtimes due to seal

failures could be of up to millions of euros. Hence, polymeric materials able to provide increased service life of seals and advanced materials with added functionalities are continuously investigated. The research on the design of new sealing solutions requires a deep knowledge on different disciplines such as material science, contact mechanics, tribology and modelling, being of vital importance to involve all of these factors at concept stage.

Within this thesis, the effect of factors such as steel roughness, design tolerances, material and operating conditions, on seal performance will be investigated.

Materials

The different geometry types of seals existing nowadays combined with appropriate materials are able to cover most of the sealing applications demanded by the industry. Elastomers, thermoplastics and plastics play the most important role in fluid sealing due to their low cost and their viscoelastic properties. Polymers are based on long-chain molecules that are usually combined with other materials in order to get tailored properties. They present a non-linear stress-strain curve and their thermal and mechanical properties are very dependent on temperature. The wide range of polymeric materials existing nowadays enable sealing solutions covering diverse applications and operating conditions including low velocity (< 0.5 m/s) and high velocity applications (up to 15 m/s).

Elastomers consist of a very long chain of organic molecules with a repeated monomer unit. They usually include curing agents, fillers and

antioxidants. Hence, their properties are very dependent on their formulation and processing. Elastomers are subjected to curing processes to create cross-linking between molecules. When the polymer is mixed with a curing agent and subjected to heat or pressure, bonds are created between cross-links. Moreover, some fillers are usually added to the elastomers in order to increase their hardness. Thus, the properties and behaviour of elastomers will depend on the type of curing agent used in the process and on the material, size, shape and quantity of fillers added to be base material. In general, an elastomer could be defined as a type of polymer that presents high elasticity, visco-elasticity and a glass transition temperature far below from room temperature. Elastomers are suitable for sealing solutions because they easily accommodate different housings, tolerances, as well as pressure and temperature variations. Their adaptability is so good due to their: low elastic modulus, high elongation to break, high hysteresis and high resilience i.e. they accept large compressive, tensile and shear strains without permanent deformations.

The main properties of elastomers are listed below:

- Low elastic modulus (E) and high elongations to break: this fact involves that they could suffer high strains during installation. Furthermore, their low moduli allow them to accommodate more easily tolerances and mounting eccentricities. Figure 6 presents the stress-strain curve ranges of metals, plastics and elastomers.
- Non-linear stress/strain curve.
- Low hysteresis and high resilience: the combinations of these properties provide elastomers the capability to respond rapidly to

interference changes i.e. to pressure changes or to dynamic eccentricities, among others.

- Low creep: creep is a time-dependent deformation at constant stress and high temperatures. This property is very important since seals have to guarantee sealing for long periods.
- High Poisson ratio (ν): elastomers present a Poisson ratio of about 0.5 what means that they are almost incompressible.
- Their chemical resistance depends on elastomer formulation.
- Their thermomechanical properties are very dependent on temperature.

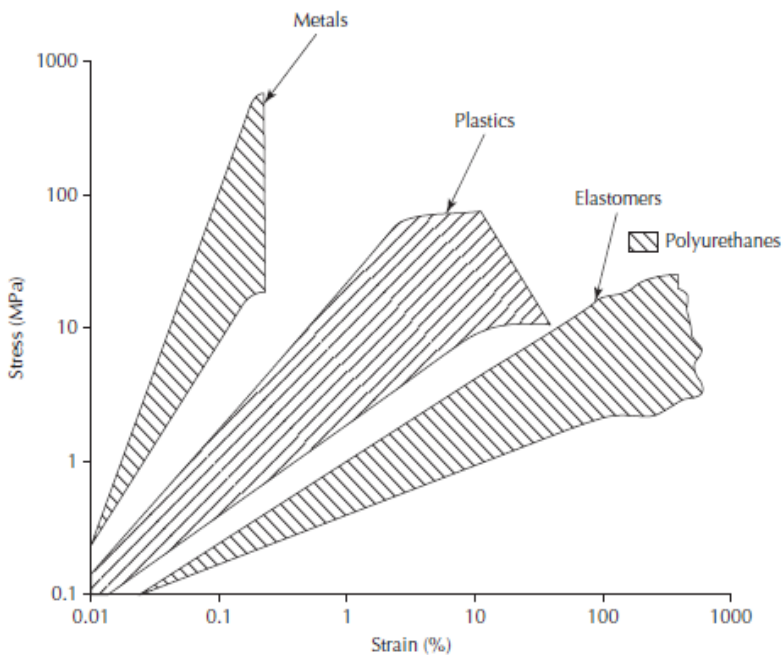


Figure 6: Stress/strain curves of different seal materials (Source: [5])

The principal limitations of elastomers are the following:

- Limited operating temperature range: the temperature is the main limitation for the use of elastomers in sealing applications. The most common elastomers suitable for dynamic sealing purposes cover a temperature range between -30°C and 100°C. Of course, nowadays there are elastomers able to cover broader temperature ranges.
- High friction: they usually generate high friction during sliding. For this reason, their use in dry application is quite limited.
- Fluid uptake: sealing fluids tend to dissolve in the surface of the material and diffuse into the interior until reaching equilibrium. This phenomenon softens the elastomer and may provoke an explosive decompression in the case of gases if a sudden depressurization happens.
- Strain memory: when seals remain stationary for long periods of time they tend to adhere to the metallic counterfaces, thus, they present high friction during the starting up of motion, and may cause stick-slip and vibrations.

Nitrile Rubbers (NBR), Polyurethanes (AU and EU), Hydrogenated Nitrile Rubbers (HNBR), Fluorocarbons (FKM), Perfluoroelastomer (FFKM), Ethylene Propylene Diene Monomer (EPDM), Fluorosilicone (FVMQ) and Silicone Rubber (Q) are some of the most commonly used elastomers for sealing purposes. This group of materials is able to cover a wide range of temperatures between -50°C and + 270°C under stable working conditions, and their used is generally limited to applications requiring sliding velocities lower than 3m/s. The working ranges of the most used elastomers are presented in Figure 7.

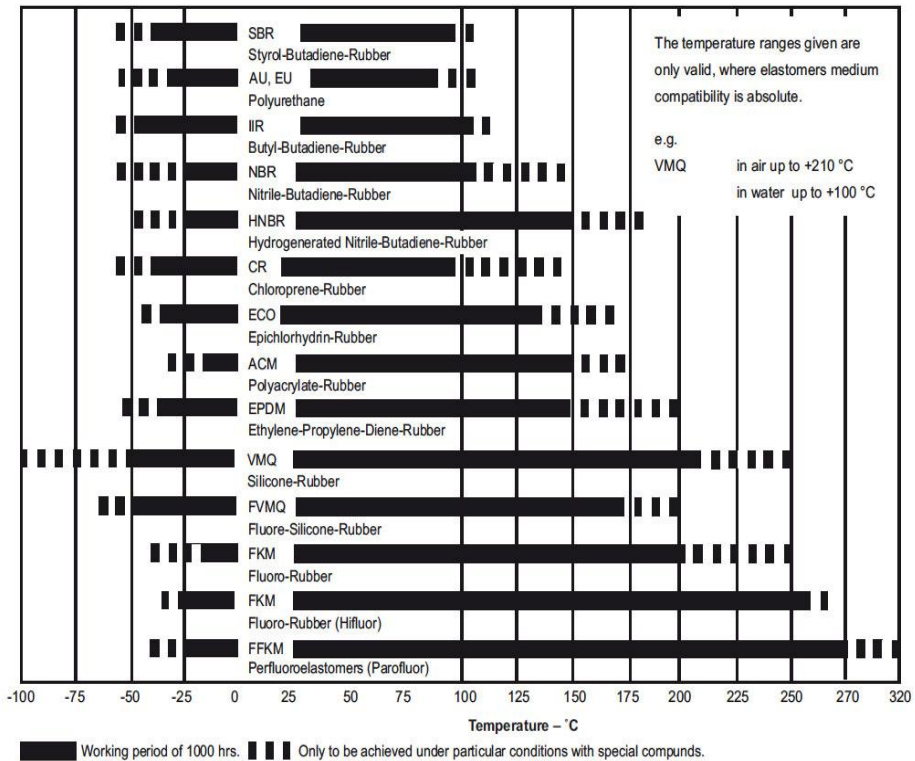


Figure 7: Operating temperature range of different elastomer materials (Source: Parker [8]).

Plastics represent another group of polymers commonly used in the sealing industry. The main difference between elastomers and plastics is that the recovery of the latter is much lower. Moreover, plastics present a lower friction and a wider operating temperature range, so they may be used in dry contact or poor lubrication applications. Furthermore, they do not present stick-slip and vibrations due to adhesion to metallic surfaces after remaining stationary for long periods of time as elastomers do.

The main advantages of plastics in comparison with elastomers are:

- Low friction and dry running potential: plastics generate lower friction forces than elastomers under the same operating conditions, so unlike elastomers, they can be used in dry contact or poor lubrication applications.
- Wide temperature range.
- Wide chemical resistance.
- Possible good wear resistance.
- Possible high hardness.

And the main disadvantages of plastics are the following:

- They have low load carrying capacity: metal springs or elastomeric components are added to plastic seals to enhance their load carrying capacity.
- Low elasticity: this fact makes the mounting or installation of plastic seals more complicated than in the case of elastomers.
- Creep: they are more likely to suffer creep i.e. sealing or variation of contact stresses with time. Thus, plastic seals are not very suitable for applications with cyclic forces acting on the seal.
- Their thermomechanical properties are very dependent on temperature.

Nowadays fillers are usually added to plastics in order to get tailored composites with an improved wear resistance, a higher load carrying capacity, a lower friction and a higher fatigue resistance. PTFE (Polytetrafluoroethylene) and PTFE composites are the plastics most commonly used in the sealing industry for their good tribological properties. Moreover, their working temperature range is around -190°C

and +260 °C, and they could be used in applications at velocities up to about 15 m/s under stable conditions. For tribological applications, PTFE is usually combined with carbon, bronze, glass fibres, graphite and molybdenum disulfide fillers in different percentages. PEEK (Polyetheretherketone) is another type of plastic commonly used in the sealing industry mainly used as a back-up ring and seal material for severe operating environments such as high temperature and pressure applications.

Thermoplastics are also widely used in the sealing industry. These materials combine properties of both plastics and elastomers. The most commonly used materials in the sealing industry are the polyurethane and the polyester.

Regarding the material of the **mating parts** in relative movement with seals, most of the manufacturers recommend to use chrome-plated 42CrMo4V according to DIN50602. The minimum hardness recommended is of HRC45 and the minimum depth of 2.5mm. The coating thickness should be in the range of 20 and 30 µm. The final roughness of the counterparts should be between 0.1 and 0.3 µm [2]. As shown in Figure 8, some polymers adapt better than others to the asperities of the metallic counterparts.

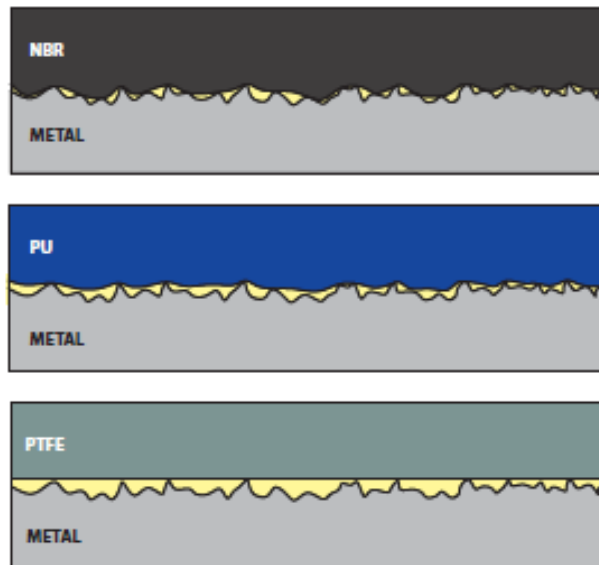


Figure 8: Contact between sealing lips and metallic counterparts
(Source: Kastas Sealing Technologies AS [7]).

Main failure mechanisms

Elastomeric seals are manufactured so that they have a minimum theoretical service life which varies depending on the final user specifications. Nevertheless, there are many factors that are inevitable or very difficult to control and that may lead to a premature seal failure. Maintenance costs associated with replacement of seals and downtimes due to failures of specific cylinders may range from a few hundreds of euros to millions in the case of offshore applications. Moreover, the failure of seals may even lead to a catastrophe in specific applications. In any case, it is of vital importance that the final user meets the specifications recommended by seal manufacturers regarding operating conditions, mating part characteristics and fluid compatibility.

The most evident sign of seal failure is an excessive fluid leakage. The causes of failure might be diverse and their origin very different. In general, the main causes of seal failure could be divided as shown in Figure 9 [5].

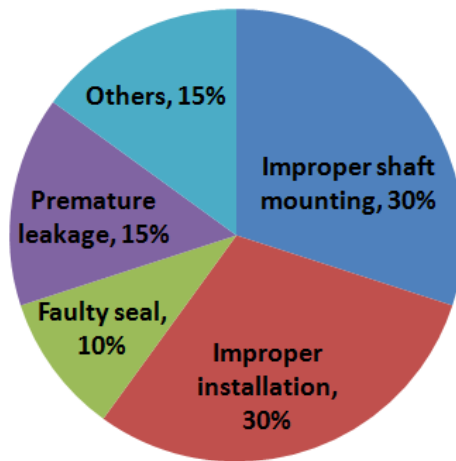


Figure 9: Pie chart of the main seal failure causes.

Hence, most of the seal failures are attributable to an improper shaft mounting (eccentricities), an improper seal installation, a faulty seal, a premature leakage and to other causes such as vibrations/contaminants/lubricant incompatibility and overheating.

Figure 10 summarizes the main failure mechanisms of radial shaft seals and the most common causes of these failure types. According to this classification, improper handling and manufacturing, contamination, vibrations, eccentricities and incorrect operating conditions are some of

the main seal failure causes, which lead to chemical and thermal damage of the seal as well as to an excessive wear.

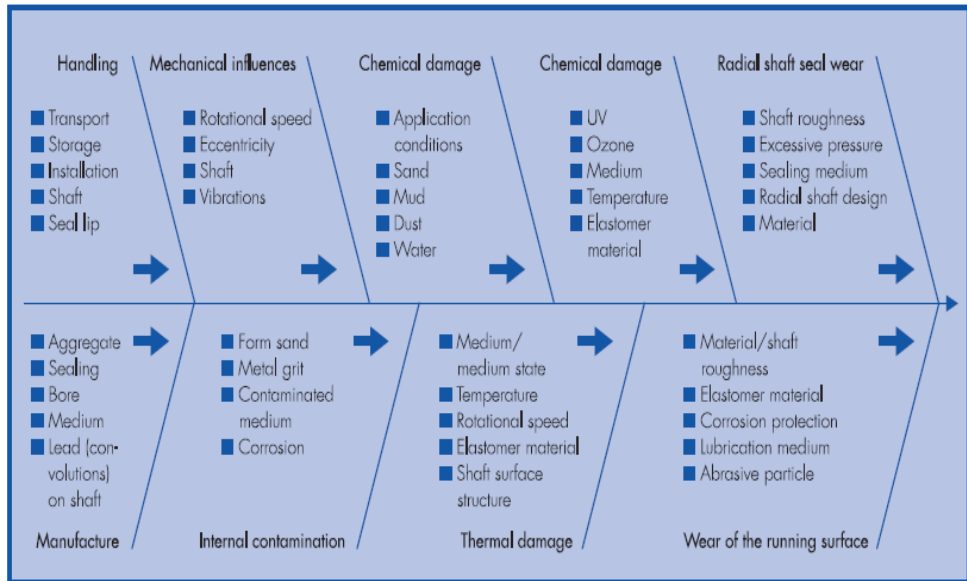


Figure 10: Possible causes of failure for radial shaft seals (Source: Freudenberg Simrit GmbH & Co.KG [9]).

Moreover, it is important to highlight that the cause of leakage or failure hardly ever is just one i.e. seals usually fail due to a combination of different factors. In any case, visual inspection and surface analysis of the system are the most important actions to carry out when trying to identify main causes of seal failure [5].

When there is leakage from new, and there is no apparent damage in the seal or no wear debris, probable causes for leakage are:

- Insufficient seal interference or contact pressure.
- High viscosity oil causing excessive oil film thickness.

- Excessive application of grease.
- System vibrations so that the sealing lip cannot follow them.

In other cases, during visual inspection mechanical damage may be appreciated on seals. In general, main sources of problems for mechanical damage of seals are the followings [4,5,9,10,11]:

- Incorrect roughness of the rod and/or the seal housing: rough surfaces may cause abrasive wear of seals.
- Use of inadequate assembly tools which may cause damage of the seal during its mounting (see Figure 12).
- Inadequate protection or handling of shafts.
- Inadequate seal material.
- Hardening of the material due to an excessive pressure or temperature: hardening of elastomers could be due to the underestimation of the frictional heating. Hardening impairs the elasticity and resilience of the polymer and leads to micro asperities deformation, weakening the dynamic sealing mechanism.
- Compression set of the seal: compression set is the permanent deformation remaining when the force is removed. It reduces sealing forces what results in poor sealing at low pressure. In general, compression set occurs due to high temperatures.
- Corrosion of the shaft and a subsequent malfunction of the system.
- Ingress of contamination that provokes premature wear.
- Poor lubrication or failure of the lubricant.

- Dirt and wear particles that cause severe damage on seals. Thus, continuous maintenance and filtering of the hydraulic fluid is required. Contaminants and wear particles cause abrasive wear in the seal and in its mating parts, and create scratches that may lead to leakage if they become too long.
- Dieseling damage caused by the air bubbles present in the oil: when the system is not purged or there is an excessive pressure rise, there may be air bubbles in the oil that may cause burning of the seal (Figure 11).



Figure 11: Dieseling damage on a seal (Source: [11]).

- Chemical and thermal attack.
- Mounting eccentricities: the combination of static and dynamic eccentricities may cause leakage. Even with lip seals which are more tolerant to eccentricities leakage may happen at high velocities because the seal can not follow the shaft. In any case, mounting eccentricities will decrease the service life of seals.



Figure 12: Seal damage due to an incorrect mounting (Source: IK4-Tekniker).

Most of these failure causes are common for static and dynamic seals, and every type of seal material. Similarly, failure causes of pneumatic seals working under dry conditions are similar to those of seals working under lubricated conditions; however, pneumatic seals are more prone to fail faster since the overheating of the material is more important. Moreover, these cause of failures are also common both for rotary and reciprocating seals. Nevertheless, in the case of reciprocating seals more failure sources such as the followings could be mentioned:

- Leakage from new due to excessive velocity that originates a too thick fluid film.
- Extrusion due to excessive pressure or temperature: extrusion usually occurs when the fluid pressure forces the seal into the clearance gap between the sealing surfaces. As a consequence, leakage and thus a premature failure of the seal may occur. Moreover, when extrusion occurs, the generated friction raises so

that the heat generated due to friction also increases. High temperatures may change the properties of the polymer substantially and cause compression set of the seal. In Figure 13 two images of seals that failed due to extrusion are shown. The best way to prevent extrusion is to design the sealing system so that the clearance or gap behind the seal is as small as possible. Other possible causes of extrusion are high operating temperatures, the use of soft materials, side loads and chemical incompatibilities, among others. Backup rings made of hard materials are usually used in order to protect the seals against extrusion. Introducing wear rings to prevent side loadings and considering harder seal materials may also help to solve extrusion problems in sealing applications.

- Overpressure generated by the reciprocating motion.
- Scoring to the seal surfaces originated by debris in the oil or damaged mating faces.

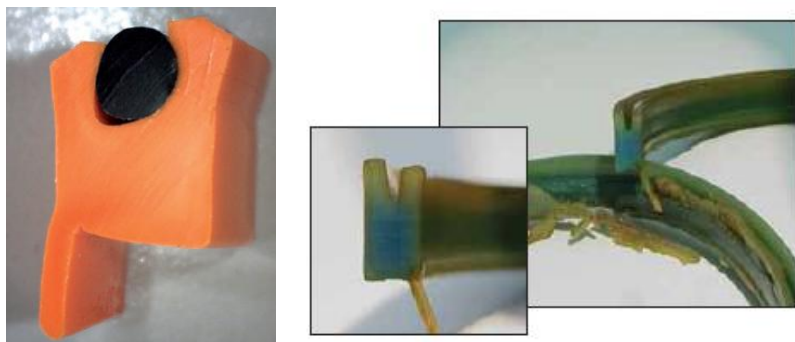


Figure 13: Extrusion damage (Source: Parker Hannifin Corporation [4]).

Chapter 1: Introduction, objectives and structure

The main failure mechanisms arising from all the mentioned failure sources are usually the following: thermal degradation of the seal, chemical damage, crack formation, seal distortion and excessive wear of the seal.

If there are carbon deposits around the sealing lip or axial cracks on it, the main cause of seal failure may be an excessive temperature i.e. material overheating. Cracks and carbon deposits are usually evident in conjunction. In the case of plastic seals, there may be also signs of plastic flow and extrusion. Solutions to this problem could be changing the seal material, the rod surface conditions or the oil in order to reduce friction, or to select another type of oil able to withstand higher temperatures.

In cases where the seal is distorted or it presents blisters, the main cause of seal failure may be incompatibility problems between the seal material and the lubricant. These kinds of compatibility problems often arise because the lubricant additives chemically react due to a temperature rise of the lubricant. In particular, the problem may be severe if both the fluid and the seal material have a similar molecular structure. Hence, in order to know if a specific fluid and a specific seal material are compatible, compatibility tests are usually carried out according to standards such as the ASTM D471 [12].

Regarding wear, it is the result of the relative sliding motion between two bodies in contact rather than a specific property of a material. Possible causes of failure when an excessive wear of seals is observed may be: inadequate cleaning or assembly, or presence of debris in the sealing area, excessive pressure or duty, and insufficient lubrication. The main

wear mechanisms of a polymer sliding against a metal surface are: adhesion, abrasion, fatigue and chemical wear. Depending on the properties of the materials themselves and on the sliding conditions, one wear mechanism or the other will be more dominant during the wear process. The main characteristics of each of these wear types are the following [13-17]:

- *Adhesive wear*

Adhesive wear is associated with the formation of adhesive bonds at the interface. Adhesive wear of polymers usually happens when the adhesive bonds formed between materials in contact are higher than the cohesive strength of the polymer. When the adhesive junctions fail, some material is usually transferred from one surface to another, and other parts are removed from the friction zone as wear debris. In the case of polymer-metal contact, under certain conditions, a thin film of the soft material (polymer) is transferred onto the hard surface (metal). This film is known as “transfer film”. If the transferred polymer is carried away from the steel surface and it is continuously formed, the wear rate will increase. If the transfer film holds in place, by contrast, the friction force will increase but the wear change will be insignificant. The strength of adhesion is found to be related to the presence of reactives such as fluorine in the polymer. Polymers adhere to other materials by means of Van der Waals forces. Even if adhesive forces in polymer-metal contact are not strong enough to induce the rupture in the contact, they are a big source of friction resistance. In some

cases, the hard material could be even transferred on the soft surface.

- Abrasive wear

Abrasive wear maybe is the most common type of wear. The simplest model of abrasive wear is that in which hard particles indent and are forced across the surface of the material. In other words, when two bodies are in contact under the action of a normal load, and both materials have different hardness, the harder surface may penetrate the softer one. Hence, the abrasive wear mechanism is mainly dominated by plastic deformation and fracture processes. In the case of elastomers, the main wear mechanisms of elastomers sliding against blunt particles are tensile tearing and fatigue. In fact, the height of asperities or the roughness of the contact bodies also influences the resultant wear of the parts. When a polymer is sliding against a very rough surface, the main wear mechanism will be abrasion. The wear rate of a specific material is determined by the penetration depth of asperities into the polymer. In fact, the evolution of the wear varies with time.

- Fatigue wear

The friction type that leads to this type of wear is the “friction fatigue”. Fatigue causes change in materials as a result of repeated stressing. Hence, even if fatigue wear is usually associated with rolling contacts, asperities also are subjected to cyclic stressing during sliding, leading to stress concentration effects, and the formation and propagation of cracks. Friction

fatigue takes place at the surface and sub-surface regions where the maximum tangential stresses occur. In general, for low friction coefficients, the maximum shear stress point is below the surface while it emerges on the surface as the friction coefficient increases. Furthermore, the initiation of fatigue cracks is assisted by the defects, which are responsible for stress concentration. In addition to crack generation, fatigue may also result in the pitting and delamination of the material. In many cases wear debris is formed as a result of the growth and intersection of small cracks at the surface of the polymer.

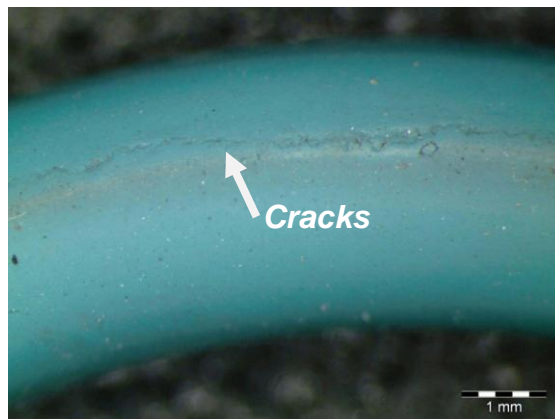


Figure 14: Fatigue damage on a seal (Source: IK4-Tekniker).

- *Chemical wear*

A tribo-mechanical reaction due to the interaction between the polymer and the metal may be originated as a result of diverse reasons such as the elevated interfacial temperatures originated due to frictional heating, and reactions originated by the clean metal or even by the fillers of the polymer. The surfaces react with the environment, creating reaction products deposited on

the surfaces. The reaction products are removed afterwards from the surface due to crack formation or abrasion.

In general, as sliding proceeds, the typical wear process usually undergoes three different stages [18]: a first running-in stage in which the wear uniformity in the contact pair is being set up by elimination of the micro-asperities of the surfaces, a second stationary stage where a constant wear rate has been attained and the surfaces are worn in a steady and uniform way, and a third accelerated or catastrophic wear stage where the wear rate increases in an exponential way and leads to catastrophic failure. In order to characterize long-term properties of systems only the steady state conditions are useful [18]. Thus, most of the existing wear models are only applicable at that stage.

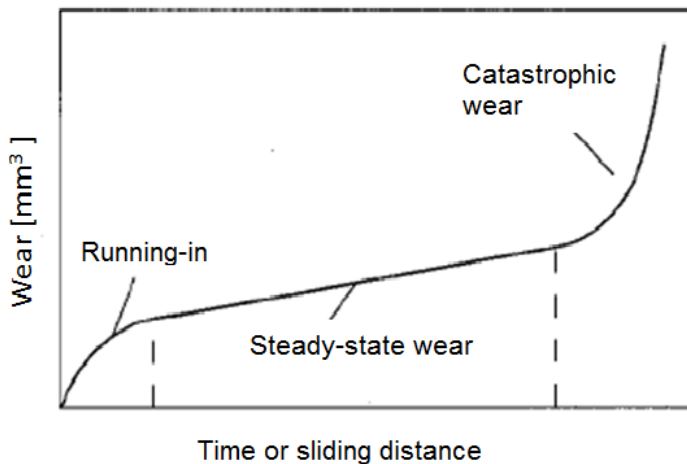


Figure 15: Typical stages of wear processes.

1.2 Objectives

Understanding the main wear mechanisms of elastomeric seals and building reliable models able to predict their life expectancy is a complex task. This thesis deals with the study of the effect of misalignments on the tribological performance of seals in an attempt to contribute to the lack of studies related to this issue. In fact, as pointed out in the previous section, among the seal failure factors that are unavoidable and difficult to control, mounting misalignments are one of the most relevant. Source of mounting misalignments comprehend mounting errors and incorrect design or manufacturing tolerances, among others. The main effect of rod mounting eccentricities is a non-uniform contact force distribution along the seal. As a consequence, some sections of the seal will be subjected to an excessive contact pressure (radial overload) whereas in other sections, the contact between parts may be lost. In the latter case, the immediate consequence is the leakage of the seal. In the former case, immediate consequence of an incorrect seal mounting is a premature seal failure due to radial overloads. Nevertheless, even if mounting eccentricities affect considerably the life expectancy of seals, their effect on the tribological performance of seals has not been studied in detail up to now. Hence the present work is mainly motivated by the need to understand how the inevitable mounting misalignments alter the performance of seals and their life expectancy.

In particular, this thesis deals with the study of the effect of rod to bore misalignments on the main tribological parameters (contact forces, friction, wear and contact temperature) by means of the combination of analytical, numerical and experimental techniques. Hence, the study

herein presented may be extrapolated to research on the performance of those seals mounted in mechanical components usually subjected to considerable misalignments such as couplings, bearings and valves, among others.

Due to the lack of studies related to the life expectancy of elastomeric seals, this work aims to contribute to this issue by determining the effect of unavoidable mounting misalignments on the tribological performance and life expectancy of elastomeric seals. To achieve this aim this thesis pursues other intermediate goals:

- To develop a methodology for carrying out a tribological characterization of seals as complete as possible combining analytical, numerical and experimental techniques.
- To design specific toolings and test rigs that enable evaluating the effect of misaligned seals, and to gain knowledge on this topic to be able to offer solutions to the industry.

Hence, in order to fulfil the main goals, the following research work has been carried out within this thesis:

- Development of a procedure to build an analytical tri-dimensional eccentricity model of seals that enables calculating the contact force distribution along them as a function of rod misalignment. This model may be useful for design purposes in order to avoid high computational costs associated with numerical 3D simulations. Moreover, the contact force eccentricity models establish the basis for further investigations about the effect of

rod to bore misalignments on the main tribological parameters: friction, wear and contact temperatures.

- Experimental validation of the contact model developed through a specific test rig designed for this purpose.
- Experimental tests on rod lip seals under both concentric and controlled rod to bore eccentricities, in order to investigate the effect of radial overloads on the service life and friction of seals.
- Development of a methodology to estimate the contact temperature distribution on seals in order to overcome the challenge of measuring contact temperatures. The methodology herein proposed enables estimating the contact temperature distribution on seals during operation combining analytical models, thermo-mechanical properties of the materials involved and some experimental inputs. This methodology may be useful for the industry considering the lack of applicable experimental techniques and given the low thermal resistance of elastomers.
- Validation of the models and methodologies developed in this thesis, and demonstration of their utility, through case studies of specific industrial applications. In particular, in line with the topic of this thesis, the models have been used for calculating contact force distributions, wear rates, and friction and contact temperature distributions of seals operating under concentric and eccentric mounting conditions.

1.3 Beneficiaries

This thesis is focused on the study of the effect of design, manufacturing and mounting on the tribological performance of elastomeric seals. Direct beneficiaries of this work may be not only seal designers and manufacturers but also a wide range of companies with sealing components mounted on their products or working tools.

The knowledge gained from this work is also very useful for IK4-Tekniker, a research centre where the author of this thesis works as a researcher in the Tribology Unit. IK4-Tekniker built a test rig for sealing system characterization (described in Chapter 3) in order to offer technological services to the industry. In fact, the aim of IK4-Tekniker is to gain knowledge about the factors affecting the service life and wear processes of elastomeric seals. In this case, the work described in this thesis has been useful in order to:

- Develop a methodology for carrying out a tribological characterization of seals as complete as possible combining analytical, numerical and experimental techniques.
- Be sensitive to the importance of the accuracy of mounting and design tolerances of the seal seats and their counter-parts.
- Meet the challenge of measuring contact forces between seals and their mating faces through the development of a tri-dimensional eccentricity model that enables calculating the contact forces distribution on seals.

- Study the effect of mounting eccentricities not only on the contact force distribution under static conditions but also on friction and wear under dynamic ones.
- Gain experience about the design of sealing systems in order to advise clients on their own specific applications.
- Gain experience on the design of specific toolings and test rigs that enable evaluating the effect of misaligned seals, in order to be able to offer solutions to the industry.
- Be sensitive to the importance of the selection of the surface conditions of the metallic parts in contact with the dynamic seals in terms of temperature rise, friction and wear.
- Identify the main wear mechanisms and failure modes of seals made of the elastomers most commonly used in the sealing industry.
- Develop a procedure that allows estimating the contact temperature of seals based on the results obtained from friction tests on seals.
- Diagnose the causes of sealing systems failures.
- Extrapolate the conclusions obtained from this work to the actual behaviour of many mechanical components that usually operate under eccentric conditions such as couplings, valves and bearings.

And finally, it results obvious that the work is interesting also from the academic point of view. This interest is substantiated by one of the co-directors of the thesis, from the Department of Mechanical Engineering of the University of the Basque Country at Bilbao.

1.4 References

- [1] “Rotary Seals”. Trelleborg Sealing solutions; 2009.
- [2] “Hydraulic Seals-Linear”. Trelleborg Sealing solutions; 2011.
- [3] Müller HK, Nau BS. Fluid sealing technology: Principles and applications. Marcel Dekker; 1998.
- [4] “Fluid Power Seal Design Guide”. Catalog EPS 5370. Parker Hannifin corporation. Engineered Polymer Systems Division. 2014.
- [5] Flitney RK. Seals and sealing handbook. 5th edition. Elsevier; 2007.
- [6] Nikas GK. Eighty years of research on hydraulic reciprocating seals: review of tribological studies and related topics since the 1930s. Proceedings of the Institution of Mechanical Engineers, Part J: Journal of Engineering Tribology 2010; 224(1), 1–23.
- [7] “Hydraulic and pneumatic Seals-Technical catalogue”. Kastas; 2009.
- [8] “O-ring handbook”. Parker Hannifin corporation. O-ring Division Europe; 2010.
- [9] “The Simmerring. Basics for preventing damage”, Freudenberg Simrit.
- [10] Chandsekaran C. Rubber Seals for Fluid and Hydraulic Systems. PDL Handbook Series. First edition. Elsevier; 2010.
- [11] “Failure analysis Guide: Eliminate Potential and Future Problems”. System Seals.
- [12] ASTM D471: “Standards Test Methods for Rubber Proper Property- Effect of Liquid”.
- [13] Friedrich K. Friction and wear of polymer composites. Elsevier; 1986.

- [14] Sinha SK., Briscoe BJ. Polymer Tribology. Imperial college Press; 2009.
- [15] Tsukruk VV, Wahl KJ. Microstructure and Microtribology of Polymer surfaces. In: Briscoe BJ. Chapter 1: Tribology of Polymers : A Perspective, American Chemical Society; 2000, p. 2–22.
- [16] Briscoe BJ, Sinha SK. Wear of polymers. Proceedings of the Institution of Mechanical Engineers, Part J: Journal of Engineering Tribology 2002; 216(6), 401–413.
- [17] Briscoe B. Wear of polymers : an essay on fundamental aspects, Tribology International 1981; 231–243.
- [18] Martínez FJ, Canales M, Bielsa JM, Jiménez MA. Relationship between wear rate and mechanical fatigue in sliding TPU–metal contacts. Wear 2010; 268(3-4), 388–398.

Chapter 2: Tri-dimensional eccentricity model of seals

2.1 Introduction

As introduced in the previous chapter, among all the existing seal variety, lip seals are maybe the most used ones. Lip seals may be found in applications such as pneumatic and hydraulic actuators, engines, machine tools and gas springs, among others. They are characterized by a sealing lip, also known as dynamic lip, properly designed to ensure the sealing and pumping mechanisms of a specific fluid under a wide range of working conditions. Moreover, the design of lip seals must reach a compromise between dynamic sealing and good lubrication [1].

The performance of a specific lip seal is affected by several factors such as the geometry, the material and the roughness of the seal and of its mating surface, and its particular operating conditions. Lip seals provide a unidirectional sealing and their contact pressure profile under particular sealing conditions strongly depends on the lip angles at the air and fluid sides. Moreover, the performance of a lip seal is very influenced by the shape of its cross section, especially at low fluid pressures [2]. Some designs may include two lips in the sealing area in order to enhance the sealing capability at low pressures and to avoid the entry of dirt from the side opened to the atmosphere. Certain designs for extreme operating conditions may include elements moulded onto the air-side of the lip in order to provide an additional inward pumping [3].

In general, most of the lip seals available for low velocity reciprocating applications (velocities lower than 0.5m/s) are made of Polyurethanes (PU) or Nitrile Rubbers (NBR) due to the low cost and good performance of these materials. Both materials, however, have a limitation in temperature since their maximum operating temperature under stable conditions is about 100°C. Furthermore, this temperature threshold limits the operation temperature of seals because of the temperature rise due to frictional heating phenomena [2,4]. Thus, the main alternative in applications with high sliding velocity requirements is a seal made of PTFE (Polytetrafluoroethylene) composites because of their higher thermal resistance and low friction properties. Regarding the roughness, both the asperities of the lip and the roughness of the counterparts play an important role in sealing operation [5-7].

Contact pressure distribution is one of the most important parameters to take into account when a specific seal is being designed. Seals are mounted in grooves with a certain interference in order to ensure an appropriate sealing at the interface and prevent leakage even at low fluid pressure. Contact pressure between seals and the mating surfaces depends on the interference value and the geometry of the sealing surface, among others. Unfortunately, measuring the contact pressure between a seal and its counterparts could be a difficult task. In order to measure static contact pressures, technologies such as photoelastic techniques [9], pressure film sensors [10,11], radial force integration techniques [12] and manganin wires [13], among others, have been widely used. In any case, however, there is not a standard technique or

device useful to measure contact forces in a rod or piston seal regardless the seal size.

In most of the cases, a seal fails as a result of a combination of factors [14,15]. Radial overload due to rod misalignment, improper shaft preparation, overheating, lubricant failure and extrusion are some of the most common causes of seal failure. This chapter is focused on the study of the effects of an eccentric mounting on the contact force distribution of a seal. In fact, an eccentric mounting leads to an irregular distribution of contact pressure, which affects seal performance [16]. Moreover, the interference stress field originated under eccentric mounting conditions of the rod tends to twist the seal in the groove. Lip seals, however, are quite resistant to spiralization due to their design itself. Furthermore, the capacity of a specific seal subjected to an eccentric mounting to follow the rod depends on: the lip seal design, the material and any temperature effects on the resilience of elastomers [14].

Some authors studied the relation between rod eccentricity and the leakage rate of rotary rod lip seals for different speed regimes: Mokhtar et al. [17] experimentally demonstrated that an increase in shaft radial eccentricity results in higher leakage rates, whereas an increase in shaft angular misalignment results in lower leakage rates. Besides, results showed that for a specific shaft misalignment, an increase in shaft rotating speed results in lower leakage rates, however, increasing the fluid pressure the opposite effect is achieved. Amabili et al. [18] found a relationship between shaft rotating speed and dynamic eccentricity. Results showed that for any eccentricity, the leakage rate increases with

the shaft rotating speed until a maximum is reached, then the leakage rate decreases with speed. The lower the dynamic eccentricity the higher the speed at which this maximum leakage rate takes place. Conte [19] analytically studied the minimum fluid pressure needed to prevent fluid leakage when a rod angular eccentricity exists, modelling a rod lip seal in 2D as a link connected to the seal body by means of a torsional spring. Leakage rate as a function of fluid pressure was also studied in the same work.

Of particular relevance are also the studies dealing with finding a correlation between the contact force and the sectional compression level of O-rings. Lindley et al. [20,21] offered a non-dimensional force-deflection relationship for an O-ring based on Hertz theory. This relationship was composed by a term derived analytically assuming plain strain conditions and another correction term for high compression levels of the seal. Green et al. [22] presented general expressions of hyperelastic O-ring seal stiffness based on numerical data and compared the results with those estimated by Lindley. They also found that the differences between the results obtained from axisymmetric and plain strain loading conditions increase with the seal compression level. Some years later, Hyung-Kyu Kim et al. [23] analyzed elastomeric O-ring contact forces under compression, comparing Lindley's analytical formula results with numerical and experimental results obtained by means of an opportune test rig. They found that the results by Lindley's formula were closer to numerical results than to the experimental ones. They also found that numerical results underestimated contact forces under compressions up to 24% and overestimated them for compressions of 32%. So far, no exact analytical model of the contact

force variation as a function of compression level has been found. The main cause of difficulties to reproduce the contact force of seals regards elastomeric materials behaviour, that is, variable elastic modulus, Poisson ratio closed to 0.5 and stress relaxation phenomenon.

Tasora et al. [24] presented a method for characterizing the deformation of an elastomeric seal under static conditions. They carried out experimental tests on a nitrile based rotating lip seal subjected to different radial loads. These results were used to calibrate a tri-dimensional finite element model by means of Mooney-Rivlin parameters and to introduce the most adequate contact conditions at different temperatures. Consequently, numerical models were used to study the effect of static interference, temperature and radial displacements on the contact force between the seal and the rod. In [34] Frölich et al. presented a simulation axisymmetric approach to calculate numerically the resultant contact force between a seal and its mounting shaft, and they use those results for predict numerically the wear, friction and temperature on seals.

This chapter aims to study the effect of an eccentric mounting on seals concerning contact force distribution along the seal and it has as main objective obtaining a reliable analytical 3D rod radial misalignment model for rod seals. Hence, the tri-dimensional analytical model herein presented enables calculating contact force distribution on seals as a function of rod position. The model not only includes normal forces between the seal and the rod, but also tangential and friction forces generated due to rod misalignment. In the specific, a thermoplastic polyurethane (TPU) reciprocating lip seal has been considered as case

study. However, the modelling method herein presented can be applied to any seal geometry. The main advantage of the modelling procedure is that it allows estimating the contact force distribution in the whole seal regardless of rod eccentricity. As a starting point, a quasi-static case was considered in absence of any supply pressure, in order to separate the contribution of the preload and the fluid pressure to the resultant contact pressure. The hyperelastic material was defined by means of a Mooney-Rivlin formulation. Thus, the proposed model is based on the characterization of the seal as an ensemble of springs subjected to traction/compression.

The analytical model is completed and adjusted by combining a geometrical interference model with the results obtained from numerical simulations. Moreover, the model was validated by means of experimental tests carried out on a test rig designed and assembled for this purpose, in order to measure the resultant contact forces on seals when the rod is radially displaced.

2.2 Static and dynamic eccentricities

Eccentricities are present in all the mechanical systems even if a lot of care is taken during the manufacturing and mounting phases. Eccentricities can be usually classified in the following types attending to their nature [28]:

- Static eccentricities (shaft to bore misalignments),
- Dynamic eccentricities (run-out).

The current work only deals with the study of static eccentricities that may be defined as the amount that the shaft or rod centre is misaligned

relative to the bore centre. In general, the static eccentricity will be the result of a combination of mounting eccentricities and manufacturing tolerances. The former type occurs due to an eccentric mounting of the shaft with respect to the bore centre. The origin of the latter, however, is an error in the manufacturing tolerances of both the shaft and the seal seat (groove). A schematic view of a shaft to bore misalignment is shown in Figure 16.

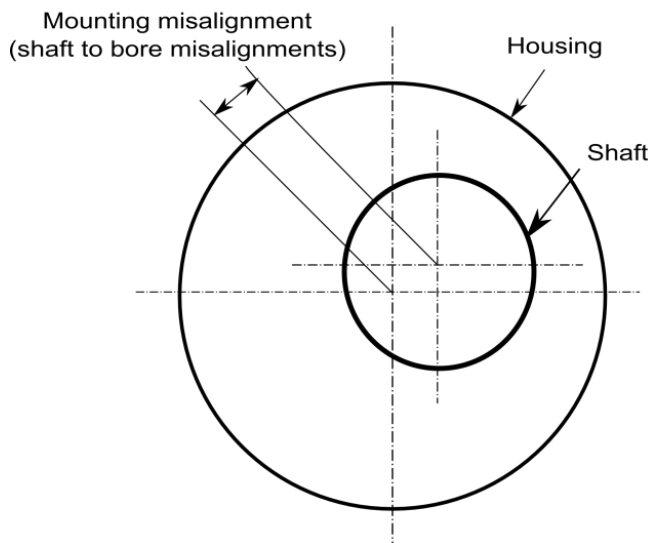


Figure 16: Static eccentricity or shaft to bore misalignment.

The main consequence of an eccentric mounting of seals is the reduction of the seal service life caused by a non-uniform contact pressure distribution and subsequently by a non-uniform wear distribution. Moreover, when the eccentricities are big enough, contact between metallic parts (rod and bore) may happen and seals may leak even if they are new. This contact between the rod and the bore may cause severe wear of parts and also system vibrations.

Dynamic eccentricity may be defined as a time dependent radial displacement of the seal. This type of eccentricity is caused by dynamic effects of the system itself such as vibrations, manufacturing inaccuracies, instabilities, etc. In the case of rotary components, dynamic eccentricities are also known as run-out and could be defined as the amount that the seal does not rotate around its centre. Figure 17 shows a schematic drawing of dynamic run-out.

Dynamic eccentricities expose the seal to repetitive loads and dimensional changes that may:

- Cause accelerated extrusion damage,
- Lubricating film breaking down,
- Fluid leakage since the seal may not be able to follow the motion of the shaft,
- Cause severe abrasion to the mating parts,
- Accelerate the wear process of the seal because wear particles may be trapped in the extrusion gap,
- Cause metal to metal contact between the rod and the bore.

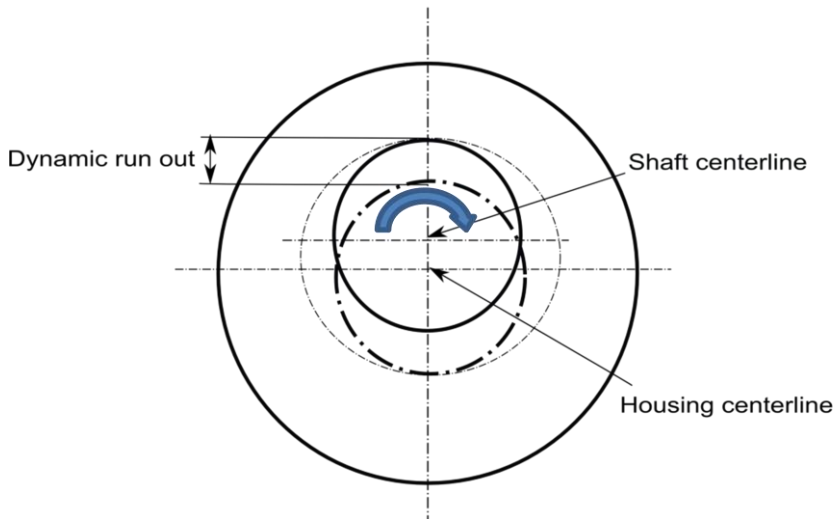


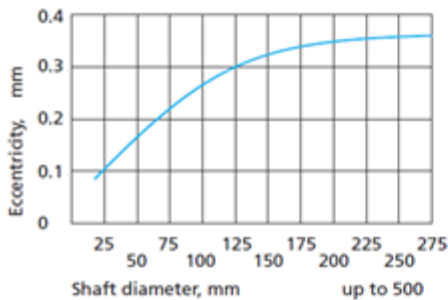
Figure 17: Dynamic run-out.

In most of the mechanical systems both types of eccentricities are present during operation even if the assembly has been carefully mounted. Hence, it is very important to bear in mind that these mounting and dynamic 'errors' are inevitable so that they will be always present. Nevertheless, while little eccentricities may be acceptable, big ones may cause significant damage to the sealing system and accelerate considerably the failure of many components. In the case of mechanical devices containing elastomeric seals, for instance, eccentricities may lead to leakage and/or a premature failure of seals. Hence, it is a parameter to take into account at the design stage.

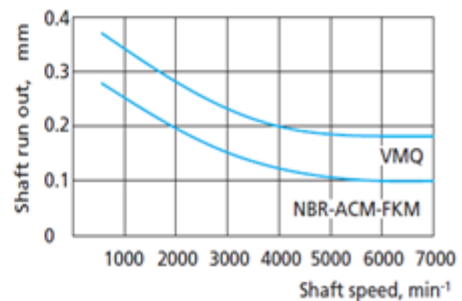
The amount of eccentricity that a specific sealing system could withstand depends on several factors such as seal geometry, size, material and operating conditions. In general, the bigger the seal size the higher the eccentricity amount that it can withstand. Moreover, seals rotating at lower velocities are often able to withstand also higher eccentricities.

Chapter 2: Tri-dimensional eccentricity model of seals

The reason is that at high speeds, due to the high inertia and viscoelastic properties of rubber materials, the sealing lip is unable to follow the shaft surface. Figure 18 shows two graphics of the acceptable eccentricity and run-out values vs. the diameter and speed of the shaft. Hence, every seal manufacturer usually defines the maximum recommended gap value between the seal and the bore for design purposes so that a critical eccentricity value is not exceeded during operation.



(a)



(b)

Figure 18: Acceptable eccentricity values: (a) shaft to bore misalignment, (b) dynamic run-out. (Source: Trelleborg Sealing Solutions [28])

2.3 Experimental measurements

First of all, experimental misalignment tests were carried out on rod lip seals made from TPU (Thermoplastic Polyurethane), suitable for hydraulic applications. The main objective is to obtain experimental data that will be used to complete and validate the tri-dimensional analytical

eccentricity model of seals proposed in this chapter. Thus, in the following sections, the same seal used for experimental tests will be modelled.

2.3.1 Experimental setup and specimens

The designed test rig consists of a gas cylinder where two test seals are located, a metallic structure, two force measurement devices (load cells), a PC for data visualization and a universal device for displacement measurements.

The gas cylinder was provided by the company Azol-Gas S.L. (from Vitoria-Gasteiz, Basque Country, Spain). A schematic drawing and the main dimensions of the gas spring designed by Azol-Gas S.L. for this particular test rig are shown in Figure 19.

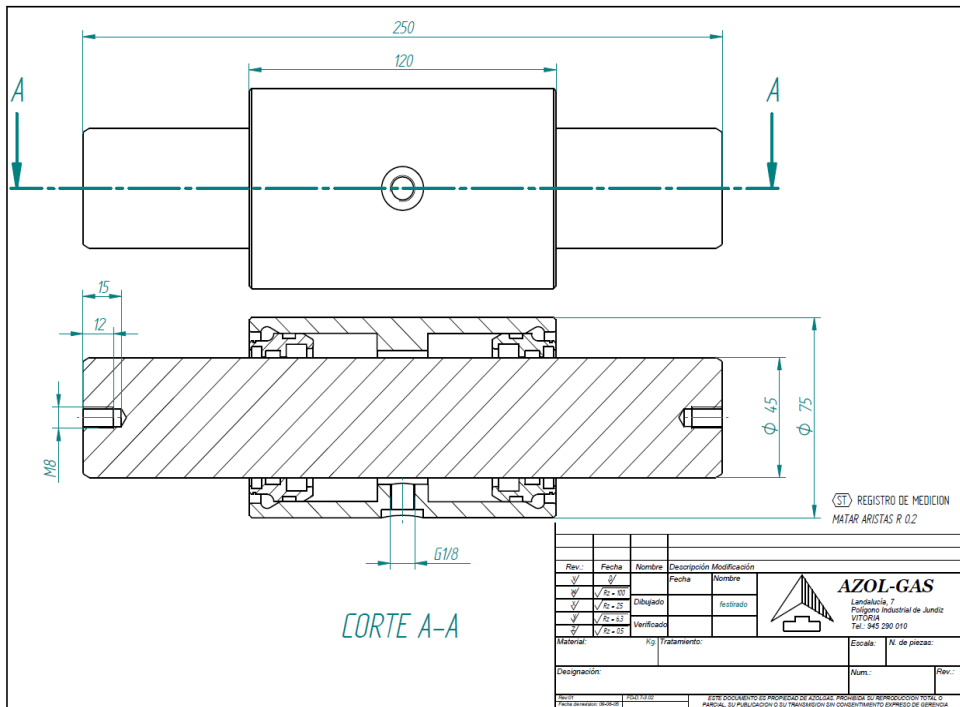
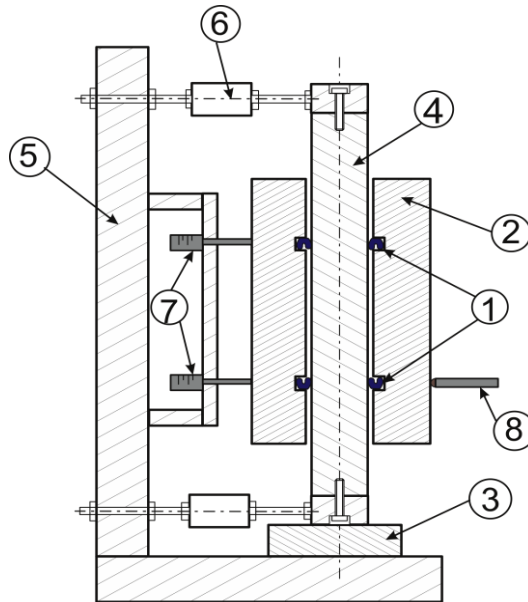
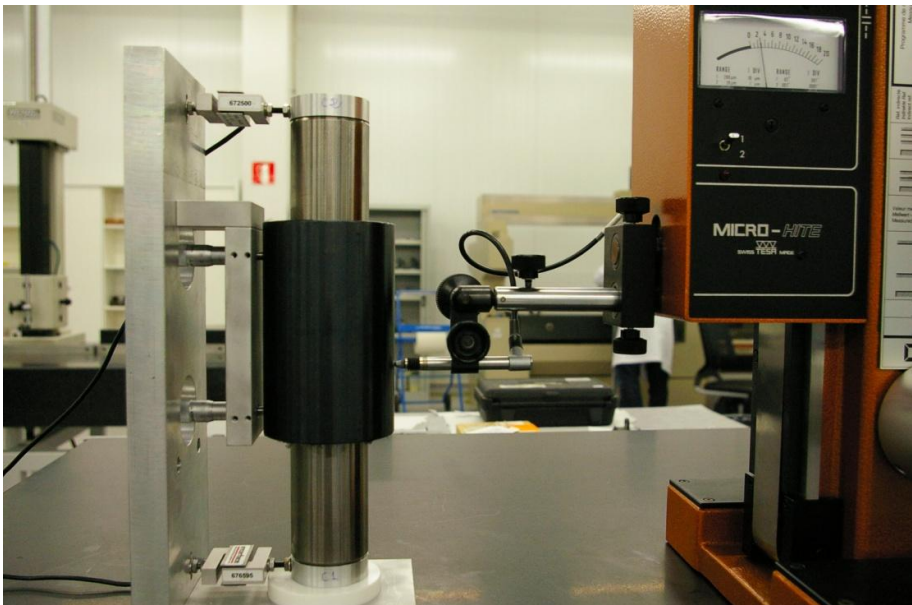


Figure 19: Drawing of the gas spring (Source: Azol-Gas S.L.).

A schematic image and a photograph of the test rig are shown in Figure 20. Seals under test (1) are mounted in the test chamber (2), one on each cylinder end. The rod rests on a low friction and high stiffness polymeric base (3) made from PTFE (Polytetrafluoroethylene) due to its low friction coefficient. The cylinder rod (4) is vertically positioned in order to minimize the weight effects and it is fixed to the frame (5) through a couple of tension/compression load cells with an accuracy of $\pm 0.01\text{N}$ (6). Misalignments are applied by means of two micrometric positioners (7) fixed to the frame. The cylinder position is controlled by means of a vertically guided probe located in a Tesa micro Hite manual (Renens, Switzerland) measuring device (8), which has a resolution of $1\mu\text{m}$.



(a)



(b)

Figure 20: Experimental setup for misalignment tests: (a) schematic view and (b) test rig assembly.

The experimental tests consist in applying different displacements to the cylinder bore and in measuring the forces generated on the rod as a consequence of the applied displacements. These reaction forces are measured by means of two load cells connected to the rod. Only seals are in contact with the bore and the rod. Hence, when applying a displacement to the cylinder, seals will be compressed and two reaction forces normal to the contact will be created, one on the bore to seal contact, and the other on the rod to seal contact.

Measurements were carried out on commercial rod lip seals, made of TPU (Thermoplastic polyurethane), suitable for a 45 mm diameter rod (Figure 21). Main details of the seals under study are shown in Table 1.

| | |
|-------------------------------|--------------|
| Seal type | Rod lip seal |
| Application | Hydraulic |
| Material | TPU |
| Rod diameter (mm) | 45 |
| Groove diameter (mm) | 55 |
| Seal width (mm) | 6 |
| Temperature range (°C) | -30 ÷ 105 |
| Maximum pressure (bar) | 400 |
| Maximum speed (m/s) | 0.5 |

Table 1: Main properties of the seal under study.

TPU is a thermoplastic elastomer very used in the sealing industry. This material is an intermediate solution between elastomers and plastics,

since it combines the properties of both. Due to its good resistance to mineral oils and excellent mechanical properties, most of the seals for hydraulic cylinders are made from this material. It presents a higher strength and wear resistance than most of the elastomers. Due to its high strength, TPU seals hardly ever require backup rings. Their operating temperature range is in general from about -30°C up to $+110^{\circ}\text{C}$, depending on the formulation. At low temperatures TPU shows a limited flexibility whereas it will be subjected to plastic flow at elevated temperatures. It is suitable to work with fluids such as mineral oils, greases, hydraulic fluids and synthetic hydrocarbons. It is not suitable for glycols, alcohols, solvents, brake fluids and acids, among others.

Misalignment tests were performed at room temperature and in absence of supply pressure. Before seal installation, a small amount of oil (0.1ml) was applied on the contact surfaces. The cylinder bore was displaced in radial direction only. Measurements were carried out under controlled environment, $20 \pm 1^{\circ}\text{C}$.

The cylinder rod has a roughness value of $R_a=0.32\mu\text{m}$; it was measured by means of a manual profilometer (Perthometer M2, Mahr, Göttingen, Germany).

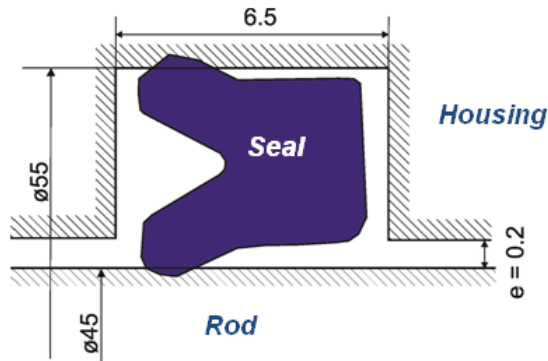


Figure 21: Principal dimensions of the seal groove (in mm).

At the beginning of the process, the cylinder rod was vertically placed adjusting the micro-positioners. Subsequently, consecutive controlled radial misalignment values were monotonically applied. The maximum applicable misalignment is limited by the nominal gap, e , with a value of 0.2mm (Figure 21). Misalignments were applied in steps of 5 μ m up to the maximum allowed one. Reaction forces at each step were measured by means of the load cells after verifying and adjusting the vertical alignment of the cylinder. Measurements were repeated 3 times.

2.3.2 Experimental results

Figure 22 shows the reaction force curves of a set of consecutive tests relative to the misalignment applied to the bore.

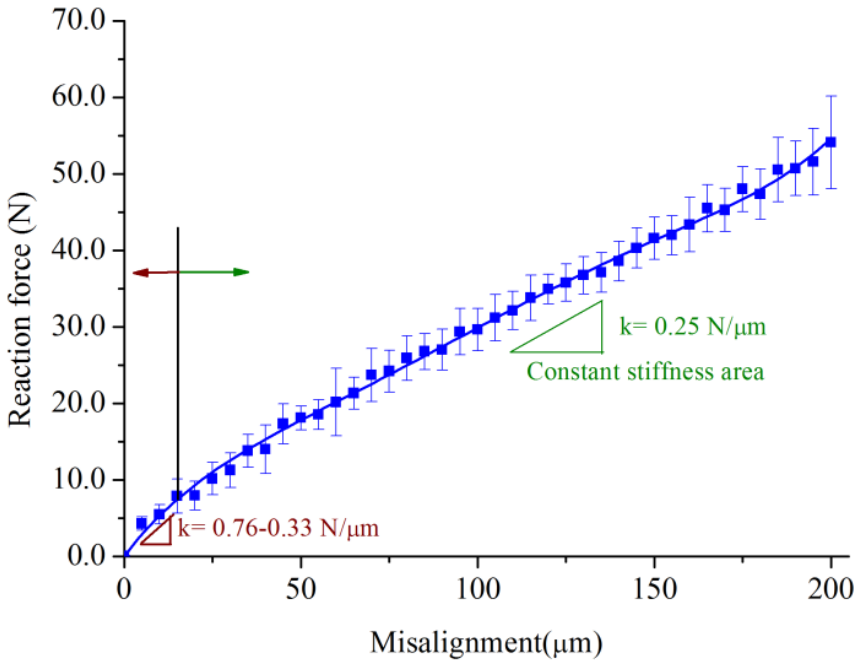


Figure 22: Reaction forces on the seal as a function of the applied misalignment.

Results showed a good repeatability. The error bars plotted show the standard deviations calculated considering all the repetitions. As can be observed, the stiffness of the whole seal in the misalignment direction is not constant. In particular, the seal under study presents the stiffest response when the rod misalignment is about 5 microns ($K \approx 0.76 \text{ N}/\mu\text{m}$). Above that eccentricity value, the stiffness decreases exponentially until reaching a nearly constant value for rod misalignments $\geq 15 \mu\text{m}$ ($K \approx 0.25 \text{ N}/\mu\text{m}$). The curve trend is in close agreement with the work of Tasora et al. [24].

2.4 Modelling method for seals

This section presents a procedure to build an analytical tri-dimensional eccentricity model of seals which expresses the contact forces between a seal and the mounting rod, as a function of rod misalignment. Even if in this work the model has been applied to a rod lip seal, the procedure herein presented may be applied also to model other seal geometries and other seal types such as piston seals, for instance.

Furthermore, it is important to remark that the model presented in this work only deals with the study of shaft to bore misalignments i.e. it has been considered that both the seal groove and the rod meet the tolerances recommended by the manufacturer. In Figure 23 the flow chart of the modelling procedure is shown.

As represented in the flow chart, the tri-dimensional contact model was built from: a *functional contact relation* between the rod and the seal, and a *geometrical interference model* that takes into account the amount of interference of each seal section. The functional contact relation was obtained through numerical 2D simulations. Then, a geometrical interference model of the system, and contact equations were formulated. Hence, the proposed analytical model has been completed and adjusted by means of numerical results. The model was validated through the experimental results presented in the previous section. Furthermore, a 3D numerical model of the sealing system (Figure 31) was also built in order to compare the results with those obtained analytically and experimentally.

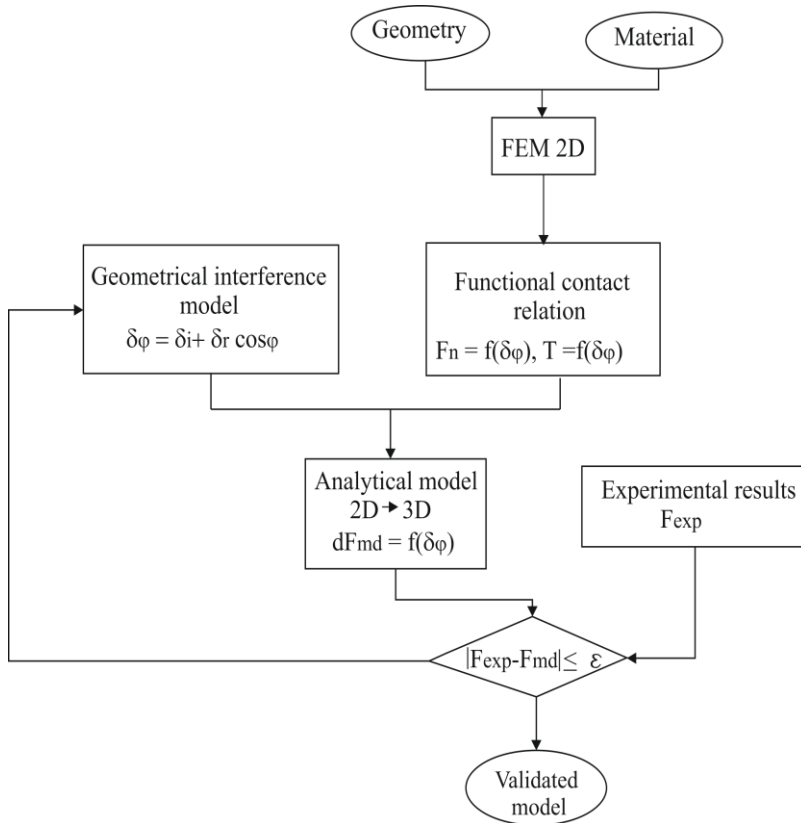


Figure 23: Proposed process scheme.

It is particularly relevant to highlight that even if a quasi-static case is being studied, contact equations are based on the kinematic Coulomb model i.e. it has not been considered that some regions of the seal may be sticking. Hence, this assumption involves a simplification of the problem that could be valid due to the nature of the tests, where an increasing load is monotonically applied to the rod.

Through the proposed methodology, a single 2D analysis is mandatory to obtain the stiffness of the seals in each section. Thus, the simplified

model may be acceptable and very useful for design purposes since the main goal of this work is to avoid time and expensive computational costs of a 3D numerical simulation.

2.4.1 Functional contact relation

2.4.1.1 Preliminary considerations

A functional contact relation expresses the relation between the contact forces and the compression or interference of an element. In order to build the eccentricity model of the seal, it is necessary to know the functional contact relation of the sealing system. For many mechanical components, the functional contact relation can be usually expressed as,

$$F = k \delta^n \quad (1)$$

where F is the contact force, k is the stiffness of the contact, δ is the relative approach between points and n is the load deflection exponent.

For example, in the case of ball bearings, the contact stiffness is a non-linear function of the materials in contact and their relative displacement, and the load deflection exponent n has a value of 3/2, due to the hertzian nature of the contact [29], which makes the contact area to be elliptic

In this case, the nature of the shaft-seal-housing contact areas is not hertzian, and in addition, the shape of the contact area varies with the load. Therefore, Equation (1) may not be directly a good form to express the Force-displacement relation. Thus, a numerical bi-dimensional

model of the seal under study and plain strain simulations were carried out in order to obtain the functional contact relation of the sealing system under study.

2.4.1.2 Numerical 2D Model

The plane model was built in Ansys Workbench environment. As previously mentioned, the main objective of this simulation is to obtain the functional contact relation between the rod and the seal, as a function of the seal section compression. Resultant normal and tangential forces taken from these numerical simulations are mandatory inputs to build the analytical model. Seal geometry was obtained by means of an optical microscope (Leitz, model Libra 200, Germany).

The model was built by means of quadrilateral and triangular elements and composed of a total of 1609 elements. The mesh used is the result of a number of analyses performed in order to determine the element sizes that do not produce significant variation in calculation accuracy. Furthermore, in order to compare the bi-dimensional and tri-dimensional numerical models it was preferable to build both of them with the same element type and size. Hence, the element size for the 2D is limited by the minimum affordable element size of the 3D due to the high computational costs and times arising from these models. Figure 24 shows the generated mesh.

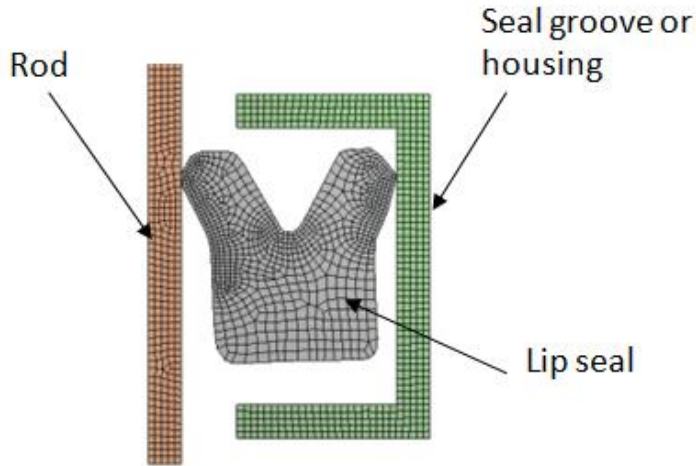


Figure 24: Bi-dimensional model of the sealing system.

A surface to surface contact formulation was chosen to simulate both the seal/rod and the seal/groove contacts. Boundary conditions take into account friction at contact surfaces in order to constrain the free movement of the seal. During the experimental tests, contact surfaces of seals were lubricated before seal installation. Hence, these conditions were assumed for numerical simulations. The friction coefficients were set to 0.1 for both the seal/rod and the seal/groove contacts [30].

The seal material, TPU, was considered incompressible, isotropic and hyperelastic. It was assumed the compressive stress-strain curve shown in Figure 25. These data were obtained as a result of compression tests carried out in the universal testing machine Instron 3369 (Massachusetts, USA) shown in Figure 26.

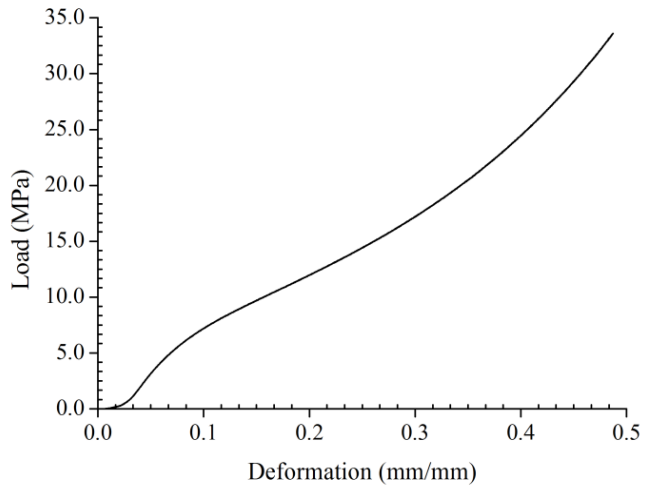


Figure 25: Experimental compressive stress-strain curve of TPU.

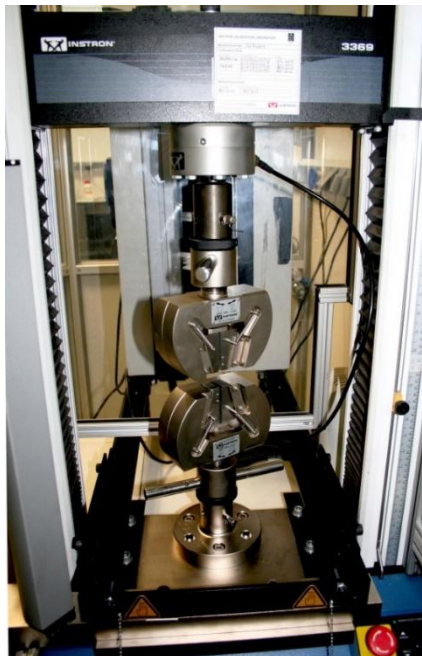


Figure 26: Instron 3369 universal machine.

Chapter 2: Tri-dimensional eccentricity model of seals

The hyperelastic material was defined by means of a second-order Mooney-Rivlin formulation. Due to the difficulties found to manufacture samples made of the seal material with the adequate shape to carry out traction tests, Mooney-Rivlin coefficients were obtained from the data provided by the manufacturers and applying the approximate formulas below.

Considering the material homogeneous and isotropic, the following relation could be applied:

$$E = 2G(1 + \nu) = 3K(1 - 2\nu) \quad (2)$$

where E is the elastic modulus, G is the shear modulus, K is the bulk modulus and ν is the Poisson ratio. Hence, in the case of elastomers, $G \approx 0.3 E$ for elastomers since the Poisson modulus is around 0.5 [31].

On the other hand,

$$K_0 = 2/D_1 \quad (3)$$

$$G_0 = 2(C_{01} + C_{10}) \quad (4)$$

The values E and ν for the TPU material under study were provided by manufacturers: $E= 12$ MPa and $\nu=0.499$. Hence, applying the equations above, the following Mooney-Rivlin coefficients are obtained: $C_{10}= 1.98$ and $C_{01}= 0.16$.

The rod and the bore were considered rigid elements since polymer stiffness is much lower than that of steel.

In Figure 27 the forces obtained numerically are illustrated. The numerical results obtained from the plain strain simulations are shown in Figure 28. A relevant aspect of the results is that seal stiffness of the lip seal varies considerably with compression. Furthermore, the stiffness of a cross section of the studied seal can be divided in two regions where it remains nearly constant: a low stiffness region ($K \approx 0.58$ N/mm) and a high stiffness region ($K \approx 6-11$ N/mm).

It is important to highlight that results showed that a sudden change in seal stiffness occurs for seal compression values nearby the nominal interference δ_i . In particular, as can be seen, seal stiffness increases considerably for seal interferences a bit higher than the nominal values.

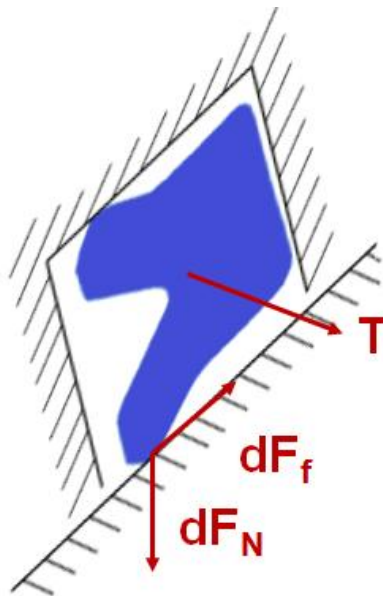


Figure 27: Forces obtained from the differential element of seal.

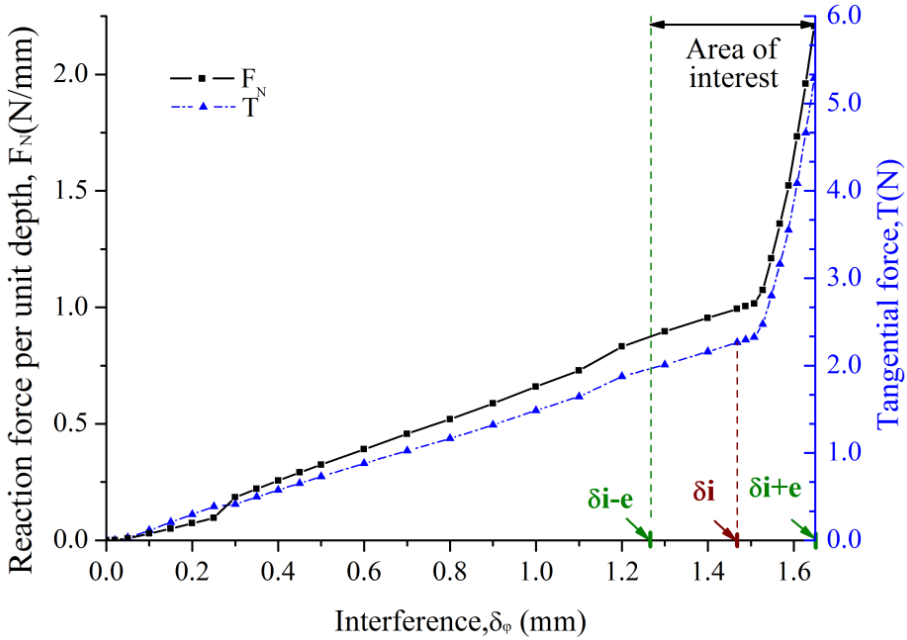


Figure 28: Reaction and tangential forces in a seal section as a function of mounting interference or compression.

In this study, the area of interest is bounded by the maximum and minimum possible interference values i.e. by $\delta i + e$ and $\delta i - e$, respectively (Figure 28). The objective is to express analytically normal forces and tangential forces of a seal section in this area, and to introduce these expressions in the equations presented in 2.6. In order to fit the data points of the forces by the most appropriate function, R-squared correlation was used. The closer the R^2 coefficient is to 1, the more accurate the fitting. In this case, both force curves were fitted by a four degree polynomial. These fittings were considered acceptable since they led to R^2 values of 0.997 in both cases.

Analytically, the functional contact relation between the rod and a differential seal section depending on the interference or compression can be expressed as,

$$F_N = 97.39 \delta_\varphi^4 - 201.71 \delta_\varphi^3 + 965.13 \delta_\varphi^2 - 821.09 \delta_\varphi + 261.24 \quad (5)$$

In the same way, the tangential forces occurring when compressing the seal as a function of the interference is,

$$T = 238.77 \delta_\varphi^4 - 1207.6 \delta_\varphi^3 + 2276.0 \delta_\varphi^2 - 1892.3 \delta_\varphi + 587.17 \quad (6)$$

These two equations describe the behaviour of a seal section under different compression values. Thus, they are mandatory inputs to build the analytical model of the sealing system studied in this work.

2.4.2 Geometrical interference model

The analytical model consists of a geometrical interference model and contact equations based on numerical results. In a specific situation, where the rod and the bore are concentric, the interference is the same along the whole seal, δ_i . Nevertheless, when there is a radial eccentricity, contact conditions will be different on each section of the seal. Figure 29 shows the geometrical interference between the rod and the seal for a specific misalignment δ_r . The polar coordinate φ defines the position of each seal section, relative to the rod misalignment direction.

Chapter 2: Tri-dimensional eccentricity model of seals

In order to express the geometrical-interference field as a function of misalignment, the following geometrical-interference model is formulated:

$$\delta_{\varphi} = \delta_i + \delta_r \cos\varphi \tag{7}$$

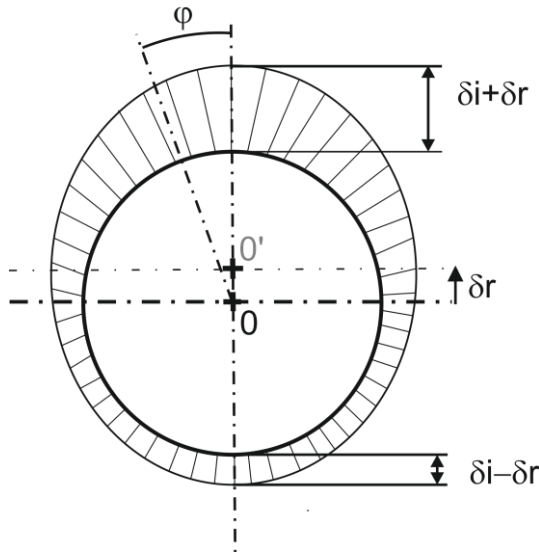


Figure 29: Geometrical interference model.

As already mentioned, the applicable maximum misalignment, e , and the nominal interference values are determined by manufacturing tolerances. Depending on the relation between δ_i and δ_r , it is possible to distinguish two different cases. Figure 30 shows the two possible interference configurations. If the radial misalignment value, δ_r , is lower than the interference between the seal and its counterparts at a concentric position, δ_i , all the seal sections will keep contact with the rod. Otherwise, contact between parts will be lost in a particular seal region.

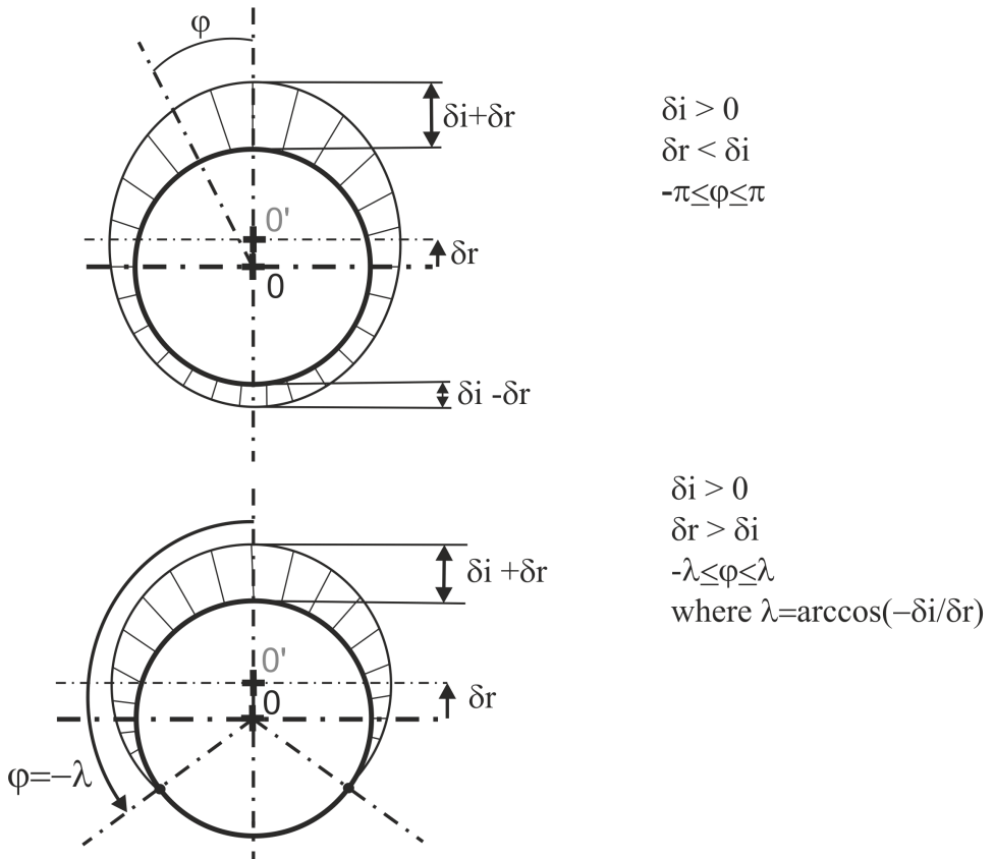


Figure 30: Possible interference configurations.

2.5 Numerical 3D model

2.5.1 Modelling

A tri-dimensional model of the considered lip seal was built in Ansys Workbench environment in order to validate the analytical 3D model.

Chapter 2: Tri-dimensional eccentricity model of seals

The same geometry, materials and contact pairs that were used to build the 2D model were assumed. Due to the symmetry of the geometry and boundary conditions, only a half of the seal was modelled. The mesh was built by means of quadrilateral and triangular elements with a size of 0.3mm. In total, 33586 elements were used. Figure 31 shows the generated mesh.

In order to build the analytical model, two similar tri-dimensional models were developed: one considering all the contacts frictionless, and the other one considering frictional contacts.

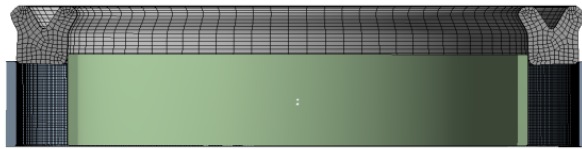


Figure 31: Tri-dimensional model of the sealing system under study.

Under perfectly concentric mounting conditions the interference or penetration between the seal and its counterparts is of about 1.47mm. Due to the high mounting interference or preload values, seal mounting was simulated step by step. Firstly, a concentric mounting was simulated. Afterwards, boundary conditions allowed rod displacement just in the selected radial misalignment direction. The simulation procedure is shown in Figure 32. Rod radial displacement was applied step by step, from a rod ideal concentric position an initial position up to the maximum allowed displacement, determined by the gap between the rod and the cylinder inner diameter. The cylinder bore was considered perfectly static in radial direction.

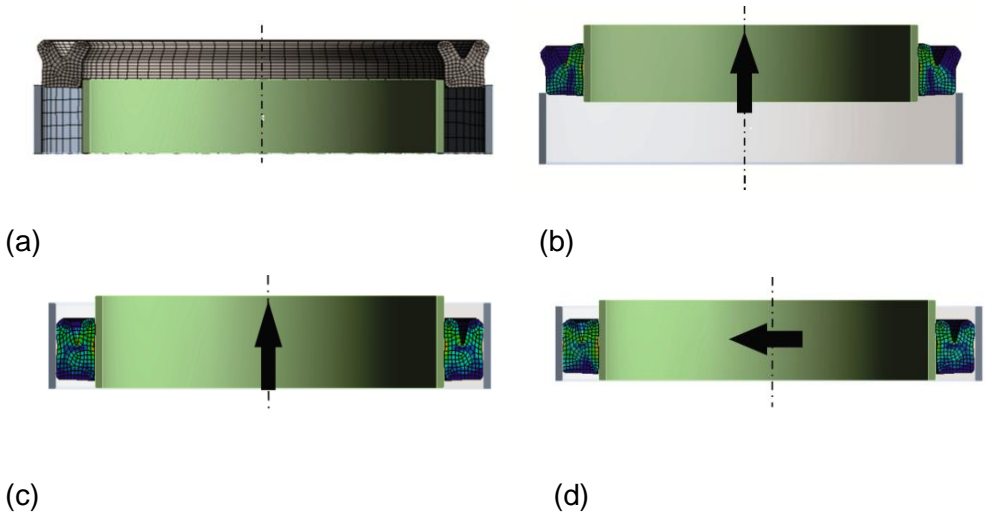


Figure 32: Simulation procedure of the seal: (a), (b) and (c) mounting, and (d) rod misalignment (d).

2.5.2 Numerical results

Resultant contact forces between the rod and the seal, in the rod misalignment direction are shown in Figure 33, for both a frictionless and a frictional model. As can be seen, results showed that resultant forces on the seal strongly depend on rod position i.e. on contact conditions. Furthermore, contact forces resulting from the frictional model are higher regardless of the misalignment value. In both cases, F_{md} increases with the rod misalignment, and the tendency of both curves is quite similar.

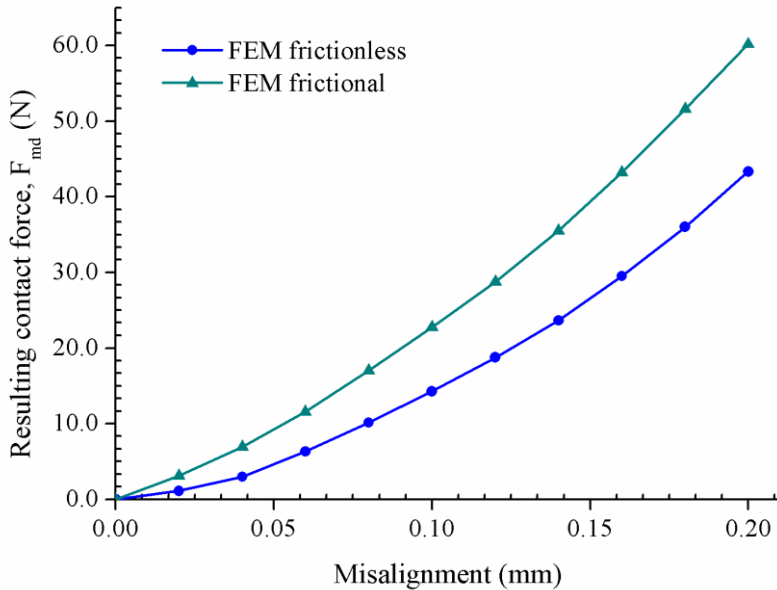


Figure 33: Numerically obtained contact forces vs. rod misalignment.

It can be observed that the tendencies of the numerical (Figure 33) and the experimental curves (Figure 22) are quite different. In particular, the main difference is that experimental results presented a high slope ramp for low rod misalignment values whereas in the case of numerical results, the slope increases with the misalignment. It is thought that the main reason for tendency difference could be the simulation procedure followed to simulate the seal mounting itself (Figure 32).

2.6 Analytical model

The contact force between a seal section and the rod depends on its compression level. Considering a frictional contact between the seal and the rod, it is possible to formulate a contact relation which integrates the

normal, tangential and frictional forces acting on a differential element of seal.

In this way, the normal and tangential differential forces on the seal under study as a function of the interference value δ_φ can be expressed as,

$$F_N = f(\delta_\varphi) \quad (8)$$

$$T = f(\delta_\varphi) \quad (9)$$

Assuming different contact conditions and force combinations acting on the seal, several contact models were formulated:

- Frictionless contact model not including tangential forces (Theor. (F_N)).
- Frictionless contact model including tangential forces (Theor. $(F_N + T)$).
- Frictional contact model not including tangential forces (Theor. $(F_N + F_f)$).
- Frictional contact model including tangential forces (Theor. $(F_N + T + F_f)$).

In all the cases, the procedure for building a tri-dimensional contact model is similar; being the main difference between models the forces considered. Formulation for each model is presented below.

The contact radius between the seal and the rod r_m depends on the angle φ , and it is measured from the rod centre, O. Under concentric

conditions, the value of the average radius is the same for every section, r_i . When the rod is misaligned, the contact radius at each section can be calculated as:

$$r_m = r_i + \delta_r \cos\varphi \quad (10)$$

In this work, the maximum admissible rod misalignment e , determined according to manufacturer's drawing, is 0.2mm and the interference δ_i is 1.47mm. Hence, the interference configuration corresponds to $\delta_i > \delta_r$.

2.6.1 Frictionless contact model not including tangential forces, (Theor. (F_N)).

In this case, an ideal situation is considered so that no friction is generated between the seal and its counterparts during compression. Thus, the contact between the seal and the rod is completely modelled by means of normal reaction forces between them. The forces acting on a compressed differential element of seal are illustrated in Figure 34 and it can be expressed as:

$$dF_N = F_N(\delta_\varphi) ds = F_N(\delta_\varphi) r_m d\varphi \quad (11)$$

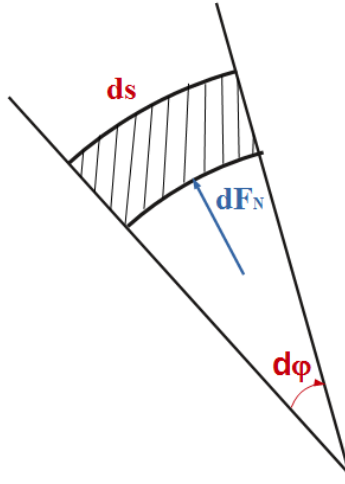


Figure 34: Forces acting on a differential element of seal when friction and tangential effects are ignored.

So the contact force between the dynamic lip of the seal and the rod in the radial direction is equal to the normal reaction force:

$$dF_r = dF_N = F_N(\delta_\varphi)r_m d\varphi \quad (12)$$

And differential contact forces in the misalignment direction can be expressed as follows:

$$dF_{md} = dF_r \cos\varphi = F_N(\delta_\varphi)r_m \cos\varphi d\varphi \quad (13)$$

Thus, integrating Equation (13) for the whole seal circumference, the resultant load acting on the seal in the misalignment direction could be calculated as:

$$F_{md} = 2 \int_0^{\pi} F_N(\delta_{\varphi}) r_m \cos\varphi d\varphi \quad (14)$$

This force F_{md} is the force measured through the experimental tests for different eccentricity values i.e. it is the force whose values experimentally and analytically calculated have to be compared.

2.6.2 Frictionless contact model including tangential forces, (Theor. ($F_N + T$))

In this case, the contact between the seal and the rod for each interference value is modelled not only by means of the normal reaction forces between the seal and the rod but also by tangential forces generated on the seal as a function of the applied misalignment. The forces acting on a compressed differential of seal are illustrated in Figure 35 and they can be expressed as:

$$dF_N = F_N(\delta) ds = F_N(\delta) r_m d\varphi \quad (15)$$

$$T = T(\delta) \quad (16)$$

And the contact force between the rod and the seal in radial direction is:

$$dF_r = dF_N - 2 T \sin\left(\frac{d\varphi}{2}\right) \quad (17)$$

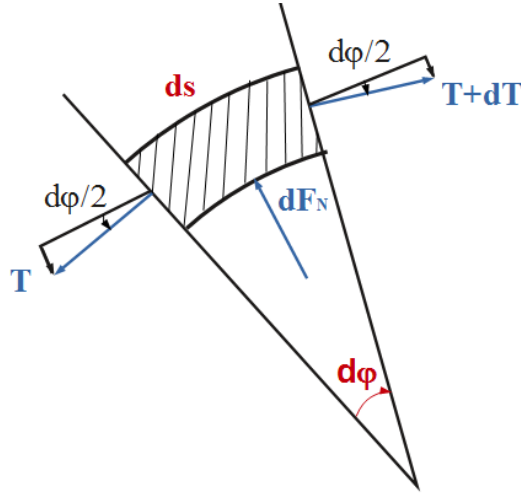


Figure 35: Forces acting on a differential of seal when friction is ignored and tangential forces are considered.

Assuming that $\sin(d\varphi/2) \approx d\varphi/2$, contact forces in radial direction as a function of section polar position can be expressed as:

$$dF_r = (F_N(\delta_\varphi)r_m - T(\delta_\varphi))d\varphi \quad (18)$$

Thus, resultant contact forces acting on a seal section can be expressed in the misalignment direction as:

$$dF_{md} = dF_r \cos\varphi = (F_N(\delta_\varphi)r_m - T(\delta_\varphi)) \cos\varphi d\varphi \quad (19)$$

Resultant contact load on the whole sealing lip can be calculated by integrating Equation (19) as follows:

$$F_{md} = 2 \int_0^\pi (F_N(\delta_\varphi)r_m - T(\delta_\varphi)) \cos\varphi d\varphi \quad (20)$$

2.6.3 Frictional contact model non including tangential effects, (Theor. ($F_N + F_f$)).

If the contact between the rod and the seal is considered frictional and tangential forces generated on the seal are not taken into consideration, the functional contact relation between the rod and a differential of seal may be defined by the following forces:

$$dF_N = F_N(\delta_\varphi)ds = F_N(\delta_\varphi)r_m d\varphi \quad (21)$$

$$dF_f = \mu(dF_N - 2T\sin\left(\frac{d\varphi}{2}\right)) \quad (22)$$

where μ is the friction coefficient between the rod and the seal. It is important to highlight that the friction equation in (22) is formulated adopting a simplified contact model which takes into account the Coulomb's friction model.

Figure 36 shows the forces acting on a differential element of seal for this specific case.

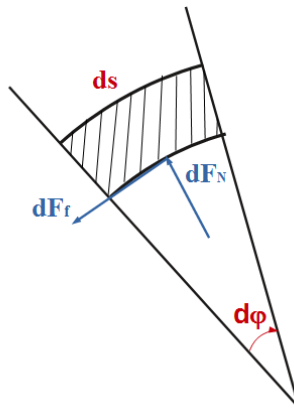


Figure 36: Forces acting on a differential element of seal when tangential forces are ignored and friction between parts is considered.

Hence, the contact force between the rod and the seal could be expressed in radial direction as:

$$dF_r = dF_N = F_N(\delta_\varphi) r_m d\varphi \quad (23)$$

And differential contact forces can be expressed in the misalignment direction as follows:

$$dF_{md} = dF_r \cos\varphi + dF_f \sin\varphi \quad (24)$$

$$dF_{md} = F_N(\delta_\varphi) r_m (\cos\varphi + \mu \sin\varphi) d\varphi \quad (25)$$

Finally, when a misalignment δ_r is applied to the rod, the resultant contact load on the whole sealing lip can be calculated as follows:

$$F_{md} = 2 \int_0^\pi F_N(\delta_\varphi) r_m (\cos\varphi + \mu \sin\varphi) d\varphi \quad (26)$$

2.6.4 Frictional contact model including tangential forces, (Theor. $(F_N + T + F_f)$)

This case represents the most complete model since it includes normal, tangential and friction effects acting on the seal. Figure 37 shows the forces acting on a differential of seal that can be expressed as:

$$F_{md} = 2 \int_0^\pi F_N(\delta_\varphi) r_m (\cos\varphi + \mu \sin\varphi) d\varphi \quad (27)$$

$$T = T(\delta_\varphi) \quad (28)$$

$$dF_f = \mu(dF_N - 2T \sin\left(\frac{d\varphi}{2}\right)) \quad (29)$$

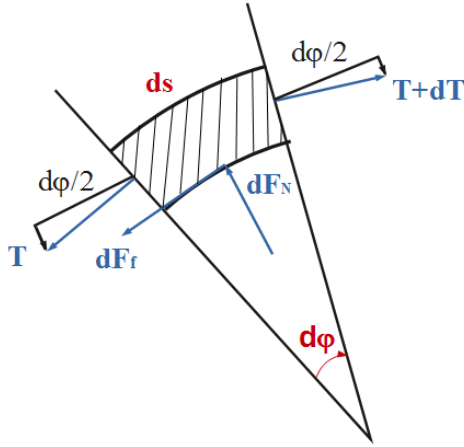


Figure 37: Forces acting on a circumferential section of the seal.

The contact force between the sealing lip and the rod in radial direction can be written as:

$$dF_r = dF_N - 2 T \sin\left(\frac{d\varphi}{2}\right) \quad (30)$$

And assuming that $\sin(d\varphi/2) \approx d\varphi/2$,

$$dF_r = (F_N(\delta_\varphi)r_m - T(\delta_\varphi))d\varphi \quad (31)$$

Considering a frictional contact between the rod and the seal, resultant contact forces acting on a seal section can be expressed in the misalignment direction as:

$$dF_{md} = dF_r \cos\varphi + dF_f \sin\varphi \quad (32)$$

$$dF_{md} = (F_N(\delta_\varphi)r_m - T(\delta_\varphi))(\cos\varphi + \mu\sin\varphi)d\varphi \quad (33)$$

Resultant contact load on the whole sealing lip can be calculated by integrating Equation (33). If $\delta_i > \delta_r$, the total load supported by the sealing lip can be expressed in the misalignment direction.

$$F_{md} = 2 \int_0^{\pi} (F_N(\delta_{\varphi}) r_m - T(\delta_{\varphi})) (\cos\varphi + \mu \sin\varphi) d\varphi \quad (34)$$

Equation (35) expresses the total contact force in the misalignment direction when $\delta_i < \delta_r$.

$$F_{md} = 2 \int_0^{\lambda} (F_N(\delta_{\varphi}) r_m - T(\delta_{\varphi})) (\cos\varphi + \mu \sin\varphi) d\varphi \quad (35)$$

In the next section, results obtained applying each of these analytical models presented are presented.

2.7 Results

2.7.1 Model validation

The analytical equations previously presented were implemented in Matlab, in order to calculate the contact forces for different rod misalignment values. Calculated radial contact forces along the seal vs. different eccentricity values are plotted in Figure 38. It can be concluded that different rod radial misalignment values result in very different contact force distributions. Contact force variations in the lip of the loaded half-seal side are consistently higher than variations in those sections in the opposite side. These results are in good agreement with results obtained from the plain simulations where it was found that the

stiffness of the seal increases considerably for interference values slightly higher than the nominal interference.

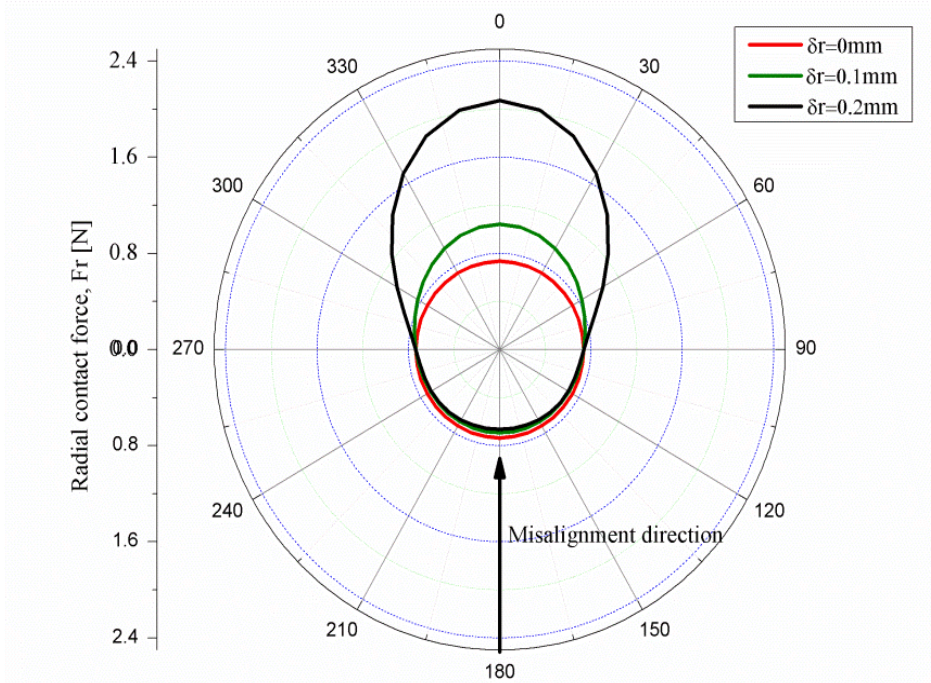


Figure 38: Radial contact forces in the sealing lip as a function of circumferential position and rod eccentricity value.

For a rod subjected to the maximum allowable interference, the maximum contact force value could even triple the minimum one. As can be seen, in this specific case all the sections in the seal are subjected to a contact force of about 0.75N, whereas for misalignments values of $\delta_r=0.2$ mm the maximum contact force in the seal is about 2N. This fact involves an irregular wear pattern and temperature distribution, and a subsequent seal life reduction that may be very significant. The effect of the irregular contact patterns on the tribological performance of seals, indeed, will be studied in the next chapters.

Substituting the geometrical interference model defined by Equation (7) and integrating results for the whole seal as described in the previous section, resultant contact forces along the whole seal can be calculated regardless of rod eccentricity. Figure 39 shows resultant contact forces in the misalignment direction, numerically and analytically calculated considering different contact models: both frictionless and frictional contacts, with and without introducing tangential effects in the analytical model (curves A-F). Results showed that tangential and frictional forces play an important role. The effect of friction forces is to overload the seal whereas tangential forces tend to decrease resultant contact forces. Good matching was found between numerical 3D results (E) and analytical results for an ideal frictionless sealing system (C). Thus, it can be concluded that tangential forces acting on the seal are mandatory inputs to complete the analytical model, so that they should not be ignored. By contrast, numerical 3D simulation results for a frictional contact model (F) and analytical results considering friction between counterparts (D) did not show a good correlation at low eccentricity values. Furthermore, as seen in Figure 39, numerical results underestimate contact forces for rod misalignments lower than 0.07mm. Tasora et al. [24] found that radial shaft seals show a high slope ramp at low radial displacements. Hence, it is thought that the major sources of discrepancies between results at low misalignment values could be: the simulation procedure itself, followed to solve the initial preload of the seal (Figure 32), and/or the omission of stick-slip regions and materials properties such as viscoelasticity.

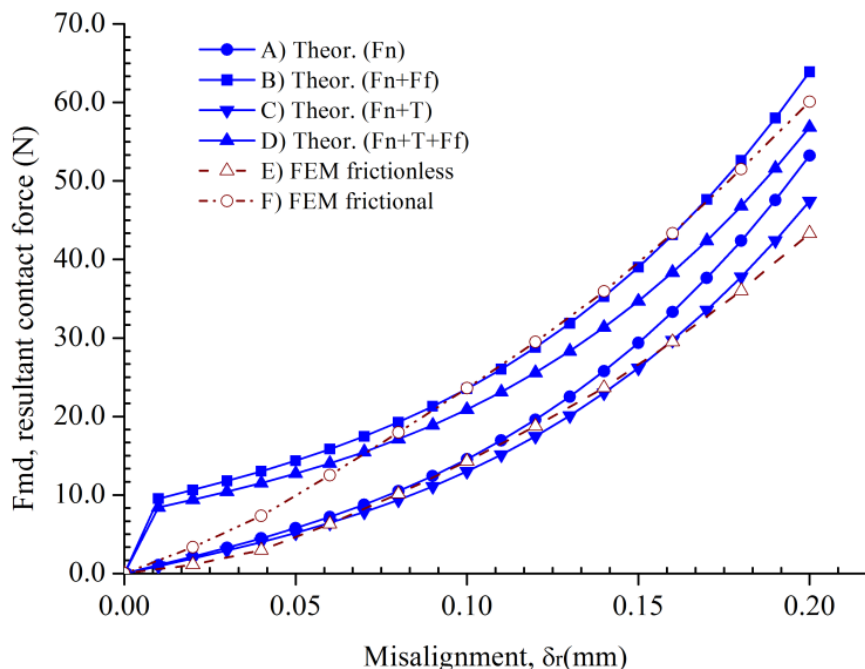


Figure 39: Analytically (Theor.) and numerically (FEM) obtained contact forces vs. misalignment.

Experimental results were used in order to validate the analytical model proposed in this work. It was found a good correlation between experimental and the analytical results of the model that includes both tangential and frictional effects, i.e. frictional contacts should be assumed. Figure 40 shows a comparison between experimental, numerical and analytical results, (D), and it also presents the error between analytical and experimental results in absolute terms. The maximum difference between the analytical and experimental results in absolute terms is approximately 6.4N, which occurs for the highest misalignment. Hence, it may be concluded that the modelling method proposed in this chapter may be a useful tool for contact force

distribution prediction on seals that avoids the high computational costs and times associated to 3D FEM simulations.

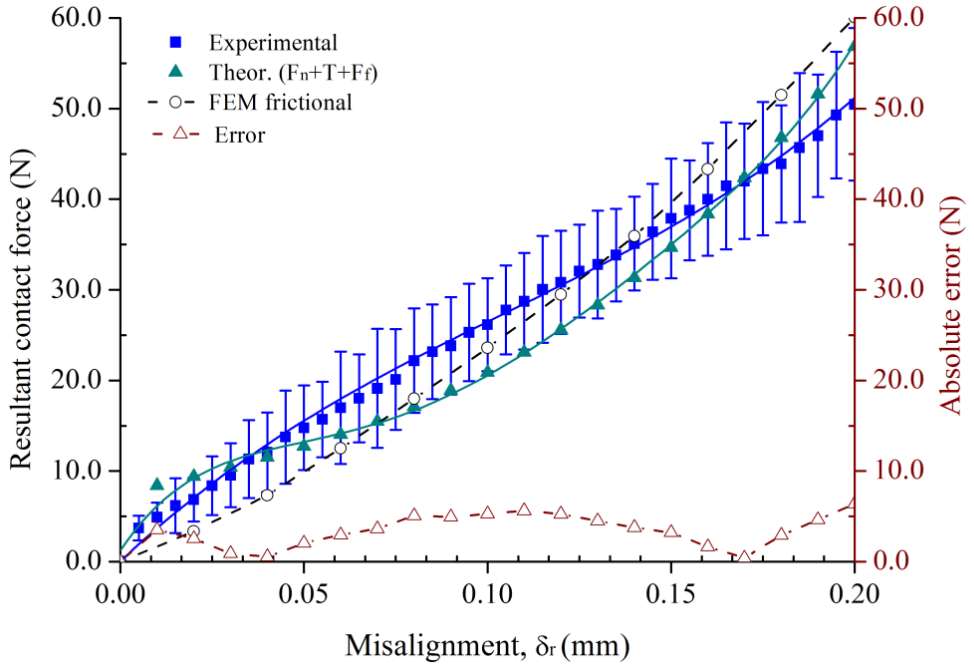


Figure 40: Comparison between experimental, numerical and analytical results.

2.7.2 Contact pressure field

The sealing force provided by every seal during operation can be expressed as the sum of two contributions: an initial preload or interference, and the fluid pressure. Every seal is designed to provide a specific interference or preload that enables sealing even at low pressures. Most of them, in general, are designed to provide an initial compression in the range between the 7 and the 30% [14]. When fluid

Chapter 2: Tri-dimensional eccentricity model of seals

pressure is applied, this pressure is also transferred to the contact. Hence, the sealing contact pressure is always higher than the fluid pressure and that is why the fluid does not leak.

The role of lip seals is to ensure an adequate sealing between two surfaces moving relative to each other providing an adequate sealing force. Furthermore, the special geometry of lip seals is essential in order to provide a specific contact pressure distribution when they are mounted in their grooves. In fact, the contact pressure distribution is the main responsible for the sealing and pumping mechanisms occurring when there is a relative movement between a lip seal and its counterparts [3]. Moreover, the advantage of U-type seals or lip seals is that due to their geometry, they provide interference under eccentric mounting and wider operations than other types of seals [14].

In the previous sections it has been studied how a mounting misalignment or a static eccentricity affects the contact force distribution of the seal under study. This section addresses how a static eccentricity affects the contact pressure distribution of the seal under study. To this end, results obtained from the tri-dimensional numerical simulations have been analyzed. Figure 41 shows the contact pressure distribution of a section of the lip seal under study under concentric mounting conditions. The shape of the contact pressure distribution is in good agreement with other curves found in literature for the case of lip seals [33].

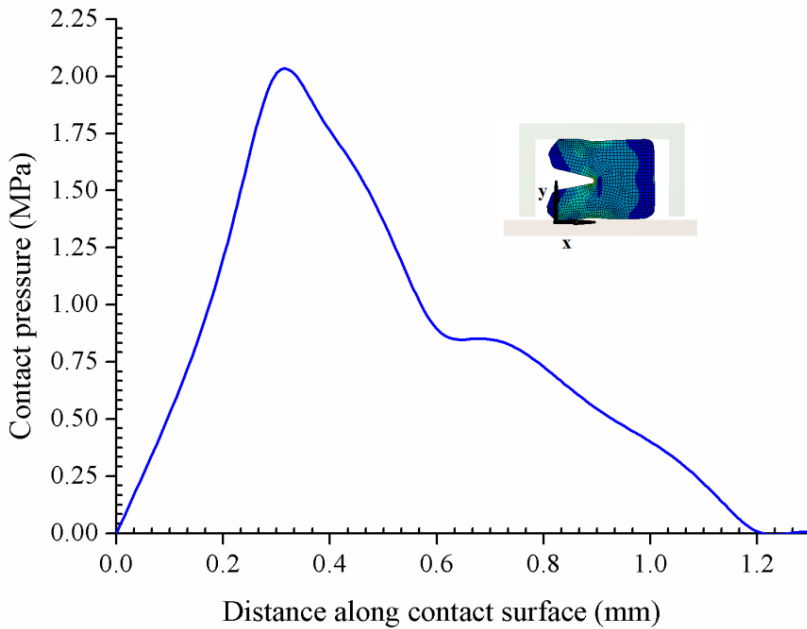


Figure 41: Contact pressure between the seal and the rod under concentric mounting conditions ($\delta_r = 0mm$).

As can be observed, the contact width under ideal concentric conditions is about 1.2mm and the maximum contact pressure is about 2MPa. Furthermore, the maximum contact pressure occurs on the oil side of the seal. In particular, contact pressures increases along the oil side up to the peak contact force, and then, it continuously decreases along the air side up to zero.

Figure 42 presents the contact pressures of those seal sections subjected to the maximum and minimum interferences for a rod to bore radial misalignment of $\delta_r=0.2mm$. For the section subjected to the minimum interference, the maximum contact pressure value is

approximately 2.3MPa; a value slightly higher than the pressure obtained for the maximum interference section which presents a maximum pressure of 2.17MPa. Hence, results showed that eccentricities do not alter the maximum contact pressure provided by the seal, but it does affect the contact pressure distribution and the contact area. In particular, the seal section subjected to the minimum interference presents a low contact width of about 0.9mm. The maximum interference section, however, presented a much higher contact width of approximately 5.5mm. Furthermore, in the latter case, the contact area was divided in two areas. As can be observed in the graph, between these two contact areas there is a zone where there is no contact between the seal and the rod i.e. where contact pressure is zero. In both cases the maximum appears again in the oil side.

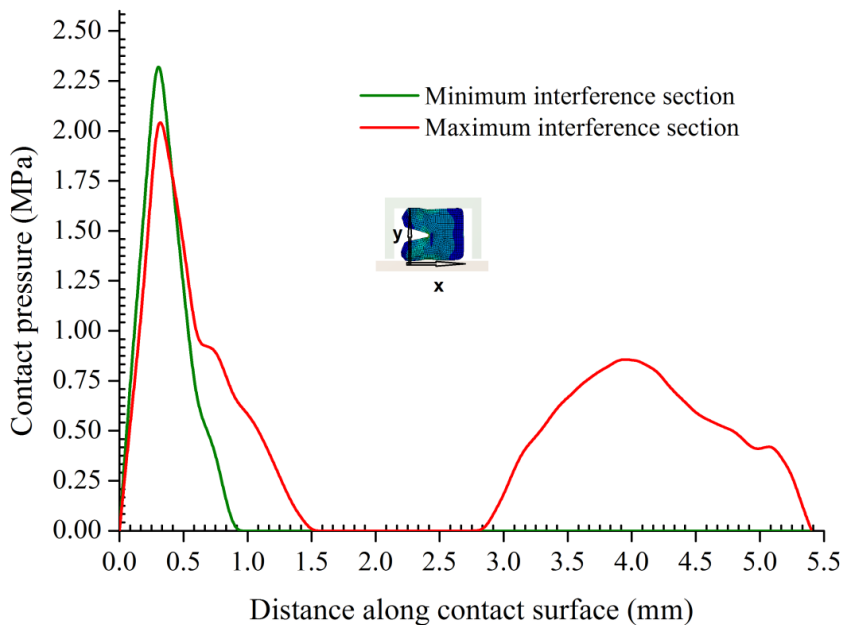


Figure 42: Contact pressure between the seal and the rod for $\delta_r = 0.2 \text{ mm}$.

Figure 43 presents the contact pressure curves of the seal under concentric and eccentric conditions.

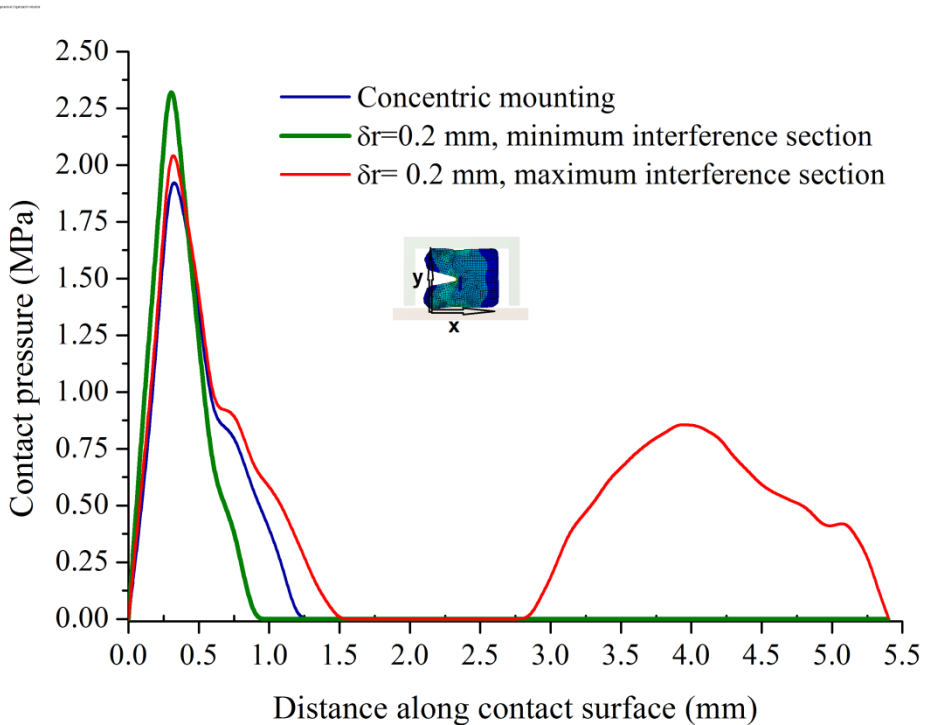


Figure 43: Comparison of the contact pressure under different contact conditions.

Figure 44 presents the contact pressure field at the inner surface of the seal when the rod is perfectly concentric to the bore center. Under this condition, the contact pressure between the seal and the shaft is the same along the whole seal. The rod and the groove have not been represented on the figure in order to have a proper visualization of the pressure field.

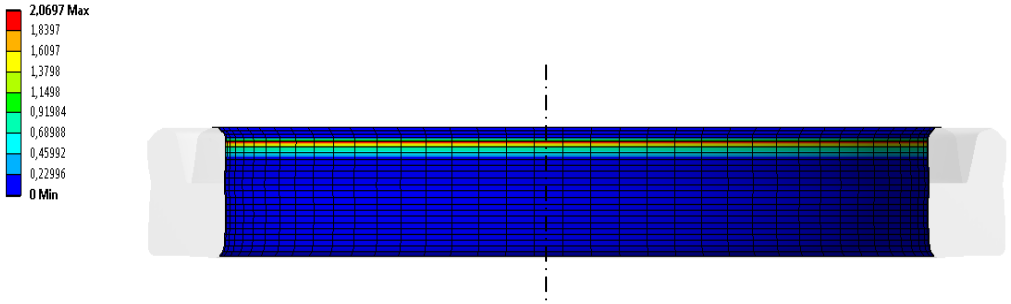


Figure 44 : Contact pressure field under ideal concentric conditions ($\delta_r = 0\text{ mm}$).

Figure 45 and Figure 46 present the contact pressure field in the dynamic lip of the seal for rod radial misalignments of 0.1mm and 0.2mm, respectively. It was found that under these conditions another contact area is formed in the most compressed sections of the seal. Moreover, comparing both graphs it can be concluded that when increasing the radial misalignments from 0.1 to 0.2 mm, the secondary contact area increases considerably both in width and in length (circumferential length) whereas the primary contact area remains almost the same.

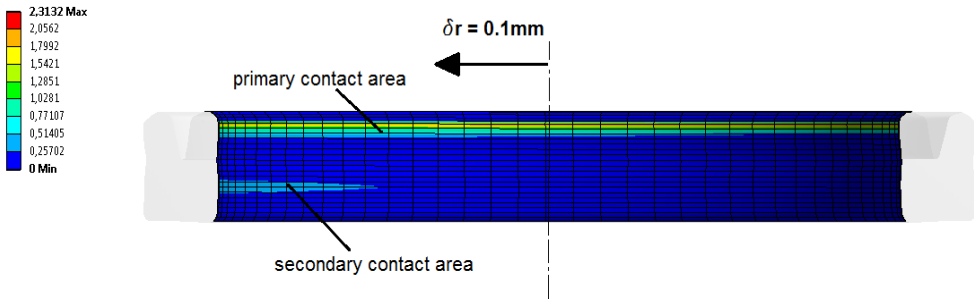


Figure 45: Contact pressure field for a rod misalignment of $\delta_r = 0.1\text{ mm}$.

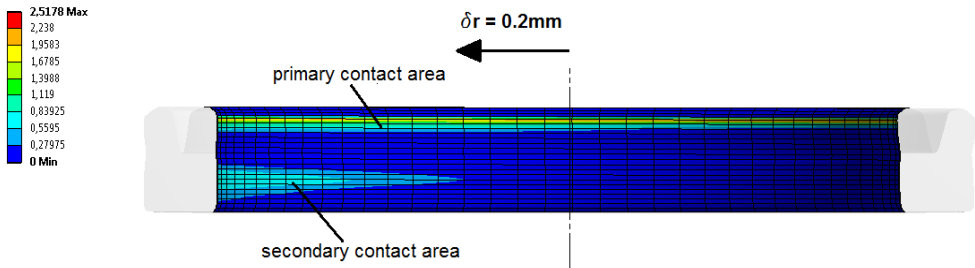


Figure 46: Contact pressure field for a rod misalignment of $\delta_r = 0.2 \text{ mm}$.

2.8 Conclusions

A procedure to develop an eccentricity tri-dimensional analytical contact model of seals was herein presented. Aim of this work was to study the effect of an incorrect mounting on seals in terms of contact forces and pressures. In this case, an eccentricity model of a rod lip seal built in TPU (Thermoplastic Polyurethane) was developed. Results showed that small rod mounting eccentricities lead to significant changes in the contact conditions between the rod and the seal. In this case, an eccentric mounting of just 0.2mm results in a very irregular contact force distribution where the maximum contact forces could even triple the minimum ones. Thus, although lip seal geometry itself facilitates its adaptation to low eccentricities, an increase in contact forces involves a reduction in the expected seal service life. Moreover, it has been also demonstrated that under eccentric conditions the contact pressure field in each seal section may change consistently from being composed of one area to be divided into two different areas. These facts highlight the importance of taking into account possible eccentricity effects when studying specific sealing systems.

The built model includes: a geometrical interference model, normal reaction forces, tangential forces and friction forces between the seal and the rod. A static case was considered in the absence of supply pressure. A satisfactory matching between experimental and analytical results was found. Results showed that tangential and frictional forces play an important role. The effect of friction forces is to overload the seal whereas tangential forces tend to decrease resultant contact forces. The methodology herein presented may be a viable tool for design purposes since it meets the challenge of measuring the contact force distribution between seals and their mating surfaces. Moreover, the model developed avoids the high computational costs and times associated to tri-dimensional numerical simulations. Moreover, the procedure herein presented can be applied to other seal sizes, geometries and materials.

It is thought that the main causes of differences in results may be that the analytical model does not include properties such as viscoelasticity and does not consider other aspects such as stick-slip regions, very important when working with elastomeric materials. In the next chapter, actual working conditions of lip seals will be reproduced including reciprocating motion and misalignment. Hence, the effect of rod to bore misalignments on seals operating under dynamic conditions will be studied. Moreover, in the next chapters the utility of the procedure herein presented for tribological studies will be proven.

2.9 References

- [1] Müller HK, Nau BS. Fluid sealing technology: Principles and applications. Marcel Dekker; 1998.
- [2] “Fluid Power Seal Design Guide”. Catalog EPS 5370. Parker Haniffin corporation. Engineered Polymer Systems Division; 2014.
- [3] Gorriño A, Angulo C, Canales J. Theoretical analysis of the pumping effect of rotary hydrodynamic seals with elastomeric lips. Tribology International 2007; 40: 896-905.
- [4] Conte M, Pinedo B, Igartua A. Frictional heating calculations for polymers. In: Proceedings of the Surface Effects and Contact Mechanics XI Congress – Siena, Italy; 2013.
- [5] Conte M, Pinedo B, Igartua A. Frictional heating calculation based on tailored experimental measurements. Tribology International 2014; 74: 1-6.
- [6] Salant RF, Shen D. Hydrodynamic effects of shaft surface finish on lip seal operation. STLE Tribology Transactions 2002; 45: 404-10.
- [7] Nikas GK. Eighty years of research on hydraulic reciprocating seals: review of tribological studies and related topics since the 1930s. Proceedings of the Institution of Mechanical Engineers Part J: Journal of Engineering Tribology 2010; 224: 1-23.
- [8] Huang Y, Salant RF. Simulation of Hydraulic Rod Seals with a Plunge - Ground Rod. In: Proceedings of the 5th World Tribology Congress – Turin, Italy; 2013.
- [9] Bignardi C, Manuello A, Mazza L. Photoelastic measurements and computation of the stress field and contact pressure in a pneumatic lip seal. Tribology International 1999; 32(1):1-13.

- [10] Lee CY, Lin CS, Jian RQ, Wen CY. Simulation and experimentation of the contact width and pressure distribution of lip seals. *Tribology International* 2006; 39: 915-20.
- [11] Belforte G, Conte M, Bernetto AM, Mazza L, Visconte C. Experimental and numerical evaluation of contact pressure in pneumatic seals. *Tribology International* 2009; 42:169-175.
- [12] Belforte G, Conte M, Mazza L, Raparelli T, Visconte C. Test rig for rod seals contact pressure measurement. *WIT Transactions on Engineering Sciences* 2010; 66: 107-114.
- [13] Goerres M. Friction force and leakage test rigs for the development of piston rod seals. *Ölhydraulik und Pneumatik* 2003; 47.
- [14] Flitney RK. *Seals and sealing handbook*. 5th edition. Elsevier; 2007.
- [15] "The Simmerring. Basics for preventing damage", Freudenberg Simrit.
- [16] "Hydraulic Cylinder Troubleshooting-avoiding Rod Seal Leakage and Premature Wear". Parker Hydraulics. Buletin 1242/1-GB.
- [17] Mokhtar MOA, Mohamed M.A.A, El-Giddawy ME, Yassen SAY. On the effect of misalignment on the performance of U-type lip seal. *Wear* 1998; 223: 139-142.
- [18] Amabili M, Colombo G, Prati E. Leakage of radial lip seals at large dynamic eccentricities. *Proceedings of the 16th international Conference on Fluid Sealing, September 18-20, Brugge, Belgium. 2000: 321-333.*
- [19] Conte M. MSc Thesis. Capitolo 3: Modello di guarnizione a labbro.
- [20] Lindley PB. Load-Compression Relationships of Rubber Units. *Jour. Of Strain Analysis* 1966; 1: 190-195.

- [21] Lindley PB. Compression Characteristics of Laterally Unrestrained Rubber O-ring. *Journal of International Rubber Inst.* 1967; 1: 202-213.
- [22] Green I, English C, Analysis of Elastomeric O-ring Seals in Compression Using the Finite Element Method. *Tribology Transactions* 1992; 1: 83-88.
- [23] Hyung-Kyu K, Sung-Han P, Hyan-Gyu L, Dong-Ryun K, Young-Ho L. Approximation of contact stress for a compressed and laterally one side restrained O-ring. *Engineering Failure Analysis* 2007; 14: 1680-1692.
- [24] Tasora A, Prati E, Marin T. A method for the characterization of static elastomeric lip seal deformation. *Tribology International* 2013; 60: 119-126.
- [25] Pinedo B, Conte M, Aguirrebeitia J, Igartua A. Effect of misalignment on a rod lip seal behaviour. *WIT Transactions on Engineering Sciences* 2012; 76: 151-161.
- [26] Aguirrebeitia J, Abasolo M, Avilés R, Fernandez de Bustos I. Theoretical calculation of general static load-carrying capacity for the design and selection of three row roller slewing bearings. *Mechanism and Machine Theory* 2012; 48: 52-61.
- [27] Aguirrebeitia J, Avilés R, Fernandez de Bustos I, Abasolo M. Calculation of General Static Load-Carrying Capacity for the Design of Four-Contact-Point Slewing Bearings *Journal of Mechanical Design* 2010; 132(6): 064501-6.
- [28] “Rotary Seals”. *Trelleborg Sealing solutions*; 2009.
- [29] Amasorrain JI, Sagartzazu X, Damián J. Load distribution in a four contact-point slewing bearing. *Mechanism and Machine Theory* 2003; 38(6): 479–496.

- [30] Conte M. Interaction between seals and counterparts in pneumatic and hydraulic components. PhD Thesis 2008. Politecnico di Torino.
- [31] Persson BNJ. Sliding Friction: Physical Principles and Applications. 2nd edition. Germany: Springer; 2000.
- [32] Pinedo B, Conte M et al. New high performance test rig for sealing systems characterization. In: Proceedings of the 5th World Tribology Congress - Turin, Italy; 2013.
- [33] Belforte G, Conte M, Bertetto AM, Mazza L, Visconte C. Experimental and numerical evaluation of contact pressure in pneumatic seals. Tribology International 2009; 42(1): 169–175.
- [34] Frölich D, Magyar B, Sauer B. A comprehensive model of wear, friction and contact temperature in radial shaft seals. Wear 2014; 311(1-2): 71–80.

Chapter 3: Effect of mounting eccentricity on seal performances – Experimental tests

3.1 Introduction

In the previous chapter, a procedure to develop a tri-dimensional eccentricity model for seals which enables calculating the contact force distribution between seals and counterparts for different rod to bore misalignment values was proposed. In this chapter, the aim is to investigate the effect of rod to bore misalignments on the tribological performance of seals during operation in terms of friction and wear. Moreover, within this chapter the utility of the methodology proposed in the previous chapter is also demonstrated. To this aim, the wear rates and the friction force distribution of the tested seals have been calculated, using the results obtained from the eccentricity contact force models.

As stated in the first chapter, the tribological behaviour of seals and other components is influenced by a big amount of parameters such as the mechanical, thermal and chemical properties of bodies in contact, surface roughness, sliding conditions, the environment and the characteristics of the lubricant film, among others. Moreover, in general, tribological conditions such as friction and wear vary in time, and in the

case of seals, also in position, since pumping conditions are different in the instroke and outstroke [1,2].

Most of the works related to seals have been devoted to gain knowledge about the main sealing parameters and mechanisms. Up to the 60s, most of the studies were related to the study of the main sealing parameters. In particular, contact pressure and contact width, film thickness, friction force and leakage rate were identified through experimental investigation as the main parameters affecting the sealing performance [3]. From that period on, and thanks to the development of technology and of new advanced numerical tools, the attempts for a better understanding of sealing mechanisms continued.

Due to the lack of standardized methods, many test rigs for seal characterization were developed in the last years [4-10]. Johnson et al. [4] developed a test rig for measuring the temperature evolution and fluid leakage of hydraulic piston seals working under reciprocating working conditions. Belforte et al. [5] developed a test rig for accelerated life testing of pneumatic piston seals for reciprocating applications. Raparelli et al. [6] and Belforte et al. [7,8] also studied friction forces in pneumatic cylinders under different working conditions by means of many test rigs developed for this purpose. They individually studied the contribution of piston seals, rod seals and valve seals to the resultant friction forces generated within the cylinder. Juoksukangas et al. [9] built an advanced test rig to test reciprocating rod seals for hydraulic applications reproducing the drilling shaft sealing system under a wide range of conditions and dynamic side loading applied by means of an electric shaker. Pinedo et al. [10] developed a high performance modular test rig

for characterization of reciprocating and rotary seals for both pneumatic and hydraulic applications. Moreover, diverse techniques have been used to measure the main sealing parameters. For instance, technologies such as photoelastic techniques [12], pressure film sensors [13,14], radial force integration techniques [15] and manganin wires [16] have been usually used for static contact pressure measurement. For measuring seal wear and leakage, new techniques such as displacement laser sensors [17] and interferometry techniques [18] have been usually used, respectively.

Apart from experimental tests, diverse lubrication models [19-23] and roughness models [24-27] of elastomeric seals have been developed during the last decades in an attempt to model the seal behaviour and to calculate the leakage rates under different operating conditions. Nevertheless, due to the non-linear behaviour of elastomers and their viscoelastic properties, obtaining analytical solutions and building feasible numerical models of seals is a difficult task. Furthermore, the strong dependence of elastomers with temperature and their high hysteresis, relaxation and creep hinder the evaluation of the seal performance.

Thus, after decades of research on the sealing mechanisms, some authors underline that there is still a lack of studies related to the surface wear of seals and to their life expectancy [3]. One of the objectives of this chapter in this field is to study the wear of reciprocating rod seals with the travelled distance and with rod to bore eccentricities. Due to the big amount of factors involved in the wear process, a wide knowledge in mechanics, material science, tribology, physics and chemistry is needed

for a better understanding of such processes. In the case of polymers, their wear behaviour depends on its non-linear mechanical and thermal properties at a great extent. Hardness and compressive strength influence load-carrying capacity, penetration and abrasion resistance. Tensile modulus accounts for deformability and cold-flow properties, and melting point shows temperature limitations [31]. Furthermore, wear prediction involves an exact identification of the main wear mechanisms under specific contact and operating conditions in order to be able to model it. Hence, modelling wear is a difficult task since the wear behaviour is complex and specific for certain sliding conditions. Consequently, even if in the history many authors have tried to develop reliable models or equations in an attempt to model the wear of components and predict their lifetime, there is no a reliable equation to do it so far [31-37]. Even so, previous studies dealing with the wear of polymers have made a great contribution to the existing knowledge in this field: Martínez et al. [36] found from experimentation with a guide shoe insert made of TPU and a steel guide, that there is a linear relationship between the TPU worn volume and the travelled distance, while the relation between the worn volume and the applied force is non-linear. Moreover, they found an analogy between the wear process and the crack formation process. The same authors, years later, developed a methodology to numerically model the wear phenomena in a TPU-steel contact [37]. Unal et al. [39] found that the wear rates of diverse PTFE compounds decrease with the applied load whereas it remains nearly constant for the pure PTFE.

In this chapter, the effect of rod to bore misalignments on the tribological behaviour of seals is investigated. To this end, sliding tests were carried

out on two commercial seals for reciprocating applications in a test rig specifically designed to test complete sealing components. Seals were tested under both concentric and eccentric controlled mounting conditions in order to compare the results. During the sliding tests, the friction generated was screened, and wear measurements were carried out after each test. Moreover, the wear rates of seals and the friction distribution along the whole seals were calculated under concentric and eccentric conditions using the outputs from the eccentricity models developed following the procedure described in Chapter 2. Thus, the applicability of the contact force eccentricity model is proven within this chapter. Therefore, the work herein presented contributes to the lack of research on two topics: wear of reciprocating seals, and the effect of eccentricities on sealing performance.

3.2 Specimens & materials

Experimental tests were performed on two rod lip seals commonly used in hydraulic applications, named as: seal A and seal B. The details of both seals are shown in Table 2. Thermoplastic Polyurethane (TPU) and Nitrile Butadiene Rubber (NBR) are two of the polymers most commonly used in the sealing industry to manufacture seals for applications involving operating velocities lower than 0.5 m/s under pressures of up to 400 bar, in the case of TPU, and up to 160 bar, in the case of NBR seals.



| Seal | Material | Dimensions(mm) | Range of application | Figure |
|----------|-------------------------------------|----------------|---|--|
| A | TPU (Thermoplastic Polyurethane) | 45x55x6 | <ul style="list-style-type: none"> ▪ Pressure: ≤ 400bar ▪ T: $-30 \div 100^{\circ}\text{C}$ ▪ Speed: ≤ 0.5m/s |  |
| B | NBR (Nitrile Butadiene Rubber) | 45x55x7 | <ul style="list-style-type: none"> ▪ Pressure: ≤ 160bar ▪ T: $-35 \div 100^{\circ}\text{C}$ ▪ Speed: ≤ 0.5m/s |  |

Table 2: Main characteristics of seals under study.

Both test seals have the same inner and outer diameters. In particular, seals for mounting rods of 45mm and for groove diameters of 55mm were selected in this work. Furthermore, seal A is exactly the same seal (same geometry, material and size) modelled in the previous chapter because the contact forces previously calculated will be used within this chapter for wear rate and friction calculations.

Regarding materials, seal A is made of TPU which is a thermoplastic elastomer that combines the mechanical properties of the rubber with the processability of thermoplastics. It usually has a good wear resistance and good load carrying capacity, a moderate service temperature range (up to about 110°C) and it is quite sensitive to humidity. TPU is widely used in the sealing industry because its low cost, high elasticity, flexibility, high load carrying capacity and resistance to oxidation, among others. It is also a good absorber of noise and vibrations, and it is resistant to most of the greases and mineral oils

used in hydraulic applications. Furthermore, it can be repeatedly melted and processed, due to the absence of chemical networks in its formulation.

Seal B is made of NBR, a thermoset elastomer that is both elastic and viscous. Typical rubber compounds consist of several ingredients added in order to improve their physical properties, enable vulcanization, improve processability, and prevent long-term deterioration. Rubbers are subjected to vulcanization processes in order to form chemical bonds between elastomer chains so that their stability, strength and resilience are increased. NBR has a good resistance to oils, good adhesion to metals, and moderate friction coefficient and thermal resistance (up to about 110°C).

Mechanical characterization of seals

Table 3 shows some mechanical properties of the seals under study. These properties were provided by the seal manufacturers. As can be seen, the TPU seal (A) is more rigid and has a considerably higher hardness than the rubber seal (B).

| Sample | Young modulus, E (MPa) | Tensile strength (MPa) | Density (g/cm ³) | Hardness |
|---------|------------------------|------------------------|------------------------------|------------|
| A (TPU) | 12 | 51 | 1.140 | 92 Shore A |
| B (NBR) | 3.8 | 19.3 | 1.187 | 68 Shore A |

Table 3: Mechanical properties of seals under study.

Thermal characterization of seals

Differential Scanning Calorimetry (DSC) and Thermogravimetric Analysis (TGA) were carried out for a better characterization of seal materials. In this way, in fact, it is possible to highlight the eventual transition phases leading to the wear mechanisms appearing during the sliding.

TGA is a technique in which the mass of a substance is measured as it is heated, cooled or held at a constant temperature. Hence, this technique examines the mass change of samples as a function of temperature and it is used to characterize the decomposition and thermal stability of materials under different conditions since mass losses are usually related to chemical reactions or/and physical transitions. In particular, it is usually used to characterize materials with regard to their composition. The analysis was performed by means of a DSC/TGA thermo-balance (Mettler Toledo, Spain) under a N₂ atmosphere of 50ml/min. Samples were heated from +25°C up to +800°C, with a heating velocity of +10°C/min. Figure 47 presents the TGA curves of both test seals. Analysis results showed that the TPU degrades in two steps: the first one corresponds to the degradation of hard segments inside the polyurethane, and the second one, to the degradation of soft segments. Results showed that in the range of +300°C and +800°C, the degradation of the material happens and that there is no almost any residual mass. In the case of NBR, it is stable up to a temperature of about +175°C and a mass of the 40% remains at high temperatures.

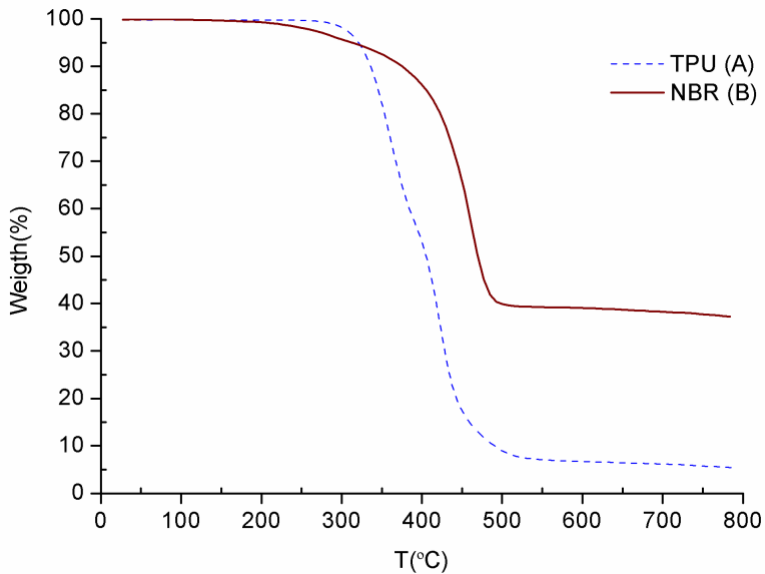
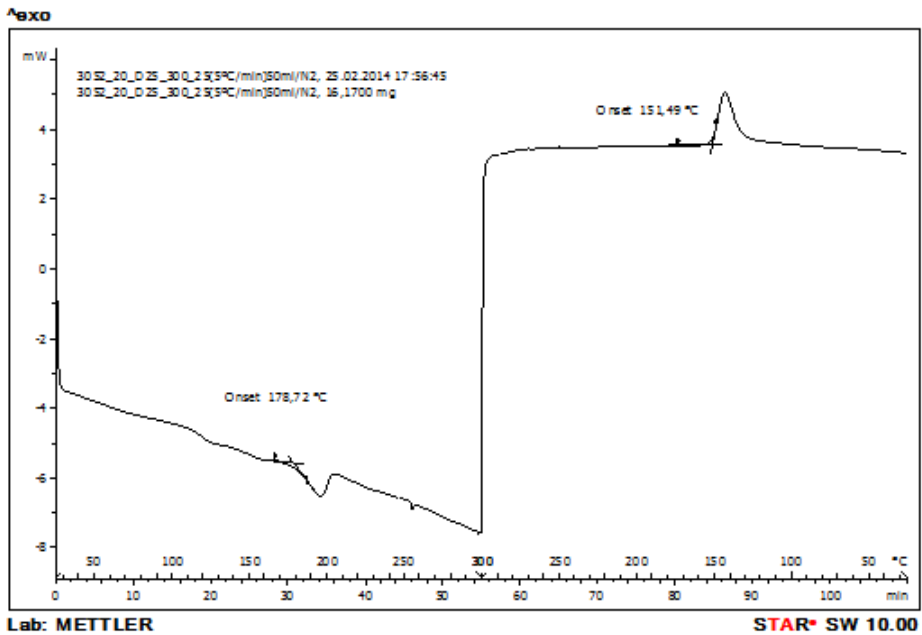


Figure 47: Thermal stability curves of seal samples with temperature studied by means of TGA analysis.

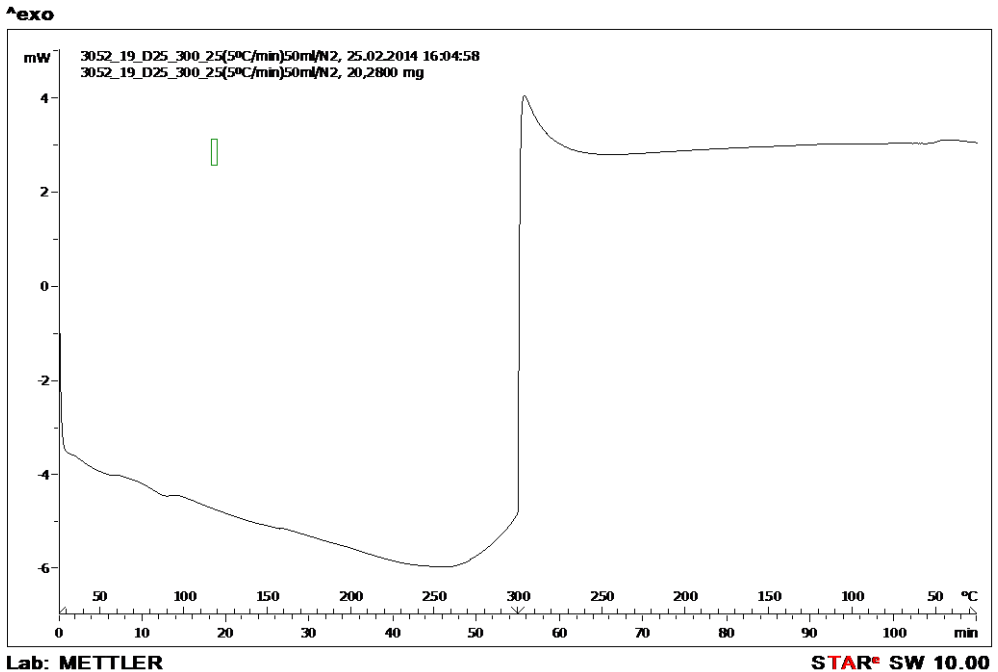
DSC was used to study the thermal transition of the seal materials. It is a technique in which the difference in the amount of heat required to increase the temperature of a specific sample and a reference sample are measured as a function of temperature. Differences in heat flow will arise when a sample absorbs or releases heat due to thermal effects such as chemical reactions, crystallization or melting, so that their corresponding enthalpy and entropy changes. Changes in heat capacity are tracked as changes in heat flow. The analyses were performed using a DSC 1-500 device (Mettler Toledo, Spain). During the analysis, the samples were heated from room temperature up to +300°C and afterwards back to room temperature. Heating and cooling of the samples were carried out at a velocity of $\pm 5^{\circ}\text{C}/\text{min}$ and in a N_2 environment of 50ml/min. DSC analysis results of the test seals are

Chapter 3: Effect of mounting eccentricity on seal performance-Experimental tests

shown in Figure 48. Seal A is made of TPU which is a thermoplastic, so it can be reshaped by application of both heat and pressure. The peak presented by the TPU material at +178°C is related to the disordering of hard segments crystallites, thus, it represents the melting temperature of the material. When cooling, it presents another peak due to material crystallization at +151°C. In the case of seal B which is made of NBR the DSC curve does not present any transition point within the studied range since the NBR is a thermoset elastomer so that it does not melt at any temperature and it does not soften but decompose when heated.



(a)



(b)

Figure 48: DSC curves of the (a) TPU (seal A) and (b) NBR (seal B).

3.3 Experimental setup

In order to investigate the tribological performance of the test seals under both concentric and eccentric conditions, a tribological characterization of seals was carried out. To this aim, sliding tests were performed in the test rig TESSA, a test bench specially designed in IK4-Tekniker to this aim [10]. In this section, the test rig as well as the specific test chamber designed for comparing the tribological behaviour of seals under different rod to bore positions are presented.

3.3.1 Test rig description

The test rig TESSA is a high performance test bench designed and manufactured in IK4-Tekniker in order to characterize seals under a wide range of working conditions. In particular, it is a modular test bench thought to evaluate the effect of critical factors, such as pressure, velocity, misalignment and temperature, etc., on the performance of sealing systems, highlighting their failure mechanisms on wide ranges of test parameters, including accelerate life tests. A tri-dimensional view of the test rig is shown in Figure 49.

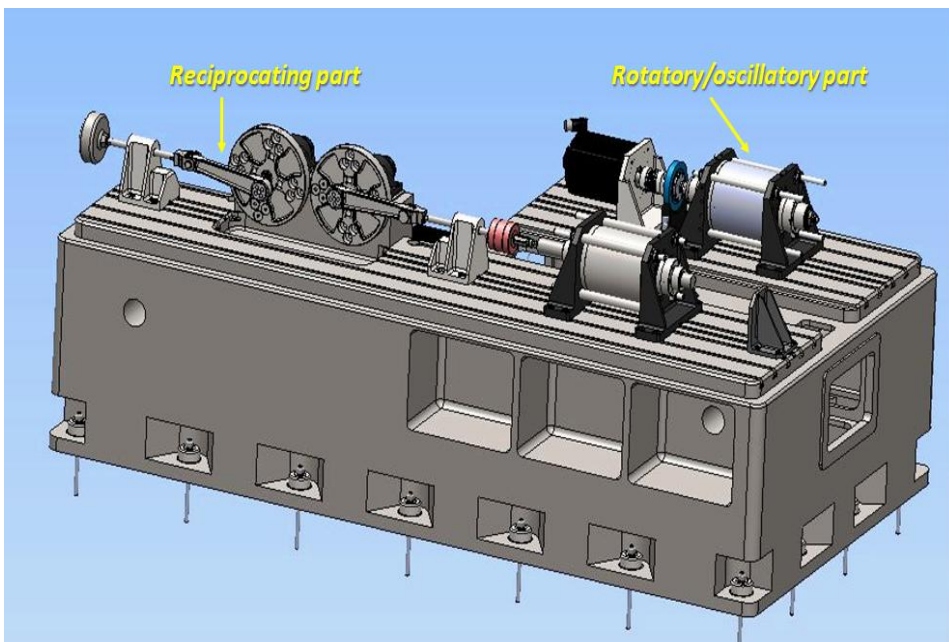


Figure 49: Test rig TESSA for seal characterization.

The test rig is composed of two main parts, a reciprocating part and a rotatory/oscillatory one, in order to test both reciprocating and rotatory seals. Both parts consist of an actuating system (electrical motor), a

friction measurement device and a modular test chamber tailor made for each application. The reciprocating and rotatory parts of the sealing test rig are shown in Figure 50 and Figure 51. The versatility of this advanced test rig allows reproducing many sealing applications commonly found in the industry. The modularity of the test chamber, in fact, allows testing a wide range of seal types, materials, geometries and configurations. Moreover, both rod and piston seals, both reciprocating and rotatory seals, and both hydraulic and pneumatic seals could be tested through this test rig. The system comprises a hydraulic and a pneumatic system in order to test seals working in oil environments and with gasses such as compressed air, nitrogen and helium could, among others.

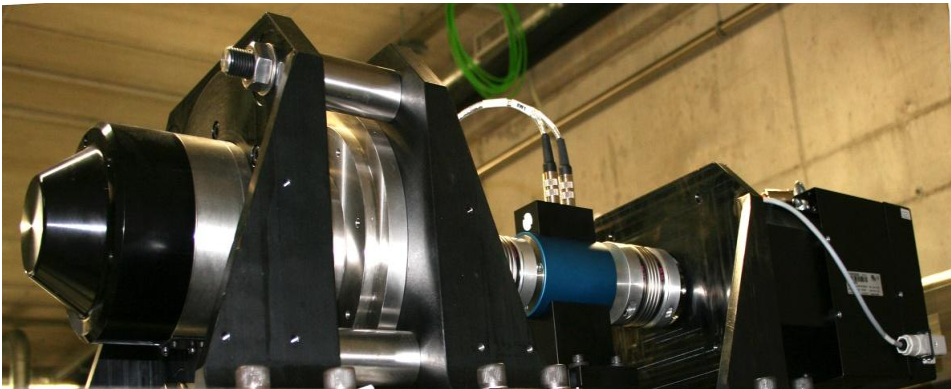


Figure 50: Rotatory part of the sealing test rig.

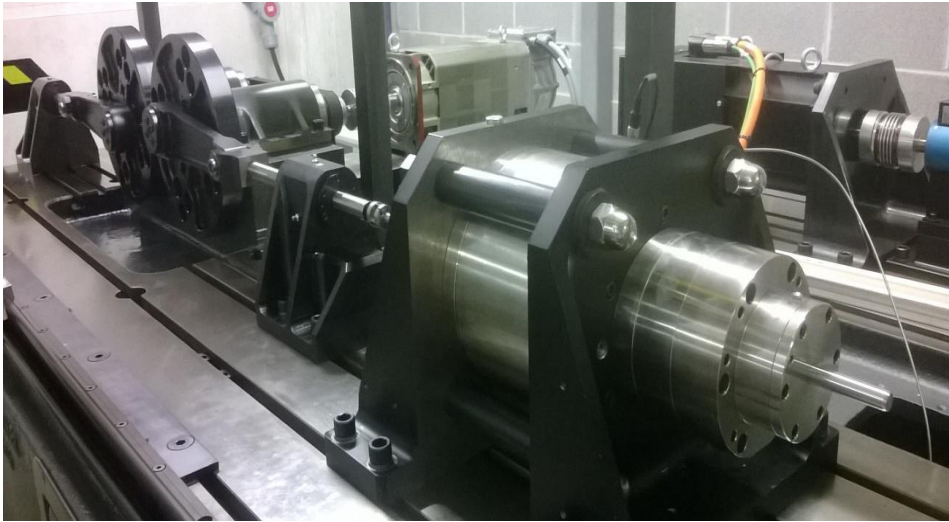


Figure 51: Reciprocating part of the sealing test rig.

For tribological characterization of the sealing systems, three kinds of tests are usually carried out: friction tests, leakage tests and accelerated life tests. During the friction tests the friction between seals and counterparts is measured over time by means of a friction force measurement device. Since life tests of seals are too long to perform at laboratory, accelerated life tests are usually carried out. The aim of the accelerated tests is to accelerate the wear process of seals so that it can be studied in a short period of time. To this end, a working parameter is usually stressed. Typical stressed parameters are pressure, velocity and a lower amount of lubricant, for instance. During the accelerated life tests the leakage is measured by fluid collectors according to the ISO 7986:1997 standard in the case of hydraulic applications, and by pressure drop inside the test chamber in the case of pneumatic applications.

3.3.2 Mounting configurations of seals under study

In this work, the selected seals are reciprocating so that they have been tested in the linear module of the test bench. In order to study the effect of an eccentric mounting of seals on their performance, a tailored test chamber was designed and manufactured (see Figure 52). The sealing system of the test chamber consists of a seal (1) (the seal under study) and four guide rings (2), two at each side of the lip seal. A controlled eccentricity was introduced in the assembly by designing the groove of the seal with a known radial eccentricity with respect to the shaft centre. In particular, two different pieces named as (3) with different seal groove designs were manufactured: one of them with the seal housing concentric to the rod centre, and the other one with the seal housing misaligned 0.15mm with respect to the rod centre. The nominal radial gap between the rod surface and the bore is 0.2 mm (the maximum applicable misalignment); the same as in the test rig designed in Chapter 2.

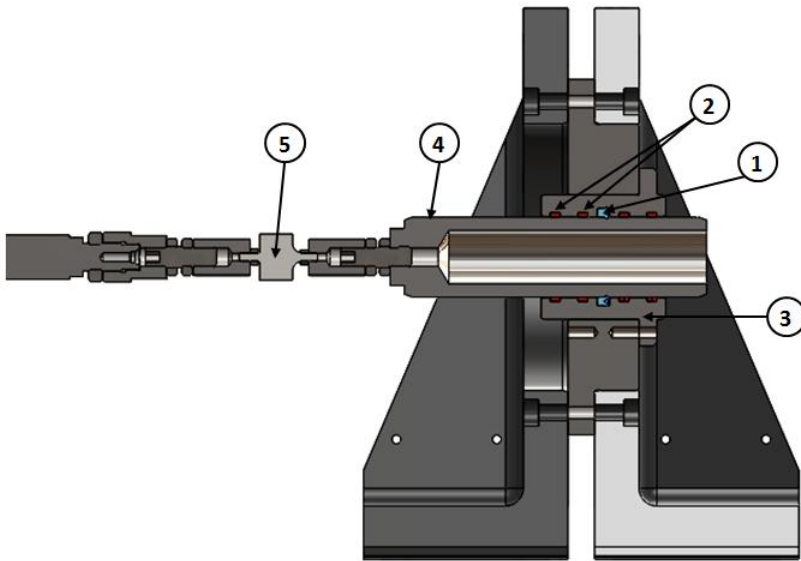


Figure 52: Experimental setup for tribological tests of seals.

A photograph of the test rig assembly is shown in Figure 53. The test chamber is composed of the sealing system, its metallic housings and the reciprocating rod. Seals under study are mounted on the seal groove with two guide rings at each side. The seal rod (4) made from F1150 (18CrMoS4) steel, with a diameter of 45mm and a roughness of $R_a=0.4\mu\text{m}$ slides against the test seals. The rod is connected to a load cell (5) which measures the friction tension-compression forces generated during sliding with an accuracy of $\pm 0.2\%$ (HBM, U9C model, 1KN, Germany). The other end of the force transducer is directly connected to the actuation system that consists of a crank mechanism that converts the rotation of the motor into a lineal movement. The entire system is mounted on a precision machine frame which maintains all the parts correctly aligned.

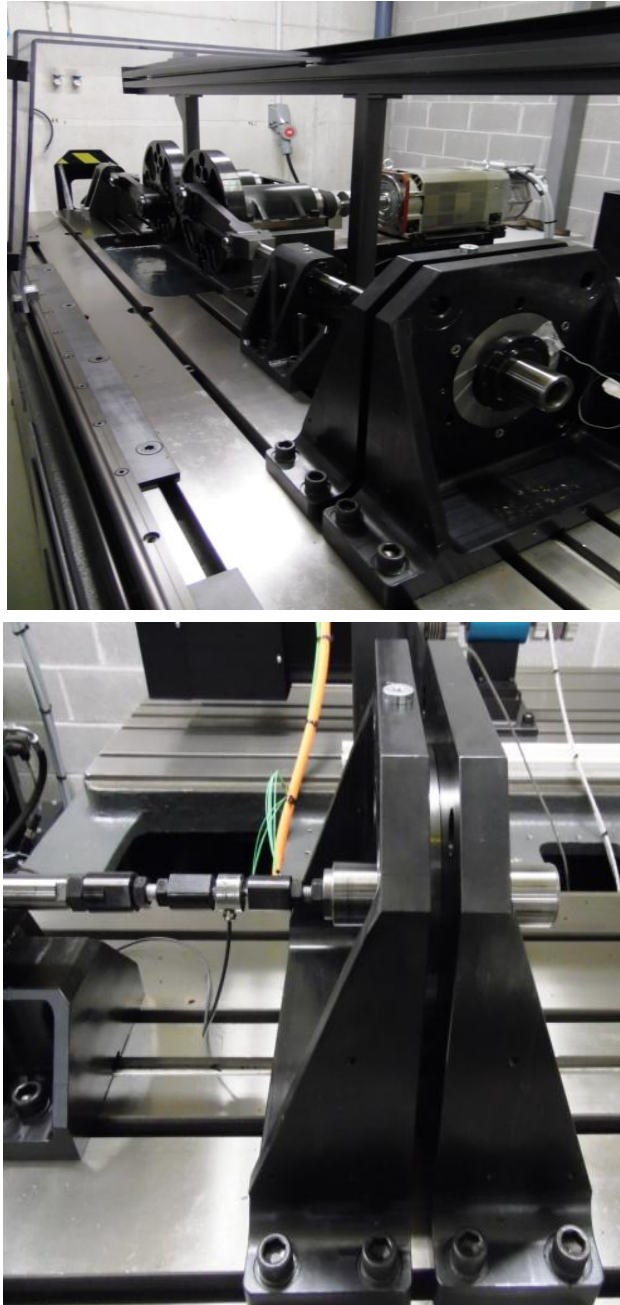


Figure 53: Test rig assembly.

3.4 Test conditions

The test conditions are summarized in Table 4.

| | | | | | |
|----------------|---------------------------------------|----------------------|----|-----------|-----|
| INPUTS | Test seals | A (TPU) | | B (NBR) | |
| | Motor velocity | 114 rpm | | | |
| | Stroke | 84 mm | | | |
| | Sliding velocity | 0.5 m/s | | | |
| | Lubrication | Dry conditions | | | |
| | Nominal rod to bore radial gap | 0.2 mm | | | |
| | Rod to bore eccentricity | 0 mm (concentric) | | 0.15 mm | |
| | Test duration | 1h | 2h | 5h | 10h |
| OUTPUTS | Measured parameters | Friction evolution | | Mass loss | |

Table 4: Test conditions.

Tests were performed at a stroke of 84mm and a sliding velocity of 0.5m/s, which is the maximum velocity recommended for both seals. The nominal gap between the rod surface and the cylinder bore is 0.2mm. As the aim of this chapter is to investigate the effect of radial mounting and manufacturing eccentricities on the tribological performance of elastomeric seals, two different test campaigns were carried out under two different mounting conditions:

- Test campaign 1: $\delta_r=0mm$, concentric test conditions.
- Test campaign 2: $\delta_r=0.15mm$. A radial misalignment of 0.15mm was introduced between the rod and the seal groove centres.

In order to measure the evolution of mass loss with time, tests with different duration were carried out. In particular, the following test durations were selected: 1h, 2h, 5h and 10h. Those test durations were selected as a result of a number of tests performed for determining the travelling distances that produce a significant mass loss on seals.

Regarding lubrication, tests were performed under dry conditions in order to have a measurable mass loss of seals in a reasonable period of time. In real applications, test seals made of the selected materials are usually used with a low amount of lubrication in the case of pneumatic applications, and with full lubrication in hydraulic applications. Nevertheless, the tests herein carried out under dry conditions are acceptable since it is thought that they reproduce the wear of seals under extreme conditions, when the lubrication fails and the wear of seals is so severe that it leads to a rapid degradation of seals. Another reason for having selected dry conditions is that when the contact is lubricated, even if the amount of lubricant is low, seals absorb oil so that estimating the wear by mass loss is not possible anymore.

During the tests, friction was measured with an acquisition frequency of 104Hz. Seals were weighted before and after each test in order to measure their mass with travelled distance.

3.5 Contact force calculation

In this section seal/rod contact forces for both the seal tested are calculated since they are mandatory inputs for further friction coefficient and wear rate calculations. In the specific, the contact forces have been

calculated through the tri-dimensional eccentricity models developed applying the procedure presented in Chapter 2.

Seal A

The contact model of the TPU seal has been already developed and presented in the previous chapter. Introducing Equations (5) and (6) in Equation (31), the following contact force values were obtained for the considered rod to bore positions:

- $\delta_r = 0mm$, concentric condition $\rightarrow F_r = 105.32N$ (considering that the rod has a diameter of 45mm, the contact force in each section has a value of 0.75 N).
- $\delta_r = 0.15mm$, eccentric condition $\rightarrow F_r = 128.66N$

Hence, a misalignment of 0.15mm produces an increase of about 23N in the resultant contact force between the seal and the moving rod.

Seal B

As done in the previous chapter for the polyurethane seal (A), the plane model for building the tri-dimensional contact model of the rubber seal (B) was built in Ansys Workbench environment. The seal was modelled by means of quadrilateral elements with a size of 0.2mm, and of 0.1mm in the contact areas. The whole seal is composed of a total of 4291 elements. Seal geometry was obtained by means of an optical microscope (Leitz, model Libra 200, Germany). The generated mesh is shown in Figure 54.

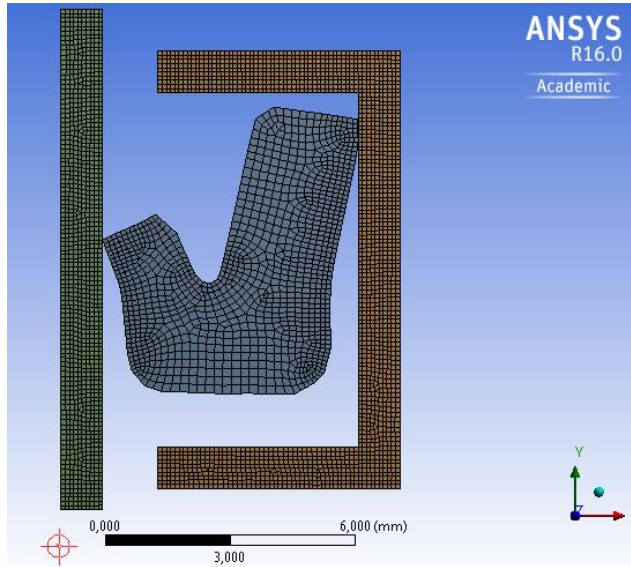


Figure 54: 2D FEM model of seal B.

A surface to surface contact formulation was chosen to simulate both the seal/rod and the seal/groove contacts. Boundary conditions take into account friction at contact surfaces in order to constrain the free movement of the seal. The friction coefficients were set to 0.1 for the seal/rod contact and to 0.4 seal/groove contacts [40]. The NBR (Nitrile Rubber) material was defined as incompressible, isotropic and hyperelastic. A second-order Mooney-Rivlin formulation with two constants was employed considering the following coefficients: $C_{10}=-2.75$ and $C_{01}=4.6$ [41]. In order to obtain the compression curve of the seal material, compression tests were carried out in the universal testing machine Instron 3369 (Massachusetts, USA). Compression curves of the both seal materials are shown in Figure 55. By comparison between the compression curves of both seal materials, it can be concluded that the compression curve tendency is similar in both cases but the

polyurethane response under compression is much stiffer than the response of the rubber material.

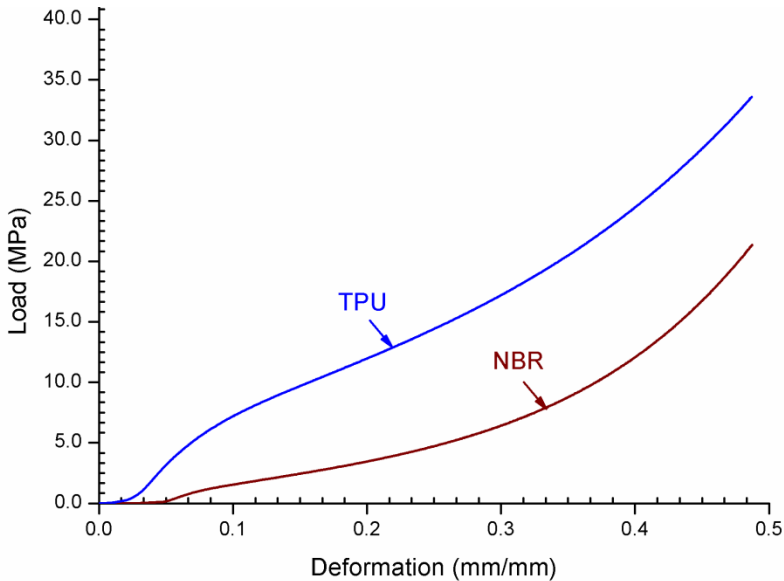


Figure 55: Experimental compressive stress-strain curve of the seal materials.

The rod and the bore were considered rigid elements since polymer stiffness is much lower than that of steel.

The interference between the seal and the rod when their centres are totally aligned has a value of $\delta_i = 1.13mm$. The nominal gap between the rod and the bore is 0.2mm as in the previous chapter; value that corresponds to the maximum applicable misalignment. In the graph shown in Figure 56, the normal forces and tangential forces acting on seal B as a function of interference or section compression are shown. These results were obtained through the plane numerical simulations. As in the case of the TPU seal (A), whose plane numerical results were

represented in Figure 28, results revealed that the stiffness of the NBR seal (B) varies considerably with compression.

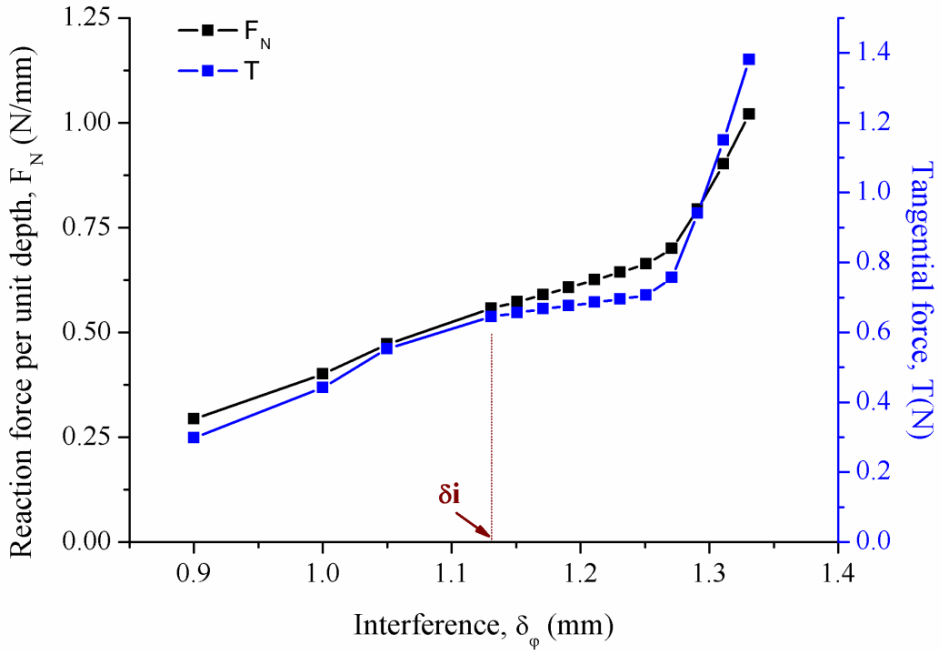


Figure 56: Reaction and tangential forces in seal B as a function of mounting interference or compression.

In this case, the stiffness of a cross section of the seal B can be also divided in two regions where it remains nearly constant: a low stiffness region ($K \approx 1 \text{ N/mm}$) and a high stiffness region ($K \approx 4.5\text{-}6 \text{ N/mm}$). Furthermore, simulations showed a sudden change in stiffness that occurs for a seal compression of 1.27mm i.e. for a rod to bore misalignment of approximately $\delta_r = 0.14 \text{ mm}$.

Chapter 3: Effect of mounting eccentricity on seal performance-Experimental tests

In the area of interest, bounded by $\delta_i + e$ and $\delta_i - e$, the normal forces the rod and the seal could be expressed as,

$$F_N = 155.69 \delta_\varphi^4 - 675.38 \delta_\varphi^3 + 1092.8 \delta_\varphi^2 - 780.45 \delta_\varphi + 207.74 \quad (36)$$

In the same way, the tangential forces acting on a compressed seal section may be expressed as a function of the interference as,

$$T = 356.97 \delta_\varphi^4 - 1549.6 \delta_\varphi^3 + 2508.2 \delta_\varphi^2 - 1792.3 \delta_\varphi + 477.25 \quad (37)$$

These two equations were used in order to calculate the seal/rod contact forces for the two different rod to bore positions considered in this chapter:

- $\delta_r = 0 \text{ mm}$, concentric condition $\rightarrow F_r = 74.64\text{N}$ (considering that the rod has a diameter of 45mm, the contact force in each section has a value of 0.53N).
- $\delta_r = 0.15\text{mm}$, eccentric condition $\rightarrow F_r = 76.27\text{N}$

Comparing the contact force results of the seals under study and their behaviour to eccentricities it can be concluded the following:

- The contact forces between the seal and the rod are considerably larger in the case of the TPU seal (A) than in the case of the NBR seal B (B). Causes for contact force differences are the geometry and the non-linear seal material. Nevertheless, in this case, the effect of the material is the main factor that leads to so different contact forces because, in fact, the stiffness and

hardness of the polyurethane are considerably higher than those of rubber.

- Both lip seals showed a change in stiffness with compression. In particular, both seals presented two regions of different stiffness where it remains constant: a low stiffness region and a high stiffness region. In the case of seal A, the change in stiffness occurs for seal compression values nearby the nominal interference, in particular, for rod misalignments of approximately $\delta_r = 0.04mm$. In the case of seal B, the change in stiffness occurs under larger compression values of approximately $\delta_r = 0.14mm$.
- From Figure 28 (seal A) and Figure 56 (seal B) it can be concluded that under the applied misalignment the response of the most compressed sections will be very stiff in the case of seal A whereas all the seal sections will still remain in the low stiffness region in the case of seal B.

3.6 Experimental results

In order to investigate the effect of rod to bore misalignments on sealing performance, the following parameters were measured during and after testing under concentric and eccentric conditions:

- Evolution of the friction force generated during sliding,
- Mass loss,
- State of the sealing surface by visual inspection,

In this section the results of the test campaign carried out are presented.

3.6.1 Effect of rod to bore misalignments on friction

Figure 57 shows the friction force curves of the seals tested under concentric mounting conditions and Figure 58 shows the friction force curves obtained when the centre of the rod is misaligned 0.15mm with respect to the seal groove centre. Results showed that, in all the cases, the friction force generated by the TPU seal (A) is larger than that generated by the NBR seal (B). The form of the friction curves is similar in both cases but the friction curves of seal B tend to reach a steady value before those of seal A. Both seals present the highest friction at the beginning of the test i.e. during the running-in period, and afterwards friction continuously decreases until a nearly steady-state condition is reached.

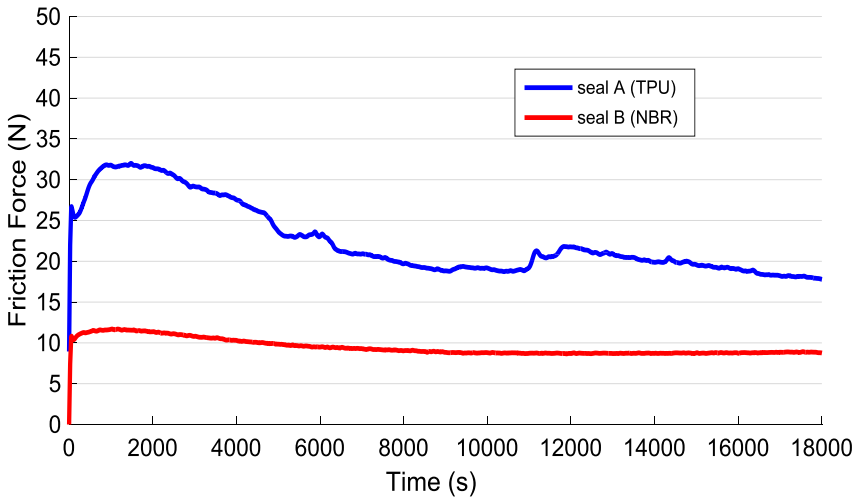


Figure 57: Friction of seals A (TPU) and B (NBR) under concentric conditions ($\delta_r = 0mm$).

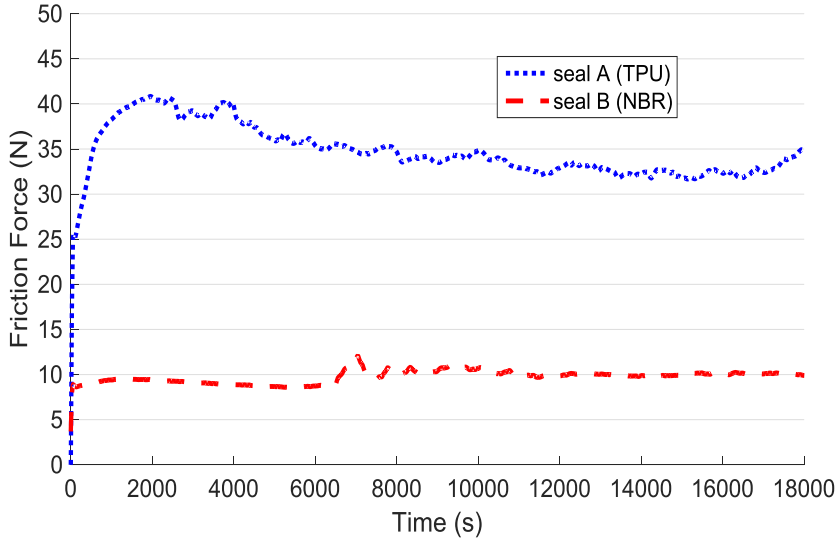


Figure 58: Friction of seals A (TPU) and B (NBR) under eccentric conditions ($\delta_r = 0.15mm$).

The behaviour shown by the seals tested is typical of polymeric components. The friction force is governed by the processes occurring at the mating surfaces, and it may be considered as the result of two components: adhesion and deformation. During the running-in, the roughness of the seal surface undergoes a large variation and this stage is characterized by a change in the friction curve shape which occurs due to topographical changes within the contact area [36,38]. In general, micro-asperities of the surfaces are eliminated during the running-in stage and a polymeric film is usually formed on the surface of the steel component. While the polymer film fills the valleys of the metallic counterface, the adhesive component of the friction increases since the adhesion in polymer/polymer contacts is higher than it is in steel/polymer contacts [38]. Then, a transient zone appears where the friction is maximum because an increasing force is required to continue the sliding

because of the cutting, forming and adhesive effects at the contact zone. At this friction peak in the transition zone re-adhesion process of the polymer film starts to provide a dynamic balance during further sliding, resulting in what is termed the steady-state of friction.

Results showed that rod to bore eccentricities considerably affect the total friction force generated between seals and the sliding rod. Under concentric conditions (Figure 57), seal A presented a maximum friction force of about 32N at the transition zone and a friction force of about 18N at the end of the test. In the case of seal B, it presented a friction peak of about 12N which remains nearly constant throughout the whole test. Under eccentric conditions (Figure 58), larger differences arise between the friction forces generated by each seal. In particular, the TPU seal (A) presented a maximum friction peak of about 40N at the transition zone whereas the friction peak originated by the NBR seal (B) was about four times lower. Under steady-state conditions, the friction presented by seal A is of 32N and the friction presented by seal B is of 10N.

Hence, results showed that the friction generated by the seal made of TPU (A) is considerably higher than that of the NBR seal (B) under the same mounting and operating conditions. In fact, both the seal geometry and the material influence the friction generated during sliding between the seal samples and the reciprocating rod. Moreover, factors such as the abrasive resistance and the work of adhesion of polymers depend to a great extent on their mechanical and chemical properties [38].

In Figure 59 and Figure 60 it is possible to observe the effect of the applied misalignments on the friction generated by both seals.

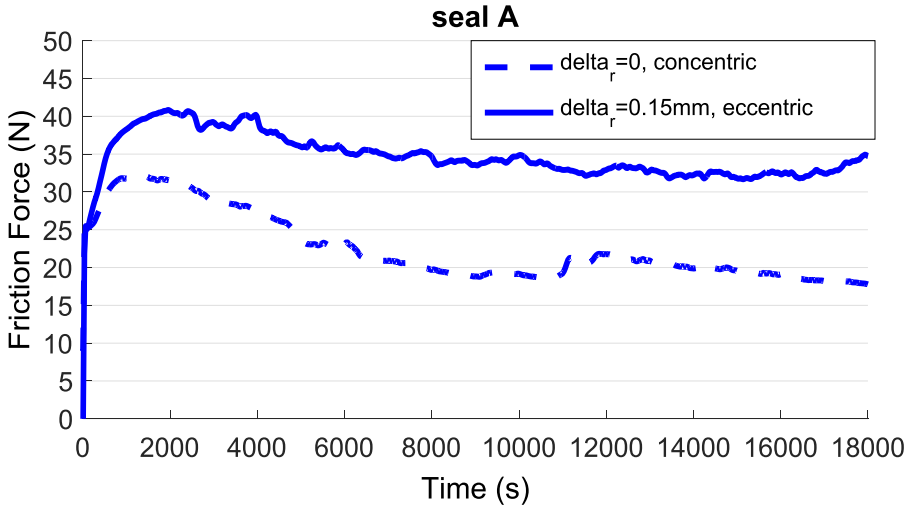


Figure 59: Comparison of the friction force generated by seal A (TPU) under concentric and eccentric conditions.

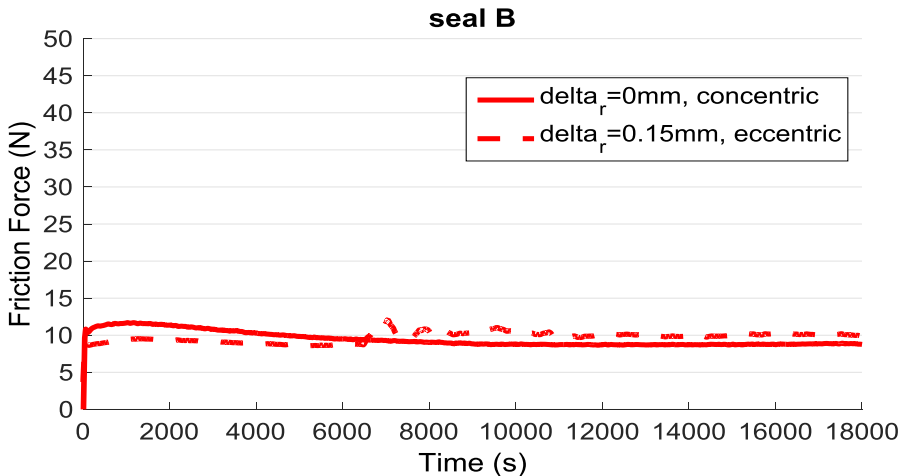


Figure 60: Comparison of the friction force generated by seal B (NBR) under concentric and eccentric conditions.

Results revealed that rod to bore misalignments lead to an increase in the friction generated between the mating parts during sliding. Subsequently, it may be concluded that the power consumption during operation will be higher in those devices with an eccentric mounting of seals. Nevertheless, it is important to remark that the effect of eccentricities on friction is more significant in the case of the seal made of TPU (seal A) than in the case of the NBR seal (seal B). In other words, it was found that the effect of misalignments on seals depends to a great extent on the seal material. In particular, in the specific, results showed that the seal made of rubber is less sensitive to possible misalignments arising from mounting and/or manufacturing errors than seals made of harder materials such as polyurethanes. The main reason for the low influence of the applied misalignment on the friction force generated by seal B is that the applied misalignment barely affects the contact forces between the seal and the rod (see Figure 56). It is thought that another reason may be seal material itself, whose main characteristics are high elasticity and a low hardness in comparison with the polyurethane so that it facilitates its adaptation to both static and dynamic misalignments.

3.6.2 Effect of rod to bore misalignments on seal wear

Wear is not a specific property of a material but it is the result of the relative sliding motion between two bodies in contact. In tribology, wear is usually measured in terms of mass loss or worn volume. In fact, the amount of the mass lost during sliding depends on the contact and sliding conditions, motion duration and material properties. The main wear mechanisms of polymers were introduced in the first chapter, and

as previously commented, the resultant wear usually combines many different wear processes.

In this section, wear results of the tested seal samples are presented with the aim of investigating the effect of rod to bore misalignments on the wear process of seals. For this purpose, weight measurements of samples were carried out and the contact surfaces were analysed through surface inspection in order to identify the main wear mechanisms.

3.6.2.1 Wear results

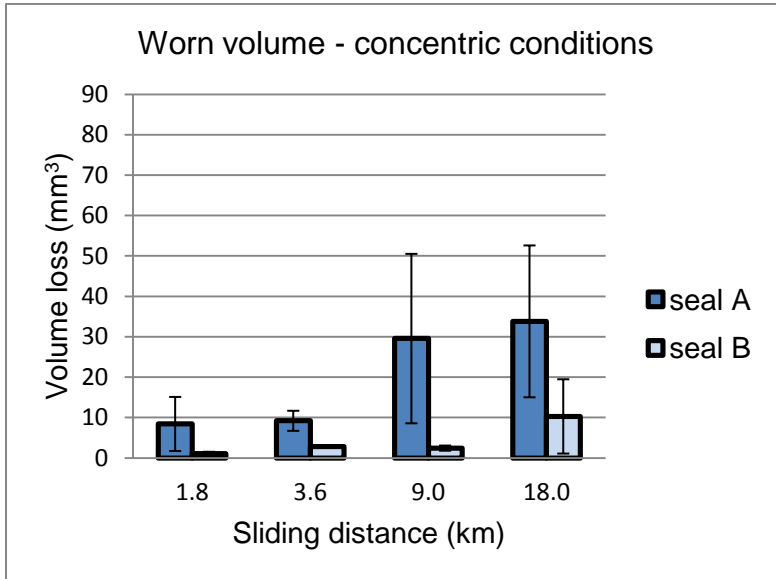
The weight of each seal sample was measured before and after each test using a high precision scale (XPE2004SC, Mettler Toledo, Spain) with a resolution of 0.1mg. In Table 5 the wear of the tested seals is presented in terms of both mass loss (in mg) and worn volume (in mm³). Wear volume calculations were done using the density values shown in Table 3.

In Figure 61 column bar diagrams showing the volume loss of seals against the travelled distance are plotted. Results revealed that the volume loss of the seal A (TPU) is higher than the volume loss of the seal B (NBR) under the both tested mounting conditions. These results are in good agreement with those obtained by Belforte et al. in [49] where the authors tested the same seal made from NBR and TPU, and they found that the life of the formers was considerably longer. That is, the wear resistance of the rubber seals is considerably higher than that of the seals made of polyurethanes.

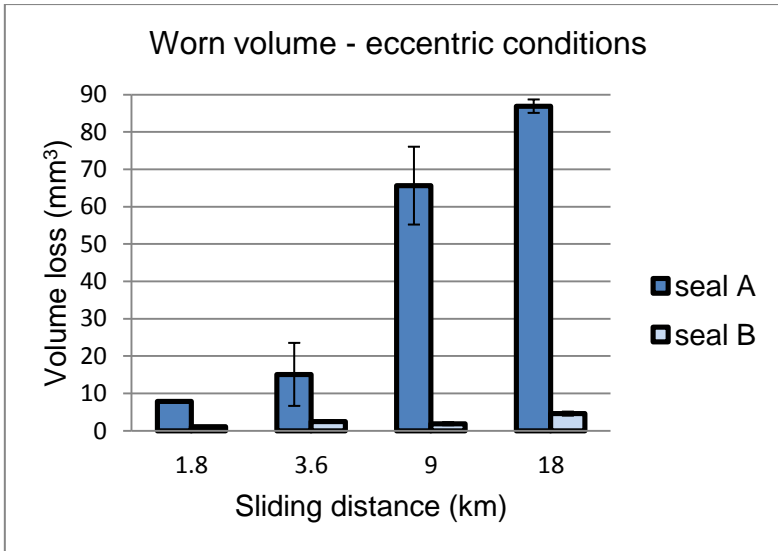
| Seal | Test time (s) | Travelled distance (km) | CONCENTRIC | | ECCENTRIC | |
|------------|---------------|-------------------------|----------------|--------------------------------|----------------|--------------------------------|
| | | | Mass loss (mg) | Volume loss (mm ³) | Mass loss (mg) | Volume loss (mm ³) |
| A (TPU) | 3600 | 1.8 | 9.60 | 8.42 | 9.00 | 7.89 |
| | 7200 | 3.6 | 10.50 | 9.21 | 17.20 | 15.09 |
| | 18000 | 9 | 33.70 | 29.56 | 74.80 | 65.61 |
| | 36000 | 18 | 38.55 | 33.82 | 99.05 | 86.88 |
| B (NBR) | 3600 | 1.8 | 1.05 | 0.88 | 1.30 | 1.09 |
| | 7200 | 3.6 | 2.85 | 2.40 | 2.95 | 2.48 |
| | 18000 | 9 | 2.45 | 2.06 | 2.25 | 1.89 |
| | 36000 | 18 | 10.30 | 8.68 | 5.45 | 4.59 |

Table 5: Wear results of the tested samples.

As can be seen in Table 5, after a travelled distance of 18km, the volume loss of the TPU seal (A) is up to four times the volume lost by seal B (NBR). Under eccentric conditions, the volume loss of the TPU seal is considerably higher than its loss of volume under concentric conditions whereas the volume loss of the NBR remains similar.



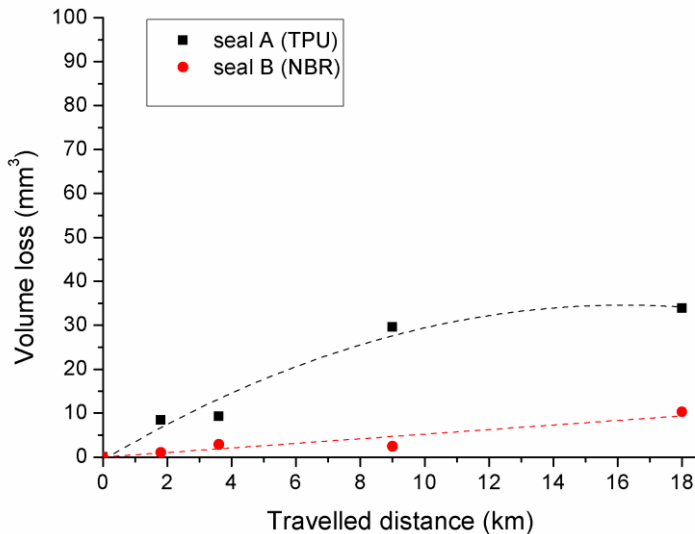
(a)



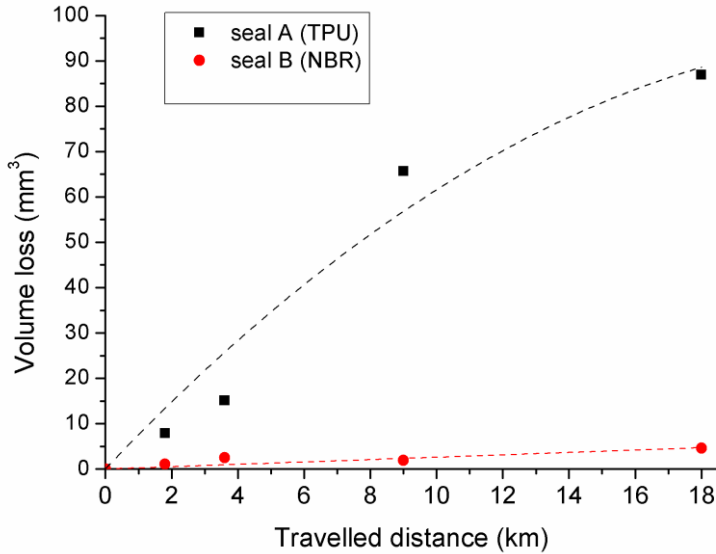
(b)

Figure 61: Evolution of the wear process on seals with the travelled distance under: (a) concentric conditions, $\delta_r = 0mm$ and (b) eccentric conditions, $\delta_r = 0.15mm$.

In Figure 62 the volume loss curves of the tested seals are plotted against the travelled distance. As can be seen from the graphs, the wear results of the NBR seal (B) tested under both concentric and eccentric mounting conditions are very similar. Therefore, results showed that mounting misalignments do not accelerate the wear of the samples made of rubber. For type A seals made of TPU, it was found that mounting misalignments lead to a considerably higher wear i.e. that rod to bore misalignments accelerate the wear process of the TPU seal. Regarding the volume loss curves tendencies, they are in good agreement with those observed in [38]. Under the running-in stage or the unsteady state wear stage, where the smoothing of the elastomer surface occurs, the volume loss of the seal due to abrasion is high. The transition to the steady-state wear regime is usually coincident with the balance between the material removed from the wear track and that transferred to the mating surface.



(a)



(b)

Figure 62: Volume loss (mm^3) vs. travelled distance for tests carried out under: (a) concentric and (b) eccentric ($\delta_r = 0.15\text{mm}$) mounting conditions.

3.6.2.2 Surface inspection

In Table 6 some photographs of the worn seals are shown. In particular, both the cross sections and the worn surfaces are presented, in order to show the evolution of wear with the travelled distance and the severity of wear with rod to bore eccentricities. In the table, only the images corresponding to the TPU seals (A) are shown since it was not found any significant wear on the NBR seals (B). The micrographs were obtained using an Olympus SZX16 microscope. Micrographs evidenced that the material loss at the contact area or dynamic lip is much severe on those seals tested under eccentric conditions. Regarding the wear

mechanism, adhesion and abrasion marks that lead to the smoothing of the lips were observed on the worn surfaces. In fact, elastomers running under dry lubrication lead to large adhesion mechanisms. Under dynamic mounting conditions and a travelled distance of 18km, the wear on the most compressed section of the seal is so severe that the contact surface has a glossy aspect and the dynamic lip has been completely flattened.

In Figure 63 SEM micrographs of the worn surfaces are shown. The micrograph presented in Figure 63a shows the surface of the seal after travelling a distance of 18km under concentric mounting conditions. As can be seen, this micrograph still presents marks of the initial stage i.e. marks formed during the manufacturing of the sealing lip. Figure 63b represents the sealing surface of the most compressed seal sections from the tests carried out under eccentric conditions. The image presents adhesive signs and a glossy aspect, usually observed in polyurethane when it fails [50].





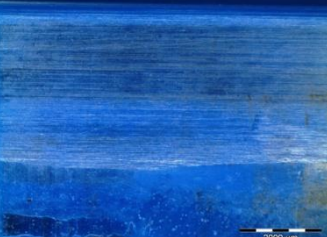




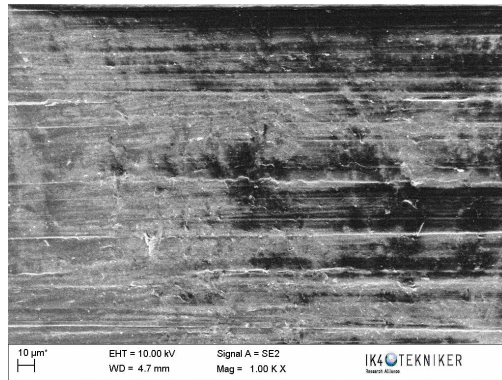
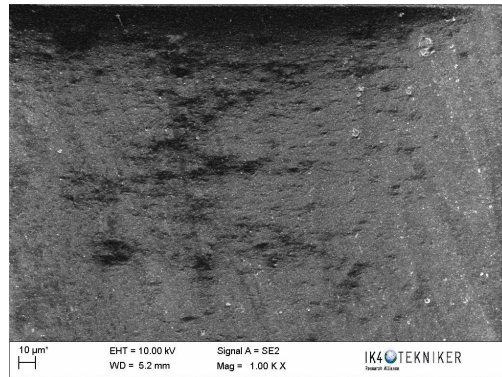
| Seal A | | | | |
|------------|--------------------|---|---|--|
| | Before tests |  | | |
| | Travelled distance | Seal Section | Contact surfaces | Wear mechanism |
| CONCENTRIC | 3.6 km |  |  | Adhesion and abrasion wear. |
| | 18 km |  |  | Adhesion and abrasion of the contact lip. |
| ECCENTRIC | 3.6 km |  |  | Adhesion and abrasion of the contact lip. |
| | 18 km |  |  | Severe wear. Smoothing of the contact lip. |

Table 6: Micrographs of the worn surfaces of seal samples A.



(a)



(b)

Figure 63: SEM micrographs of the A type seal samples after travelling 18 km under: (a) concentric conditions, $\delta_r = 0 \text{ mm}$ and (b) eccentric conditions, $\delta_r = 0.15 \text{ mm}$.

3.7 Wear rate calculations

The specific wear rate coefficient k is usually used in order to compare the wear of different materials under different combinations of contact

loads and sliding velocities. It is an indicator of the volume loss of a specific material per unit load and unit distance.

During the running-in stage and the catastrophic wear stage, the wear rates vary continuously, and only during the stationary stage a constant wear rate is attained (see Figure 15). Hence, in order to characterize the long-term properties of systems, only the steady state conditions are useful [36].

In particular, during the running-in, the wear rate is in general quite high and it is considerably influenced by the initial roughness of the mating surfaces. The transition from an unsteady to a steady wear rate is usually in line with the transition from abrasive to adhesive wear [38].

Even if modelling wear processes is extremely complex due to the big amount of parameters involved, many authors have made attempts during the last decades to model the wear of specific materials under particular contact conditions [32-37]. Table 7 presents some of the most popular wear models. In fact, all these analytical wear models apply only to relate the wear volume with the test and contact conditions, and the inherent material properties throughout the steady stage of wear.

In general, most of the analytical wear models assume that the wear rate is inversely proportional to the hardness of materials (the harder the material, the less the wear). While this is true for metals, in the case of polymers the effect may be the opposite [43]. Hill et al. [44] tested polyurethanes with different hardness and demonstrated that for polyurethanes with hardness in the range between 75A and 95A, the

wear rate is almost independent of hardness. In other words, that the thermal softening of these polyurethanes does not alter their wear performance. In fact, models differ in the main parameters they take into account to model the wear process. The model of Ratner and Lancaster [45], usually used to model the abrasive wear of polymers, relates the wear rate of polymers to their bulk mechanical properties. They found some correlation between the wear rate and the mechanical properties of polymers. Budinsky et al. [46] concluded that the abrasive wear of elastomers and polymers, in general, correlates better with a combination of friction coefficient and mechanical properties.

| Wear model | Equation | Nomenclature |
|---|-----------------------------|---|
| Archard's wear law (1953) | $V = K \frac{Ws}{H}$ | where K is the wear factor, W is the normal load, s is the sliding distance and H is the hardness of the softer material. |
| Lewis model (1964) | $V = KWvT$ | where v is the sliding velocity and T is the duration of the sliding. |
| Ratner and Lancaster correlation (1969) | $V = \frac{K\mu Wv}{H S e}$ | where μ is the friction coefficient, S is the ultimate tensile strength and e is the elongation to break. |
| Rhee's model [35], (1970) | $\Delta W = KW^a v^b t^c$ | where ΔW is the weight loss, t is the time and a, b and c are the exponents. |

Table 7: Some of the most popular abrasive wear models [42].

Hence, based on the existing wear models, the following parameters are needed to calculate the specific wear rate k of the tested seals:

- The evolution of the volume loss of seals with travelled distance,
- The relation between the worn volume and the most significant parameters, which are: the sliding distance and the interference or contact force between the seal and the mounting rod.

In this section, the specific wear rates of the seal samples tested under both concentric and eccentric conditions are calculated.

Table 8 summarizes the resultant contact forces between both considered seal types and the mounting rod before the tests, and under both concentric and eccentric mounting conditions. This data was obtained applying the procedure presented in Chapter 2. Nevertheless, it is obvious that the contact forces between the seals and the mounting rod may change during sliding as the seals wear out.

| Rod to bore position | Contact force, F_r (N) | |
|-----------------------------|--|-------------------------|
| | Seal A (TPU) | Seal B (NBR) |
| $\delta_r = 0mm$ | 105.32 | 74.64 |
| $\delta_r = 0.15mm$ | 128.66 | 76.27 |

Table 8: Contact forces between the seals and the rod before the tests.

In the case of seal B, the volume loss of the tested samples was negligible for every test condition (see Figure 62). Therefore, it may be

assumed that the contact force remains constant throughout all the tests.

In Figure 64 the relationships between the volume losses per unit contact force (calculated using the values in Table 8) vs. the travelled distance of the test seal B (NBR) are shown. As can be seen, a quite linear relationship was found between the volume loss and the sliding distance i.e. the wear rate is constant over the whole range of selected test durations. Hence, the wear of samples corresponds to the steady-wear-stage so that the application of a wear equation law may be justified. Furthermore, friction results (Figure 60) showed a steady behaviour from the beginning of the tests. In this work, the law of Archard has been used for wear rate calculation since it establishes a relationship between the main measurable parameters: travelled distance, worn material volume and contact force. In fact, the specific wear rates in Archard's equation comprehend many other variables such as geometric parameters, material properties and frictional performance, among others.

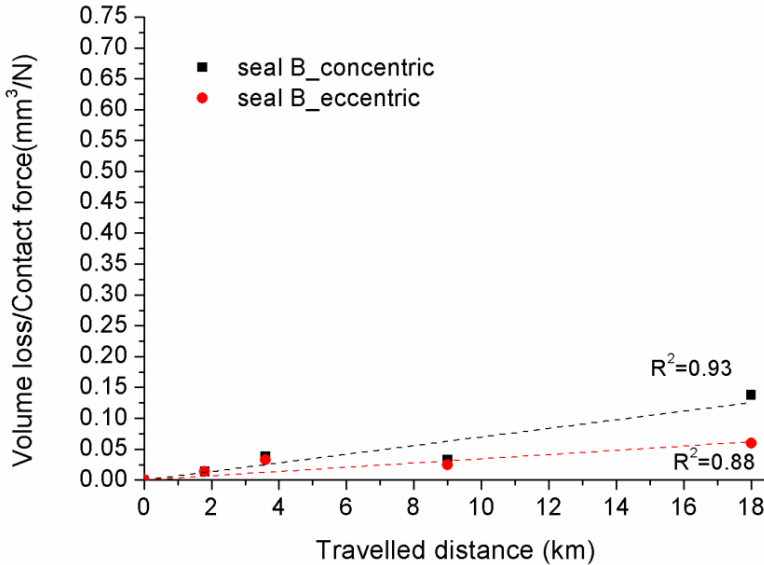


Figure 64: Relationship between the volume loss of the seal sample B (NBR) and the travelled distance.

Archard wear equation could be expressed as follows [47]:

$$V = \frac{K}{H} F_r s \quad (38)$$

where V is the volume removed from the surface per unit of sliding distance, F_r is the normal load applied (W in Table 8), s is the sliding distance and H is the indentation hardness of the softer material. K is a dimensionless quantity which is known as “wear coefficient” and it is extremely useful to compare the severity of different wear processes. In the case of materials whose hardness cannot be easily defined such as elastomers, the wear rate is usually defined as:

$$k = \frac{K}{H} = \frac{V}{F_r s} \quad (39)$$

k is known as the “specific wear rate” of a material (mm^3/Nm). In other words, in order to avoid uncertainties related to material hardness which in the case of polymers are usually measured in Shore A and Shore D according to the ASTM 2240 standard, the ratio K/H is usually expressed as k .

The specific wear rate values of the test seal B under both eccentric and concentric conditions are presented in Table 9. Results showed a lower specific wear rate under eccentric mounting conditions than under concentric ones. Nevertheless, considering the low volume loss of the seals of type B and that some deviation in results always exists, it may be concluded that the specific wear rate is similar under concentric and eccentric conditions. In other words, rod to bore misalignments do not affect the wear rate of the seals made from rubber.

| Rod to bore position | Specific wear rate, k (mm^3/Nm) |
|----------------------------|--|
| $\delta_r = 0\text{mm}$ | 7E-6 |
| $\delta_r = 0.15\text{mm}$ | 3.4E-6 |

Table 9: Specific wear rates for seal B (NBR).

In the case of seal A (TPU), results revealed that the wear of the samples increases with the sliding distance and that the wear resulted to be considerably more severe under eccentric test conditions than under concentric ones (see Figure 62). In order to calculate the effect of a differential of travelled distance (dD) on a differential of worn volume (dV), Archard equation could be applied differentially as:

$$dV = k F_r dD \quad (40)$$

Considering that the contact force between the seal and the rod may vary as the differential of seal wears out, the previous equation may be expressed as:

$$\int_0^{V_D} \frac{dV}{F_r(V)} = \int_0^D k dD = k D \quad (41)$$

where D is the travelled distance and V_D is the worn volume for a travelled distance D .

Thus, the wear rate may be calculated as:

$$k = \frac{1}{D} \int_0^{V_D} \frac{dV}{F_r(V)} \quad (42)$$

Equation (42) may be also formulated expressing the contact force as a function of the travelled distance D instead of the worn volume V as:

$$k = \frac{V_D}{\int_0^D F(D)dD} \quad (43)$$

In this work, in order to calculate the seal/rod contact force variation with the travelled distance, the worn sections of the tested seals were modelled and plain strain simulations were carried out.

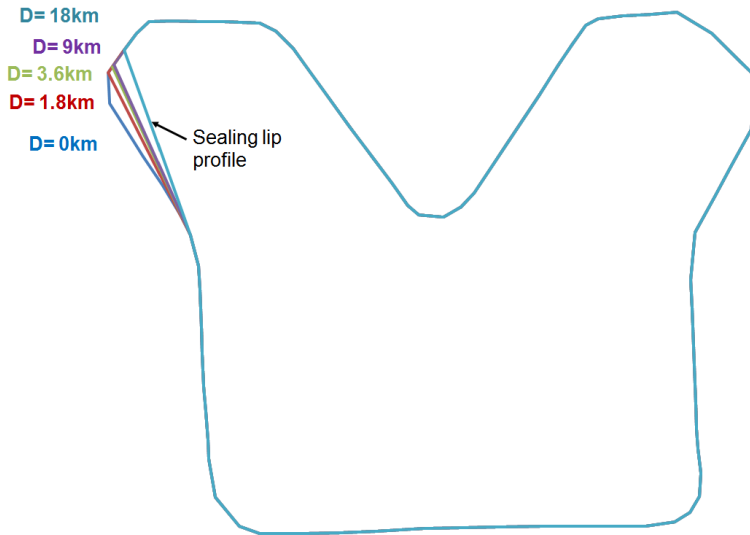
First of all, the worn volumes of the differential seal sections tested under different mounting conditions and different tests durations were

calculated from the micrographs obtained through the microscope. The evolution of the measured worn volumes with the travelled distance D are shown in Table 10.

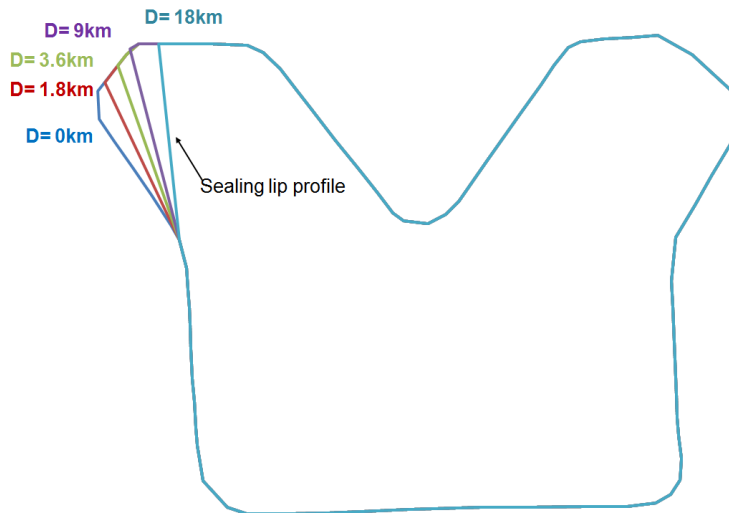
| | Worn volume, V [mm^3] | |
|----------------------|------------------------------------|----------------------------|
| | $\delta_r = 0\text{mm}$ | $\delta_r = 0.15\text{mm}$ |
| $D = 1.8 \text{ km}$ | 0.21 | 0.37 |
| $D = 3.6 \text{ km}$ | 0.28 | 0.53 |
| $D = 9 \text{ km}$ | 0.34 | 0.82 |
| $D = 18 \text{ km}$ | 0.43 | 1.2 |

Table 10: Worn volume evolution of a differential of seal tested under different mounting conditions.

In Figure 65 the evolution of wear along the sealing lips with the travelled distance are shown for the tests carried out under both concentric and eccentric mounting conditions.



(a)



(b)

Figure 65: Evolution of the wear along the sealing lip with the travelled distance D and under: (a) concentric conditions, $\delta_r = 0\text{mm}$ and (b) eccentric conditions, $\delta_r = 0.15\text{mm}$.

The plain models of the worn section were built in Ansys Workbench using the same parameters and contact conditions described in section 2.4.1.2. Plain strain simulation results under concentric conditions are shown in Figure 66. As can be seen, under concentric conditions (for a $\delta = \delta_i = 1.47\text{mm}$), results revealed that the contact force between the seal A and the rod remains nearly constant with the travelled distance and subsequently, with wear.

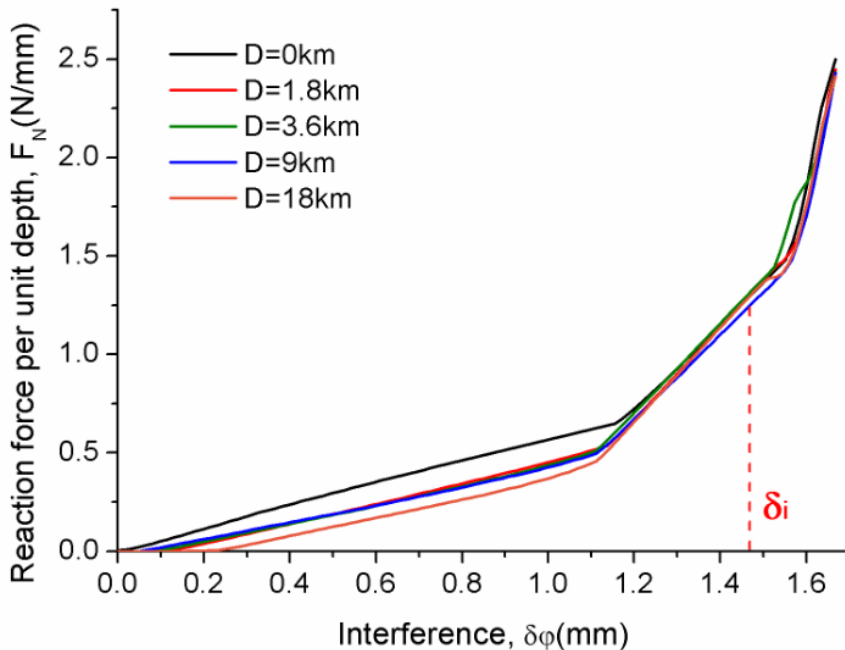


Figure 66: Seal/rod contact force evolution with the travelled distance under concentric conditions ($\delta_r = 0\text{mm}$).

Figure 67 presents the contact force between the seal A and the rod as a function of the interference, for a new seal and for the seal after travelling 18km under eccentric mounting conditions with a rod to bore misalignment of 0.15mm. It was found that the contact force provided by

the most compressed section of the eccentric seal (with an interference of $\delta = \delta_i + \delta_r = 1.61mm$) is similar before and after travelling a distance of 18km. In other words, the results obtained demonstrate that the lip seal geometry is able to provide a nearly constant contact force as the seal wears out.

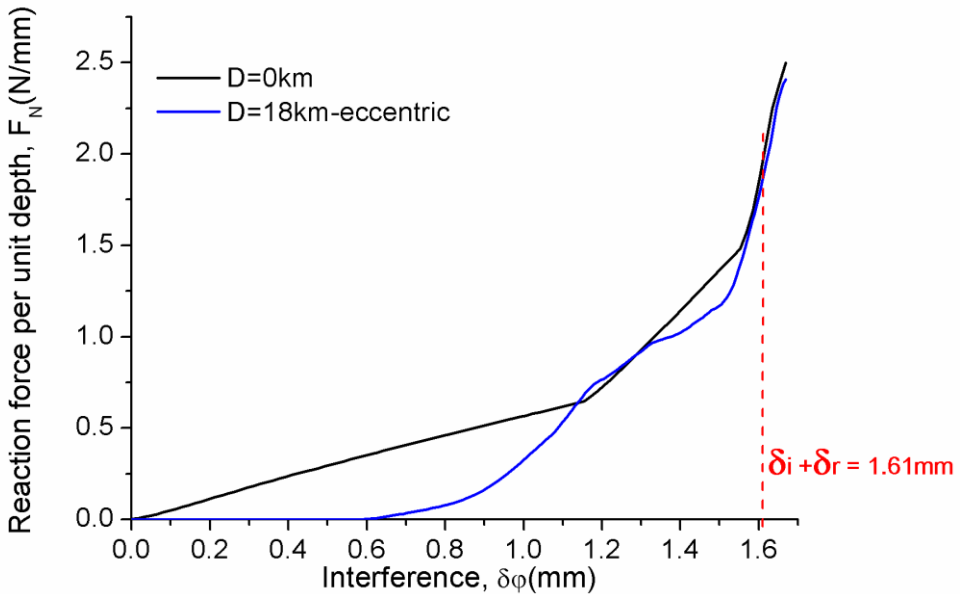


Figure 67: Contact force evolution of the most compressed seal section under eccentric conditions ($\delta_r = 0.15mm$).

Thus, considering that simulations predicted a constant contact force with travelled distance and regardless of the mounting conditions, the use of the contact force values shown in Table 8 for wear rate calculation is justified. Figure 68 presents the volume loss per unit contact force curves of the seal A (TPU) tested under both concentric and eccentric conditions vs. the travelled distance.

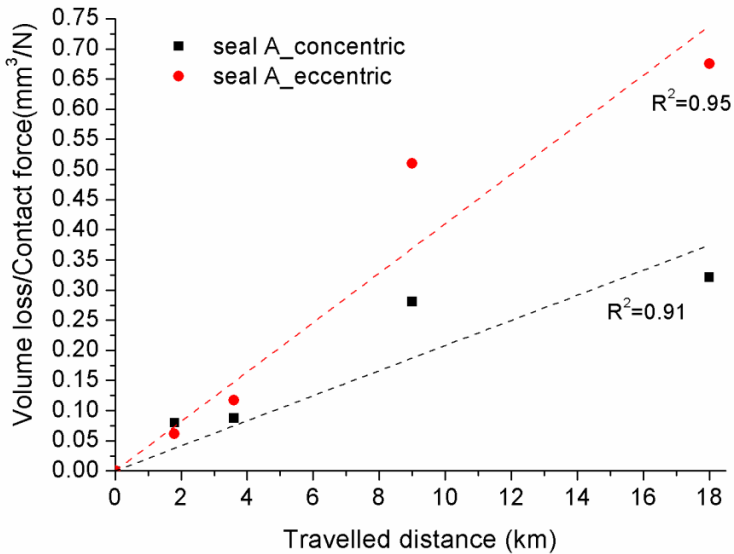


Figure 68: Relationship between the volume loss of the seal sample A (TPU) and the travelled distance.

The specific wear rate values of the test seal A under both eccentric and concentric conditions are presented in Table 11. In Figure 59 it was shown that the friction curves of the seal A reach a steady-state after a test time of about 7000s (3.5km). Hence, for wear rate calculations only the wear results obtained from those tests with longer durations were considered. Results showed that the wear rate under eccentric conditions is twice the wear rate under concentric conditions. The results obtained are in good agreement with those presented in [36] by Martinez et al. Moreover, it was found that the wear rates of the test seal A are an order of magnitude higher than those obtained for the test seal B.

| Rod to bore position | Specific wear rate, k ($\text{mm}^3/\text{N m}$) |
|----------------------------|---|
| $\delta_r = 0\text{mm}$ | 2.08E-5 |
| $\delta_r = 0.15\text{mm}$ | 4.1E-5 |

Table 11: Specific wear rates for seal A (TPU).

3.8 Friction coefficient curves and friction force distribution along seals

3.8.1 Approach

Under ideal concentric conditions, the contact forces between the rod and the seal are the same along the whole seal. Hence, the friction distribution and the wear pattern on a seal whose centre matches the centre of the shaft when mounted, will be uniform. In this case, the friction coefficient along the whole seal may be calculated dividing the total friction force by the total contact force between the seal and the mating surfaces. Thus, in an ideal situation where the rod and the bore are completely aligned, the friction coefficient between the seal and the mating part at any instant may be calculated as:

$$\mu_{con} = F_{f_con}/F_{N_con} \quad (44)$$

And the friction force per unit of differential seal length (N/mm) is:

$$dF_{f_con} = F_{f_con}/\pi d \quad (45)$$

where μ_{con} is the friction coefficient between the seal and its mating part under concentric conditions, d is the rod diameter and F_{f_con} and F_{N_con} are the resultant friction and contact forces when the centre of the bore and the centre of the rod are perfectly aligned, respectively.

In general, the resultant friction force may be expressed as the sum of the friction forces generated in each differential of seal as:

$$F_f = \mu_i dF_{r_i} + \mu_{i+1} dF_{r_{i+1}} + \mu_{i+2} dF_{r_{i+2}} + \dots \quad (46)$$

where F_f is the resultant friction force generated on the seal, and μ_i and dF_{r_i} are the friction coefficients and the contact forces in the i section of the seal.

When a specific misalignment exists between the rod and the seat of a seal, friction forces in each differential of seal will be variable and Equation (46) may have as many solutions as possible combinations of friction coefficients and contact forces. In this work, the following assumption has been made in order to calculate the friction coefficients on seals tested under eccentric conditions: it has been considered that the friction force distribution is similar to the contact force distribution. This hypothesis implies assuming a constant friction coefficient along the seal, which may be a valid simplification considering that the contact force range is quite small.

3.8.2 Friction coefficient curves

In Figure 69 and Figure 70 the friction coefficient evolution curves of the seals throughout the tests are presented. These results were obtained through the load cell measurements during the tests and the resulting contact forces obtained from the analytical contact model (Table 8); it has been already demonstrated that contact forces remain nearly constant during the tests performed. Thus, the friction curves plotted correspond to the friction coefficients of a whole seal over time.

For the TPU seal (A), results showed steady friction coefficients of about 0.2 for the tests carried out under concentric mounting conditions, and friction coefficients of about 0.3 for those tests carried out under eccentric conditions. In the case of the NBR seal (B), the friction coefficients between the seal and the rod are lower. In particular, steady friction coefficients of about 0.12 and 0.14 were obtained during concentric and eccentric tests, respectively.

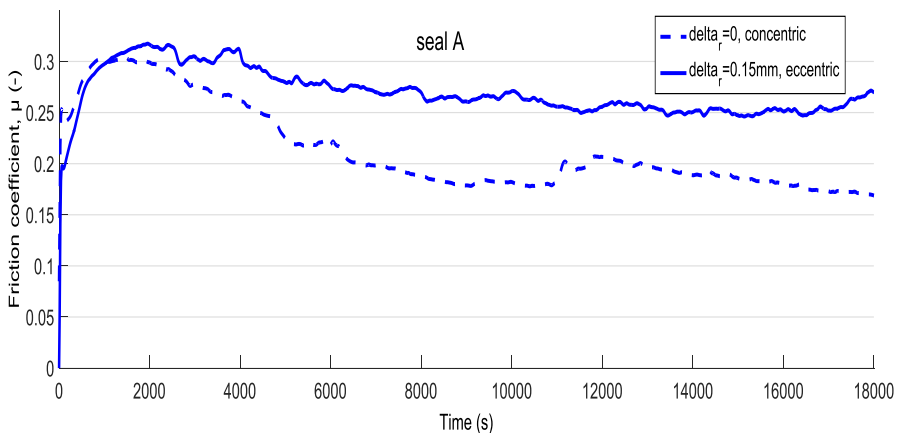


Figure 69: Comparison of the friction coefficient curves of seal A (TPU) under concentric and eccentric conditions.

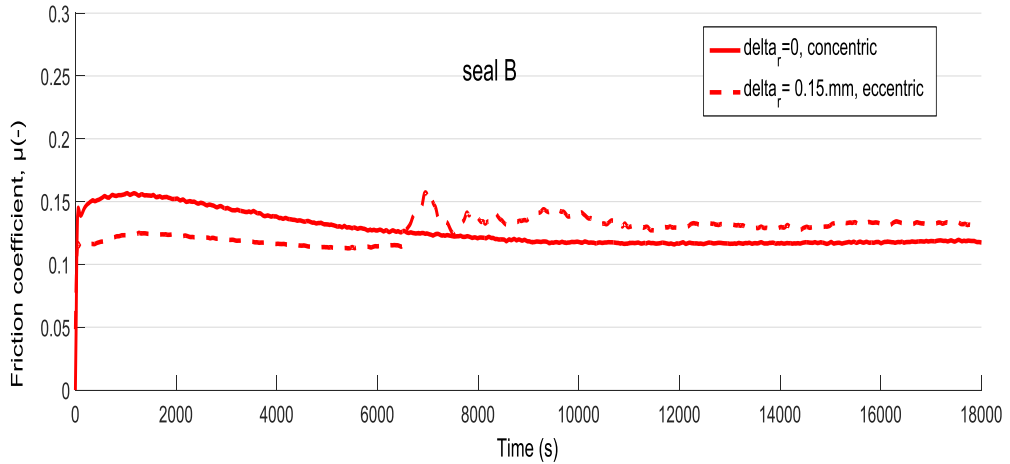


Figure 70: Comparison of the friction coefficient curves of seal B (NBR) under concentric and eccentric conditions.

3.8.3 Case study: Friction force distribution along an eccentric seal

The aim of this section is to calculate the friction force distribution along a seal subjected to an eccentric mounting. Thus, as a case study, the friction force distribution along the seal sample A (TPU) under stable conditions has been investigated.

Figure 71 presents the contact force distribution between the seal and the rod for the both considered mounting conditions. The forces were calculated using the same custom Matlab script developed in Chapter 2 for calculating the contact forces as a function of rod eccentricity. As can be seen, in the eccentric case, the maximum contact force between the seal and the rod, which takes place in the most compressed section, is

of 1.45N. This value is about the double of the contact force predicted for the concentric case.

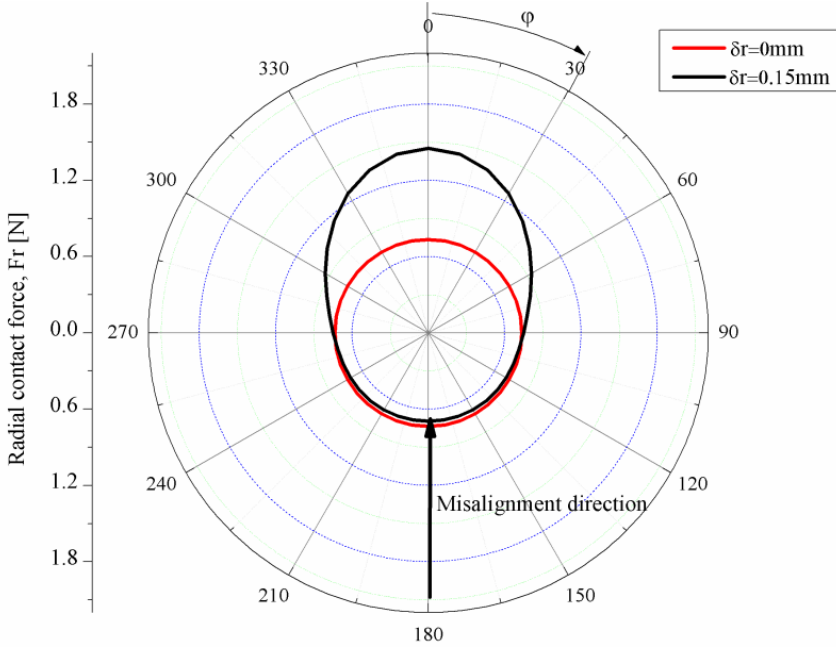


Figure 71: Radial contact forces in the sealing lip along the whole seal A as a function of rod to bore eccentricity value.

Table 12 summarizes the resulting contact forces (calculated) and friction forces (measured) acting on the seal during steady-state conditions.

| <i>Eccentricity</i> | <i>Resulting contact force</i> | <i>Steady friction force</i> |
|--------------------------------------|---------------------------------------|-------------------------------------|
| <i>(mm)</i> | <i>F_r</i> | <i>F_f</i> |
| | <i>(N)</i> | <i>(N)</i> |
| $\delta_r = 0$ (<i>concentric</i>) | 105.32 | 20 |
| $\delta_r = 0.15$ | 128.66 | 32 |

Table 12: Resultant contact and friction forces on the seal.

Concentric conditions

Under ideal concentric conditions, because the contact forces between the rod and the seal are similar along the whole seal, the friction coefficients and friction forces at any instant can be easily calculated applying Equations (44) and (45). In this case study, being the rod 45mm in diameter, a steady friction force and friction coefficient of about 0.75N and 0.2 were obtained, respectively.

Eccentric conditions, $\delta_r = 0.15\text{mm}$

Though in the previous section the resulting friction forces of seal A were calculated, the non-uniform friction force distribution along a seal due to its misaligned condition has not been studied yet.

The relation between the resulting friction force and contact force on the seal under eccentric conditions is $F_{f_{\delta_r=0.15}}/F_{N_{\delta_r=0.15}} \approx 0.25$.

The contact force distribution of the seal under study when $\delta_r = 0.15\text{mm}$ (see Figure 71) may be expressed as a function of the circumferential angle or position (in radians) as:

$$F_{N_{\delta_r=0.15}}(\varphi) = 0.149\varphi^2 - 0.725\varphi + 1.551 \text{ [N]} \quad (47)$$

In order to estimate the friction force distribution along the seal, the simplifications previously introduced were assumed. The friction coefficient in each section was considered to be equal to the resulting friction coefficient i.e. 0.25. Hence, applying the assumptions

mentioned the friction force curve of the seal under study may be expressed as:

$$F_{f\delta_r=0.15}(\varphi) = 0.037\varphi^2 - 0.181\varphi + 0.388 \text{ [N]} \quad (48)$$

In Figure 72 the contact force and friction force distributions of the seal sample A under steady-state conditions and for a rod to bore misalignment of $\delta_r = 0.15mm$ are plotted. Results revealed that rod to bore misalignments affect considerably the friction force distribution on seals and subsequently the temperature distribution which directly depends on friction. The relation between friction and temperature will be studied in detail in the next chapter.

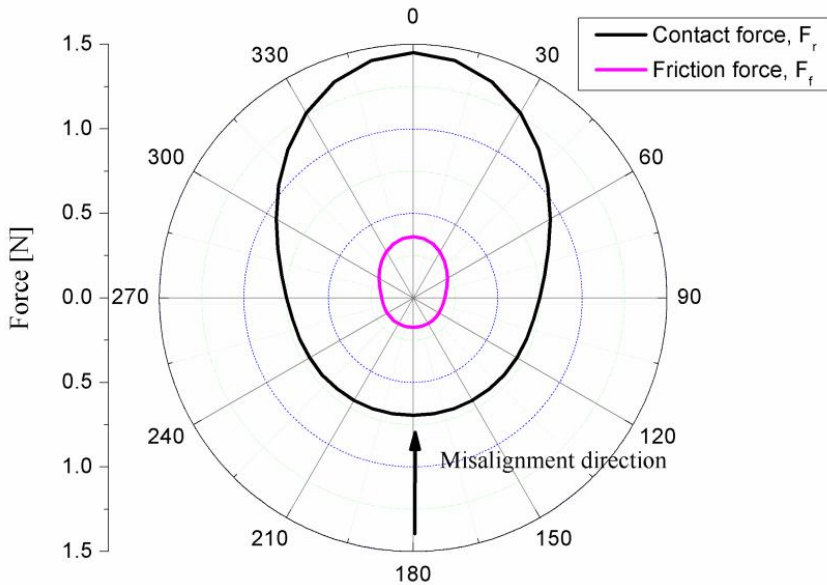


Figure 72: Steady contact and friction force distribution of seal A (TPU) for a rod to bore misalignment of $\delta_r = 0.15mm$.

3.9 Conclusions

In this chapter the effect of rod to bore misalignments on the tribological performance and service life of elastomeric seals has been experimentally investigated. To this aim, sliding tests were carried out on commercial seals at different test durations and under both concentric and controlled eccentric mounting conditions. During the tests, the friction generated was measured, and also the wear of the seal samples through weight measurements before and after the tests. Results demonstrated the great relevance of mounting misalignments on the friction generated and wear of seals during operation, and subsequently, on their service life. Furthermore, it was found that the effect of misalignments on the tribological performance of seals depends to a great extent on the seal material. In this specific case results showed that misalignments increase considerably the friction force of TPU seals and that accelerate their wear process whereas their effect on NBR seals is negligible. It is thought that the high elasticity and low hardness of rubber seals in comparison with those made of polyurethane facilitate its adaptation to both static and dynamic misalignments.

Moreover, experimental results have enabled validating the methodology presented in the previous chapter for the development of tri-dimensional analytical contact model of seals. Furthermore, the analytical contact model results have been herein used for friction coefficient and wear rate calculations of the seals tested under concentric and eccentric mounting conditions. In other words, within this chapter, the utility of the contact force eccentricity model for tribological calculations as well as for design purposes has been demonstrated through specific case studies.

Chapter 3: Effect of mounting eccentricity on seal performance-Experimental tests

Results revealed that mounting misalignments lead to an irregular friction distribution and wear pattern on seals, and therefore to a non-uniform temperature distribution along seals. The effect of rod to bore misalignments on the temperature rise of seals due to frictional heating will be studied in detail in the next chapter.

3.10 References

- [1] Flitney RK. Seals and sealing handbook. 5th edition. Elsevier; 2007.
- [2] Müller HK, Nau BS. Fluid sealing technology: Principles and applications. Marcel Dekker; 1998.
- [3] Nikas GK. Eighty years of research on hydraulic reciprocating seals: review of tribological studies and related topics since the 1930s. Proceedings of the Institution of Mechanical Engineers, Part J: Journal of Engineering Tribology 2010, 224(1), 1–23.
- [4] Johnson J, Frame E, Moses C. Design and operation of a Device for Evaluating Shaft Seals in Dynamic Applications. U.S. Army Tardec fuels and lubricants Research Facility, Southwest Research Institute 2003.
- [5] Belforte G, Conte M, Manuello Bertetto A, Mazza L. Accelerated life tests on piston seals for pneumatic cylinders. Ecotrib 2009. June 7-10.Pisa, Italy.
- [6] Raparelli T, Manuello Bertetto A, Mazza L. Experimental and numerical study of friction in an elastomeric seal for pneumatic cylinders. Tribology International 1997; 30: 547-552.
- [7] Belforte G, Mattiazzo G, Mauro S et al. Measurement of friction force in pneumatic cylinders. Tribotest Journal 2003; 10: 33-48.
- [8] Belforte G, Conte M, Manuello Bertetto A, Mazza L. Test rig for friction force measurements in pneumatic components and seals. Proc IMechE Part J: Journal of Engineering Tribology 2012; 227 (1), 43-59.

- [9] Juoksukangas J, Lehtovaara A, Miettinen J, Tolvanen P, Jarvella P, Niemi AM. Development of a Test Rig for Reciprocating Seals in Heavy Load Conditions. Nordtrib 2010, Sweden.
- [10] Pinedo B, Conte M et al. New high performance test rig for sealing systems characterization. In: Proceedings of the 5th World Tribology Congress - Turin, Italy; 2013.
- [11] Conte M. Interaction between seals and counterparts in pneumatic and hydraulic components. PhD Thesis, 2008.
- [12] Bignardi C, Manuello A, Mazza L. Photoelastic measurements and computation of the stress field and contact pressure in a pneumatic lip seal. Tribology International 1999; 32(1):1-13.
- [13] C-Y Lee, C-S. Lin, R-Q. Jian, C-Y. Wen. Simulation and experimentation of the contact width and pressure distribution of lip seals. Tribology International 2006; 39: 915-20.
- [14] Belforte G, Conte M, Manuello Bernetto A, Mazza L, Visconte C. Experimental and numerical evaluation of contact pressure in pneumatic seals. Tribology International 2009; 42:169-175.
- [15] Belforte G, Conte M, Manuello Bernetto A, Mazza L, Visconte C. Test rig for rod seals contact pressure measurement. WIT Transactions on Engineering Sciences 2010; vol 66.
- [16] M. Goerres. Friction force and leakage test rigs for the development of piston rod seals. Öhdraulik und Pneumatik 2003; 47 Nr.1.
- [17] Belforte G, Conte M, Mazza L, Visconte C. Non contact wear measurement on pneumatic seals. Ecotrib 2009. Pisa, Italy.
- [18] Visconte C, Conte M, Mattone MC. Analysis of the leakage path in air-lubricated seal. Tribology International 2009; 42:844-848.
- [19] Salant RF. Modelling rotary lip seals. Wear 1997; 207: 92-99.

- [20] Nikas GK., Sayles RS. Nonlinear elasticity of rectangular elastomeric seals and its effects on elastohydrodynamic numerical analysis. *Tribology International* 2004; 37: 651-660.
- [21] Nikas GK. Theoretical study of solid back-up rings for elastomeric seals in hydraulic actuators. *Tribology International* 2004; 37: 689-699.
- [22] Nikas GK, Sayles RS. Computational model of tandem rectangular elastomeric seals for reciprocating motion. *Tribology International* 2006; 39: 622-634.
- [23] Nikas GK, Sayles RS. Study of leakage and friction of flexible seals for steady motion via a numerical approximation motion. *Tribology International* 2006; 39: 921-936.
- [24] Salant RF, Thatte A, Transient EHL analysis of an elastomeric hydraulic seal. *Tribology International* 2009; 42: 1424-1432.
- [25] Salant RF, Shen D, An unsteady mixed soft EHL model, with application to a rotary lip seal. *Tribology International* 2007; 40: 646-651.
- [26] Shen D, Salant RF. A transient mixed lubrication Model of a Rotary Lip Seal with a Rough Shaft. *Tribology Transactions* 2006; 49: 621-634.
- [27] Wenk JF, Stephens LS, Lattime SB, Weatherly D. A multi-scale finite element contact model using measured surface roughness for a radial lip seal. *Tribology International* 2016; 97: 288–301.
- [28] Tsukruk VV, Wahl KJ. Microstructure and Microtribology of Polymer Surfaces. In: Briscoe, B. J. *Tribology of Polymers : A Perspective*. American Chemical Society 2000; 2–22.

- [29] Briscoe BJ, Sinha SK. Wear of polymers. Proceedings of the Institution of Mechanical Engineers, Part J: Journal of Engineering Tribology 2002; 216(6): 401–413.
- [30] Briscoe B. Wear of polymers : an essay on fundamental aspects, Tribology International 1981; 231–243.
- [31] Sinha SK, Briscoe BJ. Polymer Tribology. Imperial College Press; 2009.
- [32] Meng HC, Ludema KC. Wear models and predictive equations: their form and content. Wear 1995; 181-183: 443-457.
- [33] Williams JA. Wear modelling: analytical, computational and mapping: a continuum mechanics approach. Wear 1999; 225-229, 1–17.
- [34] Viswanath N, Bellow DG. Development of an equation for the wear of polymers. Wear 1995; 181-183: 42-49.
- [35] Rhee SK. Wear equation for polymer sliding against metal surfaces. Wear 1970; 16: 431-445.
- [36] Martínez FJ, Canales M, Bielsa JM, Jiménez MA. Relationship between wear rate and mechanical fatigue in sliding TPU–metal contacts. Wear 2010; 268(3-4), 388–398.
- [37] Martínez FJ, Canales M, Izquierdo S, Jiménez MA, Martínez MA. Finite element implementation and validation of wear modelling in sliding polymer–metal contacts. Wear 2012; 284-285, 52–64.
- [38] Abdelbary A. Wear of Polymers and Composites. Woodhead Publishing, Elsevier; 2014.
- [39] Unal H, Mimaroglu A, Kadioglu U, Ekiz H. Sliding friction and wear behaviour of polytetrafluoroethylene and its composites under dry conditions. Materials & Design 2004; 25(3), 239–245.

- [40] Conte M. Interaction between seals and counterparts in pneumatic and hydraulic components. PhD Thesis 2008. Politecnico di Torino.
- [41] Tasora A, Prati E, Marin T. A method for the characterization of static elastomeric lip seal deformation. *Tribology International* 2013; 60: 119-126.
- [42] Stachowiak GW. *Wear: Materials, Mechanisms and Practice*. John Wiley & Sons, Ltd; 2005.
- [43] Shipway P, Ngao, N. Microscale abrasive wear of polymeric materials. *Wear* 2003; 255(1-6): 742–750.
- [44] Hill DJT, Killeen MI et al. Laboratory wear testing of polyurethane elastomers. *Wear* 1997; 208: 155-160.
- [45] Lancaster JK. Abrasive wear of polymers. *Wear* 1969; 14(4): 223–239.
- [46] Budinski KG. Resistance by wear abrasion to selected plastics. *Wear* 1997; 203-204: 302-309.
- [47] Archard JF. Contact and Rubbing of Flat Surfaces. *Journal of Applied Physics* 1953; 24: 981.
- [48] Bhushan B. *Modern Tribology Handbook*. CRC; 2001.
- [49] Belforte G, Raparelli T, Mazza L. Life Tests on Elastomeric Lip Seals for Pneumatic Cylinders. *Lubrication Science* 1997; 3: 251-266.
- [50] Kim H, Kim R-U, Chung K-H et al. Effect of test parameters on degradation of polyurethane elastomer for accelerated life testing. *Polymer Testing* 2014; 40: 13.

Chapter 4: Frictional heating on elastomeric seals during operation: An approach

4.1 Introduction

It has been already introduced in the previous chapters that thermal degradation of elastomeric seals is one of the most common seal failure mechanisms. Thus, given that temperature is one of the most limiting factors of polymers, it is of great interest for the industry to know the temperature of seals during operation. The temperature of a specific seal under operation may be expressed as the sum of the room temperature and a temperature rise due to frictional heating effects arising at the interface between contact bodies during sliding. Hence, special care should be taken with the surface temperature rise of seals during operation in order to avoid possible seal failures due to overheating, considering that most of the frictional energy generated during sliding is dissipated as heat. Although the exact energy transformation mechanism is not clear, most of the tribologists agree that almost all the energy is transformed into heat [1]. As a result, a local and usually consistent temperature rise occurs. This phenomenon is known as “*frictional heating*”.

Experimental work showed that about the 95% of the energy occurs within the top 5 microns of the surfaces in contact [2]. Maximum contact

temperatures are reached at spot to spot asperity contact and they are usually temperatures of a very high magnitude, even at low velocity, and short duration because of the small size of each asperity. The temperature rise due to the dissipation of frictional heat at asperity contact spots is known as “*flash temperature*”. The heat is generated at the real contact area and it is transferred by conduction to the bulk of the material through the asperities [3]. Hence, surface asperities act as heat flow regulators from the contact to the bulk.

In the last decades, a wide range of techniques have been used in order to experimentally measure on contact surfaces the temperature rise due to frictional heating, however, none of them have been widely accepted. The main problem for measuring temperatures between the contact surfaces is that thermal processes occur in a closed area. Hence, any technique based on placing a measuring device at the contact, will alter the contact. For example, this is the case of thermocouples. Several types of thermocouples such as embedded subsurface thermocouples, dynamic thermocouples and contact thermocouples have been used to measure contact temperature evolution [2-4]. Nevertheless, thermocouples are more suitable to measure subsurface bulk temperatures rather than interface temperatures. So far, one of the best options to measure the temperatures reached at the contact spots are the thin film thermocouples [5-7]. These type of devices are able to measure the temperatures at the real contact area due to their small dimensions (thickness of about 0.5-1 microns) and rapid response ($<1\mu\text{s}$); however, more investigation is needed in this area to get a lateral resolution of microns so that flash temperatures can be measured [4]. Other techniques that avoid altering the contact, such as analysing

phase transformations and micro-structural changes in materials (indirect techniques), and optical techniques have been also widely used. Indirect techniques consist in analysing the phase changes and structural changes in materials after operation, and relating them to specific temperatures [4]. However, these methods are diagnostic tools i.e. they are not useful to measure the contact temperature evolution during sliding. Thus, they may be used to estimate an operating temperature range rather than an approximated temperature value. These indirect methods are not accepted nowadays even if they were in the past. Regarding optical techniques, infrared imaging [8-11] and pyrometry [3] techniques have been also widely used for measuring the evolution of temperature at the interface during sliding. Nevertheless, the use of these techniques is limited since one of the bodies needs to be transparent in order to be able to focus the contact. Hence, even if these techniques may be useful to measure the temperatures at the interface between bodies at laboratory tests, their use is very limited for real industrial applications where the contact area is hardly ever visible and accessible. Moreover, their use is extended to the measurement of surface temperatures very close to the contact rather than at the contact spots.

Thus, due to all these difficulties to measure contact temperatures, many authors have made attempts in the last decades in order to build analytical models able to predict the temperature rise on surfaces during sliding for design purposes. These attempts resulted in a wide range of analytical equations for estimating the temperature rise at the interface. Some of the most popular models are: Archard's average and maximum flash-temperature model (1959), Holm's average and flash temperature

model, Tian-Kennedy's average and maximum temperature model (1993), Greenwood-Greiner's average flash temperature model (1991), Ashby flash temperature model (1991), Jaeger (1942) and Blok (1937) models, among others. Nevertheless, none of these models are able to estimate accurately enough the contact temperatures at the surface. Furthermore, calculations using different models lead to very different results. Kalin et al. [13] carried out ball on flat tests with a silicon nitride ceramic sliding against steel under both dry and lubricated conditions, and they used the results to calculate the temperature rise by means of different analytical models. Results showed that different models lead to very different flash temperature values of up to 700°C.

The main difficulty for building reliable temperature models is that the surface temperature rise during sliding depends on several factors such as the contact and operating conditions, as well as the properties of the materials and surfaces of the components involved. Moreover, contact conditions may vary considerably in time and location during sliding, and furthermore, several interfacial properties and phenomena are very difficult to model [13]. Therefore, most of these models are based on different physical, dynamic and geometrical assumptions. For example, a special care should be taken when selecting the contact area to be used for calculations since even if it deeply affects the results obtained, there is no a standard criterion. Furthermore, Kalin et al. [13] found that the effect of the apparent contact area determination is even larger than the effect of friction and that depending on the method used for real contact area determination, predicted temperatures may be very different. Existing analytical models use different methods for estimating the contact areas. Ashby's and Archard's flash temperature models, for

instance, use their own criteria to determine the contact areas whereas the rest of models estimate them by dividing the normal force by the hardness of the softer material. The latter is a broadly accepted criterion for contact area determination [14]. Surface roughness is another very important parameter that deeply affects the contact temperatures reached during sliding because flash temperatures take place in the contact between asperities [13]. Hence, many analytical flash temperature models integrate the effect of interacting asperities [23,24]. The importance of considering thermal changes in polymers with temperature, as well as the evolution of the friction coefficient with time has also already been demonstrated by many authors [18,19]. Thus, due to the big amount of unknown parameters or uncertainties involved in analytical models, as many techniques as possible should be used when trying to determine the maximum contact temperatures. Furthermore, experimental and analytical results hardly ever show a good matching, and existing models just give us approximate maximum contact temperature rise values due to frictional heat. In fact, a better optimization of the models is needed for more reliable and accurate results.

In the case of polymers, contact temperature estimations are even more complex by the fact that their thermo-mechanical properties are strongly influenced by temperature. Hence, so far, few studies analyse the frictional heating phenomena when polymers are involved [5,10,12,16,18,19,20]. Moreover, due to the complex nature of elastomers and because the properties of each elastomer may be completely different, it is not possible to come to any general conclusion. Tzanakis et al. [16] studied the effect of roughness, friction coefficient,

contact pressure and velocity on the flash temperatures reached on a PTFE composite elastomer tip seal in contact with a high carbon steel plate under dry sliding conditions. The authors found that there is a specific value of roughness which leads to a higher temperature rise, and that the effect of roughness and sliding velocity was larger than the effect of load in that specific case. They experimentally measured surface temperatures by means of a high precision thermal camera and they compared these results with those calculated analytically applying Bowden and Tabor model. They found a good matching except at low contact pressures (<0.4MPa). Conte et al. [18,19] highlighted the importance of estimating flash temperature at the contact surface of a PTFE rubbing against steel. Therefore, they calculated analytically the contact temperatures at the surfaces of different polymers considering both constant and variable thermal properties, and the evolution of friction over the test time. Results demonstrated the importance of considering the evolution of material properties, at least in the case of PTFE.

The main goal of this chapter is to investigate about the effect of rod to bore misalignments on the temperature rise of seals due to frictional heating. To meet the challenge of measuring the surface temperature on seals during operation, a specific methodology for contact temperature estimation has been developed. The proposed methodology combines analytical models, thermo-mechanical properties of materials and experimental inputs, and it was developed in two stages. In a first stage, an experimental investigation on the frictional heating phenomenon on elastomeric seals was carried out at laboratory scale. In a second stage, a methodology to estimate the contact temperature on seals during

operation has been developed. The methodology was applied to a specific case study in order to estimate the contact temperature distribution on eccentric seals, and afterwards the results were compared with those obtained for the concentric case. In particular, the temperatures reached at the contact surfaces of seals during the tests carried out in Chapter 3 have been calculated. Given that the measurement of the contact temperature on seals is a complex task, the validation of the proposed methodology has been carried out through surface analysis of the samples.

4.2 Contact temperature concept

The energy dissipation in the form of heat is known as frictional heating, and it is the responsible of the temperature rise on surfaces sliding against each other. The maximum temperature rise takes place at the contact between asperities. For this reason, it is important to control the temperature evolution at the mating surfaces in order to avoid their thermal degradation. Nevertheless, as introduced at the beginning of this chapter, measuring the temperatures at the contact is not always possible, and that is why several attempts have been made in the last decades with the aim of building reliable analytical models. Hence, even if modelling the frictional heating phenomenon is a challenge due to the big amount of parameters involved and their variability, analytical models may be considered as useful tools, at least for an approximate estimation of the contact temperatures.

Some authors express temperature at the contact as the sum of two components [28]:

$$T_{cmax} = T_b + T_{fmax} \quad (49)$$

where T_{cmax} is the maximum contact temperature [°C], T_b is the bulk temperature of the mating bodies before entering the contact [°C] and T_{fmax} is the maximum flash temperature [°C] which is a local temperature rise that occurs between asperities.

However, Equation (49) is only applicable to a body with a semi-infinite size, and when the heat source does not repeat the same path over the surface. Tian, Kennedy et al. [5,33,34] found that under certain circumstances an extra temperature rise over the localized flash surface temperature rise at the contacting asperities must be taken into account. This temperature rise will affect the entire contact area and it is known as “*nominal contact temperature*”. Some examples in which this nominal temperature rise should be considered include cases such as the following: when the heat source moves continuously over the same path of a finite body, when there is insufficient convective cooling, or/and under dry sliding conditions. Thus, the local surface temperature rise is only affected by a small area while the nominal temperature rise affects the entire finite body. Taking into account these aspects, the total contact temperature may be expressed as:

$$T_c = T_b + \Delta T_{nom} + \Delta T_f \quad (50)$$

defining ΔT_{nom} as the average temperature of all the points at the contact, ΔT_f as the flash temperature rise that takes place at the contact spots and T_b as the environment temperature.

Regarding flash temperature calculations, Blok (1937), Jaeger (1942) and Archard (1959) were the first authors formulating flash temperature theories. According to their theories, flash temperature is the temperature rise above the temperature of the solids. Years later, Greenwood (1991), Tian and Kennedy (1993) and Bos and Moes (1994) also formulated equations for maximum flash temperature determination. They integrated expressions for temperature rise estimation considering a single heat source of a specific shape, on both static and moving bodies. Moreover, steady and quasi-steady conditions are assumed by most of researchers since they consider that the maximum flash temperatures are reached in a very short time after sliding starts. All these models were formulated on the basis that the heat generated at the contact is modelled as a heat source moving over a surface.

Some of the simplifications assumed by most of the authors in order to model the temperature rise phenomenon on surfaces in relative motion are the following [28]:

1. Thermal properties of the contacting bodies are independent of temperature,
2. There exists a unique area of contact and it is regarded as a plane source of heat,
3. Frictional heat is uniformly generated along the area of contact,

Chapter 4: Frictional heating on elastomeric seals during operation: An approach

4. All the heat generated is conducted into the solids in contact (this means that others forms of energy partition such as noise, vibrations, material deformation and creation of new surfaces by adhesion are not considered),
5. The coefficient of friction between the contacting solids is known and attains some steady value,
6. A steady state condition is attained ($\frac{\partial T}{\partial t} = 0$).

Hence, even if most of the existing theoretical contact temperature models are based on the same abovementioned assumptions, temperature values estimated using one model or another may be very different. The main reasons are mainly that each author uses different physical, dynamic and geometrical assumptions, as well as that the interfacial properties that affect the behaviour (for example, the real contact area) are usually unknown. In other words, the main source of discrepancy between the results obtained through different analytical models is the uncertainty of the physical phenomenon itself since both mechanical and thermal properties of the contact are continuously varying during sliding in time and position [4].

The heat rate originated during sliding can be estimated as follows:

$$q = Q/A \quad (51)$$

where Q is the heat generated [W] and A is the contact area [m²].

Considering that the origin of this heat flux is the relative motion between the bodies A and B , the frictional heat generated may be expressed as:

$$Q = \mu F_N |v_A - v_B| \quad (52)$$

where μ is the friction coefficient between surfaces, F_N is the normal load, and v_A and v_B are the sliding velocities of the bodies A and B [m/s], respectively.

Moreover, most of the analytical models use different formulations depending on the speed regime. For determination of the speed regime, the dimensionless “*Peclet number, Pe*” is usually used:

$$Pe = \frac{v b}{2 \chi} \quad (53)$$

where v is the velocity of the solid [m/s], b is the main contact dimension [m], and χ is the thermal diffusivity of the body [m²/s]. Pe is an indicator of the heat penetration into the bulk of the solid and three different regimes are usually defined based on its value [28]:

- If $Pe < 0.1$ → one surface is static or moves very slowly with respect to the other. Thus, there is enough time for the temperature distribution at the contact to be established in the stationary body.
- If $0.1 < Pe < 5$ → one surface moves faster with respect to the other and it may be modelled by a slow moving heat source.
- If $Pe > 5$ → one surface moves much faster with respect to the other and it may be modelled by a fast moving heat source. In this case, there is no much time for the heat to penetrate into the stationary body.

4.3 Experimental study of the frictional heating phenomenon on TPU and NBR elastomers

In this section an experimental study of the frictional heating phenomenon on TPU (Thermoplastic Polyurethane) and NBR (Nitrile Butadiene Rubber) elastomers is presented. The objective is to investigate the temperature rise on elastomeric seals under actual operating conditions. To this end, friction tests were carried out at laboratory scale on elastomers sliding against steel counterparts, and the temperature evolution of the tribo-system was acquired during the tests through an infrared camera. The friction and temperature curves resulting from the experimentation were analyzed, and the effect of parameters such as the seal material, sliding velocity, and steel surface conditions on the temperature rise of elastomers has been herein studied. Moreover, these experimental results are mandatory inputs for the analytical calculations presented in section 4.4 as well as for their validation.

4.3.1 Specimens and characterization

In order to reproduce the contact between an elastomeric seal and the moving rod at laboratory scale, the cylinder on flat configuration was chosen. This configuration is an approximation of the line contact between a differential of seal and the moving rod, in the case of rod seals, or between a seal and the piston, in the case of piston seals. Figure 73 presents an image of the cylinder (steel part) and the flat (polymer) samples. The cylinder samples were made from a 42CrMo4V (F1252) steel, with a diameter of 10mm and a hardness of 1004HV. Flat samples with a length of 15mm and a thickness of 5mm were

Chapter 4: Frictional heating on elastomeric seals during operation: An approach

manufactured from the same elastomers studied in the previous chapters: TPU and NBR. Regarding the temperature limit of polymers, both of them are stable up to temperatures in the range between +100°C and +110°C.

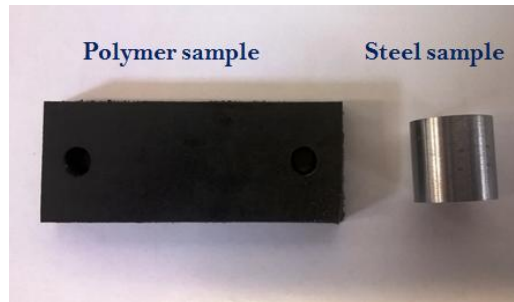


Figure 73: Tribo-pair selected for the study of the frictional heating phenomenon at laboratory scale.

Even if the elastomer samples were selected as to have very similar properties to those seal materials tested in Chapter 3, prior to the friction tests, a complete characterization of the elastomeric samples was carried out by means of several thermal and microscopic analysis techniques. In particular, TGA (Thermogravimetric analysis) and DSC (Differential Scanning Calorimetry) analyses were carried out, and the thermal diffusivity, heat capacity, density, hardness, roughness and the emissivity of the samples were measured. TGA and DSC analyses are mainly useful to study the stability of polymers with temperature, and to figure out their transition points so that the main wear mechanisms can be related to them. Other property results such as heat capacity, diffusivity and density are mandatory outputs for understanding the frictional heating phenomenon itself and for contact temperature calculations. Roughness measurements and surface inspection

techniques were also used in order to investigate physical changes on surfaces after the friction tests. Finally, the emissivity of the polymers was also measured and used for calibration of the thermal camera.

Thermogravimetric analysis (TGA) and Differential Scanning Calorimetry (DSC)

TGA and DSC analyses were performed under the same conditions presented in section 3.2. Results showed that the TGA and DSC curves of the materials selected for the tests at laboratory scale are very similar to those curves obtained in the previous chapter in the characterization of seals (see Figure 47 and Figure 48). Thus the conclusions and the main results obtained from the laboratory tests may be extrapolated to the seals tested in the previous chapters.

Heat capacity (C_p), Thermal diffusivity (χ) and Thermal conductivity (K)

The *heat capacity* (C_p) of a material is the amount of heat needed to raise its temperature by one degree. The higher the specific heat, the higher the heat needed to raise its temperature. In this work, heat capacity evolution of samples with temperature was measured by means of the DSC 1-500 device (Mettler Toledo, Spain). Dry nitrogen was used for venting at a rate of 50ml/min. Measurements were carried out in the range between 0°C and +250 °C.

Thermal diffusivity (χ) of a material expresses its ability to conduct thermal energy relative to its ability to store it. Thermal diffusivity of samples was measured by means of a high resolution ac photopyroelectric calorimeter available at the UPV/EHU (Euskal Herriko

Unibertsitatea/ University of the Basque Country). A test velocity of $\pm 0.5^\circ\text{C}/\text{min}$ was used.

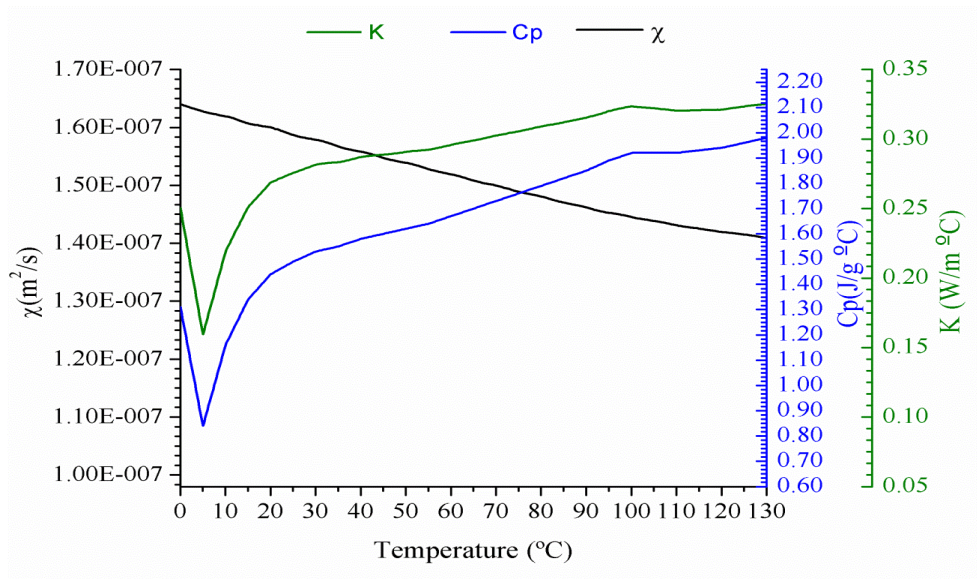
Thermal conductivity (K) of the samples was calculated using the following equation:

$$K = \rho C_p \chi \quad (54)$$

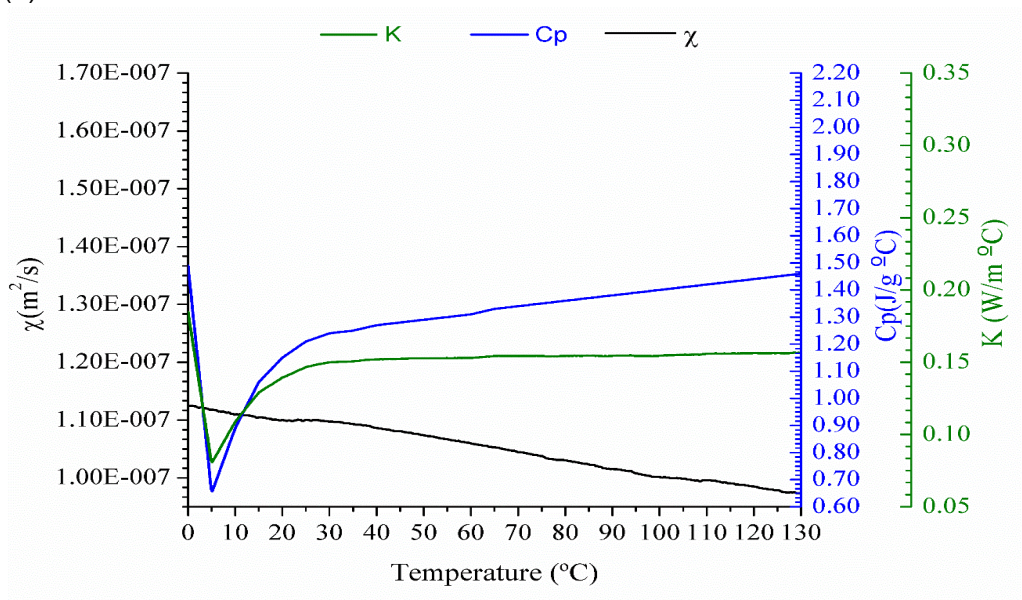
Density (ρ) of samples was measured by means of a XP205 precision micro-scale (Mettler Toledo, Spain).

Figure 74 presents the thermal characteristics of the NBR and TPU samples. Results showed that in both cases, heat capacity and thermal conductivity increase with temperature whereas thermal diffusivity decreases. An increase in conductivity means that as temperature increases both materials conduct temperature faster, leading to lower temperatures of polymers. However, in this case, conductivity increase goes hand in hand with a heat capacity rise; this means that less amount of heat is needed to raise their temperature by one degree (room temperature).

Comparing both graphics, it can be seen that the heat capacity, diffusivity and thermal conductivity of the TPU are lower than those of the NBR. This means that the NBR needs more amount of heat to raise its temperature by one degree and that the heat moves more rapidly through the NBR than through the TPU i.e. thermal equilibrium will be reached in the NBR in a shorter period of time. Values in Table 13 correspond to the thermal property values at 25°C .



(a)



(b)

Figure 74: Thermal properties of the test samples: (a) NBR and (b) TPU.

Shore A hardness

Hardness of samples was measured using a Shore A durometer. The results are shown in Table 13. The hardness of the TPU sample is considerably higher than the hardness of the rubber. Some authors reported that the wear of materials and their hardness are related, however, this dependence varies from one material to another. Most of the analytical models for wear estimation predict that the harder the material, the lower is the wear, but in the case of polymers this is not necessarily true [25,30]. In fact, results in Chapter 3 revealed that the mass loss of the harder seal was higher under the same conditions.

Some other thermal and mechanical properties of the samples are summarized in Table 13:

| Property | NBR | TPU |
|--|-----------------------|-----------------------|
| <i>Density, ρ (kg/m³)</i> | 1166 | 1102 |
| <i>Specific heat, C_p (J/g °C)</i> | 1.49 | 1.21 |
| <i>Diffusivity, α (m²/s)</i> | 1.5869e ⁻⁷ | 1.1005e ⁻⁷ |
| <i>Conductivity, K (W/m K)</i> | 0.32 | 0.15 |
| <i>Hardness, H (Shore A)</i> | 70 | 93 |

Table 13: Main properties of the polymer samples at room temperature (+25°C).

Surface roughness

The friction generated during the sliding of bodies in close contact depends to a great extent on their surface roughness. In fact, it is widely

accepted that the friction resistance and wear mechanisms of polymers are governed by the roughness of the mating surfaces [39]. In particular, roughness is especially relevant during the running-in period where the asperities are worn out. In this work, surface inspections were carried out using optical microscopy and confocal scanning interferometer microscopy techniques in order to measure the roughness and to evaluate the wear of the test samples. In particular, the following roughness values were measured using the Confocal Eclipse ME600 (Nikon):

- Thermoplastic polyurethane (TPU) samples: $R_a \sim 0.93 \mu\text{m}$
- Nitrile rubber (NBR) samples: $R_a \sim 0.45 \mu\text{m}$

Figure 75 presents the surface profiles of the polymeric samples.

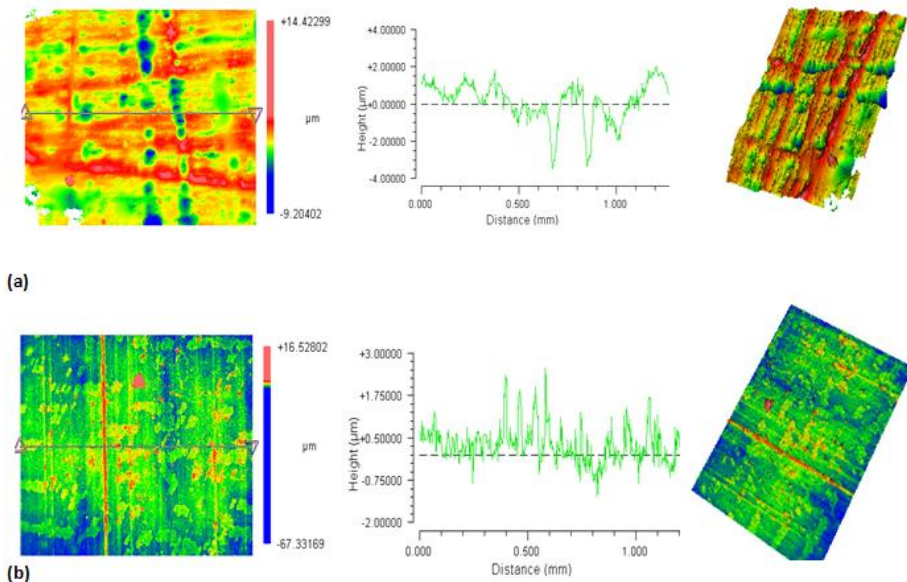


Figure 75: 3D roughness of the (a) TPU and (b) NBR samples.

In Figure 76 some graphs of the samples before the tests, obtained through optical microscopy, are shown.

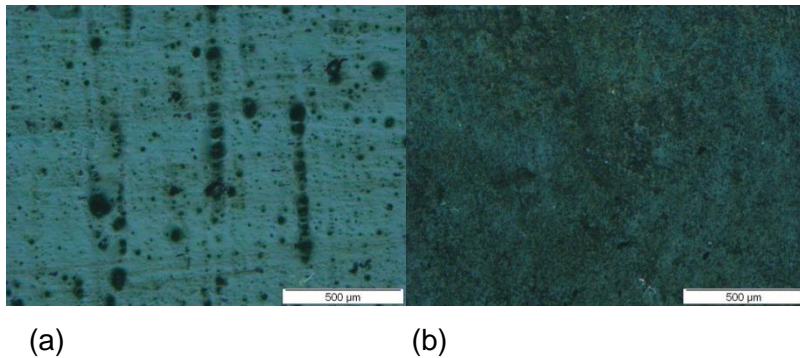


Figure 76: Optical examination of polymer surfaces before the tests: (a) TPU and (b) NBR.

Regarding the roughness of the steel parts, cylinders with three different R_a roughness were manufactured: 0.1, 0.2 and 0.5µm.

4.3.2 Experimental setup

Polymer samples were tested at laboratory scale sliding against steel parts of different roughness and surface conditions. Sliding tests were carried out by means of a high frequency friction machine reproducing as close as possible the actual working conditions of the seals made from these materials. Temperature field of the system was recorded by means of an infrared thermo-camera in order to study its evolution throughout the sliding tests. The effect of seal material and mating surface conditions, as well as the effect of sliding velocity on the surface temperatures reached during the friction tests, has been also studied within this chapter.

Even if seals made of polyurethanes and rubbers are mainly used in hydraulic applications i.e. under lubricated conditions, in this work, tests were carried out under dry conditions for several reasons:

- Measurements with the infrared thermo-camera in presence of lubricants are complicated.
- Avoiding the use of lubricant will enable to stabilise a direct relation between frictional heating and the test parameters, avoiding extra uncertainties added by the use of lubricants.
- Tests under dry conditions represent the most critical situation, when the lubricant film has failed or an excessive leak has taken place so that the seal is subjected to dry running that may lead to its thermal degradation.

4.3.2.1 Friction tests

Friction and wear tests were carried out in the TE77 high-frequency sliding machine (Plint tribology products, England). This rig is a versatile test bench thought to evaluate the tribological behaviour of materials under reciprocating sliding conditions in controlled atmospheres or pressures above atmospheric. The lower sample is connected to an electric motor and linearly actuated by it. The upper body is connected to a load cell that enables acquiring the evolution of the friction force generated during motion. Figure 77 shows a view of the cylinder on flat assembly. A more extended view of the assembly is shown in Figure 78. The elastomeric sample is loaded by the steel cylinder which is supported by a holder. In this case, the elastomeric sample moves in reciprocating motion perpendicularly to the sliding direction.

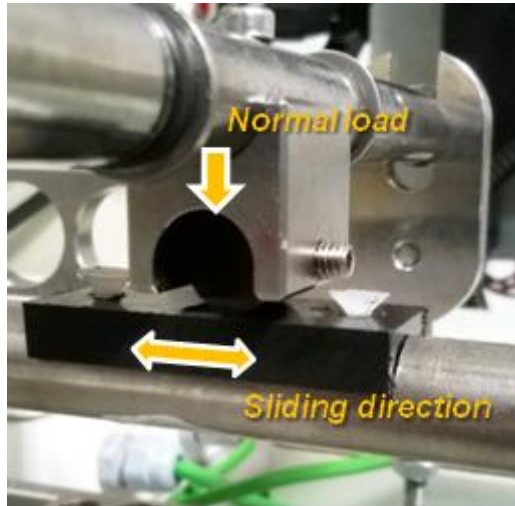


Figure 77: Cylinder on flat assembly.

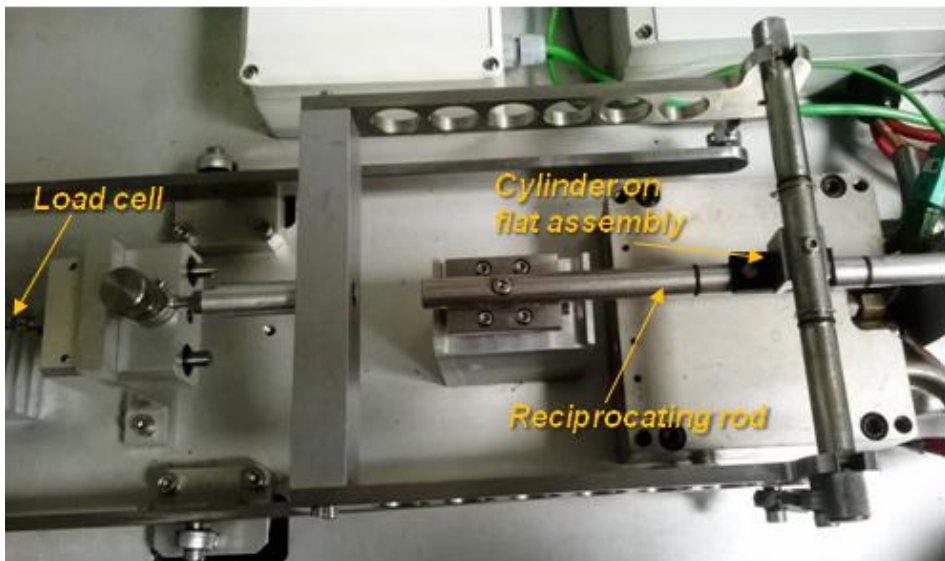


Figure 78: Test assembly for sliding tests in the TE77 friction machine.

Friction tests were carried out at room temperature and under dry sliding conditions. A stroke of 5mm was set, a normal load of 15N and two different sliding velocities, 0.1 and 0.25 m/s. These velocities were

Chapter 4: Frictional heating on elastomeric seals during operation: An approach

chosen because they are in the range of the actual working conditions of seals made of these materials. Seal manufacturers recommend using seals made of these materials up a maximum sliding velocity of 0.5m/s under high pressure conditions. The main reason for this velocity constraint is the low temperature resistance of these materials (approximately about +100°C). Coefficient of friction and surface temperatures were recorded for 10 minutes and each test was repeated a minimum of 2 times.

Seal manufacturers usually recommend the use of chromed steel shafts made from 42CrMo4V, with a minimum hardness of 45HRC, a Ra roughness in the range between 0.1 and 0.3 μm , and a coating thickness of about 20-30 μm [29]. Thus, in order to study the effect of the mating surface conditions on the generated friction and the surface temperatures reached, chromed and non-chromed steel cylinders with Ra roughness values of 0.1, 0.2 and 0.5 μm were tested. Test conditions are summarized in Table 14.

| | | |
|------------------------|--|---|
| <i>Upper specimen</i> | <i>Material</i> | 42CrMo4V |
| | <i>Cylinder length</i> | 15mm |
| | <i>Cylinder diameter</i> | 10mm |
| | <i>Cylinder roughness (R_a)</i> | 0.1 μm , 0.2 μm , 0.5 μm |
| <i>Lower specimen</i> | <i>Materials</i> | TPU, NBR |
| | <i>Polymer sample thickness</i> | 5.8mm |
| <i>Test parameters</i> | <i>Normal Load</i> | 15N |
| | <i>Stroke length</i> | 5mm |
| | <i>Oscillation frequency</i> | 10Hz, 25Hz |
| | <i>Sliding velocities</i> | 0.1m/s, 0.25m/s |
| | <i>Test duration</i> | 10 min |

Table 14: Test parameters.

4.3.2.2 Temperature measurement by means of thermography

Theory of thermography

Every object emits a specific energy that depends on its temperature and radiation wavelength. The amount of radiation increases with temperature. If the temperature of the object is lower than +500°C, emitted radiation lies completely within IR wavelengths [26]. An infrared radiation (IR) camera is a device that converts the radiation into a visual image that represents the temperature field of objects captured by it. The main components of an IR camera are: a lens that focuses the radiation onto a detector, electronics and a software to process the signal and images (see Figure 79). The radiation captured by the camera comes from different sources: the camera receives radiation from the target objects, from the surroundings (reflected radiation) and from the atmosphere.

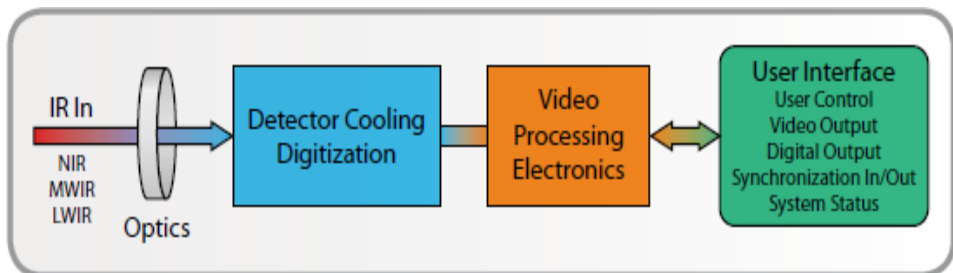


Figure 79: Scheme of the components of an IR camera [26].

Thermal setup for temperature measurements & IR camera calibration

The temperature field on the tribo-pair was measured and acquired during the sliding tests by means of a Flir SC300 high precision thermo-

camera (FLIR systems, Inc.). In Figure 80 a complete image of the TE77 test rig and the infrared camera assembly are shown. An infrared camera measures and images the infrared radiation emitted from an object which varies with temperature and radiation wavelength. Thus, being the radiation a function of the surface temperature of objects, it is possible for the camera to calculate and display this temperature. The radiation measured by the camera also depends on the object emissivity. The Flir SC 3000 camera works in the spectral range of 8-9 μ m.

The camera was installed at a distance of 100mm from the contact of the tribo-pair in order to obtain an adequate focus. The thermal camera has a working range from -20°C to +2000°C with an accuracy of $\pm 1\%$ or $\pm 1^\circ\text{C}$, for measurement ranges up to +150°C. The system has a sensitivity of 20mK at 30°C and a resolution of 320x240 pixels. In order to get temperatures as close as possible to the reality, calibration of the camera was carried out following the procedure described by manufacturers. In particular, the system was calibrated by means of the determination of the emissivity (ϵ) of the target objects which are mandatory inputs for the infrared camera SC 3000 software. The emissivity of a surface is a measure of its ability to emit infrared energy, and it is a function of the temperature and radiation wavelength. Radiative properties of a body are usually given in relation to a perfect blackbody. Thus, the emissivity of a body can be calculated as:

$$\epsilon = \frac{W_{obj}}{W_{bb}} \quad (55)$$

where W_{bb} is the radiation of a blackbody and W_{obj} the radiation of the object under study. Thus, emissivity is a number between 0 and 1. The higher the emissivity of an object, the better its radiative properties.

In this work, the emissivities of the samples were measured using the Fourier transform infrared spectroscopy (FTIR) by means of the FT/IR-4700 Spectrometer (Jasco). At 25°C (room temperature), the following emissivities were measured:

- Thermoplastic polyurethane (TPU): $\varepsilon \sim 0.89$
- Nitrile rubber (NBR): $\varepsilon \sim 0.85$

Beside, emissivities were also measured at +125°C in order to see its evolution with temperature. It was found that the emissivity values of both polymers at +125°C are the same as at room temperature i.e. the emissivity of the elastomers under study remain nearly constant in the range between +25°C and +125°C.

In order to avoid possible errors arising from reflections, all the metallic parts of the system were properly insulated. Room temperature was measured before each test by means of a high precision thermometer. These values were introduced in the camera software in order to calibrate the image.



Figure 80: TE77 high frequency sliding test rig (Plint tribology).

A thermal image of the assembly is shown in Figure 81.

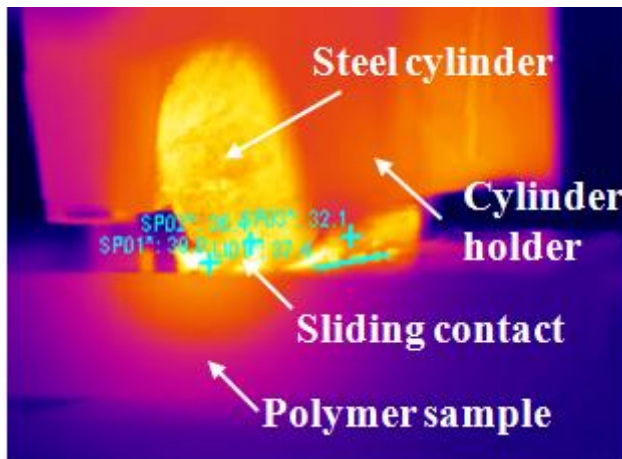


Figure 81: Thermal image example from the tribo-system.

4.3.3 Experimental results

In this section the results of friction and surface temperature measurements are presented for the different considered test conditions.

4.3.3.1 Friction test results

Figure 82 and Figure 83 show the friction coefficient curves obtained from the tribological tests carried out on the TPU and NBR samples, respectively, while sliding against steel cylinders with different R_a roughness at two different velocities, 0.1 and 0.25 m/s.

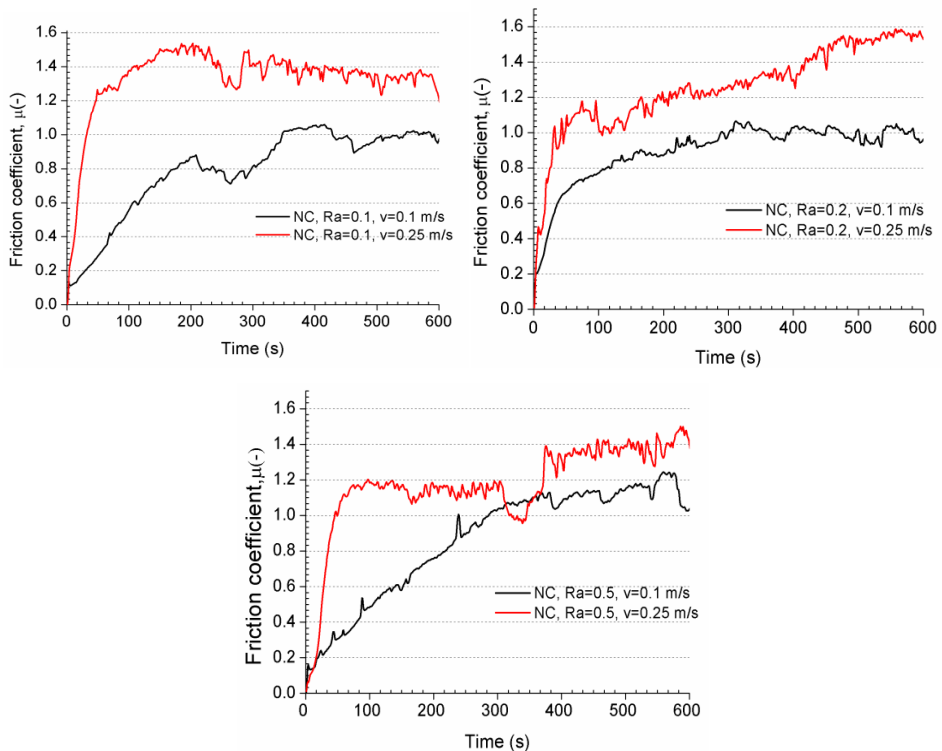


Figure 82: Friction of Non-Chromed plated (NC) cylinders sliding against TPU.

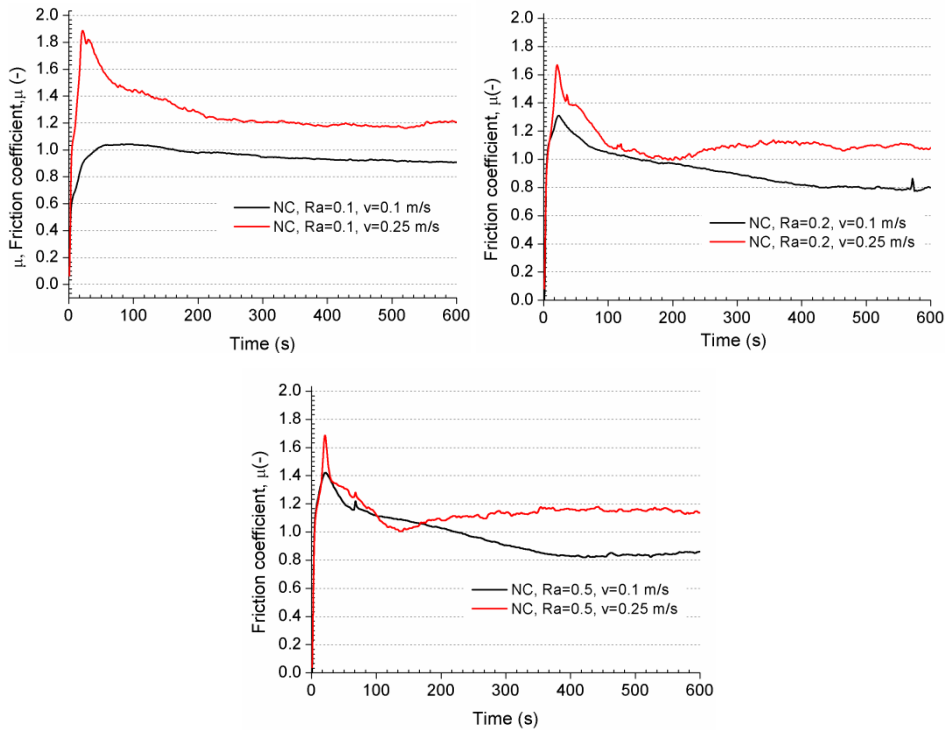


Figure 83: Friction of Non-Chromed plated (NC) cylinders sliding against NBR.

Effect of sliding velocity on friction

Results showed that the friction generated increases with velocity. During each test, the friction coefficient raises very fast during the running-in period until a nearly steady-state is reached. In the case of tests carried out at 0.1m/s, the friction coefficient raises gradually whereas at 0.25m/s friction rise occurs within the first minute. TPU samples presented a steady friction coefficient in the range of about 1 and 1.2, at 0.1m/s, and a coefficient between 1.4 and 1.6, at 0.25m/s. NBR samples presented a bit lower friction coefficients; between 0.8 and

1 at 0.1m/s, and a coefficient of about 1.2 at 0.25m/s. In general, results showed that the higher the velocity, the faster the friction coefficient increases during the first cycles.

Effect of steel roughness on friction

The friction resistance of polymers depends to a great extent on the counterface roughness [39]. When a polymer is sliding against a metallic counterface, the friction force generated decreases during the running-in until a minimum roughness value is reached. From then on, the friction generated will increase as the roughness decreases. The transition point is usually coincident with the transition from abrasive wear to adhesive wear.

Regarding the effect of cylinder roughness on the steady friction, results revealed that it is negligible in the case of the NBR. Nevertheless, it was found that the cylinder roughness does affect the friction force generated during the running-in period, as well as the form of the friction curve during the first sliding cycles. In particular, results revealed that higher cylinder roughness lead to larger friction peaks during the running-in. For the TPU, the effect of roughness is negligible at 0.25m/s whereas at 0.1m/s the friction coefficient raises from 1 to 1.2 when the roughness raises from 0.1 to 0.5 μ m.

The main reason for being almost independent roughness and friction after some sliding cycles may be the severe operating conditions of the tests due to the absence of lubrication. In other words, the severe test conditions do not allow appreciating the effect of steel cylinder roughness on the friction generated.

Effect of the chromium plating process on friction

Figure 84 shows the friction coefficient curves of the TPU samples in relative motion with both chromed (C) and non-chromed (NC) steel cylinders with different roughness and under different sliding velocities. Results revealed that, in general, C cylinders lead to higher friction coefficients than NC ones. This effect, however, is more appreciable within the tests carried out at low velocities and with low roughness cylinders. At 0.1m/s, and with NC cylinders with a roughness of 0.1 and 0.2 μm , steady friction coefficients of about 1 were reached. Under the same conditions but with C cylinders, friction coefficients in the range between 1.3 and 1.4 were obtained. During high velocity tests or/and tests carried out with cylinders with a R_a roughness of 0.5 μm , test conditions were again so aggressive for the elastomeric samples that the chromium plating process had no significant influence on friction.

Figure 85 presents the friction results obtained from the tribological tests with NBR samples. As can be seen, the effect of the chromium coating on friction is almost negligible in all the cases.

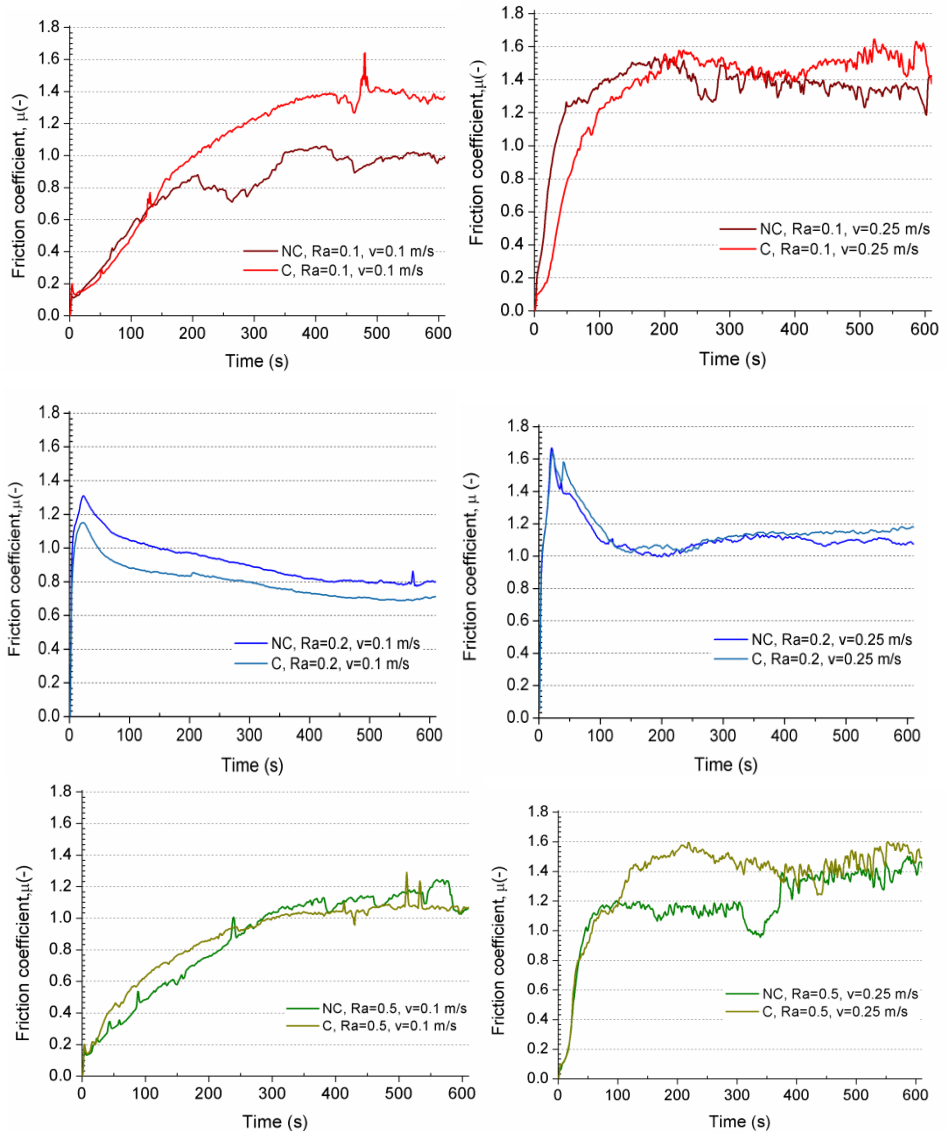


Figure 84: Effect of the chromium-plating process on the friction of the TPU samples.

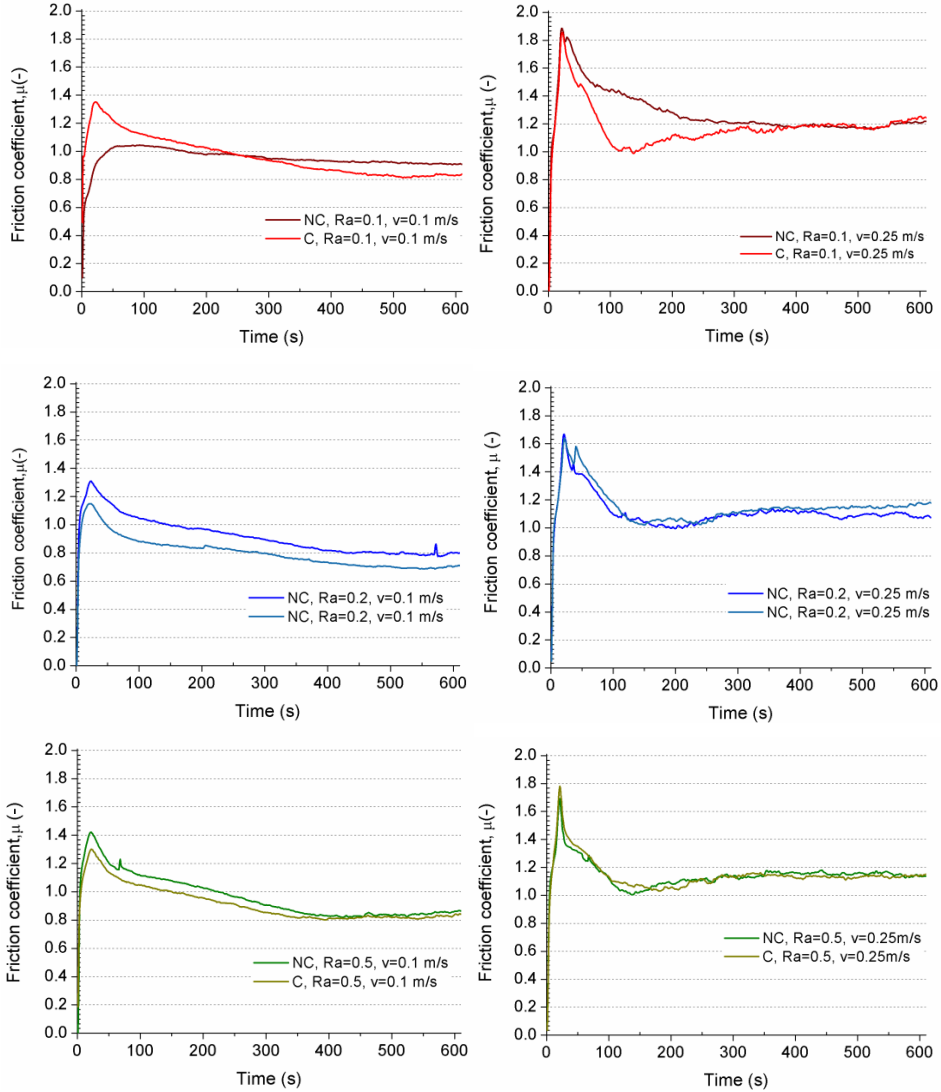


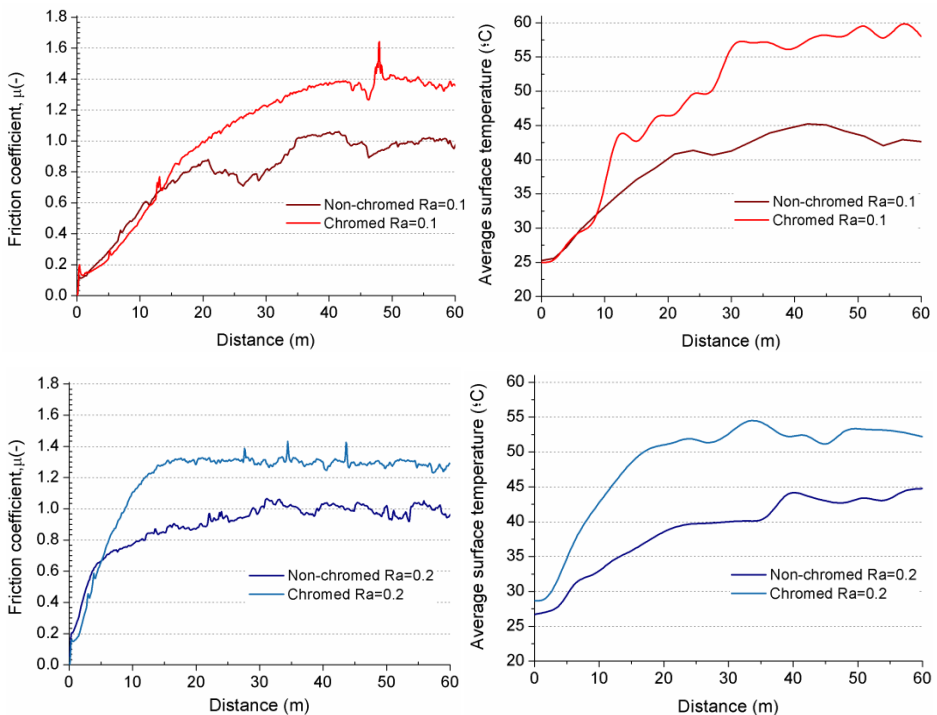
Figure 85: Effect of the chromium-plating process on the friction of the NBR samples.

4.3.3.2 Surface temperature measurements

In this section, friction and temperature evolution curves of the tested tribo-pairs throughout the tests are presented. The temperatures plotted correspond to the average temperature values and they were measured at the surface of the elastomers.

Sliding velocity of 0.1m/s

Figure 86 shows the temperature curves of the TPU samples at a velocity of 0.1m/s (10 Hz) vs. the travelled distance. In the same figure, the friction coefficient evolution is shown in order to investigate similarities in the progression or tendency of friction and temperature curves.



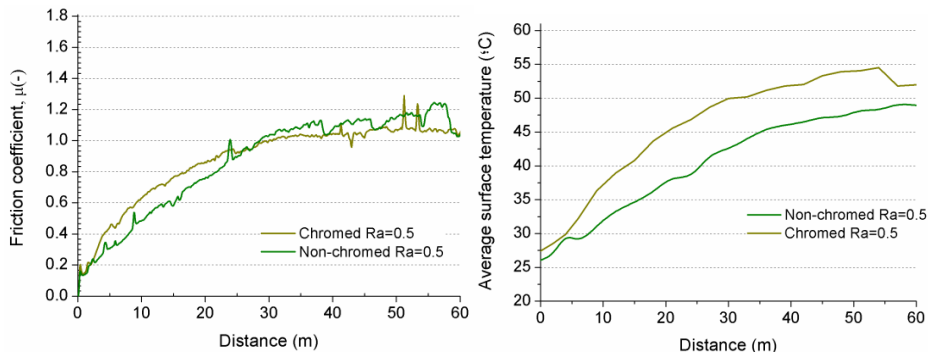


Figure 86: Friction and temperature curves of the TPU samples sliding against steel mating surfaces with different roughness and surface conditions at 0.1m/s.

Results showed that the tendencies of the friction and surface temperature curves are similar in all the cases. In particular, both friction and temperature tend to increase monotonically until a steady value is reached. The reason for such a similar behaviour is that there is a direct correlation between both parameters as stated in the existing analytical models (see section 4.4). During the running-in, the friction force generated between the elastomer and the steel part increases progressively. Some of the main reasons for the friction rise during this stage are associated to the smoothing of the surfaces and to an increase in the adhesive component of the friction generated in the case of elastic materials. A temperature rise is mainly associated to a heat flux rise which directly depends on friction considering that most of the frictional energy generated is dissipated as heat and wear. Moreover, the heat flux is also influenced by the contact area which increases during the running-in. In other words, during motion there exists a continuous energy balance between friction, wear and temperature.

Results revealed that at 0.1m/s, C cylinders led to considerably higher temperatures at the surface of the TPU samples than NC cylinders. In particular, with C cylinders steady temperatures between +55 and +60°C were registered, whereas under the same conditions but with NC cylinders these temperatures were in the range of about +45°C and +50°C. Regarding the effect of roughness on temperature, it was found that it is almost negligible. In the case of tests carried out with C cylinders, slightly higher temperatures were obtained during the tests with cylinders of low roughness (0.1µm).

Figure 87 presents the average temperature and the friction curves of the NBR samples vs. the travelled distance for the different test conditions. Temperature curves on the NBR samples showed the same tendency as in the case of the TPU. Nevertheless, in this case it was found that the surface conditions of the steel cylinders (surface treatment and roughness) barely affect the temperatures reached at the surface of the NBR samples. At 0.1m/s, the NBR presented a steady friction coefficient between 0.7 and 0.9, and average surface temperatures between +40°C and +45°C, for the different cylinder surface conditions.

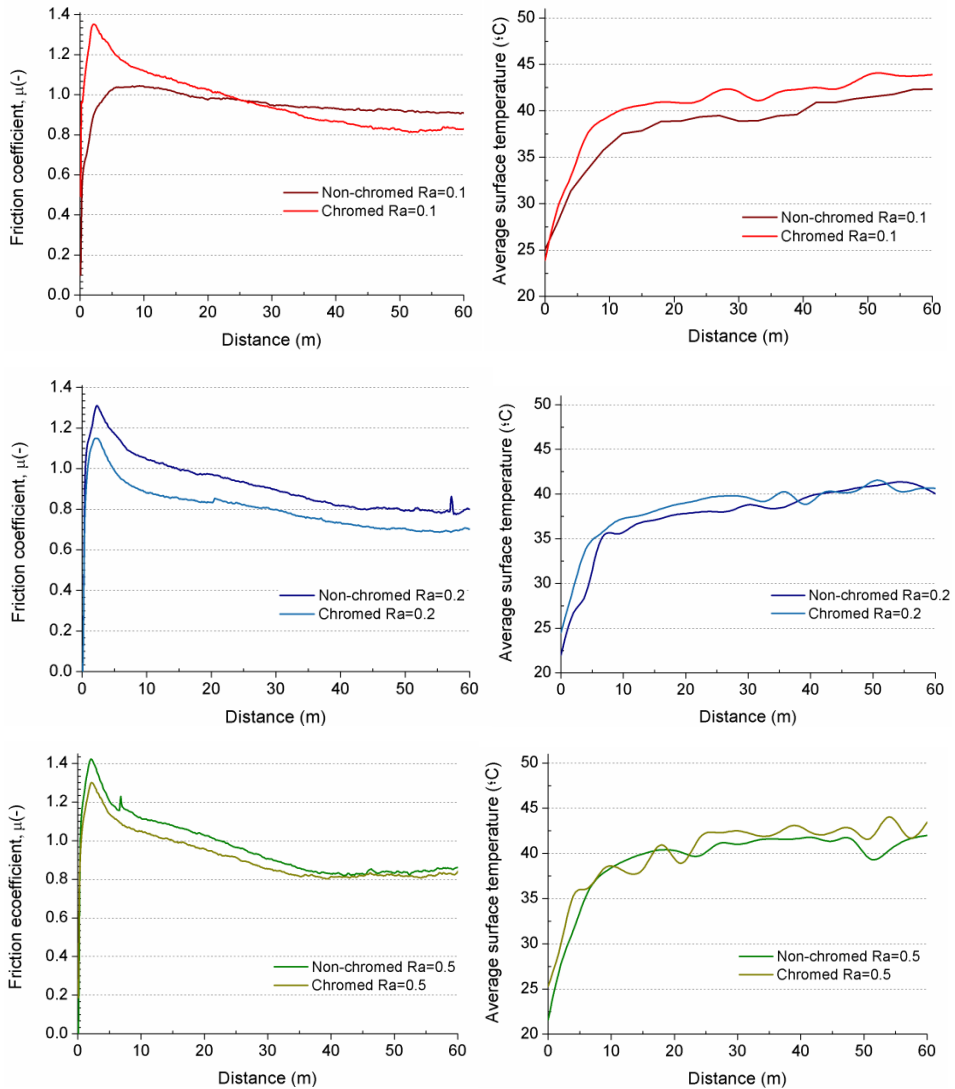
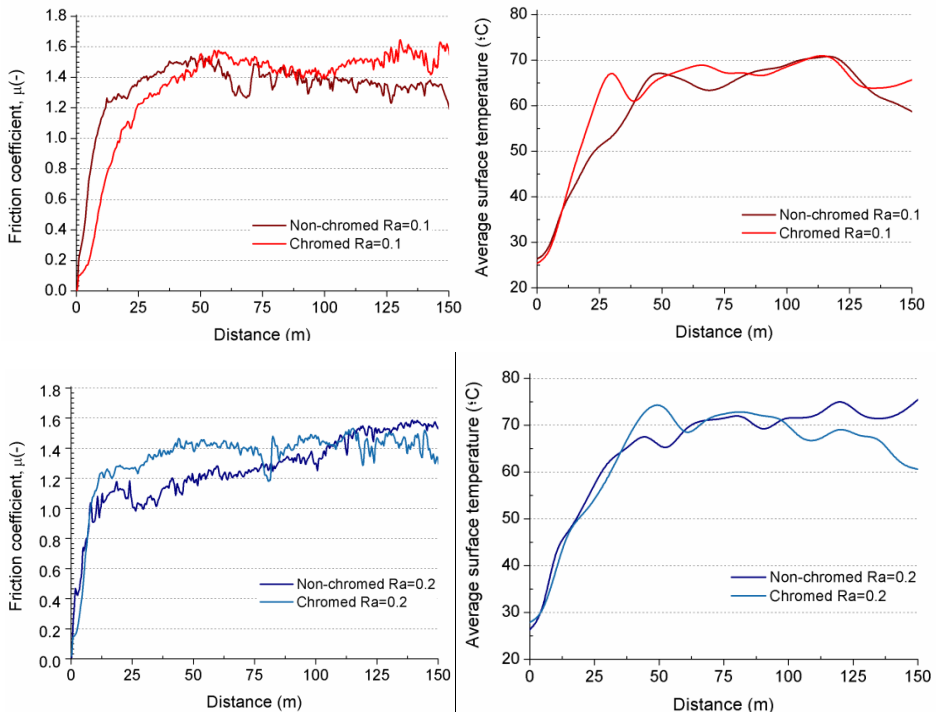


Figure 87: Friction and temperature curves of NBR samples sliding against steel mating surfaces with different roughness and surface conditions at 0.1m/s.

Sliding velocity of 0.25m/s

Friction coefficient and surface temperature curves of the TPU samples at a reciprocating velocity of 0.25m/s (25Hz) vs. the travelled distance are shown in Figure 88. At 0.25m/s, again a good matching was found between friction and thermal results in all the cases. In particular, both increase monotonically with the sliding distance until a nearly steady value is reached. Moreover, results showed that more time is needed to reach steady temperatures in this case than at lower temperatures, mainly due to the instabilities presented by the friction curves. Stable temperatures in the range of +66°C and +77°C were registered in all the cases, and it was found that the effect of the surface conditions of the steel parts on the temperatures reached on the TPU samples is almost negligible.



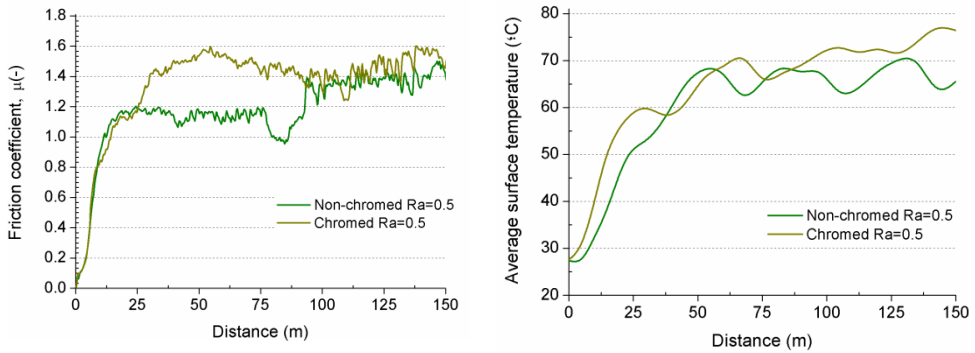


Figure 88: Friction and temperature curves of the TPU samples sliding against steel mating surfaces with different roughness and surface conditions at 0.25m/s.

In Figure 89 the temperatures measured at the surfaces of the NBR samples during the tests are shown. As happened with the TPU, temperature curves also increase monotonically with the running distance in this case, but more time is needed at 0.25m/s to reach a steady temperature, compared to the time needed at 0.1m/s. Regarding the effect of the surface conditions of the steel parts on temperature, results showed that the effect of both surface treatments and surface roughness is negligible at 0.25m/s. Under steady-state conditions, all the tribo-pairs showed similar temperature values of about +60°C.

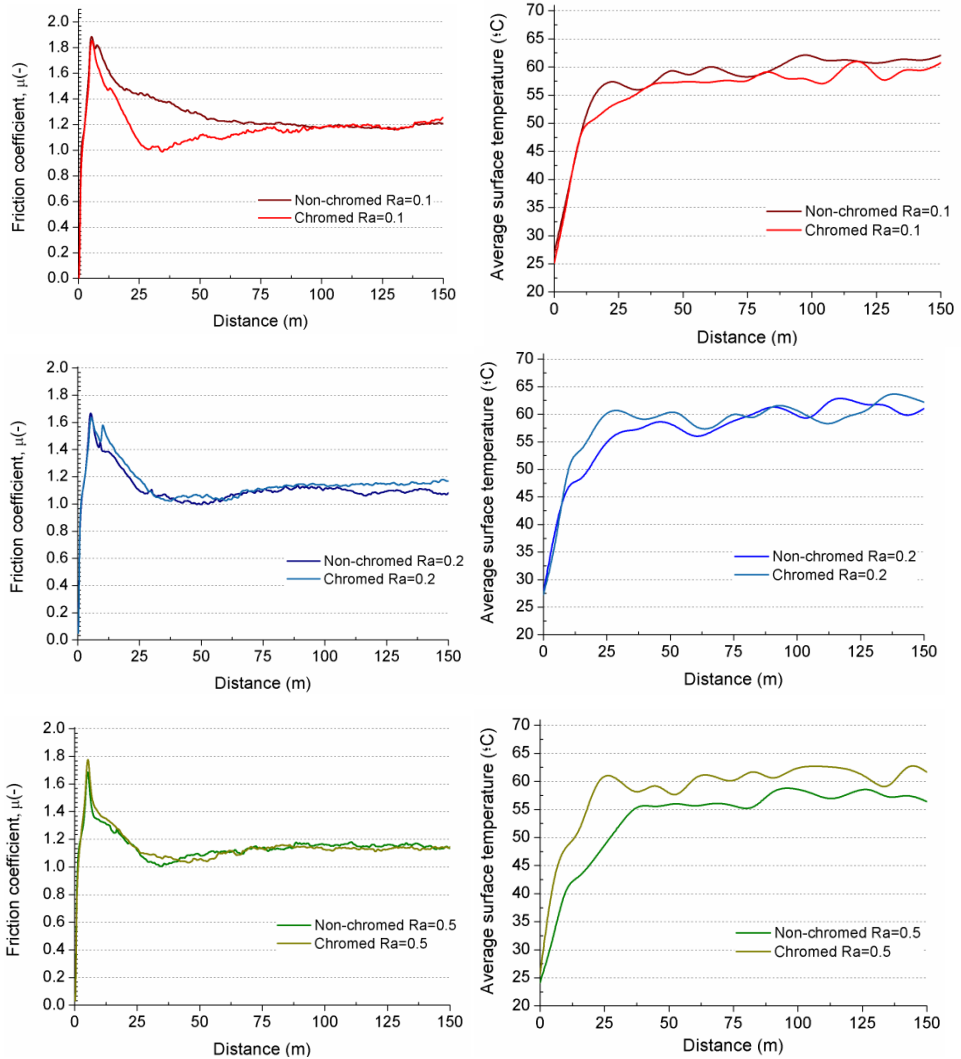
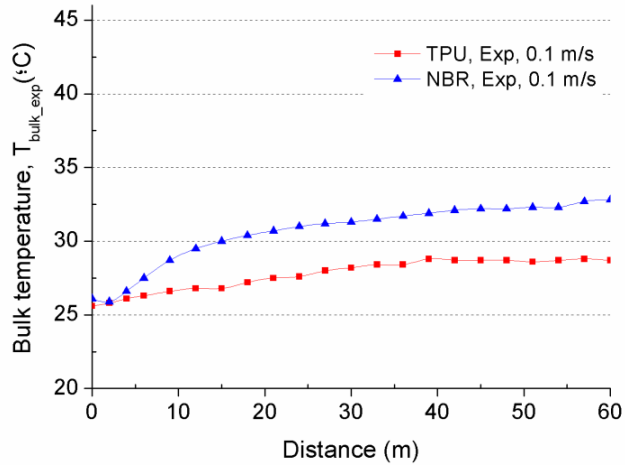


Figure 89: Friction and temperature curves of the NBR samples sliding against steel mating surfaces with different roughness and surface conditions at 0.25m/s.

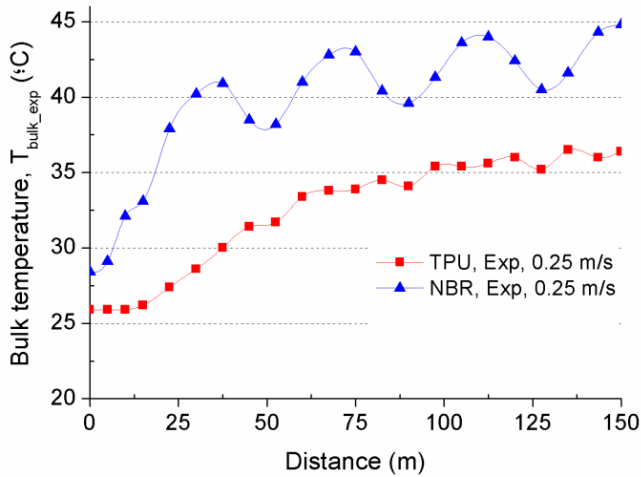
Temperature rise on finite thickness bodies

In section 4.2 it was reported that Tian et al. [33,34] found that in the case of bodies with a finite thickness subjected to heat sources moving over the same path continuously, there is a temperature rise known as nominal temperature rise that affects the entire contact area. In this work, the thickness of the tested elastomeric samples was about 5mm, hence, the heat generated at the surface will be transmitted to the bulk affecting the entire sample.

Figure 90 presents the temperature of the test samples, measured at the centre of the contact area, at a distance of 4mm from the surface. Results showed that the temperatures in the bulk of the polymer increase gradually during motion until reaching steady temperature conditions. Moreover, it was found that the temperature inside the samples becomes stable faster during the tests carried out at low velocity (0.1m/s) rather than at those performed at the higher velocity (0.25m/s). This effect was also observed for the temperatures at the surface of the elastomers. Moreover, the temperatures reached in the bulk of the NBR samples are higher than those measured in the TPU samples while the surface temperatures were higher on the latter. The main reason for this is that the thermal diffusivity of the NBR is higher so that the heat moves more rapidly through it.



(a)



(b)

Figure 90: Temperature measurement in the bulk of the elastomeric samples throughout the tests: (a) at 0.1m/s and (b) at 0.25m/s.

4.3.3.3 Wear measurements

In order to evaluate the wear mechanisms of the samples, SEM micrographs were taken on the test samples. Figure 91 and Figure 92 show the SEM micrographs of the surfaces of some of the TPU and NBR samples, before and after the tests. As can be seen, Schallamach waves are present in all the wear scars. These waves are characteristic of rubber-like materials and its stick-slip motion, and they are oriented perpendicularly to the sliding direction. Furthermore, they are the result of periodic fluctuations between compression and tension along the contact surface. In other words, Schallamach waves are the result of consecutive contact adhesions occurring at the surface during sliding due to the visco-elasticity of elastomers and their ability to extend giving local recoverable strains [25].

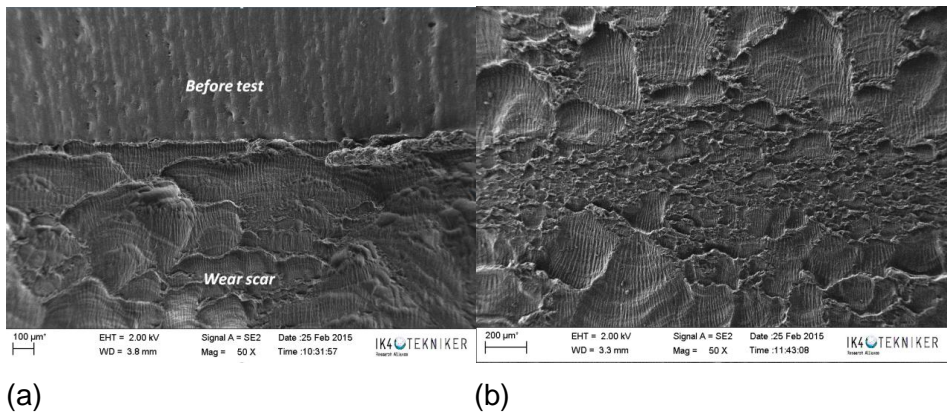


Figure 91: TPU surface (a) before and (b) after the tests.

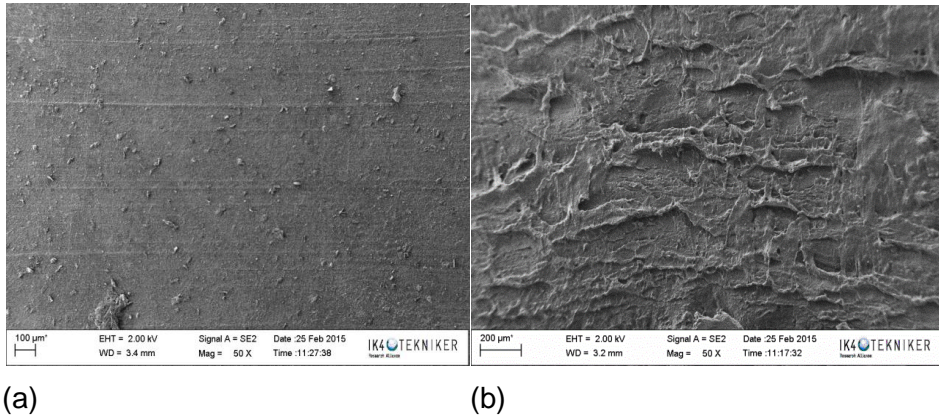
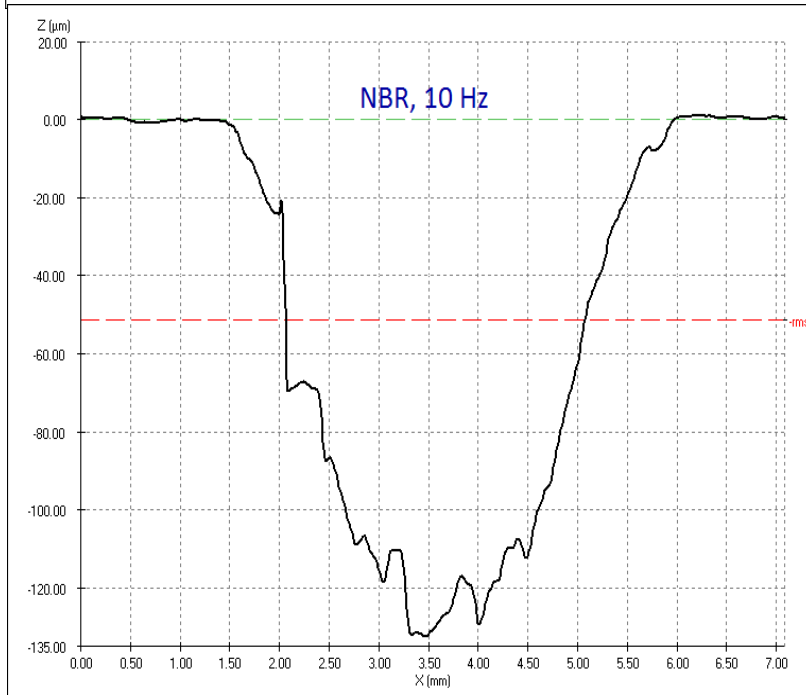
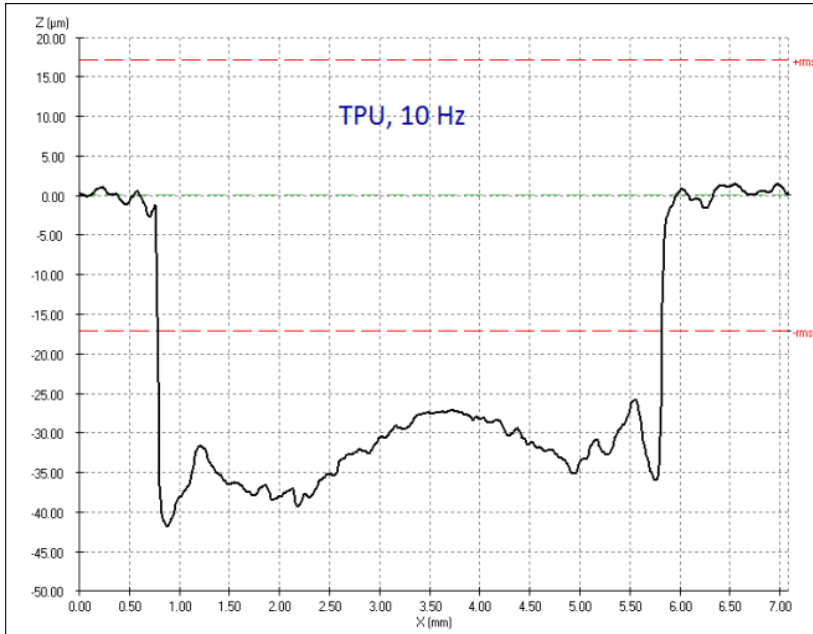


Figure 92: NBR surface (a) before and (b) after the tests.

In order to evaluate the wear of the samples, their weight was measured before and after each test. Moreover, confocal microscopy was used to measure the profile of the wear scar and for a better visualization of the mass loss (Figure 93). As can be observed, the depths of the wear scars of the NBR samples are considerably greater than those of the TPU samples (more than 3 times greater). Furthermore, it was found that TPU samples in contact with steel cylinders tend to wear out more in the extremes of the wear scar rather than at the centre.



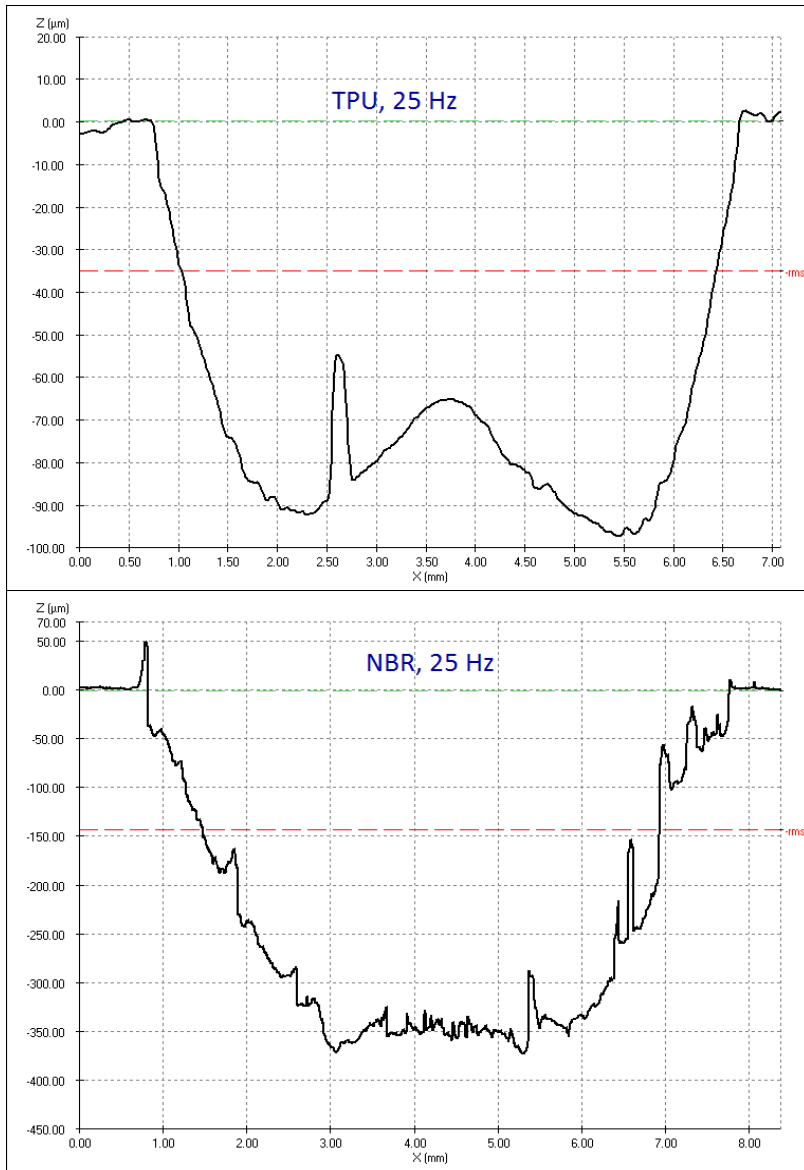


Figure 93: Micrographs of the wear scars under different conditions.

In order to compare tribologically the samples, both friction coefficients and wear rates are needed because samples exhibiting the same friction may present different wear rates depending on how the energy is

partitioned within and between the materials. Figure 94 presents the frictional energy of the samples under different test conditions vs. the mass loss. In particular, three values have been plotted per test condition, one for each cylinder roughness. In the graph, specific wear rate intervals (E_w) for each test condition are shown. The specific wear energy can be calculated as the ratio of the friction work to the mass loss due to wear:

$$E_w = \frac{E}{\Delta m} = \frac{v N \int_{t_i}^{t_f} \mu(t) dt}{\Delta m} \quad (56)$$

where E_w is the specific wear energy, E is the energy dissipated by friction, v is the mean relative sliding velocity, N is the normal load, μ is the coefficient of friction, t_i the initial time, t_f is the time at the end of the test, and Δm is the total mass loss. As can be observed, both materials present similar frictional energy at every velocity, however, the specific wear energy of the TPU is considerably higher i.e. more energy is required to wear out the TPU polymer.

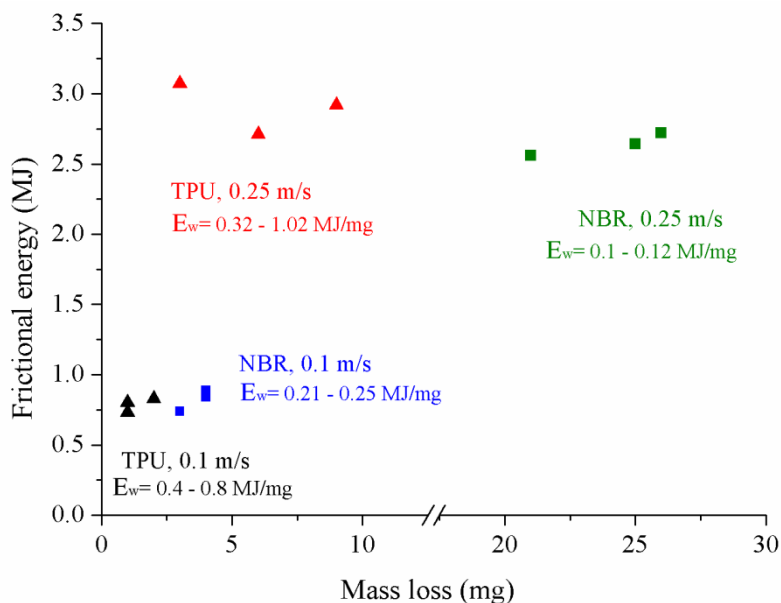


Figure 94: Frictional energy vs mass loss.

4.3.3.4 Main conclusions

In Figure 95 and Figure 96 a summary of all the friction and thermal results is presented. It can be observed at a glance that the frictional behaviours of the TPU and NBR are completely different. Friction coefficient curves of the TPU samples continuously increase with the travelled distance until reaching steady-state values. In the case of NBR samples, by contrast, friction curves present a peak during the running-in, and afterwards decrease until becoming stable. These friction peaks are characteristic of rubber materials and appear when the relative motion between mating surfaces starts [27].

In general, it may be concluded that the NBR samples presented lower friction and lower surface temperatures than the TPU samples under the different test conditions. Moreover, it is important to remark that the

Chapter 4: Frictional heating on elastomeric seals during operation: An approach

friction curves of the rubber samples were more stable in all the cases than the curves obtained with the polyurethane ones. It is thought that the main reason for those instabilities in the friction curves of the TPU samples may be the high hardness of the material (93 Shore A).

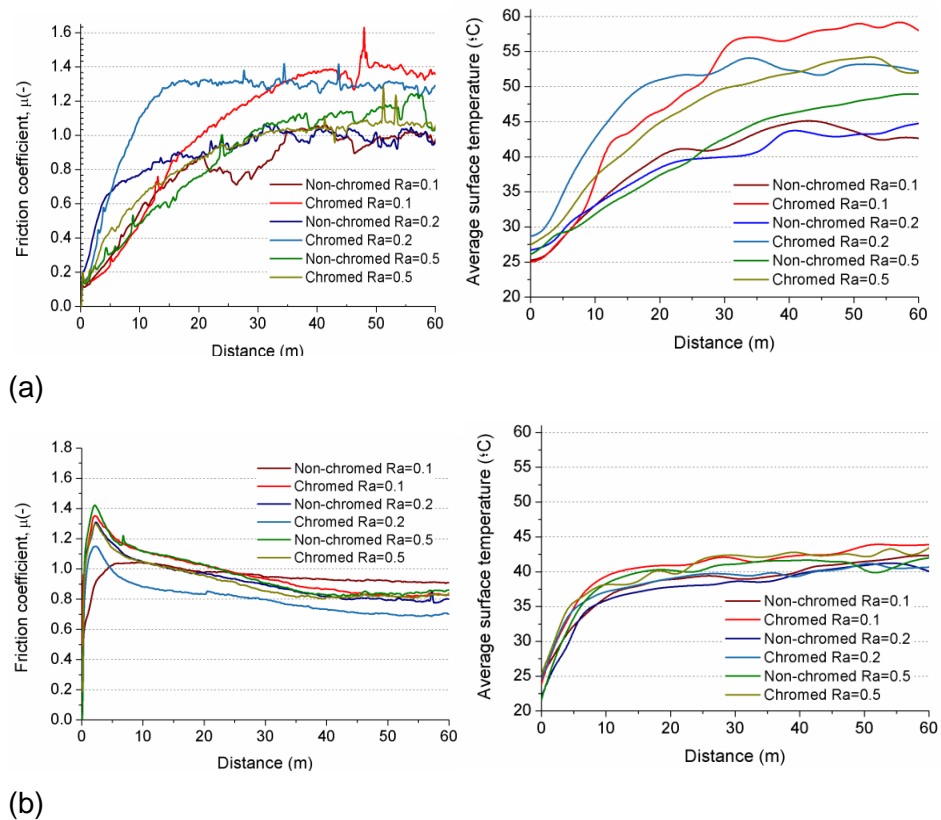


Figure 95: Comparison between test results at 0.1m/s for the (a) TPU and (b) NBR samples.

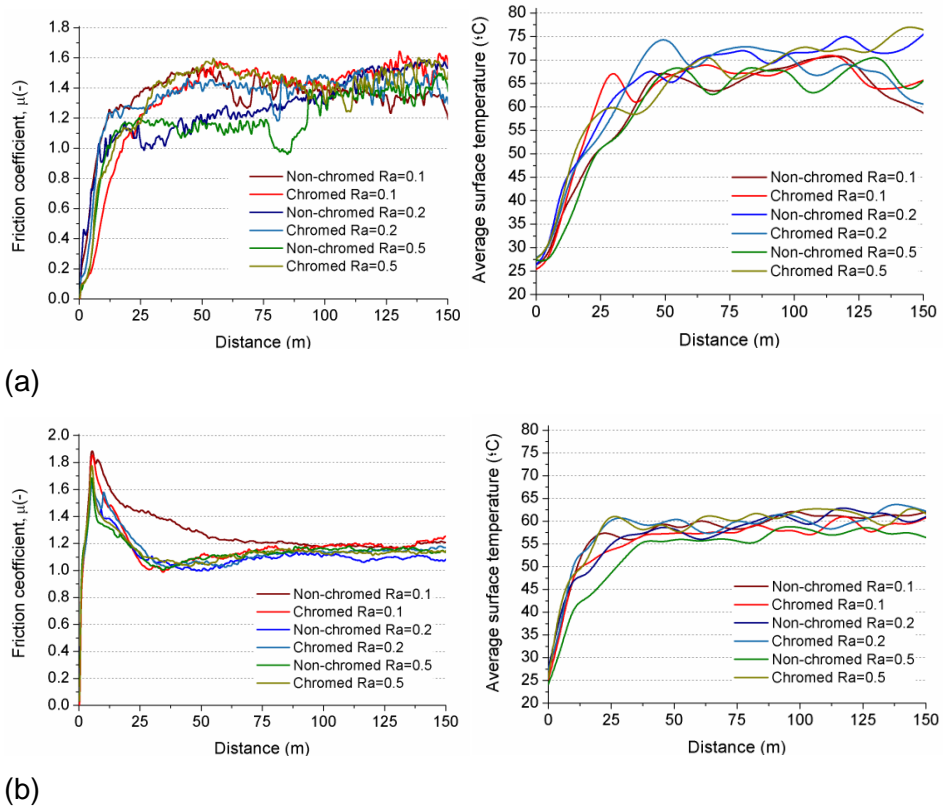


Figure 96: Comparison between test results at 0.25 m/s for the (a) TPU and (b) NBR samples.

From the experimental study on the frictional heating phenomenon of elastomers, it may be concluded that the effect of sliding velocity on temperature is considerably larger than the effect of the steel part surface conditions. In particular, results revealed that at 0.1m/s the TPU samples are sensitive to the surface conditions of the steel parts while their effect on the performance of the NBR samples is almost negligible. At 0.25 m/s, it is difficult to establish any relation between the surface conditions of the steel cylinders, and friction and temperature. As Blau et al. reported in [36], in some cases wear quickly alters the contact

surfaces so that any attempt to correlate the frictional performance with the initial surface conditions may be inappropriate. Regarding the effect of velocity on temperature, the TPU samples presented surface temperatures in the range of +40°C and +60°C at 0.1m/s, and temperatures in the range of +60°C and +77°C at 0.25m/s. In the case of the NBR samples, they presented surface temperatures between +40°C and +45°C at 0.1m/s, and between +56°C and +62°C at 0.25m/s.

Moreover, it was found a good correlation between the friction generated and the temperatures reached at the surface of the elastomers. Thus, the results obtained validate somehow the temperature measurements carried out by means of IR thermography. Furthermore, the curve trends are in close agreement with those presented by Tzanakis et al. in [16].

Temperature measurements through infrared thermography revealed that the temperatures in the bulk of the tested elastomers are also affected by the frictional heating. In particular, due to the low thickness of the samples and the severe sliding conditions (dry lubrication, high velocity and short stroke) the bulk temperature of the elastomeric samples increase gradually during motion until reaching steady temperature conditions. Moreover, the temperatures reached in the bulk of the NBR samples are higher than those measured in the TPU samples while the surface temperatures were higher on the latters. The main reason for this is that the thermal diffusivity of the NBR is higher so that the heat moves more rapidly through it.

Regarding the wear mechanisms of elastomeric samples, all the tested samples presented Schallamach waves which result from consecutive contact adhesions occurring at the surface during sliding due to the visco-elasticity of elastomers and their ability to extend giving local recoverable strains. Results showed that under the same test conditions the mass loss of the NBR samples was larger in all the cases than that of the TPU samples. Moreover, specific wear energy calculations revealed that both materials present similar frictional energies under the same conditions whereas the specific wear energy of the TPU is considerably higher i.e. more energy is required to wear out the TPU polymer.

4.4 Analytical calculations and comparison with experimental results

The aim of this section is to investigate if any of the existing analytical contact temperature models is useful to predict the temperatures reached on the tested elastomers, and under the considered test conditions. In [13] it was demonstrated that temperature rise calculations depend up to a great extent on the considered real contact area, friction coefficients and thermal properties.

Even if a broadly accepted criterion consists in calculating the real contact area by dividing the load by the hardness of the softer material, in this case it is not possible to apply this criterion since the hardness of elastomers must be measured by means of Shore A and Shore D durometers. Hence, in this work, the contact area was measured after each test and those values were considered for calculations. In other

words, it has been assumed that the real contact area is similar to the apparent contact area. This assumption may be valid since the materials under study are elastomers. The average contact widths measured under each test condition are shown in Table 15. Regarding friction, in this work the friction coefficient evolution captured during the tests was used for calculations (assumption 5 in section 4.2 is not considered). The thermal properties from Figure 74 were considered for calculations. In [18] it was demonstrated that taking into account the variation of material thermal properties with temperature. In this case, however, thermal properties variation is so slight within the operating temperature range that it does not almost influence the results obtained.

| | | Contact width, 2b (mm) | |
|------------|-----|-------------------------------|----------------|
| | | 0.1m/s | 0.25m/s |
| TPU | 4.1 | 6.3 | |
| NBR | 4.5 | 7.2 | |

Table 15: Measured contact widths.

For flash temperature calculations, two of the most popular analytical models were used: Jaeger model and Tian-Kennedy model for maximum flash temperature calculation. The equations of these models are shown in Table 16. It is important to remark that the Jaeger equations presented in Table 16 estimate the average flash temperature along the contact area whereas Tian & Kennedy's equations calculate the maximum one. In this first stage, both models were applied in order to find out which model works better for these particular test conditions and materials. The heat generated during sliding was calculated applying Equations (51) and (52).

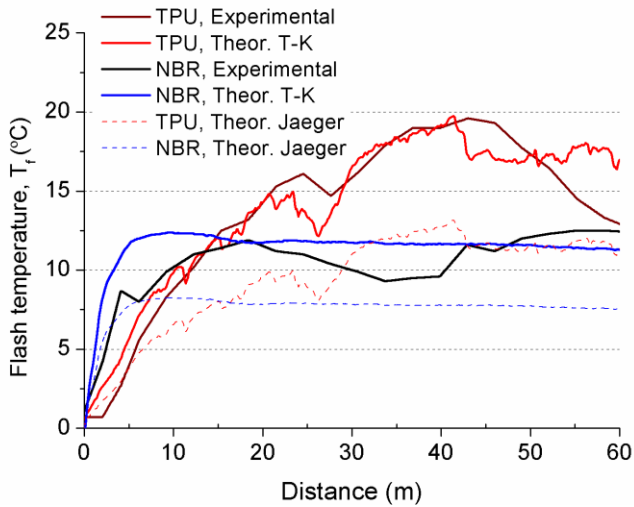
| Model | Equation | |
|-----------------------------|-----------------------------------|---|
| Jaeger (1942) | Stationary or low speed Pe<0.1 | $T_{fave} = 0.946 \frac{q b}{k}$ |
| | Moving Pe>10 | $T_{fave} = \frac{1.064 q}{k} \left(\frac{X b}{v} \right)^{1/2}$ |
| Tian & Kennedy (1994) | Stationary or low speed Pe<0.1 | $T_{fmax} = \frac{2 q b}{k \sqrt{\pi}}$ |
| | Moving Pe>10 | $T_{fmax} = \frac{2 q b}{k \sqrt{\pi Pe}}$ |

Table 16: Analytical models for flash temperature calculations.

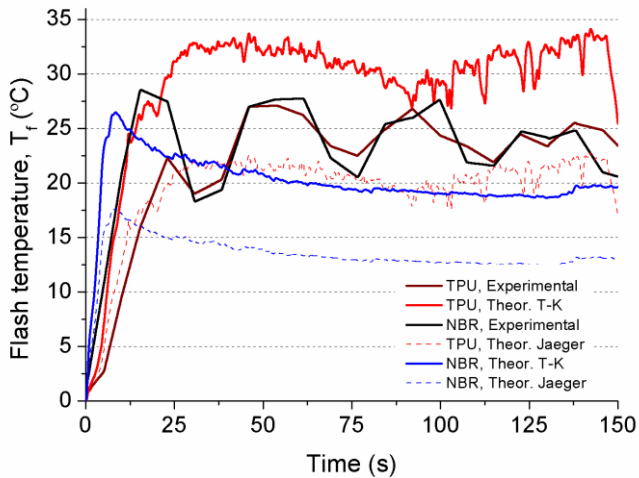
Figure 97 presents a comparison between the flash temperatures on the samples obtained experimentally and analytically applying equations in Table 16. The experimental flash temperature curves have been calculated as the difference between the surface temperatures and those temperatures measured in the bulk:

$$T_{f_exp} = T_{surf} - T_{bulk_exp} \quad (57)$$

where T_{surf} is the temperature at the surface of the elastomers experimentally measured, T_{bulk_exp} is the bulk temperature of the elastomer experimentally measured and T_{f_exp} is the experimental flash temperature.



(a)



(b)

Figure 97: Comparison between experimental and analytical flash temperature curves at (a) 0.1m/s and (b) 0.25m/s.

In general, a good matching was found between the experimental flash temperature curves and the analytical curves calculated using the model of Tian&Kennedy for maximum flash temperature calculation. Hence, it

was found that this model predicts better than Jaeger the flash temperatures reached at the surface of the elastomers studied in this work, and under the specific conditions considered. Furthermore, it can be noted that a better matching was achieved at the low velocity case study.

4.5 Effect of misalignments on the temperature rise of dynamic seals due to frictional heating

It has already been discussed about the existing difficulties to measure the temperatures originated at the contact between mechanical components in relative motion during operation. Hence it is of great interest for the industry to find techniques able to predict as accurately as possible the temperatures reached at the contact between mating surfaces.

In this section a methodology to estimate the contact temperature distribution on seals during sliding has been developed based on the knowledge gained from the experimental study. In line with the topic of this thesis, the methodology developed has been used to research on the effect of misalignments on the temperature rise of seals due to frictional heating. In particular, the methodology has been applied to a specific case study in order to estimate the contact temperature distribution on eccentric seals. Afterwards, these results were compared with the results obtained for the concentric case under the same conditions. As a case study, the contact temperature distribution along the seal sample A (TPU) during the sliding tests carried out in Chapter 3 has been calculated. In particular, the contact temperatures reached

during steady-state conditions (at the end of the tests) have been calculated.

The methodology herein proposed combines temperature models, thermo-mechanical properties of materials, experimental data and the contact model presented in Chapter 2. For flash temperature calculations, the model Tian-Kennedy was used because it was identified in the previous section as the most appropriate model to estimate the flash temperatures on the materials under study. Apart from this, experimental friction results, numerical contact areas and contact forces from the applied models are necessary inputs for the calculations.

4.5.1 Procedure to estimate contact temperatures on dynamic seals during operation. General approach.

The total heat flux generated during the sliding of the rod lip seal against its steel mating surface may be calculated as:

$$q_{tot} = \mu F_r v / A \quad (58)$$

where μ is the friction coefficient, F_r is the contact force, v is the sliding velocity and A is the contact area.

In fact, the heat generated in frictional contacts is divided between the mating bodies [28]. Thus, a part of the heat generated due to frictional heating will enter the seal, q_s , and the rest will enter the counterface, q_c . Of course, this affirmation involves assuming that all the energy is converted into heat and that there are no heat losses [21]. Hence, at any

point of the contact, the sum of both heat fluxes must be equal to the total heat rate generated at that point:

$$q_{tot} = q_s + q_c \quad (59)$$

In this specific case, the seal under study is a rod type seal so that during operation the seal remains stationary ($v=0$) while its mounting rod moves at a sliding velocity of $v \left[\frac{m}{s} \right]$. A schematic image of the heat partitioning within the sealing system is shown in Figure 98. As introduced in the previous sections, the temperature reached at the contact, T_c , may be expressed as the sum of the ambient or room temperature, T_{amb} , a local temperature rise, ΔT_f , and a nominal temperature rise, ΔT_{nom} :

$$T_c = T_{amb} + \Delta T_f + \Delta T_{nom} \quad (60)$$

The quasi-steady flash temperature rises on the seal, ΔT_{fs} , and on the moving rod, ΔT_{fc} , may be calculated applying the Tian-Kennedy model as [34]:

$$\Delta T_{fs} = \frac{2q_s b}{k_s \sqrt{\pi}} \quad (61)$$

$$\Delta T_{fc} = \frac{2q_c b}{k_c \sqrt{\pi (1.011 + Pe)}} \quad (62)$$

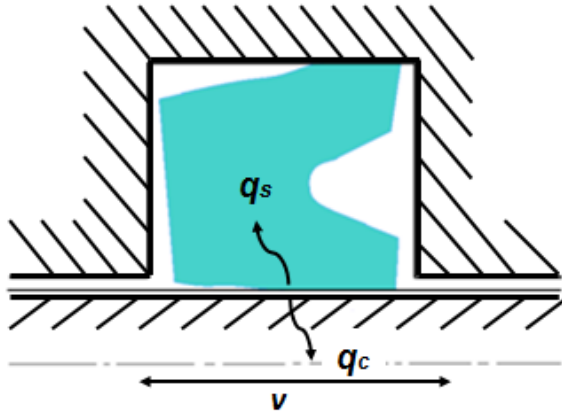


Figure 98: Heat flux partitioning.

Regarding the nominal temperature rise on the seal, it may be calculated assuming that all the heat entering the seal is dissipated by conduction along its cross section or thickness, l_s , as in [35]:

$$\Delta T_{nom s} = \frac{q_{nom s} l_s}{k_s} \quad (63)$$

where $q_{nom s} = \left(\frac{b}{B}\right) q_s$, being B the width of the seal cross section and b the contact width.

The nominal temperature rise at the rod may be calculated applying a thermal balance between the heat generated and the heat evacuated by convection [35,37].

$$q_{ave} = (A_r/A_s)h\Delta T_{nom c} \quad (64)$$

where A_s is the swept contact area, h is the average convective heat transfer coefficient and $q_{ave} = q_c (A/A_s)$.

Defining α as the heat partitioning coefficient, the heat entering each body in contact may be expressed as:

$$q_s = \alpha q_{tot} \quad (65)$$

$$q_c = (1 - \alpha) q_{tot} \quad (66)$$

The heat partitioning coefficient depends obviously on time and position, so the calculation of this function is quite complex. In order to solve the problem, and as an approximation, many authors have estimated this factor by equating the surface temperatures of the bodies within the contact. This approximation was proposed many years ago by Blok [38], who assumed that the heat partitioning factor is a constant factor and that the contact is so perfect that the contact temperatures in both bodies are equal. This approximation may be expressed as:

$$T_{c\ seal} = T_{c\ counterface} \quad (67)$$

4.5.2 Comparison of the contact temperature distribution on concentric and eccentric seals. Case study.

In this section, the methodology presented above has been used to research on the effect of radial misalignments on the contact temperature distribution of elastomeric seals, in line with the topic of this thesis. To this aim, the methodology has been applied to a specific case study. In particular, the contact temperatures reached at the interface between the seal A (TPU) and the rod during the concentric and eccentric tests carried out in Chapter 3 are herein calculated.

For contact temperature calculations, the resulting friction forces measured during the sliding tests were used. In the case of the seals tested under concentric conditions, the contact temperature distribution will be uniform along seals; in the case of eccentric seals, by contrast, the temperature distribution will be non-uniform. Thus, for the eccentric mounting case, temperatures in opposite sections of the seal have been estimated. In particular, temperatures in the most compressed (section where the interference between the rod and the seal is maximum) and in the less compressed sections were calculated. The friction force distribution along the considered seal during the tests carried out under eccentric mounting conditions was estimated in section 3.8.3. In all the cases, steady-state friction force values were used for calculations. Regarding the contact widths, those values obtained from the numerical models of the seals under study were considered (Chapter 2).

In

In Table 17 a summary of the main data used for temperature rise calculations is shown:

| | |
|---|--|
| Resulting friction force, F_f | $F_f(\delta_r = 0mm) = 20N$ $F_f(\delta_r = 0.15mm) = 32N$ |
| Differential Friction force | $F_f(\delta_\varphi = \max) = 0.36N$ $F_f(\delta_\varphi = \min) = 0.17N$ |
| Contact width, $2b$ | $\delta_r = 0mm \rightarrow 1.25mm$ $\delta_r = 0.15mm \rightarrow$ for $\delta_\varphi = \max = 3.8mm$ / for $\delta_\varphi = \min = 1mm$ |
| Heat convection coefficient, h | 10 W/m °C (air-free convection) |
| Sliding velocity, v | 0.5m/s |
| Length of the seal cross section, l_s | 5mm |

Table 17: Main data used for temperature calculations.

4.5.2.1 Concentric conditions

The total heat flux generated as a result of the sliding between the seal and the rod under concentric conditions and at a velocity of 0.5m/s, has a value of 56589.9 W/m². Considering a static heat source relative to the seal, the following expression of the contact temperature was obtained applying the equations introduced in the previous section:

$$T_c = T_{amb} + 0.01178q_s \quad (68)$$

In the case of the rod, the heat source is in motion relative to it. Hence, in this case the following expression was obtained:

$$T_c = T_{amb} + 0.000712q_c \quad (69)$$

Equating the contact temperatures of both surfaces, it was calculated that in the concentric case the heat flux entering the seal has a value of 3225.4 W/m^2 , and the heat flux entering the steel rod a value of 53364.5 W/m^2 . Hence, it was found that the 94.3% of the heat generated due to frictional heating penetrates the steel part sliding against the seal.

Hence, when the seal and the rod are totally concentric, the maximum temperature reached at the contact of the seal under the considered operating conditions may be expressed as:

$$T_c = T_{amb} + 38 \text{ (}^\circ\text{C)} \quad (70)$$

4.5.2.2 Eccentric conditions, $\delta_r = 0.15\text{mm}$

$\delta_\phi = \text{max, maximum interference section}$

The total heat flux generated in the maximum interference section as a result of the sliding between the seal and the rod under eccentric conditions, and at a velocity of 0.5m/s , has a value of 47723.7 W/m^2 . This value was calculated considering a friction force value of 0.36N between this seal section and the rod, and a contact width of about 3.8mm , obtained from numerical simulations. For the seal, the following contact temperature expression was estimated considering that the heat source is stationary with respect to the seal section:

$$T_c = T_{amb} + 0.03612q_s \quad (71)$$

And the contact temperature at the surface of the moving rod may be expressed as:

$$T_c = T_{amb} + 0.00213q_c \quad (72)$$

Equating the contact temperatures of both surfaces, it was calculated that under eccentric conditions, when the rod to bore misalignment is of 0.15mm, the heat flux entering the maximum interference seal section has a value of 2658.7 W/m², and the heat flux entering the steel rod, a value of 45065 W/m². Hence, it was found that the 94.4% of the heat generated due to frictional heating enters the steel part in motion relative to the seal. This result is similar to that obtain for the concentric case since the calculations have been carried out on the basis that the heat partitioning factor is constant as assumed by Blok [38].

Thus, the maximum temperature reached at the contact between the most compressed section of the seal and the moving rod is:

$$T_c = T_{amb} + 96 \text{ } (^{\circ}C) \quad (73)$$

Comparing Equations (70) and (73), it may be concluded that mounting eccentricities influence considerably the temperature rise on seals due to frictional heating. In particular, in this case, the temperature rise on the most compressed section of the eccentric seal was found to be up to 58°C higher than the temperature estimated for the concentric case.

Moreover, considering an ambient temperature of +25°C, the resultant contact temperature has a value of +121°C. This temperature is slightly above the stable temperature limit of the seal A which is made in Thermoplastic Polyurethane (TPU). In particular, the stable temperature limit of the seal under study is +105°C. From the TGA and DSC curves

of the seal A (plotted in Figure 47 and Figure 48), it may be concluded that at +121°C the elastomer does not decompose, however, its chemical bonds may be altered.

$\delta_{\phi} = \min$, minimum interference section

In the minimum interference section, the total heat flux generated as a result of the sliding between the seal and the rod under eccentric conditions, and at a velocity of 0.5m/s, has a value of about 86800 W/m². For this calculation, it was considered a friction force value between the seal section and the rod of 0.17N, and a contact width of about 1mm, obtained from numerical simulations. The contact temperature at the surface of the minimum interference seal section is:

$$T_c = T_{amb} + 0.0095q_s \quad (74)$$

And the contact temperature at the surface of the moving rod may be expressed as:

$$T_c = T_{amb} + 0.00056q_c \quad (75)$$

Equating the contact temperatures of both surfaces, results showed that under eccentric conditions and for a rod to bore misalignment of 0.15mm, the heat flux entering the minimum interference seal section has a value of 4848.1 W/m², and the heat flux entering the steel rod a value of 81951.9W/m². Hence, in this case also the 94.4% of the heat generated enters the steel part in motion relative to the seal.

Thus, the maximum temperature at the contact between the less compressed section of the rod lip seal and the moving rod is:

$$T_c = T_{amb} + 46 \text{ (}^\circ\text{C)} \quad (76)$$

Hence, results showed differences of up to +50°C in the same seal under eccentric conditions.

4.5.3 Methodology validation

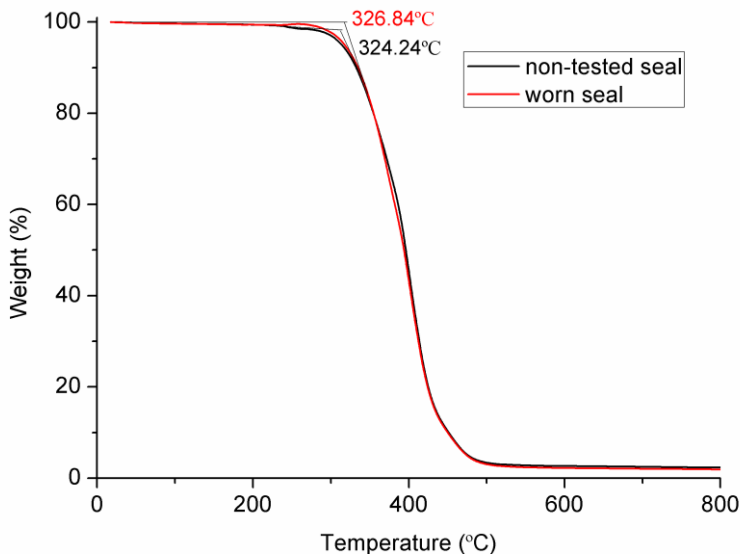
Due to the difficulties found to measure experimentally the contact temperature evolution during the friction tests carried out in Chapter 3, the validation of the methodology developed in this chapter is not an easy task. Nevertheless, in an attempt to validate somehow the results obtained in section 4.5.2, the surface of the tested seals has been characterized. In particular, the aim is to characterize the surface of the seal section subjected to the maximum interference where that according to calculations in the previous section, a steady contact temperature of approximately +121°C has been reached. For this purpose, TGA, DSC and FTIR spectroscopy analyses of a non-tested seal and of the worn seal surfaces were carried out. The TGA and DSC analyses were carried out through the same equipments and conditions described in section 3.2. The FTIR spectroscopy is a technique used to obtain the infrared spectrum of absorption or emission of a material. The analysis was carried out by means of a FT/IR-4700 Spectrometer (Jasco).

Thermal degradation of polymers occurs due to their molecular deterioration resulting from excessive temperatures and it usually involves changes in their molecular weight. Figure 99 presents a comparison between the characterization results of a non-tested seal

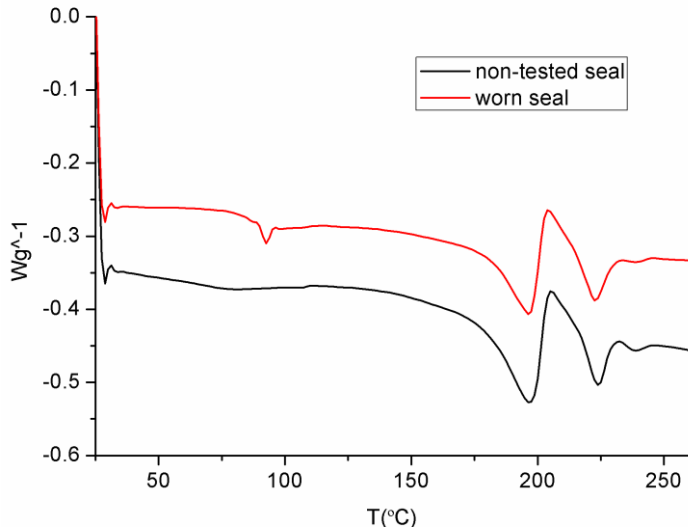
Chapter 4: Frictional heating on elastomeric seals during operation: An approach

section and the worn surface of the most compressed seal section. As can be seen, the results of the non-tested samples and of the worn samples are similar in all the cases. This means that the surface of the tested samples did not suffer any chemical degradation. In fact, in this case study, the maximum temperature predicted analytically (+121°C) is very close to the steady thermal limit of the TPU seal material and below the melting point (~178 °C), and therefore chemical degradation of the sample was not expected.

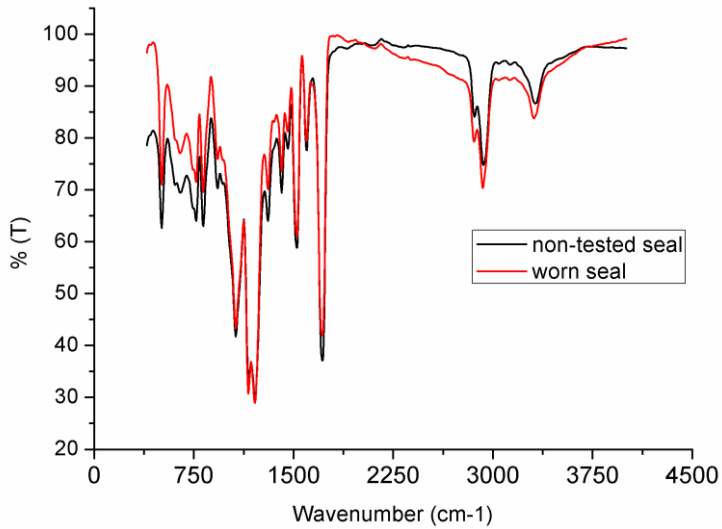
In section 5.2 some possible future lines for a better and more accurate validation of the methodology herein developed have been proposed.



(a)



(b)



(c)

Figure 99: (a) TGA, (b) DSC and (c) FTIR characterization results on the surface of the most compressed seal section.

4.6 Conclusions

In this chapter the study of the effect of rod to bore misalignments on the temperature rise of seals due to frictional heating has been addressed through the development of a specific methodology for contact temperature estimation on seals. The proposed methodology combines analytical models, thermo-mechanical properties of materials and experimental inputs, and it was developed in two stages.

In a first stage, an experimental investigation on the frictional heating phenomenon on elastomeric seals was carried out at laboratory scale. In particular, sliding tests were carried out on steel parts against TPU (Thermoplastic Polyurethane) and NBR (Nitrile Butadiene Rubber) elastomers, and the friction coefficient as well as the surface temperature evolution of the samples were measured through infrared thermography during the tests. Tests were carried at different sliding velocities, and using steel parts with different surface treatments and roughness, in order to study the effect of velocity and surface conditions (roughness and chromium-plating) on the temperature rise of elastomers. Moreover, experimental results were used to identify which of the existing analytical contact temperature models matches better the experimental measurements. Results demonstrated that there is a direct correlation between the evolution of friction and temperatures at the surface of elastomers as a result of an energy balance between the energy generated and dissipated as wear and heat. In all the cases results showed that under the same operating conditions the friction and temperature rise on the TPU samples was higher than that observed in NBR samples, whereas the latter's wear is considerably higher. Results

revealed that the sliding velocity considerably affects the temperature reached at the surface of the elastomers during sliding while the effect of steel-part roughness and treatment may be considered negligible under dry conditions. It was only found a clear dependency of temperature with surface conditions during the tests carried out on TPU samples at low sliding velocity. In this case, results showed that chromed plated cylinders led to higher temperature rises than the non-chromed ones. A good matching was found between the experimental and analytical results. In particular, it was identified the Tian-Kennedy analytical model for flash temperature calculations as the most appropriate model for calculations with the considered elastomers.

In a second stage, the knowledge gained from the experimental work was used to develop a procedure to estimate the contact temperatures on seals during operation. The methodology herein proposed may be of great interest for the industry considering the lack of applicable experimental techniques. In fact, given the low thermal resistance of elastomers, knowing the contact temperatures reached on seals during operation is of great interest for the industry. Nevertheless, contact temperature measurements on seals are still a challenge due to the fact that they are mounted in closed grooves difficult to access while moving relative to their mating faces. The methodology was applied to a specific case study in order to estimate the contact temperature distribution on eccentric seals, and afterwards the results were compared with those obtained for the concentric case. For calculations, the contact distributions obtained from the tri-dimensional eccentricity model developed in this thesis are mandatory inputs. Contact temperature calculations of eccentric seals revealed that mounting misalignments

lead to very irregular contact temperature distributions along seals. Moreover, it was found that small misalignments may result in relevant temperature rises on the most compressed sections of the seals that may lead to a premature failure of seals due to an accelerated wear or even to their thermal damage. In this specific case study, contact temperature differences of up to 50°C were predicted along the same seal.

4.7 References

- [1] Myshkin NK, Petrokovets MI, Kovalev AV. Tribology of polymers: Adhesion, friction, wear, and mass-transfer. *Tribology International* 2005; 38 (11-12): 910–921.
- [2] Bhushan B. *Modern Tribology Handbook*, In: Kennedy FE. Chapter 6: Surface Temperatures and Their Significance. CC Press LLC; 2001, p. 235-272.
- [3] Sutter G, Rank N. Flash temperature measurement during dry friction process at high sliding speed. *Wear* 2010; 268: 1237-1242.
- [4] Kalin M. Influence of flash temperatures on the tribological behaviour in low-speed sliding: a review. *Materials Science and Engineering: A* 374 2004, 390–397.
- [5] Kennedy FE, Frusescu D, Li J. Thin film thermocouple arrays for sliding surface temperature measurement. *Wear* 1997, 207(1-2): 46–54.
- [6] Heichal Y, Chandra S, Bordatchev E. A fast-response thin film thermocouple to measure rapid surface temperature changes. *Experimental Thermal and Fluid Science* 2005; 30(2): 153–159.
- [7] Kennedy FE, Tian X. The effect of Interfacial Temperature on Friction and Wear of Thermoplastics in the Thermal Control Regime. *Dissipative Processes in Tribology* 1994; Elsevier Science.
- [8] Lancaster JK. *Dry bearings: a survey of materials and factors affecting their performance*. Tribology 1973.
- [9] Kuhlmann-Wilsdorf D. What role for contact spots and dislocations in friction and wear?. *Wear* 1996; 200:8-29.

- [10] Wieleba W. The role of internal friction in the process of energy dissipation during PTFE composite sliding against steel. *Wear* 2005; 258: 870-876.
- [11] Ingram M, Reddyhoff T, Spikes HA. Thermal Behaviour of Slipping Wet Clutch Contact. *Tribology Letters* 2010.
- [12] Rowe K, Bennett A, Krick B, Gregory Sawyer W. In situ thermal measurements of sliding contacts. *Tribology International* 2013; 62: 208-214.
- [13] Kalin M, Vizintin J. Comparison of different theoretical models for flash temperature calculation under fretting conditions. *Tribology International* 2001; 34: 831-839.
- [14] Stolarski TA. *Tribology in Machine Design*. Oxford: Butterworth-Heinemann; 2000.
- [15] Guha D, Roy Chowdguri S. The effect of surface roughness on the temperature at the contact between sliding bodies. *Wear* 1996; 197: 63-73.
- [16] Tzanakis I, Conte M, Hadfield M, Stolarski TA. Experimental and analytical thermal study of PTFE composite sliding against high carbon steel as a function of the surface roughness, sliding velocity and applied load. *Wear* 2013; 303: 154-168.
- [17] Yevtushenko A, Ivanyk E. Effect of the roughness surface on the transient frictional temperature and thermal stresses near a single contact area. *Wear* 1996; 197:160-168.
- [18] Conte M, Pinedo B, Igartua A. Frictional heating calculation based on tailored experimental measurements. *Tribology International* 2014; 74: 1-6.

Chapter 4: Frictional heating on elastomeric seals during operation: An approach

- [19] Conte M, Pinedo B, Igartua A. Frictional heating calculations for polymers. In: Proceedings of the Surface Effects and Contact Mechanics XI Congress – Siena, Italy; 2013.
- [20] Frölich D, Magyar B, Sauer B. A comprehensive model of wear, friction and contact temperature in radial shaft seals. *Wear* 2014; 311(1-2): 71–80.
- [21] Jaeger JC. Moving sources of heat and the temperatures at sliding contacts. *J. Proc. Soc. N.S.W.* 1942; 76: 205-224.
- [22] Blok H. The dissipation of frictional heat. *Applied Scientific Research, Section A*, 1955; 5(2): 151-181.
- [23] Van der Heide E, Schipper DJ. On the Frictional Heating in Single Summit Contacts: Towards Failure at Asperity Level in Lubricated Systems. *Journal of Tribology* 2004; 126(2), 275.
- [24] Vick B, Furey MJ. A basic theoretical study of the temperature rise in sliding contact with multiple contacts. *Tribology International* 2001; 34(12), 823–829.
- [25] Stachowiak GW. *Wear: Materials, Mechanisms and Practice*. Wiley; 2005.
- [26] “The Ultimate Infrared Handbook for R&D Professionals”. Flir Systems Inc.
- [27] Bhushan B. Adhesion and stiction: Mechanisms, measurement techniques and methods for reduction. *J. Vac. Sci. Technol. B* 2003; 21 (6).
- [28] Stachowiak GW, Batchelor AW. *Engineering Tribology*. Butterworth-Heinemann; 2005.
- [29] “Hydraulic Seals-Linear”. Trelleborg Sealing solutions; 2011.

- [30] Kim H, Kim R-U, Chung K-H et al. Effect of test parameters on degradation of polyurethane elastomer for accelerated life testing. *PolymerTesting* 2014; 40: 13-23.
- [31] Conte M, Pinedo B, Igartua A. Role of crystallinity on wear behavior of PTFE composites. *Wear* 2013, 307(1-2): 81–86.
- [32] Kalin M, Vižintin J. High temperature phase transformations under fretting conditions. *Wear* 2001; 249(3-4), 172–181.
- [33] Tian X, Kennedy FE. Contact Surface Temperature Models for Finite Bodies in Dry and boundary Lubricated Sliding. *Journal of Tribology* 1993; vol. 115.
- [34] Tian X, Kennedy FE. Maximum and Average Flash Temperatures in sliding Contacts. *Journal of Tribology* 1993; vol. 116.
- [35] Kennedy FE, Lu Y, Baker I. Contact temperatures and their influence on wear during pin-on-disk tribotesting. *Tribology international* 2015; 82: 534-542.
- [36] Peter J. Blau. *Friction Science and technology: From concepts to applications*. Second Edition. STLE. CRC Press Taylor & Francis Group; 2009.
- [37] Laraqi N, Alilat N, de Maria JMG, Baïri A. Temperature and division of heat in a pin-on-disc frictional device-Exact analytical solution. *Wear* 2009; 266(7-8): 765–770.
- [38] Blok HA. Theoretical study of temperature rise at surfaces of actual contact under oiliness lubricating conditions. *Proc. General Discussion on Lubrication and Lubricants* 1937, I.Mech.E., London, 222-235.
- [39] Abdelbary A. *Wear of Polymers and Composites*. Woodhead Publishing, Elsevier; 2014.

Chapter 5: General conclusions & Future work

5.1 General conclusions

Understanding the wear mechanisms of rubber seals as well as predicting their life is a complex task. The main difficulty for building reliable life expectancy models lies in the wide variety of factors that influence the performance of seals (see Figure 100) as well as in the complexity of the physical phenomena occurring on the mating surfaces. Due to the lack of studies related to this issue, in this thesis the effect of misalignments on the performance of elastomeric seals has been studied in order to establish the cause-effect relationships between rod to bore misalignments and seal failure. In fact, even if misalignments are unavoidable, this topic has not been addressed so far. The material non-linearity as well as the need for estimating factors presenting high difficulty in being measured led to build a complex tri-dimensional eccentricity model for seals that enables calculating the contact force distribution on eccentric seals. Moreover, in this thesis it has been established a methodology based on this contact model in order to carry out a complete tribological characterization of seals, predicting the friction, wear and temperature distributions along eccentric seals. The model has been validated at each step through case studies of general industrial applications and through different test rigs, some of them specifically designed for this purpose. At the same time, the utility of the model for life expectancy considerations has been demonstrated

through those case studies considered. The research carried out within this thesis has demonstrated the large influence that rod to bore misalignments have on the tribological performance of seals.

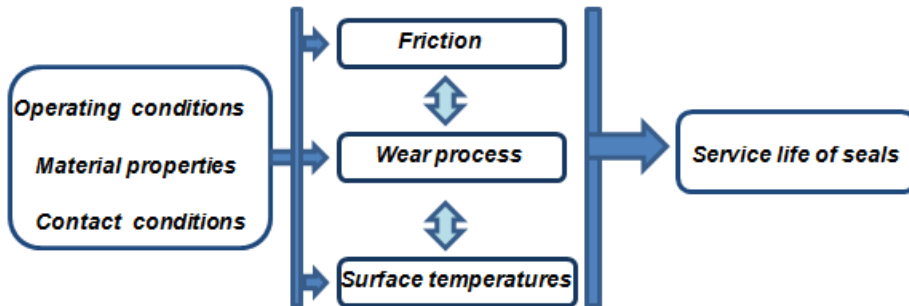


Figure 100: Factors affecting the service life of seals.

The model developed consists of a tri-dimensional analytical eccentricity model for seals that enables calculating the contact force distribution along seals as a function of rod eccentricity value. To the best knowledge of the author, it had not been published any analytical model for calculating the tri-dimensional contact force distribution on seals in bibliography before. Thus the methodology herein proposed is innovative and may be useful for design purposes, among others. The model developed includes normal reaction, tangential and friction forces, and it was formulated on the basis of a functional contact relation between the rod and the seal, and a geometrical interference model. Moreover, it was completed and adjusted by means of numerical results. In order to validate the tri-dimensional contact eccentricity model, a specific test rig was designed. For the specific case study considered, validation tests revealed that the contact model may predict the contact force distribution on seals with a mean approximate accuracy of 85%. Furthermore, through the experimental validation of the model, it was

demonstrated that the modelling procedure may be a ready-to-use and a useful tool for designers that avoids high computational costs and times associated to numerical 3D simulations. Furthermore, this methodology may be extrapolated to any seal geometry and size. It is thought that small discrepancies between analytical and experimental results may be due to the fact that the analytical model does not consider viscoelasticity or stick-slip regions, among others. Validation test results revealed that mounting misalignments lead to very irregular contact force distributions and contact areas along the seals. In fact, differences in contact forces between the most and less compressed sections of the eccentric seal depend on diverse factors such as the nominal gap or clearance between the bore and the rod, seal geometry and material.

In an attempt to determine the effect of rod to bore misalignments on seals operating under actual sliding conditions, experimental tests were carried out on complete seals under both concentric and eccentric controlled conditions. It was demonstrated through experimentation that rod to bore misalignments affect considerably the friction and wear generated during operation. Results revealed larger friction forces and worn volumes under eccentric conditions than under concentric ones, and very irregular wear patterns on eccentric seals. Furthermore, it was found that the seal material also plays an important role in this regard. Results showed that misalignments lead to larger wear rates of seals, and subsequently to a reduction in their service life. The calculations of the wear rates and friction force distributions were addressed applying the contact model. Thus, the model was validated and its utility demonstrated through the experimentation carried out under dynamic conditions.

The study of the effect of rod to bore misalignments on the temperature rise of seals due to frictional heating was addressed by the development of a specific methodology for contact temperature estimation on seals. The methodology herein proposed has been validated at laboratory scale at an early stage and subsequently applied for estimating the contact temperature field on eccentric seals. Given the low thermal resistance of elastomers, knowing the contact temperatures reached on seals during operation is of great interest for the industry. Nevertheless, contact temperature measurements on seals are still a challenge due to the fact that they are mounted in closed grooves and moving relative to their mating faces. Thus, the methodology developed in this work for contact temperature estimations which combines analytical models, thermo-mechanical properties of materials and some experimental data may be useful for the industry considering the lack of applicable experimental techniques. On the one hand, results revealed that the analytical equations to be applied for contact temperature calculations should be selected at random since the selection may depend on each specific application. Moreover, contact temperature calculations of eccentric seals revealed that mounting misalignments lead to very irregular contact temperature distributions along seals. Moreover, it was found that small misalignments may result in relevant temperature rises on the most compressed sections of seals that may lead to a premature failure of seals due to an accelerated wear or even to their thermal damage.

In general, this thesis has contributed to the research on the wear process of elastomeric seals by the development of a tri-dimensional contact model that has been applied to determine the effect of rod misalignments on the tribological behaviour of elastomeric seals.

Moreover, a methodology for a complete tribological characterization of seals has been developed, which may be extrapolated to other mechanical components.

5.2 Future work

In this work a contact tri-dimensional model has been developed, and used for wear rate calculations of seals as well as for prediction friction and temperature distributions of seals subjected to misalignments. Future research might be directed towards the development of an algorithm that enables predicting the tri-dimensional wear, friction and temperature distributions along elastomeric seals through the implementation of the contact model herein developed. Furthermore, a challenge for the future may be the application of the methodology herein developed to other seal types as well as to seals operating under fluid pressure.

Moreover, it is thought that there may be two possible lines in order to validate the methodology to estimate the contact temperature on complete seals. On the one hand, in an attempt to validate the methodology for contact temperature predictions the same tests herein developed on complete seals (Chapter 3) may be carried out but under more severe conditions i.e. at a higher sliding velocity so that contact temperatures above the stable thermal limit are reached. Another possibility may be to design a transparent tooling to contain the seals so that the temperatures at the contact or close to it may be captured through an infrared camera. In this second case, a direct validation of the methodology may be achieved.

Another challenge for the future may be the application of the methodology herein proposed for tribological characterization of seals to

other mechanical components (even those that entail metal-to-metal contact) in order to determine its applicability to other components.

Relevant publications of the author

- ❖ Pinedo B, Aguirrebeitia J, Conte M, Igartua A. Tri-dimensional eccentricity model of a rod lip seal. *Tribology International* 2014; 78: 68–74.
- ❖ Pinedo B, Conte M, Aguirrebeitia J, Igartua A. Effect of misalignment on a rod lip seal behavior. *WIT Transactions on Engineering Science* 2012; 76: 151-161.
- ❖ Pinedo B, Conte M at al. New high performance test rig for sealing systems characterization. In: *Proceedings of the 5th World Tribology Congress-Turin, Italy; 2013.*
- ❖ Laske S, Witschnigg A. New Developments in Polymer Composites research. In: Conte M, Pinedo B, Igartua A. Chapter 11: Effect of contact temperature on the tribological behavior of PTFE composites. *Nova publications; 2013, p. 279-300.*
- ❖ Conte M, Pinedo B, Igartua A. Frictional heating calculations for polymers. In: *Proceedings of the surface effects and contact mechanics XI congress-Siena, Italy; 2013.*
- ❖ Conte M, Pinedo B, Igartua A. Role of crystallinity on wear behaviour of PTFE composites. *Wear* 2013; 307: 81-86.

- ❖ Conte M, Pinedo B, Igartua A. Frictional heating calculation based on tailored experimental measurements. *Tribology International* 2014; 74: 1–6.
- ❖ Pinedo B, Hadfield M, Conte M, Igartua A. Experimental study of the frictional heating phenomenon on elastomers. In: *Proceedings of the surface effects and contact mechanics XII congress-Valencia, Spain*; 2015.

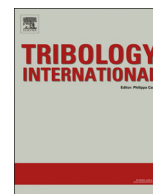
Appendix: Relevant Journal Publications



ELSEVIER

Contents lists available at ScienceDirect

Tribology International

journal homepage: www.elsevier.com/locate/triboint

Tri-dimensional eccentricity model of a rod lip seal

B. Pinedo^{a,*}, J. Aguirrebeitia^b, M. Conte^{c,d}, A. Igartua^a

^a Ik4- Tekniker, Tribology Unit, Iñaki Goenaga 5, Gipuzkoa, 20600 Eibar, Spain

^b ETSI-BILBAO, Department of Mechanical Engineering, University of Basque Country, Alameda Urquijo, 48013 Bilbao, Spain

^c Anton Paar, Rue de la Gare 4, CH-2034 Pesoux, Switzerland

^d EMPA, Laboratory of Materials and Nanostructures, Feuerwerkstrasse 39, CH-3602 Thun, Switzerland

ARTICLE INFO

Article history:

Received 7 November 2013

Received in revised form

28 April 2014

Accepted 1 May 2014

Available online 13 May 2014

Keywords:

Lip seal

Rod misalignment

Eccentricity

Contact force

ABSTRACT

In this work, an analytical tri-dimensional eccentricity model of a rod lip seal is presented. In the specific, a thermoplastic polyurethane (TPU) rod lip seal was considered. The analytical model was completed and adjusted by means of numerical results. Experimental tests on selected seals were carried out on a suitable test rig designed to measure reaction forces on seals as a function of rod misalignment. A cross validation between the analytical model and experimental results is provided. The model is used to calculate the contact force distribution on a seal when it is subjected to an eccentric mounting.

© 2014 Elsevier Ltd. All rights reserved.

1. Introduction

Lip seals are commonly used in many mechanical devices, such as pneumatic and hydraulic actuators, engines, machine tools and gas springs, among others. They are characterized by a sealing lip, also known as dynamic lip, properly designed to ensure the sealing and pumping mechanisms of a specific fluid under a wide range of working conditions. Moreover, the design of lip seals must reach a compromise between dynamic sealing and good lubrication [1].

The performance of a specific lip seal is affected by its geometry, the material and roughness of the seal and its counterparts, and its operating conditions. Lip seals provide a unidirectional sealing and their contact pressure profile under particular sealing conditions strongly depends on the lip angles at the air and fluid sides. Some designs may include two lips in the sealing area in order to enhance the sealing capability at low pressures and to avoid the entry of dirt from the side opened to the atmosphere.

In general, most of the lip seals available for reciprocating applications are made of polyurethanes (PU) and nitrile rubbers (NBR) due to the low cost and good performance of these materials. Both materials, however, have a limitation in temperature since their maximum operating temperature is about 100 °C. Furthermore, this temperature constraint involves a working velocity limitation of seals due to frictional heating phenomena

[2,3]. Thus, the main alternative in applications with high sliding velocity requirements is seals made of PTFE composites because of their thermal resistance and low friction properties. Regarding the roughness, both the asperities of the lip and the roughness of the counterparts play an important role in sealing operation [4–6].

Seals are mounted in grooves with a degree of interference in order to ensure an appropriate sealing at the interface. Hence, contact pressure distribution is one of the most important parameters to take into account when a specific seal is being designed. Unfortunately, measuring the contact pressure between a seal and its counterparts could be a difficult task. In order to measure static contact pressures, technologies such as photoelastic techniques [7], pressure film sensors [8,9], radial force integration techniques [10] and manganin wires [11], among others, have been widely used. In any case, however, there is not a standard technique or device useful to measure contact forces in a rod or piston seal regardless the seal size.

Seal failure is often the result of certain problems in a system. Radial overload due to rod misalignment, improper shaft preparation, overheating, lubricant failure and extrusion are some of the most common causes for seal failure. In most of the cases, a seal fails as a result of a combination of factors [12,13]. This work is focused on the study of the effects of an eccentric mounting on the contact force distribution of a seal. In fact, an eccentric mounting leads to an irregular distribution of contact pressure, which affects seal performance. Moreover, the interference stress field originated under eccentric mounting conditions of the rod tends to twist the seal in the groove. Lip seals, however, are quite resistant to spiralization due to their design itself. Furthermore, the capacity

* Corresponding author. Tel.: +34 943206744.

E-mail addresses: bihotz.pinedo@tekniker.es, bpinedoa@gmail.com (B. Pinedo).

Nomenclature

| | |
|------------------|---|
| δ_i | rod/seal interference at concentric position |
| δ_r | rod radial misalignment value |
| δ_φ | mounting interference of a differential seal section which forms an angle φ with the misalignment direction |
| φ | polar coordinate |
| e | nominal gap between the seal and the bore |
| r_m | average radius |
| r_i | average radius at concentric position |

| | |
|-----------|--|
| F_N | normal force between the seal and the rod |
| T | tangential force generated in the seal |
| F_f | friction force between the seal and the rod |
| μ | friction coefficient |
| F_r | contact force between the seal and the rod in radial direction |
| F_{md} | contact force between the seal and the rod in the misalignment direction |
| λ | value of φ at which the contact between the seal and the rod is lost |

of a specific seal subjected to an eccentric mounting to follow the rod depends on: the lip seal design, the material and any temperature effects on the resilience of elastomers [12].

Tasora et al. [14] presented a method for characterizing the deformation of an elastomeric seal under static conditions. They carried out experimental tests on a nitrile based rotating lip seal subjected to different radial loads. These results were used to calibrate a tri-dimensional finite element model by means of Mooney–Rivlin parameters and to introduce the most adequate contact conditions at different temperatures. Consequently, numerical models were used to study the effect of static interference, temperature and radial displacements on the contact force between the seal and the rod. In a previous work [15], our research group presented an initial idea of a modelling procedure for estimating the effects of an eccentric mounting of seals, based on contact forces. A TPU lip seal was analytically modelled by means of the linear elastic approach. Contact equations were formulated based on geometrical models designed for rolling bearings [16,17] and considering the effect of normal forces only.

In this work, an improved tri-dimensional eccentricity model of rod seals is presented. In fact, the enhanced model includes not only normal forces between the seal and the rod, but also tangential and friction forces generated due to rod misalignment. Hence, contact forces along a whole seal are analytically and numerically studied as a function of rod radial position. The main objective of this paper is to obtain a reliable analytical 3D rod radial misalignment model of a thermoplastic polyurethane (TPU) reciprocating lip seal. The main advantage of the modelling procedure is that it allows estimating the contact force distribution in the whole seal regardless of rod eccentricity. As a starting point, a quasi-static case has been analysed in the absence of any supply pressure, in order to separate the contribution of the preload and the fluid pressure to the resultant contact pressure. The hyper-elastic material was defined by means of a Mooney–Rivlin formulation. The model is based on the characterization of the seal as an ensemble of springs subjected to traction/compression.

The analytical model is completed and adjusted by combining a geometrical interference model with the results obtained from numerical simulations. Moreover, the model was validated by means of experimental tests carried out on a test rig designed for this purpose.

2. Experimental measurements

2.1. Experimental setup and specimens

A suitable test rig was designed and assembled to measure the resultant contact forces on seals when the rod is radially displaced (Fig. 1). Seals under test (1) are mounted in the test chamber (2), one on each cylinder end. The rod rests on a low friction and high

stiffness polymeric base (3). The cylinder rod (4) is vertically positioned in order to minimize the weight effects and it is fixed to the frame (5) through a couple of tension/compression load cells with an accuracy of ± 0.01 N (6). Misalignments are applied by means of two micrometric positioners (7) fixed to the frame. Cylinder position is controlled by means of a vertically guided probe located in a Tesa micro Hite manual measuring device (8), which has a resolution of $1 \mu\text{m}$.

Measurements were carried out on commercial rod lip seals, made of TPU (thermoplastic polyurethane), suitable for a 45 mm diameter rod (Fig. 2). Misalignment tests were performed at room temperature and in the absence of supply pressure. Before seal installation, a small amount of oil (0.1 ml) was applied on the contact surfaces. The cylinder bore was displaced in radial direction

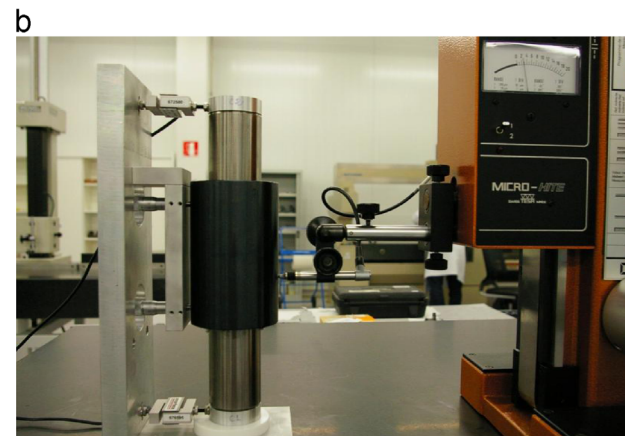
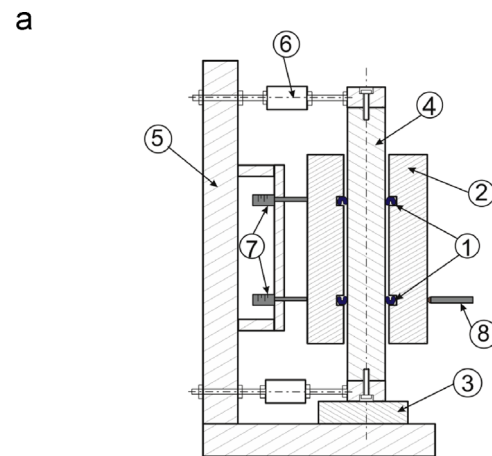


Fig. 1. Experimental setup for misalignment tests: (a) schematic view and (b) test rig assembly.

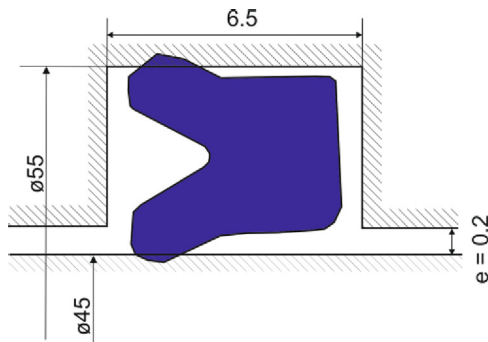


Fig. 2. Principal dimensions of the seal groove (in mm).

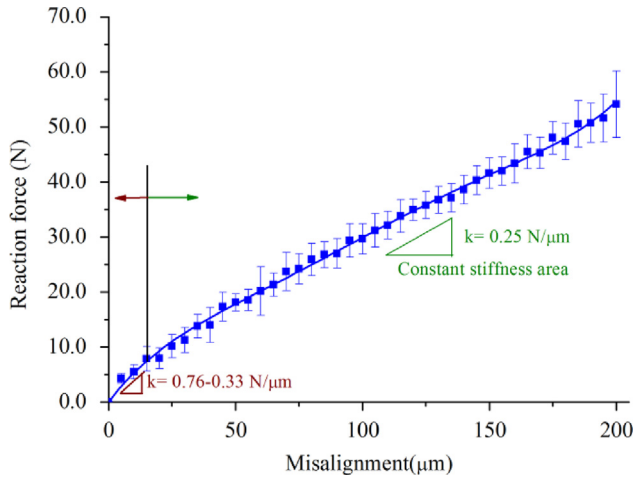


Fig. 3. Reaction force as a function of the applied misalignment.

only. Measurements were carried out under the controlled environment, 20 ± 1 °C.

At the beginning of the process, the cylinder rod was vertically placed adjusting the micro-positioners. Subsequently, consecutive known radial misalignment values were applied. The maximum applicable misalignment is limited by the nominal gap, e , with a value of 0.2 mm (Fig. 2). Misalignments were applied in steps of 5 μm up to the maximum allowed one. Reaction forces at each step are measured by means of the load cells after verifying and adjusting the vertical alignment of the cylinder. Measurements were repeated 3 times.

2.2. Experimental results

Fig. 3 shows the reaction force curves of a set of consecutive tests relative to the misalignment applied to the bore.

Results showed a good repeatability. As can be observed, the stiffness of the whole seal in the misalignment direction is not constant. In particular, the seal presents the stiffest response when the rod misalignment is about 5 μm ($K \approx 0.76 \text{ N}/\mu\text{m}$). Above that eccentricity value, the stiffness decreases exponentially until reaching a nearly constant value for rod misalignments $\geq 5 \mu\text{m}$ ($K \approx 0.25 \text{ N}/\mu\text{m}$). Curve tendency is in close agreement with the work of Tasora et al. [14].

3. Method

This section presents a procedure to build a tri-dimensional eccentricity model of seals. The model expresses the contact forces

between a seal and the mounting rod, as a function of rod misalignment.

The proposed analytical model has been completed and adjusted by means of numerical results. To this end, first of all, a plane model and a tri-dimensional model of the selected seal (Fig. 2) were developed and numerical simulations were carried out. Then, a geometrical interference model and contact equations were formulated.

It is particularly relevant to highlight that even if a quasi-static case is being studied, contact equations are based on the kinematic Coulomb model. Hence, this assumption involves a simplification of the problem that could be valid due to the nature of the tests, where an increasing load is monotonically applied to the rod. Moreover, the simplified model may be acceptable since the main goal of this work is to avoid time and expensive computational costs of a 3D numerical simulation.

The analytical model was validated by means of the experimental results presented in the previous section. Fig. 4 shows the flow chart of the modelling procedure.

3.1. Numerical model

A numerical study was performed to complete the analytical model described in detail in the next section. Both, a plane model and a tri-dimensional model of the rod lip seal were developed in an Ansys Workbench environment. Seal geometry was obtained by means of an optical microscope (Leitz, model Libra 200).

The plane strain model was built in order to obtain the functional contact relation between the rod and the seal, as a function of the seal section compression. Normal and tangential forces taken from simulations on the plane model are mandatory inputs to build the analytical model.

Two tri-dimensional models were developed in order to validate the analytical model results step by step: an ideal frictionless one, and another one which considers frictional contacts.

Both numerical models were built by means of quadrilateral and triangular elements. Due to the symmetry of the geometry and boundary conditions, only a half of the seal was modelled in the case of the tri-dimensional model. Moreover, this simplification allows reducing the computational cost of each simulation. The bi-dimensional model was composed of 1609 elements and the tri-dimensional one of 33,586 elements. The mesh used is the result of a number of analyses performed in order to determine

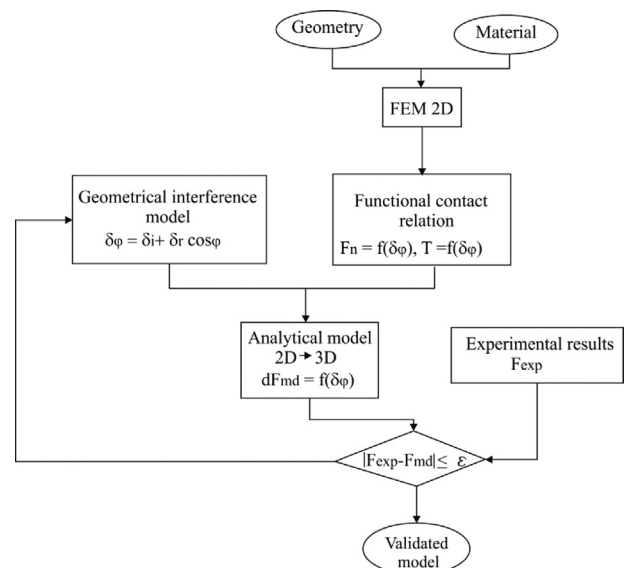


Fig. 4. Proposed process scheme.

the element sizes that do not produce significant variation in calculation precision. Fig. 6 shows the mesh generated in each case.

In both models, a surface to surface contact formulation was chosen to simulate both the seal/rod and the seal/groove contacts. Boundary conditions take into account friction at contact surfaces in order to constrain the free movement of the seal. During the experimental tests, contact surfaces of seals were lubricated before seal installation. Hence, these conditions were assumed for numerical simulations. The friction coefficients were set to 0.1 for both, the seal/rod and the seal/groove contacts [18].

The seal material, TPU, was considered incompressible, isotropic and hyperelastic. It was assumed that the compressive stress–strain curve is shown in Fig. 5. These data were obtained as a result of compression tests carried out in the universal testing machine Instron 3369. The hyperelastic material was defined by means of a second-order Mooney–Rivlin formulation employing the following coefficients: $C_{10}=1.98$ and $C_{01}=0.16$; these coefficients were obtained from the data provided by the manufacturers. The rod and the bore were considered rigid elements since polymer stiffness is much lower than that of steel.

The interference or penetration between the seal and its counterparts is about 1.47 mm under concentric mounting conditions. Due to the high mounting interference or preload values, seal mounting was simulated in some steps. First, a concentric mounting was simulated. Afterwards, boundary conditions allowed rod displacement just in the selected radial misalignment direction. Simulation procedure is shown in Fig. 7. Radial displacements were applied to the rod step by step, starting from a concentric position of the rod up to the maximum allowed displacement, e . The cylinder bore was considered totally static in radial direction.

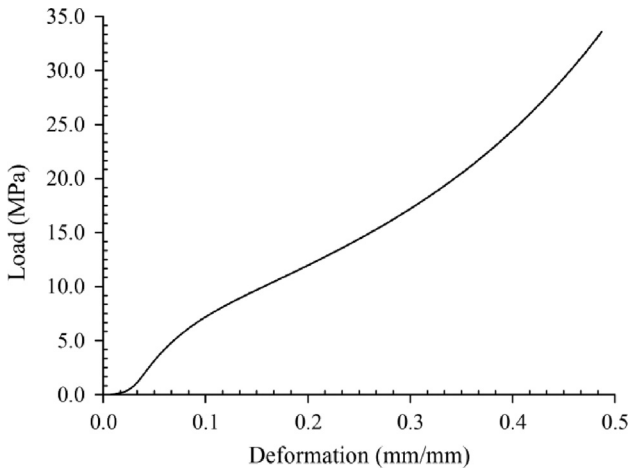


Fig. 5. Experimental compressive stress–strain curve of TPU.

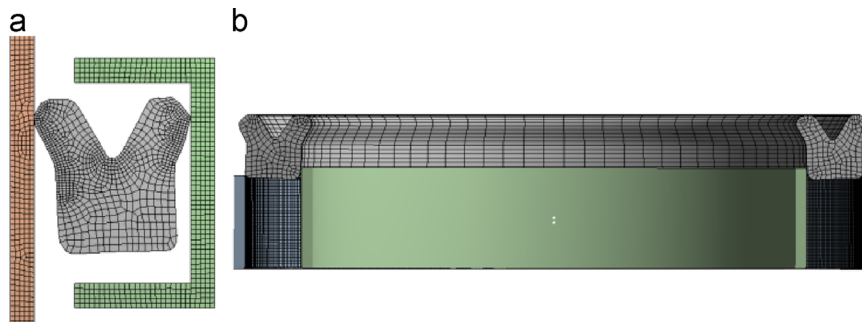


Fig. 6. Bi-dimensional (a) and tri-dimensional (b) models of the sealing system.

3.2. Analytical model

The analytical model consists of a geometrical interference model and contact equations based on numerical results. In a specific situation, where the rod and the bore are concentric, the interference is the same along the whole seal, δ_i . Nevertheless, when there is a radial eccentricity, contact conditions will be different on each section of the seal. Fig. 8 shows the geometrical interference between the rod and the seal for a specific misalignment δ_r . The polar coordinate φ defines the position of each seal section, relative to the rod misalignment direction.

In order to express the geometrical-interference field as a function of misalignment, the following geometrical-interference model is formulated:

$$\delta_\varphi = \delta_i + \delta_r \cos \varphi \tag{1}$$

As already mentioned, the applicable maximum misalignment, e , and the nominal interference values are determined by manufacturing tolerances. Depending on the relation between δ_i and δ_r , it is possible to distinguish two different cases. Fig. 9 shows the two possible interference configurations. If the radial misalignment value, δ_r , is lower than the interference between the seal and its counterparts at a concentric position, δ_i , all the seal sections will keep contact with the rod. Otherwise, contact between parts will be lost in a particular seal region.

Contact force between a specific seal section and the rod depends on its compression grade. Considering frictional contacts, it is possible to formulate a contact relation that integrates normal, tangential and frictional forces acting on a circumferential seal section. Fig. 10 illustrates the forces acting on a seal section when it is subjected to compression.

In this way, differential normal and tangential forces can be expressed as a function of the interference δ_φ as

$$F_N = f(\delta_\varphi) \tag{2}$$

$$T = f(\delta_\varphi) \tag{3}$$

So the forces acting on a seal section are

$$dF_N = F_N(\delta_\varphi)ds = F_N(\delta_\varphi)r_m d\varphi \tag{4}$$

$$dT = T(\delta_\varphi) \tag{5}$$

$$dF_f = \mu \left(dF_N - 2dT \sin \left(\frac{d\varphi}{2} \right) \right) \tag{6}$$

where μ is the friction coefficient between the rod and the seal. As previously mentioned, Eq. (6) is formulated adopting a simplified contact model which takes into account Coulomb's friction model.

The contact force between the sealing lip and the rod in radial direction can be written as

$$dF_r = dF_N - 2dT \sin \left(\frac{d\varphi}{2} \right) \tag{7}$$

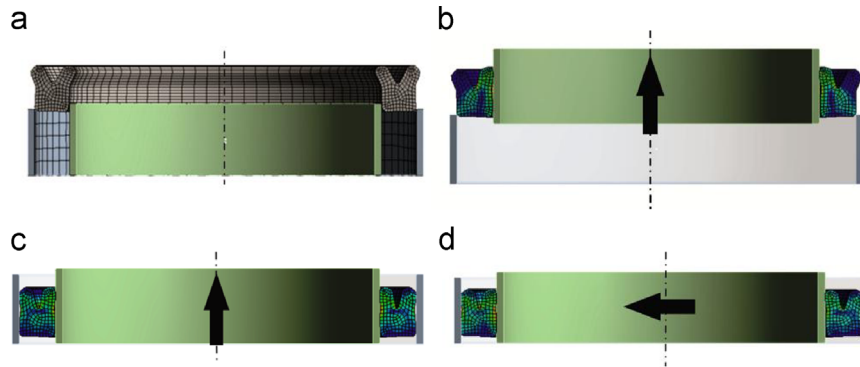


Fig. 7. Simulation procedure of the seal: (a)–(c) mounting and (d) rod misalignment.

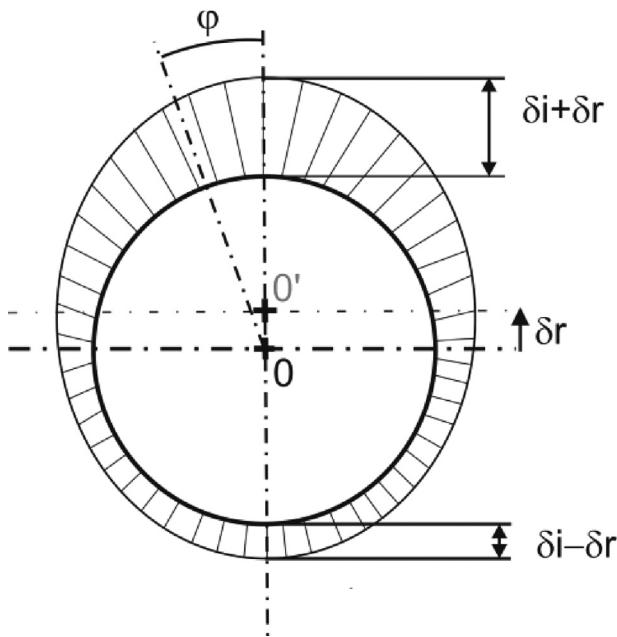


Fig. 8. Geometrical interference model.

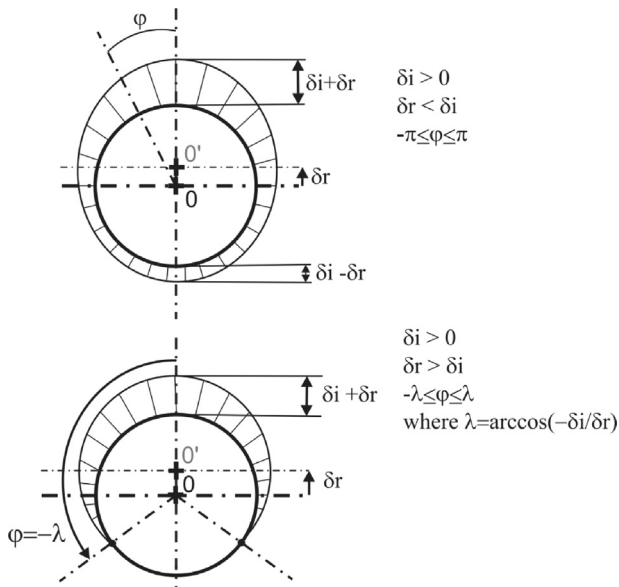


Fig. 9. Possible interference configurations.

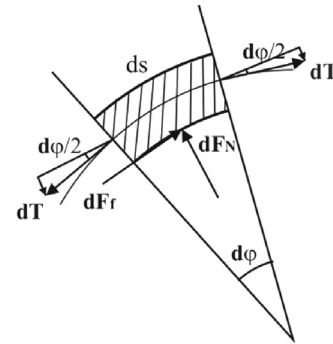


Fig. 10. Forces acting on a circumferential section of the seal.

And assuming that $\sin(d\varphi/2) \approx d\varphi/2$,

$$dF_r = (F_N(\delta_\varphi)r_m - T(\delta_\varphi))d\varphi \quad (8)$$

Considering a frictional contact between the rod and the seal, resultant contact forces acting on a seal section can be expressed in the misalignment direction as

$$dF_{md} = dF_r \cos \varphi + dF_f \sin \varphi \quad (9)$$

$$dF_{md} = (F_N(\delta_\varphi)r_m - T(\delta_\varphi))(\cos \varphi + \mu \sin \varphi)d\varphi \quad (10)$$

Resultant contact load on the whole sealing lip can be calculated by integrating Eq. (9). If $\delta_i > \delta_r$, the total load supported by the sealing lip can be expressed in the misalignment direction as

$$F_{md} = 2 \int_0^\pi (F_N(\delta_\varphi)r_m - T(\delta_\varphi))(\cos \varphi + \mu \sin \varphi)d\varphi \quad (11)$$

Eq. (12) expresses the total contact force in the misalignment direction when $\delta_i < \delta_r$

$$F_{md} = 2 \int_0^\lambda (F_N(\delta_\varphi)r_m - T(\delta_\varphi))(\cos \varphi + \mu \sin \varphi)d\varphi \quad (12)$$

The contact radius between the seal and the rod r_m depends on φ and it is measured from the rod centre, O. Under concentric conditions, the value of the average radius is the same for every section, r_i . When the rod is misaligned, the contact radius at each section can be calculated as

$$r_m = r_i + \delta_r \cos \varphi \quad (13)$$

In this work, the maximum admissible rod misalignment e , determined according to manufacturer's drawing, is 0.2 mm and

the interference δ_i is 1.47 mm. Hence, the interference configuration corresponds to $\delta_i > \delta_r$.

4. Results and discussion

At first, plain strain simulations were carried out in order to develop an analytical model able to reproduce the lip seal behaviour. Simulation results are shown in Fig. 11. A relevant aspect of the results is that seal stiffness of the lip seal varies considerably with compression. Furthermore, the stiffness of a cross section of the studied seal can be divided in two regions where it remains nearly constant: a low stiffness region ($K \approx 0.58$ N/mm) and a high stiffness region ($K \approx 6\text{--}11$ N/mm). It is important to highlight that a sudden change in seal stiffness occurs for seal compression values nearby the nominal interference δ_i .

In this study, the area of interest is bounded by the maximum and minimum possible interference values i.e. by $\delta_i + e$ and $\delta_i - e$, respectively (Fig. 11). The objective is to express analytically normal forces and tangential forces in this area, and to introduce these expressions in Eq. (10). In order to fit the data points of the forces by the most appropriate function, R -squared correlation was used. The closer the R^2 coefficient to 1, the more accurate the fitting. In this case, both force curves were fitted by a four degree polynomial. These fittings were considered acceptable since they led to R^2 values of 0.997 in both cases.

Fig. 12 shows radial contact forces along the seal vs. different eccentricity values. It can be concluded that different rod radial misalignment values result in very different contact force distributions. Contact force variations in the lip of the loaded half-seal side are considerably bigger than variations in those sections in the opposite side. For a rod subjected to the maximum allowable interference, the maximum contact force value could even triple the minimum one. This fact involves an irregular wear pattern and temperature distribution, and a subsequent seal life reduction that may be very significant.

Substituting the geometrical interference model defined by Eq. (1) and integrating results for the whole seal as described in Section 3, resultant contact forces along the whole seal can be calculated regardless of rod eccentricity. Fig. 13 shows resultant contact forces in the misalignment direction, numerically and analytically calculated considering different contact models: both frictionless and frictional contacts, with and without introducing tangential effects in the analytical model (curves A–F). Results showed that tangential and frictional forces play an important role. The effect of friction forces is to overload the seal whereas

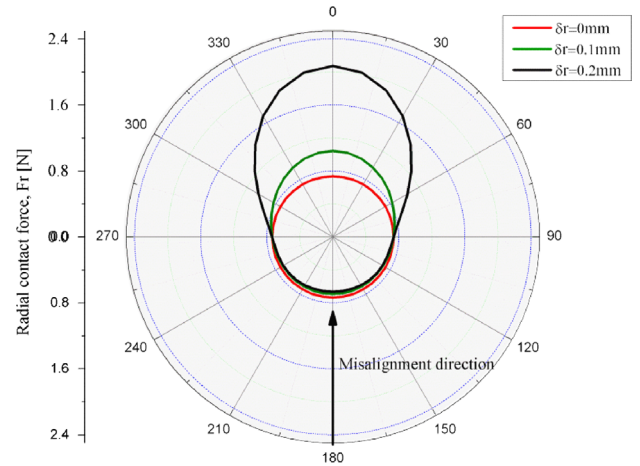


Fig. 12. Radial contact forces in the sealing lip as a function of circumferential position and rod eccentricity value.

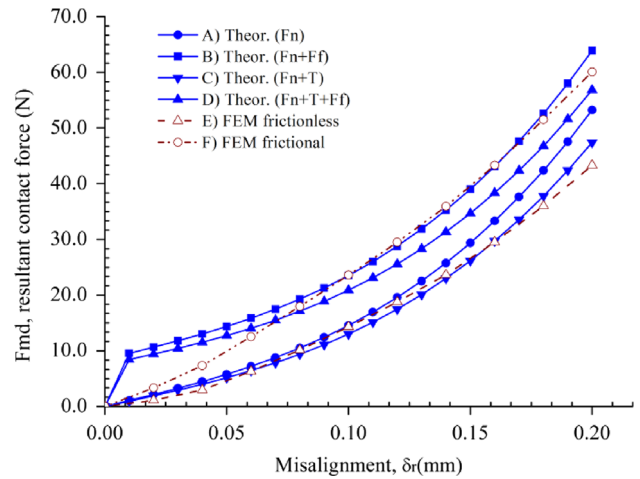


Fig. 13. Analytically (Theor.) and numerically (FEM) obtained contact forces vs. misalignment.

tangential forces tend to decrease resultant contact forces. Good matching was found between numerical results (E) and analytical results for an ideal frictionless sealing system (C). Thus, it can be concluded that tangential forces acting on the seal are mandatory inputs to complete the analytical model; they should not be ignored. By contrast, numerical simulation results for a frictional contact model (F) and analytical results considering friction between counterparts (D) did not show a good correlation at low eccentricity values. Furthermore, as seen in Fig. 13, numerical results underestimate contact forces for rod misalignments lower than 0.07 mm. Tasora et al. [14] found that radial shaft seals show a high slope ramp at low radial displacements. Hence, it is thought that the major sources of discrepancies between results at low misalignment values could be: the simulation procedure itself, followed to solve the initial preload of the seal (Fig. 7), and/or the omission of stick-slip effects.

Experimental results were used in order to validate the analytical model proposed in this work. It was found a good correlation between experimental and the analytical results of the model that includes tangential and frictional effects, i.e. frictional contacts, should be assumed. Fig. 14 shows a comparison between experimental, numerical and analytical results, (D), and it also presents the error between analytical and experimental results in absolute terms. The maximum difference between the analytical

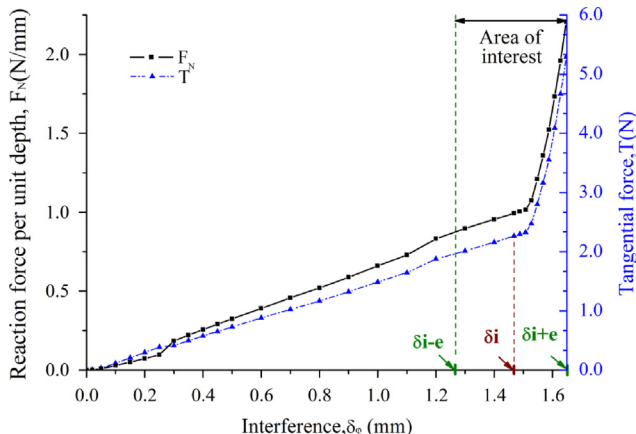


Fig. 11. Reaction and tangential forces in a seal section as a function of mounting interference or compression.

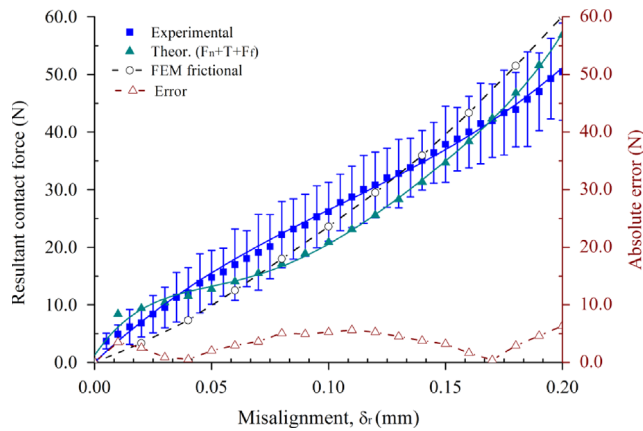


Fig. 14. Comparison between experimental, numerical and analytical results.

and experimental results in absolute terms is approximately 6.4 N, which occurs for the highest misalignment.

5. Conclusions

A procedure to develop an eccentricity tri-dimensional analytical model of seals was herein presented. Aim of this work was to study the effect of an incorrect mounting on seals. In this case, an eccentricity model of a rod lip seal built in TPU was developed. Results showed that small rod mounting eccentricities lead to significant changes under contact conditions between the rod and the seal. Moreover, an eccentric mounting of just 0.2 mm results in a very irregular contact force distribution, where the maximum contact forces could even triple the minimum ones. Thus, although lip seal geometry itself facilitates its adaptation to low eccentricities, an increment of contact forces involves a reduction of the expected seal life. This fact evidences the importance of taking into account possible eccentricity effects when studying specific sealing systems.

The built model includes: a geometrical interference model, and tangential, friction and normal reaction forces between the seal and the rod. A static case was considered in the absence of supply pressure. A satisfactory matching was found between experimental and analytical results. Hence, this method could be a viable tool to calculate the contact force distribution on seals in order to avoid high computational costs and long times of numerical simulations. Moreover, the procedure herein presented can be applied to other seal geometries and materials, and it could be useful for design purposes.

It is thought that the main cause of differences in results could be that the analytical model does not include properties such as viscoelasticity and stick-slip effects, very important when working with elastomeric materials. Future developments will address

friction and accelerated life tests carried out on a suitable test rig [19]. Actual working conditions of lip seals will be reproduced including reciprocating motion, supply pressure and a specific mounting misalignment. Possible effects of temperature due to frictional heating will be also studied.

Acknowledgements

The authors would like to thank their colleagues Peio Orbea for measuring the geometry of the seal and Juan Carlos Rodriguez for his help with the design and manufacturing of the experimental test rig. Acknowledgements are also addressed to Azol-Gas for supplying us the cylinder components.

References

- [1] Müller HK, Nau BS. Fluid sealing technology: principles and applications. New York: Marcel Dekker; 1998.
- [2] Conte M, Pinedo B, Igartua A. Frictional heating calculations for polymers. In: Proceedings of the surface effects and contact mechanics XI congress—Siena, Italy; 2013.
- [3] Conte M, Pinedo B, Igartua A. Frictional heating calculation based on tailored experimental measurements. Tribol Int 2014;74:1–6.
- [4] Salant RF, Shen D. Hydrodynamic effects of shaft surface finish on lip seal operation. Tribol Trans 2002;45:404–10.
- [5] Nikas GK. Eighty years of research on hydraulic reciprocating seals: review of tribological studies and related topics since the 1930s. J Eng Tribol: Proc Inst Mech Eng Part J 2010;224:1–23.
- [6] Huang Y, Salant RF. Simulation of hydraulic rod seals with a plunge-ground rod. In: Proceedings of the 5th world tribology congress—Turin, Italy; 2013.
- [7] Bignardi C, Manuella A, Mazza L. Photoelastic measurements and computation of the stress field and contact pressure in a pneumatic lip seal. Tribol Int 1999;32(1):1–13.
- [8] Lee CY, Lin CS, Jian RQ, Wen CY. Simulation and experimentation of the contact width and pressure distribution of lip seals. Tribol Int 2006;39:915–20.
- [9] Belforte G, Conte M, Bernetto AM, Mazza L, Visconte C. Experimental and numerical evaluation of contact pressure in pneumatic seals. Tribol Int 2009;42:169–75.
- [10] Belforte G, Conte M, Mazza L, Raparelli T, Visconte C. Test rig for rod seals contact pressure measurement. WIT Trans Eng Sci 2010;66:107–14.
- [11] Goerres M. Friction force and leakage test rigs for the development of piston rod seals. Ölhydraul Pneum 2003;47(1):1–23.
- [12] Flitney RK. Seals and sealing handbook. 5th edition. Oxford: Elsevier; 2007.
- [13] The Simmerring. Basics for preventing damage, Freudenberg Simrit, 2004.
- [14] Tassara A, Prati E, Marin T. A method for the characterization of static elastomeric lip seal deformation. Tribol Int 2013;60:119–26.
- [15] Pinedo B, Conte M, Aguirrebeitia J, Igartua A. Effect of misalignment on a rod lip seal behaviour. WIT Trans Eng Sci 2012;76:151–61.
- [16] Aguirrebeitia J, Abasolo M, Avilés R, Fernandez de Bustos I. Theoretical calculation of general static load-carrying capacity for the design and selection of three row roller slewing bearings. Mech Mach Theory 2012;48:52–61.
- [17] Aguirrebeitia J, Avilés R, Fernandez de Bustos I, Abasolo M. Calculation of general static load-carrying capacity for the design of four-contact-point slewing bearings. J Mech Des 2010;132(6):064501–6.
- [18] Conte M. Interaction between seals and counterparts in pneumatic and hydraulic components [Ph.D. thesis]. Politecnico di Torino; 2008.
- [19] Pinedo B, Conte M et al. New high performance test rig for sealing systems characterization. In: Proceedings of the 5th world tribology congress—Turin, Italy; 2013.



Role of crystallinity on wear behavior of PTFE composites[☆]



Marcello Conte^{*}, Bihotz Pinedo, Amaya Igartua

Tribology Unit, IK4-TEKNIKER, C/Inñagi Goenaga 5, 20600 Eibar, Spain

ARTICLE INFO

Article history:

Received 20 May 2013

Received in revised form

9 August 2013

Accepted 12 August 2013

Available online 30 August 2013

Keywords:

PTFE

Wear

Crystallinity

Polymer

Tribology

ABSTRACT

Tribological behavior of PTFE composites is well known to be affected by factors depending mainly by matrix and filler properties. However, the mechanism taking place has not still been fully explained. In this work, the attention was focused on the variation of crystallinity due to the presence of fillers and it was connected with the transition phases to which the PTFE is subjected. In particular, a simplified frictional heating calculation method was used for estimating the maximum contact temperature and results were connected with differential scanning calorimetry analyses (DSCs).

© 2013 Elsevier B.V. All rights reserved.

1. Introduction

Reduction of lubricants is a goal of great importance in many tribological applications nowadays. One of the materials most used to this purpose is Polytetrafluoroethylene (PTFE), well known for its tribological characteristics, in particular its low friction, the quasi-absence of sticking effect, its resistance to high temperatures and good compatibility with several chemical products.

These semicrystalline polymers have a microstructure with a specific orientation of the chains which is formed during the final steps of the production process and affects their ultimate tribological properties.

In the market of polymers for tribological applications composites and nano-composites are continuously added for satisfying requests coming from industry regarding enhanced mechanical properties.

New (nano)-composites are continuously introduced on the market to meet industry demands.

One of the main bottle necks of these materials is their thermal resistance. Most of them only have a limited resistance to heat, causing a reduction in life time.

Starting from a previous study carried out by the authors [1] and considering the results of Tzanakis et al. [2] this paper deals with the correlation between crystallinity and tribological behavior of PTFE composites. PTFE exhibits complex crystalline phase behavior: at atmospheric pressure three crystalline structures

(phase II, IV and I) are observed with transition between them occurring at 19 and 30 °C (Fig. 1), the first few working cycles in practical situations.

Brown, Dattelbaum [3] found that crack propagation in PTFE is strongly phase dependent with a brittle-to-ductile transition in the crack propagation behavior associated with the two room temperature phase transitions.

According to Persson's investigation [4], due to the strong temperature dependence of viscoelastic properties of rubber-like materials, local temperature calculation should be considered in order to explain the frictional behavior of the tribo-pair, so an estimation of flash temperature at the polymer to metal contact surface is herein proposed for a better understanding of the tribochemical and tribophysical phenomena occurring at the contact.

Aim of this study is to explain the link between structural information and wear mechanism using considerations on frictional heating at the contact surface formulated earlier by the authors [5]. The structural state of the polymer (its crystallinity) not only affects its physical properties such as density, permeability and thermal characteristics [6], but also its tribological properties, and adds information to the transfer film material concept, investigated thoroughly by Bahadur [7].

The introduction of fillers into a crystalline polymer matrix, changes many factors simultaneously, which have dissimilar dependence on composition and filler characteristics. This makes it very difficult to determine the dominating factor affecting the polymers tribological characteristics. In this work Differential Scanning Calorimetry is used which was demonstrated earlier by Wang et al. [8] to be useful for studying crystallization kinetics of polymers.

[☆]This paper was presented at the 2013 World Tribology Congress.

^{*} Corresponding author. Tel.: +34 943256900; fax: +34 943202757.

E-mail addresses: marcello.conte@tekniker.es, conte.marcello@gmail.com (M. Conte).

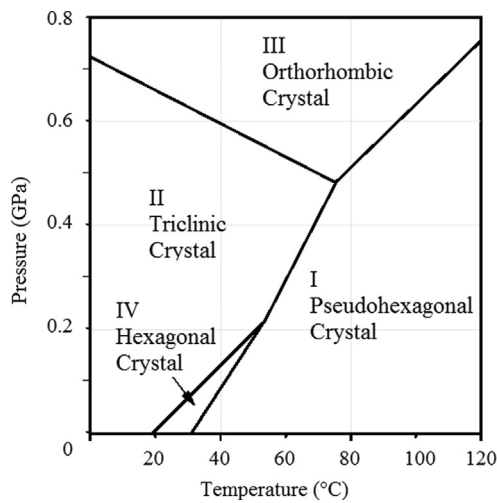


Fig. 1. PTFE phase diagram at low pressure.

Table 1
PTFE samples relative crystallinity.

| Sample | ΔH_f (J/g) | Relative crystallinity (%) | Mass loss (mg) | Wear specific energy (MJ/g) |
|------------------------------|--------------------|----------------------------|----------------|-----------------------------|
| (1) PTFE | 27.80 | 68 | 5.3 | 1.8 |
| (2) PTFE+25 wt% carbon | 19.09 | 47 | 0.4 | 26.5 |
| (3) PTFE+60 wt% bronze | 11.73 | 29 | 13.0 | 1.1 |
| (4) PTFE+25 wt% glass fibers | 18.91 | 46 | 0.7 | 14.2 |

A better understanding of the material behavior could provide important input to experimental testing of components and integrating knowledge coming from laboratory tests [9–11].

2. DSC analysis and tribological tests

Four PTFE samples were considered (Table 1). In particular, carbon and bronze fillers enhance the load carrying capacity of the virgin PTFE but crystallinity is much different. Crystallinity of glass fibers composite is similar to crystallinity of carbon filled PTFE but the former has lower load carrying capacity and the latter higher thermal conductivity. The PTFE samples were prepared by compression molding of powder mixtures of PTFE and filler, followed sinterization and cooling. The PTFE dispersion has a median particle size of 0.25 μm ; the average carbon particle diameter is about 10–25 μm ; the average bronze particle size is about 25 μm ; the glass fibers have a diameter of about 5 μm and a length of about 90–120 μm . The density of the PTFE composites is in the range 2.15–2.20 g/cm^3 , the density of PTFE with bronze is about 3.8–4.0 g/cm^3 . PTFE composites with carbon, bronze and glass fibers fillers were chosen in order to evaluate the effect of their presence and their different ways of acting. Optical microscopy was used for investigating the worn surface.

2.1. DSC analysis

Differential Scanning Calorimetry (DSC) was used to study the thermal transition of the polymers and to evaluate the crystallinity of the semi-crystalline materials. The dimension of the crystals depends on the mobility of the polymeric chains. This mobility is higher at higher temperatures, and is influenced by the content of

fillers and their nature. The test samples were warmed up and cooled down again from 30–350 $^{\circ}\text{C}$ with a cooling/heating rate of 10 $^{\circ}\text{C}/\text{min}$ in inert environment of N_2 .

2.2. Tribological tests

The PTFE composites (sample dimensions: longitude 18 mm, length 14 mm, width 5 mm) were tested in sliding contact against a quenched tempered CrVNiMo rod (15 mm diameter, 22 mm length) of HRC $> 60 \pm 1$ and surface texture according to the standard D6425-02 as represented in Fig. 2. A PTFE sample (1) is mounted on a frame (2) and loaded by an axially sliding rod (3) supported and fixed by two holders (4) on which normal constant load W is applied and transmitted to the axis of the rod. The holders and a couple of screws avoid rotation of the rod around its axis. The system is located in a climate chamber in order to set temperature and humidity percentage. Normal load was set on 50 N for the first 30 s and then at 100 N, 60 Hz frequency and 2 mm stroke for each sample. Coefficient of friction (CoF) was recorded at regime condition for 30 min; each test was repeated 2–3 times. Corresponding frictional energy was estimated analytically and reported vs mass loss.

3. Results and discussion

Fig. 3 represents the trends of the friction coefficients along the time. At regime, formation of a transfer film on the rod causes a relatively steady friction coefficient for all the tested grades, indifferent to the presence of fillers.

As previously explained by the authors in [5] the transfer film, and consequently the friction properties, are greatly influenced by the prevailing interfacial temperature and also by the kinematics of the relative motion between the two bodies.

The temperature at the interface between rubbing bodies is known as “surface conjunction temperature”; the calculation of this temperature is possible by applying the laws of energy conservation and heat transfer. In fact, most of the energy dissipated during the process of friction is converted into heat [12] resulting in local temperature rise called “flash temperature” that could be divided into transient and steady state flash temperature rise. As reported by Bowden and Tabor [13] in dry contacts the transient flash temperature may become larger than the steady state component. The flash temperature calculation method was formulated firstly by Block [14] and then improved by Jaeger [15] and Archard [16]. It provides a set of formulae for various velocity ranges and contact geometries and it is based on the following assumptions: (1) a planar source of heat is considered; (2) a steady state condition is attained; (3) the thermal properties of the bodies do not change with temperature; (4) the coefficient of friction is known and reaches a steady value.

A well-defined friction dependent heat source at the contact between the two bodies in stationary condition is herein considered suitable. The component of energy lost in deformation of the bodies can be considered negligible due to the high mobility of the polymeric chains, and an appropriate test configuration (like high velocity reciprocating movement on a short stroke) could avoid the calculation of the Peclet number [14]. Furthermore, the experimental curve of the coefficient of friction can be used in the calculation allowing involving a direct correlation with the work done by the friction force, expressed as:

$$E = Wv\mu(t) \quad (1)$$

where μ is the coefficient of friction, W the normal load and v the sliding velocity. The contact temperature can be then described as

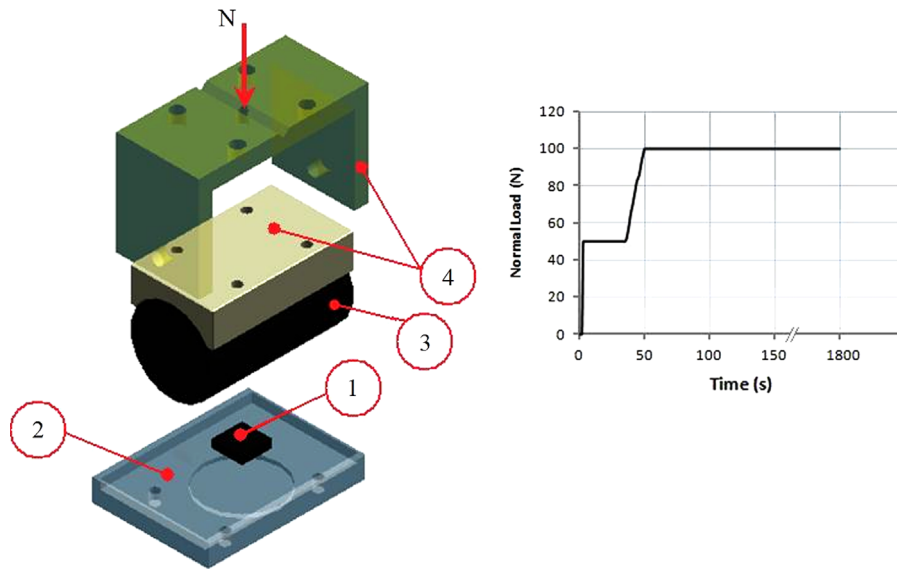


Fig. 2. Test rig configuration.

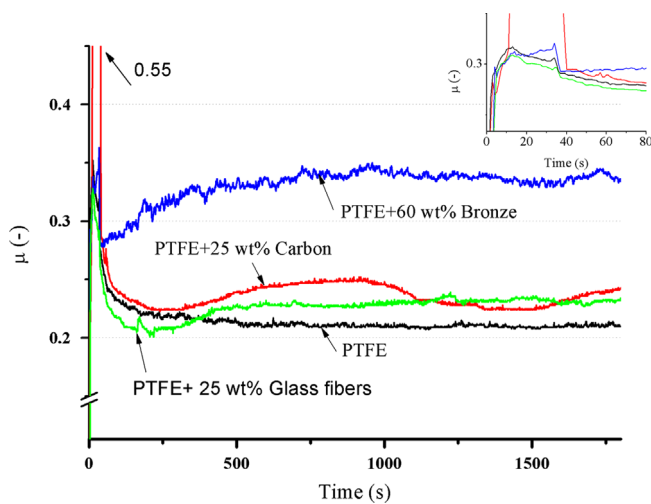


Fig. 3. Coefficient of friction along the tests.

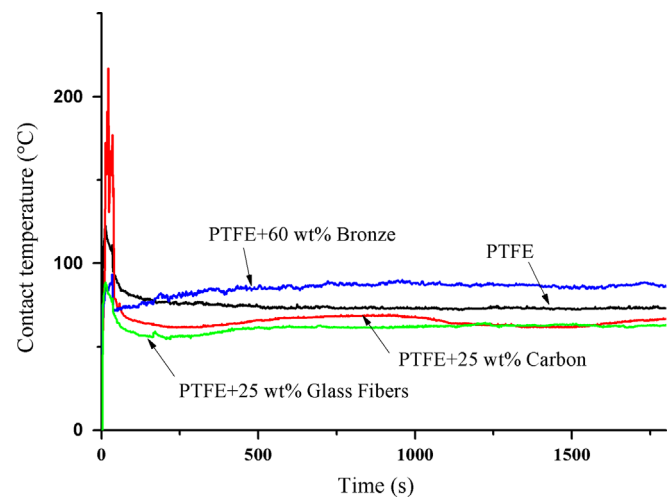


Fig. 4. Calculated contact temperature.

function of the time by:

$$T_{f \max}(t) = \frac{2E(t)}{KA} \sqrt{\frac{2\chi b}{\pi A}} \quad (2)$$

where E is the frictional energy (work done by the friction force), K is the thermal conductivity, χ the thermal diffusivity, A the contact surface (the cylindrical sector of the contact zone at the end of the test, being not reliable to measure or to hypothesize its evolution over the time) and $2b$ the contact width. The following assumptions are made: (a) a well-defined friction dependent heat source at the contact between the two bodies in stationary condition is considered as suitable approximation of the real situation; (b) the component of energy lost in deformation of the bodies can be considered negligible due to the high mobility of the polymeric chains, and an appropriate test configuration (like high velocity reciprocating movement on a short stroke) could avoid the calculation of the Peclet number; (c) the experimental curve of the coefficient of friction can be used in the calculation, having as result a direct correlation with the work done by the friction force; (d) thermal properties are considered constant (it was shown by the authors in [17] that non-constant thermal properties only lower the running in the temperature calculation). This matter will be investigated in more depth elsewhere.

Maximum surface temperature is then calculated with the following equation:

$$T_{\text{contact}} = T_{\text{bulk}} + T_{f \max} \quad (3)$$

In the first few seconds of the experimental tests, temperature increases rapidly, reaching the transition point where the material converts into a pseudo-hexagonal disordered phase from a partially ordered hexagonal phase. After this initial rise, temperature drops again and settles somewhere around 50–100 °C as can be seen in Fig. 4.

PTFE fails along weak intermolecular bonds due to the minor temperature rise which involves slippage of crystalline formations of the bond structure.

In other words, temperature is quite stable as equilibrium is reached between the heat dissipated and the heat generated. As a consequence, the carbon-to-fluorine bonds, which have high bond dissociation energy, are broken.

The energy that is generated as a consequence of the frictional contact can be dissipated (conversion to heat, vibration, material deformation, and new surface creation) or stored into the tribosystem. Therefore, materials exhibiting the same friction coefficient can have different wear rates if the energy is partitioned differently between and within the materials. Both friction coefficient and wear

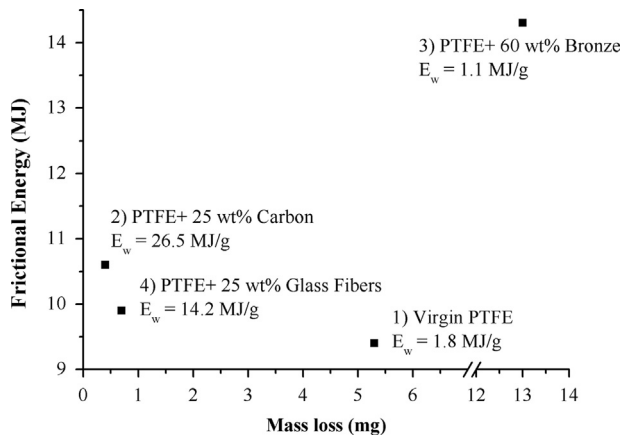


Fig. 5. Tribological behavior of PTFE composites.

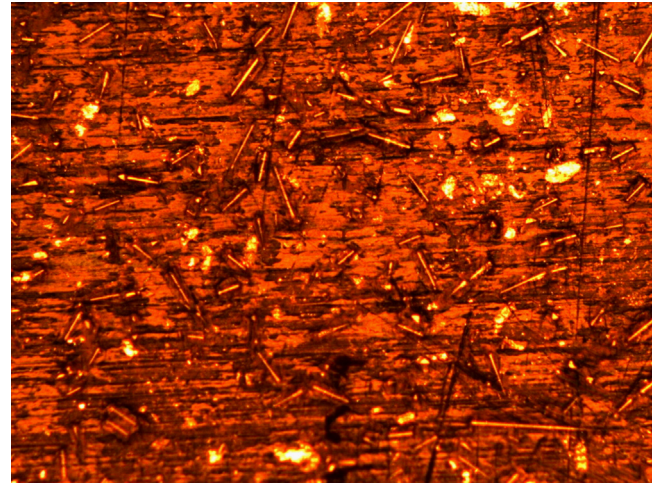


Fig. 6. SEM images of the worn PTFE surfaces: following the same numbering of Table 1.

rates are needed for a good understanding of the test. Specific wear energy E_w is a criterion that takes into account both: it is the ratio of friction work dissipated at the interface (between the initial time t_i and the time at the end of the test t_f) and the mass loss Δm due to wear:

$$E_w = \frac{E}{\Delta m} = \frac{vW \int_{t_i}^{t_f} \mu(t) dt}{\Delta m} \quad (4)$$

where μ is the coefficient of friction, W the normal load and v the sliding velocity.

The values are shown in Fig. 5.

In Fig. 6 the surface of the four PTFE samples after testing can be seen. In particular, as expected, in the lower part of the figure, virgin PTFE (1) shows plucked marks due to the transfer film formation and subsequent adhesion. The upper part represents the original (not tested) surface.

The black carbon PTFE composite (2) surface appears smooth and flat. The self-lubricating properties of the dispersed carbon particles have prevented abrasion. Faint scars are visible and attributed to the deformation occurring due to the high dynamics of the test.

Bronze filled PTFE (3) is characterized by a severe wear due to the displacement of the bronze particles in the bulk matrix. The bronze particle appears flattened and not very well sunk into the matrix. The regeneration of the transfer layer is more difficult as the countersurface is abraded during the sliding friction.

Glass fiber filled PTFE (4) presents a uniform friction contact surface where the fibers are well sunk in the bulk matrix and oriented in the sliding direction after few cycles. The damage created by the glass fibers during the test can be seen in Fig. 7.

In general, PTFE is transferred in the form of flakes of very small size during the initial period of friction, due to its change of phase. Other mechanisms are also involved in the transfer layer formation; therefore, a better understanding of this behavior needs further information coming from DSC analysis. The thermal traces in Fig. 8 can be interpreted beginning with the concept of the heat of fusion: the ratio between the total heat input (the area between the melting peak and the linear extrapolation of the curve after the glass transition) and the mass of the sample. It represents the amount of heat absorbed per unit mass of the material during melting. The thermal traces in Fig. 8 show no additional reaction between the filler materials and the matrix and no variation in the position of the transition-melting peak. On the other hand, the heat of fusion of the bulk PTFE polymer is significantly greater than that of the bulk composites. This indicates a higher thermal stability for the pure polymer even if great importance has to be given to the slope of the samples (1), (2) and (3) between the glass transition phase and the starting of the melting transition phase (approximately between 30 and 290 °C) and related reduction of the supplied heat flow. After glass transition, in fact, polymers

have high mobility increasing their temperature up to creating ordered dispositions called crystals and subsequently they release heat. Observing the behavior of the PTFE composite (4), it seems that glass fibers constrain the polymer chains more than carbon and bronze particles probably due to their larger size and content in wt%, introducing a higher level of stability.

The first important information is that the melting temperature is not dependent on the filler content and type of filler while PTFE crystallinity changes as reported in Table 1. The crystallinity fraction χ_c was calculated as:

$$\chi_c = \Delta H_m / \Delta H_{m0} \quad (5)$$

where ΔH_{m0} is the enthalpy of fusion of a sample of the same polymer fully crystalline. However, this value cannot be experimentally determined due to the difficulties in obtaining fully crystalline samples. Its value was assumed to be 80 J/g in accordance with literature [18,19].

In the working range temperature the slope of the DSC curve indicates the formation of small crystals during the cooling phase. The direct consequence is that a reduced amount of energy is needed in order to break such crystals: the work done by the friction force is mainly dissipated in heat and deformation which concur to the regeneration of the transfer film and the wear of the polymer.

As can be seen from Table 1, the relative crystallinity of bronze filled PTFE is low as the matrix is mainly occupied by bronze particles avoiding the formation of large crystals. As a consequence, wear rate is extremely high. Furthermore, the coefficient of friction reaches high values due to the sliding of the hard phase against the counterpart.

Black carbon particles, in addition to their lubricating properties, allow the formation of large crystals and gives better heat dissipation, that is, more energy is needed to break them.

Glass fibers play the same role of black carbon fillers but a slight difference is given by the transversal position of such fibers into the polymer matrix.

Crystallinity of virgin PTFE is the highest, but well known conformation of alternated amorphous and crystalline parts results in their relative sliding facilitating wear.

4. Conclusions

Wear of PTFE composites is regulated by different factors depending on:

- Matrix properties;
- Fillers properties.

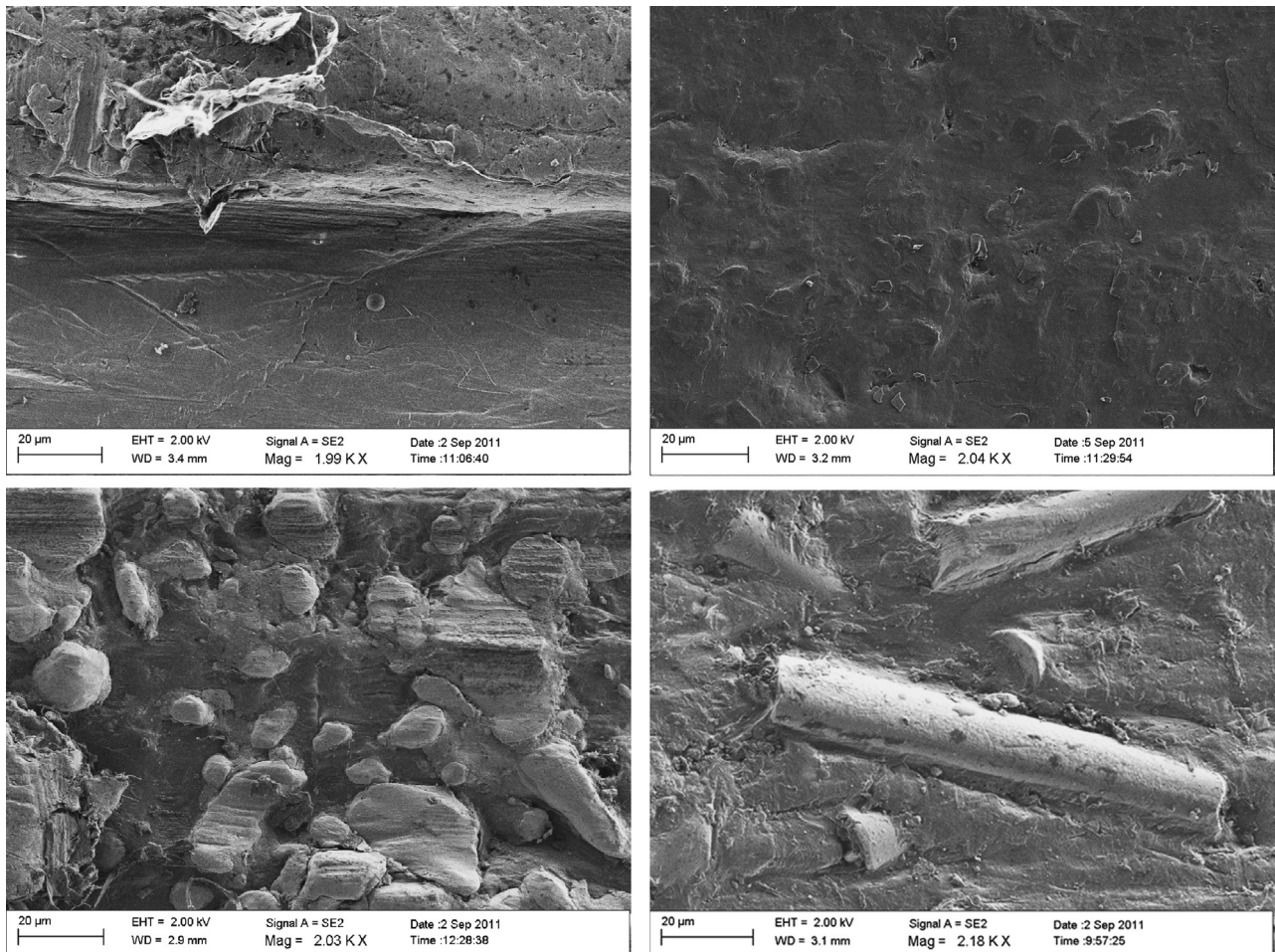


Fig. 7. Optical microscopy images of the worn PTFE composite (4) surfaces.

The presence of fillers does not affect the polymer melting point and the transition phase points but plays an important role in strengthening of the bulk PTFE and on its tribological behavior. In particular, if the fillers are more thermally conductive, the frictional heating is less as heat is conducted away more effectively. As a consequence less heat is available to break crystals. Glass fibers and black carbon particles reduce frictional heating by about 10% with respect to the virgin PTFE as they dissipate faster the heat through the polymer. Modeling of the heat flow generated by friction force permits the following considerations:

1. The presence of fillers increases the stability of the structure improving the wear resistance;
2. The increment in thermal conductivity and diffusivity improves wear resistance of the material to adhesion;
3. Bronze and glass fibers fillers can reduce the wear mass loss of PTFE under dry conditions significantly but their large size can affect the countersurface and the transfer film;
4. Carbon filled PTFE has good a combination of thermal characteristics and structure due to the small size of carbon particles.

Transition phase at low temperature (from hexagonal to pseudo-hexagonal crystals) allows the formation of the transfer layer, while the crystallinity of the polymer participates in its regeneration.

When polymer composites are considered, thermal characteristics should be checked with respect to temperature and,

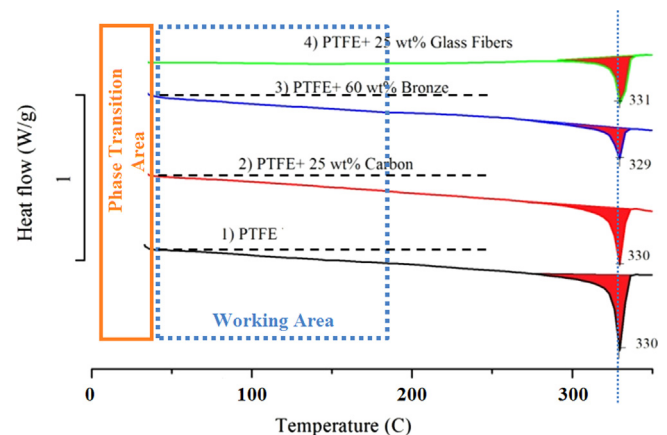


Fig. 8. DSC analysis of PTFE composites.

furthermore, frictional heating calculations should be carried out when a hard filler is present in the bulk material.

References

- [1] M. Conte, A. Igartua, Study on PTFE composites tribological behavior, *Wear* 296 (2012) 568–574.
- [2] I. Tzanakis, M. Conte, M. Hadfield, T.A. Stolarski, Experimental and analytical thermal study of PTFE composite sliding against high carbon steel as a function of the surface roughness, sliding velocity and applied load, *Wear* 303 (2013) 154–168.

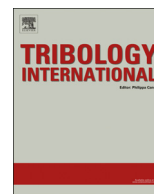
- [3] E.N. Brown, D.M. Dattelbaum, The role of crystalline phase on fracture and microstructure evolution of polytetrafluoroethylene (PTFE), *Polymer* 46 (2005) 3056–3068.
- [4] B.N.J. Persson, Rubber friction: role of the flash temperature, *Journal of Physics: Condensed Matter* 18 (2006) 7789–7823.
- [5] M. Conte, B. Fernandez, A. Igartua, Effect of surface temperature on tribological behavior of PTFE composites, *WIT Transactions on Engineering Science* 71 (2011) 151–161.
- [6] D.M. Price, et al., Thermal conductivity of PTFE and PTFE composites, in: *Proceedings of the 28th Conference of the North American Thermal Analysis Society*, October 4–6, 2000, Orlando, USA.
- [7] S. Bahadur, The development of transfer layers and their role in polymer tribology, *Wear* 245 (2000) 92–99.
- [8] X.Q. Wang, D.R. Chen, J.C. Han, S.Y. Du, Crystallization behavior of PTFE, *Journal of Applied Polymer Science* 83 (2002) 990–996.
- [9] G. Belforte, A. Manuello, L. Mazza, Test rig for friction force measurements in pneumatic components and seals, *Proceedings of the Institution of Mechanical Engineers, Part J: Journal of Engineering Tribology* 227 (2013) 43–59.
- [10] B. Pinedo, M. Conte, et al., New high performance test rig for sealing systems characterization, in: *Proceedings of the WTC2013*, 8–13 September, 2013, Turin, Italy.
- [11] R. Grassi, L. Mazza, A. Trivella, High speed friction and wear measurements on guide rings for reciprocating compressors, in: *Proceedings of the 8th International Conference on Fluid Power – IFK*, Dresden, 2012.
- [12] G.W. Stachowiak, A.W. Batchelor, *Engineering Tribology*, Elsevier, UK, 2005.
- [13] F.P. Bowden, D. Tabor, *Friction and Lubricating Wear of Solids Part 1*, Clarendon press, UK, 1964.
- [14] H. Blok, Theoretical study of temperature rise at surfaces of actual contact under oiliness lubricating conditions, in: *Proceedings of the General Discussion on Lubrication and Lubricants*, vol. 2, London, 1937, pp. 222–235.
- [15] J.C. Jaeger, Moving sources of heat and the temperature at sliding contact, *Proceedings of the Royal Society of New South Wales* 76 (1943) 203–224.
- [16] J.F. Archard, The temperature of rubbing surfaces, *Wear* 2 (1958–1959) 438–455.
- [17] M. Conte, B. Fernandez, A. Igartua, Frictional heating calculation based on tailored experimental tests, in: *Proceedings of the 15th NordTrib Conference*, 12–15 June 2012, Trondheim, Norway.
- [18] W.G. Sawyer, K.D. Freudenberg, P. Bhimaraj, L.S. Schadlerb, A study on the friction and wear behavior of PTFE filled with alumina nanoparticles, *Wear* 254 (2003) 573–580.
- [19] R.L. Blaine, Polymer heats of fusion, *Thermal Applications Note*, TA123, Determination of Polymer Crystallinity by DSC, TA Instruments, New Castle, DE.



ELSEVIER

Contents lists available at ScienceDirect

Tribology International

journal homepage: www.elsevier.com/locate/triboint

Frictional heating calculation based on tailored experimental measurements



M. Conte*, B. Pinedo, A. Igartua

IK4-Tekniker, Calle Iñaki Goenaga 5, 20600 Eibar, Spain

ARTICLE INFO

Article history:

Received 23 October 2013

Received in revised form

7 January 2014

Accepted 28 January 2014

Available online 11 February 2014

Keywords:

Frictional heating

Sliding wear

Polymers

PTFE

ABSTRACT

New composites and nano-composites polymers are continuously developed satisfying more and more exigent demands in terms of mechanical and tribological properties. Nevertheless a wide working velocity range has been achieved; one of the main bottlenecks of these materials is related to their thermal resistance. Semi-crystalline materials have a wide range of temperature; however, their operative life decreases exponentially with increasing temperature. For several applications, knowing the contact temperature can give a considerable help in choosing the right polymer to be used. An adequate frictional heating calculation based on Block and Jaeger equations is herein proposed matching experimental tests configuration at laboratory scale and theory to overtake restrictive assumptions.

© 2014 Elsevier Ltd. All rights reserved.

1. Introduction

Frictional heating calculation in metal to metal contact has been deeply investigated and accordingly many reviews have shown it is still not well defined and the contact conditions vary in time and location [1,2]. In [3] a comparison of some calculation model was presented showing high disagreement between the results, due to two important concepts: the right way to calculate the contact area and the variation of the materials properties with temperature, both to be included in the equations. In polymer to metal contact, the first assumption does not affect calculations otherwise temperature reached at the asperities contact would overtake the melting point of the materials. Nevertheless the coefficient of friction, which enters calculation to the first power, is still of great importance. In metal to metal contact, flash temperature was estimated determining the phase transformations and microstructural changes in materials and relating them with the temperature needed for these transformations [4,5]. In polymer to metal contact, the authors [6] have used a Differential Scanning Calorimetry (DSC) technique [7–10] to evaluate the effects of fillers on the crystallinity ratio of some PTFE (Polytetrafluoroethylene) composites, and observed relevant structural changes at the polymers contact surfaces. It was also observed in [11] how the crystallinity of transfer film was higher than the bulk material. According to Persson's investigation [12], due to

the strong temperature dependence of viscoelastic properties of rubber-like material, local temperature calculation should be considered in order to explain the frictional behavior of the tribo-pair, so an estimation of flash temperature at the polymer to metal contact surface is herein proposed for a better understanding of the tribochemical and tribophysical phenomena occurring at the contact. Direct experimental measurement of contact temperature is not viable due to different reasons [13,14]. Taking into account the low diffusivity of this kind of materials, a high velocity thermo camera has been seen to be a good but expensive tool [15]. A frictional heating calculation method for polymers based on tailored experimental tests is herein presented. Aim of this work is to propose a reliable and cheap method for estimating at laboratory scale the frictional heating of polymer to metal contact. First of all, the assumptions limiting one of the most suitable methods have been overtaken by means of an opportune experimental configuration. Particular attention has been then given to the variation of the thermal characteristics of the polymer and to the evolution of the friction force.

A first validation of the method is proposed for PTFE material. In particular, it was chosen due to four reasons: 1) because of its high resistance to high temperature with a melting point of about 330 °C; 2) because of its particular case to have two phase transitions in the range 19–31 °C; 3) because the fluorine chains are not cross linked like in the elastomers, so the mechanical work done for overtaking the friction force can be considered quasi-entirely transformed in frictional heating [16]; and 4) to have a correspondence with experimental tests found in the literature [15].

This method can have not only a practical use in the selection of the most appropriate materials for industrial applications like

* Corresponding author.

E-mail addresses: marcello.conte@tekniker.es, conte.marcello@gmail.com (M. Conte).

seals, bearings and slides, but it can also play an important role in choosing the most opportune operative parameters (velocity, break time, maintenance, etc.).

2. Contact temperature calculation method

The temperature at the interface between rubbing bodies is known as “surface conjunction temperature” [17]; the calculation of this temperature is possible by applying the laws of energy conservation and heat transfer. In fact, most of the energy dissipated during the process of friction is converted into heat [17] resulting in local temperature increment called “flash temperature” that could be divided into transient and steady state flash temperature rise. As reported by Bowden and Tabor [18] in dry contacts the transient flash temperature may become larger than the steady state component. The flash temperature calculation method was formulated firstly by Block [19] and then improved by Jaeger [20] and Archard [5]. It provides a set of formulas for various velocity ranges and contact geometries and it is based on the following assumptions: 1) a planar source of heat is considered; 2) a steady state condition is attained; 3) the thermal properties of the bodies do not change with temperature; and 4) the coefficient of friction is known and reaches a steady value.

The following hypotheses are considered for the calculations:

- the heat source considered corresponds to the final contact area and it is friction dependent;
- the component of energy lost in deformation of the bodies can be considered negligible due to the high mobility of the polymeric chains, and an appropriate test configuration (like high velocity reciprocating movement on a short stroke) avoids the calculation of the Peclet number [17];
- the thermal properties of the bodies change with temperature;
- the experimental curve of the coefficient of friction can be used in the calculation, having as result a direct correlation with the work done by the friction force as shown in the following equation:

$$Q(t) = \mu(t)Wv \quad (1)$$

where μ is the coefficient of friction, W is the normal load and v is the sliding velocity. The contact temperature can be then described also as a function of time as follows:

$$T_{f \max}(t) = \frac{2Q(t)}{KA} \sqrt{\frac{2\chi b}{\pi v}} \quad (2)$$

where K is the thermal conductivity, χ is the thermal diffusivity, A is the contact surface and $2b$ is the contact width. Both K and χ are temperature dependent, so the maximum flash temperature is also a function of temperature itself, $T_{f \max} = T_{f \max}(t, T)$, and they should be evaluated experimentally. The contact area considered for calculations in Eq. (2) is the cylindrical sector of the contact zone at the end of the test, being not reliable to measure or to hypothesize its evolution over time: it means that the calculated temperature was under-estimated.

Eqs. (1) and (2), thus, describe the progressive evolution of the work done by the friction force and the temperature evolution at the contact. Maximum surface contact temperature T_{contact} is calculated considering the following equation:

$$T_{\text{contact}} = T_{\text{bulk}} + T_{f \max} \quad (3)$$

where T_{bulk} is the bulk temperature of the sample before entering the contact.

The energy that is transformed as a consequence of frictional contact can be dissipated (conversion to heat, vibration, material deformation, new surface creation) or stored into the tribosystem.

Specific wear energy (E_w) is a criterion which takes coefficient of friction and wear rate into account: it is the ratio of the friction work spent in the interface along the test (between the initial time t_i and the time at the end of the test t_f) divided by the mass loss (Δm) due to the wear as shown in the following equation:

$$E_w = \frac{Q}{\Delta m} = \frac{vW \int_{t_i}^{t_f} \mu(t) dt}{\Delta m} \quad (4)$$

The amount of material removed from the surface is a function of the energy expended on it by the friction force.

3. Experimental setup and specimens

3.1. Specimens

Polytetrafluoroethylene (PTFE) is a well known semicrystalline polymer having relevant tribological characteristics, in particular low friction and quasi-absence of sticking effect, high resistance to temperature and good compatibility. Compared to other polymers, PTFE has high density and high melting point (around 330 °C).

According to the information obtained from the producer (Polifluor, 20159 Asteasu, Spain), the PTFE sample comes from a process of compression molding of the PTFE powder with subsequent sinterization and cooling. The PTFE dispersion has a median particle size of 0.25 μm . The thermal properties of the samples are reported in Table 1.

The PTFE undergoes several phase changes at atmospheric pressure from sub-ambient temperature to the melting point. DSC analysis was carried out by heating the sample in the temperature range of 30–350 °C with a heating rate of 10 °C/min (Fig. 1) using nitrogen as inert gas.

Above 30 °C the material converts into a pseudo-hexagonal disordered phase from a partially ordered hexagonal phase, so thermal diffusivity temperature dependence above 25 °C is low [9]. Therefore the thermal properties of virgin PTFE cannot be considered to be independent of temperature; measurement of its diffusivity, specific heat and density is needed.

Table 1
Thermal properties of virgin PTFE.

| Property | Value |
|--|-----------------------|
| Thermal conductivity K at 30 °C (W/m K) | 0.14 |
| Thermal diffusivity χ (m^2/s) | 1.11×10^{-7} |
| Melting temperature T_m (°C) | 330 |
| Heat of fusion H (J/g) | 24.80 |

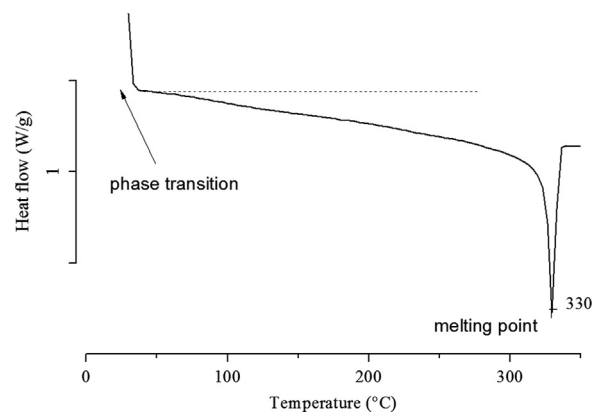


Fig. 1. DSC analysis of virgin PTFE.

Thermal diffusivity (χ) of PTFE was measured by means of a high resolution ac photopyroelectric calorimeter in the standard back detection configuration. A mechanically modulated He–Ne laser beam of 5 mW illuminates the upper surface of the sample under study. Its rear surface is in thermal contact with a 350 μm thick LiTaO₃ pyroelectric detector with Ni–Cr electrodes on both faces, by using an extremely thin layer of high heat-conductive silicone grease (Dow Corning, 340 Heat Sink Compound). The photopyroelectric signal is processed by a lock-in amplifier in the current mode.

Heat capacity (C_p) of PTFE was measured in a modulated differential scanning calorimeter MDSC, TA Instruments, series Q200. Dry nitrogen was used for venting at a rate of 50 ml/min. The measurement was conducted within a range comprised between 0 °C and 100 °C, when a constant value is reached.

Density (ρ) of the PTFE was measured by means of a METTLER Toledo XP205 precision micro-scale using the Archimedes' principle and it was found to be of about 2.104 g/cm³.

Measuring the heat capacity, the thermal diffusivity and the density of the material, thermal conductivity (κ) along temperature was estimated by means of the following equation:

$$\kappa = \chi \rho C_p \quad (5)$$

Fig. 2 shows the changes of the PTFE thermal characteristics due to the temperature increment, especially around the ambient temperature. Such behavior can be easily linked to the phase changes experienced by the material [22].

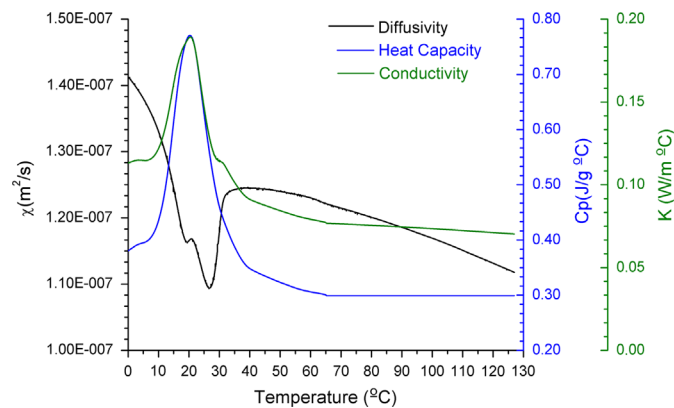


Fig. 2. Virgin PTFE thermal characteristics.

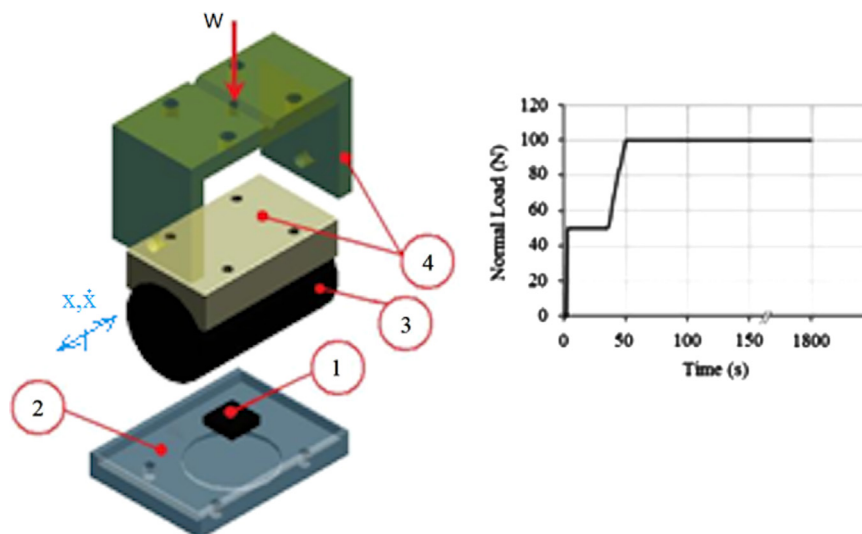


Fig. 3. Test rig configuration.

It can be appreciated as the values reported in Table 1 do not completely agree with the measured data.

3.2. Test configuration

The PTFE samples have dimension as follows: 15 mm length, 12 mm width, 5 mm depth. The virgin PTFE was tested in the High Frequency Oscillating Tribometer “SRV” against a quenching tempered CrNiMo rod (15 mm diameter, 22 mm length) of HRC > 60 ± 1 and surface texture following the standard D6425-02.

Friction and wear tests are carried out in the test rig represented in Fig. 3: a PTFE sample (1) is mounted on a frame (2) and blocked for 2/3 of its depth. It is loaded by an axially sliding rod (3) supported and fixed by two holders (4) on which normal constant load is applied and transmitted to the axle of the rod. The so formed tribo-pair is placed in a climatic chamber 2 h before the test where temperature is maintained at 25 °C and relative humidity at 25%.

The holders and a couple of screws avoid rotation of the rod around its axle. Normal load was set on 50 N for the first 30 s and then at 100 N, 2 mm stroke and maximum sliding velocities v of about 0.1, 0.16 and 0.24 m/s. The velocities were chosen considering the working conditions of the application. Coefficient of friction (CoF) was recorded at regime condition for 30 min. Three repetitions have been conducted.

4. Results and discussion

In the first step the influence of sliding velocity on the frictional behavior of virgin PTFE was studied. As can be appreciated in Fig. 4, the influence of velocity on frictional behavior of virgin PTFE is negligible. The mass loss measured at the end of the experimental measurements is of the same order of magnitude. The work done by the friction force at the three velocities is almost the same. It can be explained by considering that the major part of such work is done in the running in cycles [21,22].

Considering the thermal transition curves of PTFE composites in Fig. 1 it is possible to see how the PTFE material can be affected by the heat flux generated at the contact. In particular the small crystals formed in that range of temperature start wear processes. In fact, the small crystals formed at lower temperature are destroyed resulting in flakes separation being less stable: PTFE fails along weak intermolecular bonds due to the minor temperature rise which involve slippage of crystalline formations of the

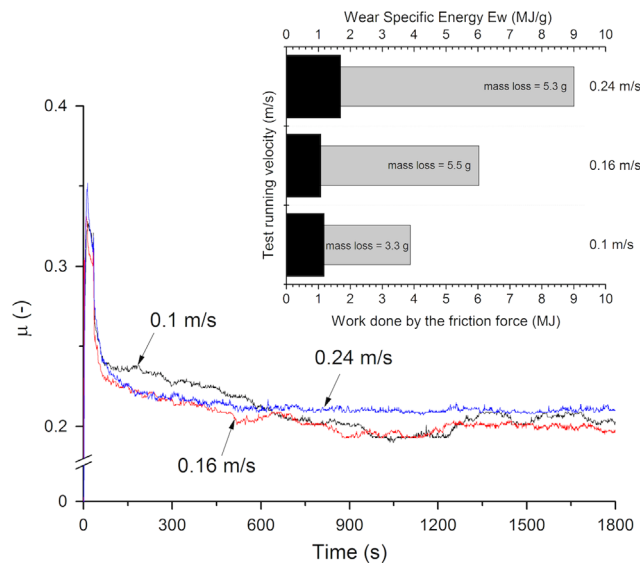


Fig. 4. Friction test results at different sliding velocities, work done by the respective friction forces Q (gray bars) and wear specific energy E_w (black bars).

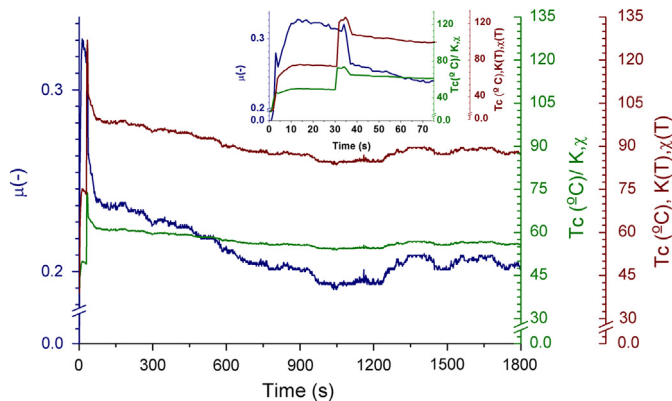


Fig. 5. Coefficient of friction and calculated contact temperature evolution of the PTFE sample. The small figure represents the “zoom in” of the first 70 s. (For interpretation of the references to color in this figure legend, the reader is referred to the web version of this article.)

bond structure. In other words, the increment of temperature at the contact, due to the low thermal conductivity of the polymer, plays an important role in the wear process of the surface.

Bulk temperature was considered to be of about 25 °C as the sample has been placed in the climatic chamber for 2 h before the test. The calculation of the contact temperature, considering thermal diffusivity and consequently thermal conductivity constants, results in a regime contact temperature values slightly below 60 °C (Fig. 5, green color axes). On the other hand, recalculation of the flash temperature considering the variation of the PTFE’s thermal properties implies finding higher regime contact temperature (Fig. 5, red color axes) [15]. It remarks a 40% difference in calculations. The actual working temperature is then much higher than expected, reducing consistently the working hours expectation of the polymeric material. The authors do not exclude that when the polymer becomes softer, the energy dissipated in deformation is higher.

The work done by the friction force and the mass loss is reported in Table 2. Wear specific energy was calculated according to Eq. (4).

In the initial stage of the test the high degree of lateral mobility of PTFE chains quickly induces molecular orientation in the sliding direction. This phenomenon is also aided by a PTFE smooth linear molecular profile and ability of the electron clouds of the large

Table 2
Work done by the friction force, mass loss and relative wear specific energy during the tests.

| Calculated and measured factors | Values |
|-----------------------------------|--------|
| Frictional energy Q (MJ) | 9.0 |
| Mass loss Δm (mg) | 5.3 |
| Wear specific energy E_w (MJ/g) | 1.70 |

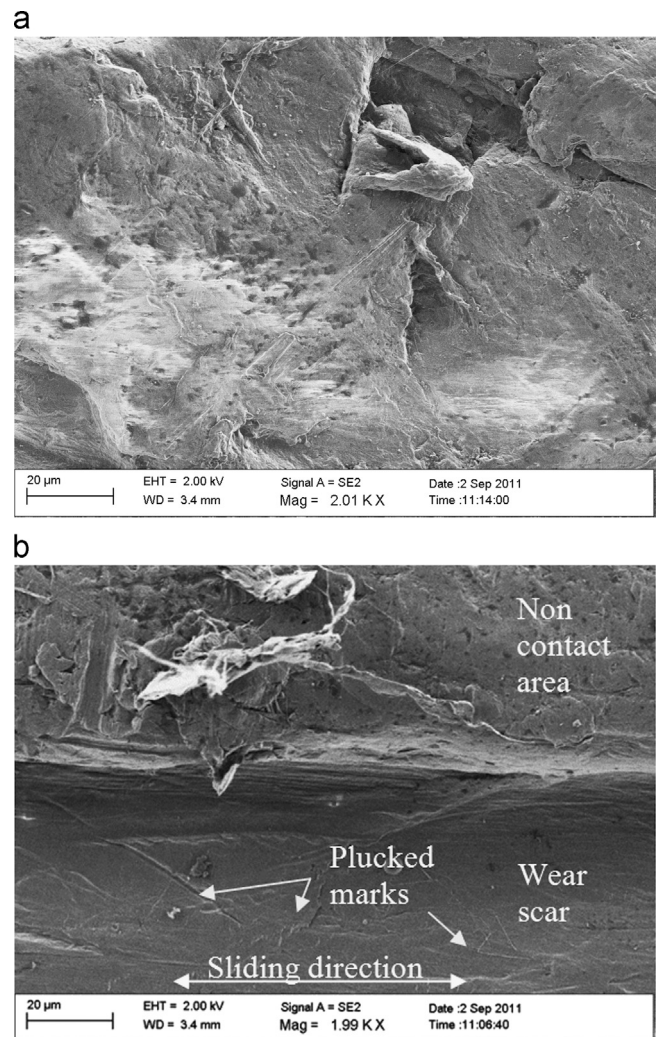


Fig. 6. SEM captions of PTFE contact surface before (a) and after (b) the tribological test.

fluorine ions to screen bonding forces between neighboring molecules. The measured dynamic friction coefficient is directly related to the molecular structure of the polymer. PTFE, which is composed of rigid rod-like molecules with a smooth molecular profile, shows a low coefficient of friction because of an easy slip between the aligned molecule chains at the interface [16].

Before the test, the polymer surface is bevelled and irregular (Fig. 6a) while the steel surface has the surface finishing due to its machining (Fig. 7a). During the sliding, adhesive wear is generated as a consequence of PTFE molecular reorientation in the direction of sliding. Such reorientation occurs for the surface of PTFE in contact with the countersurface (Fig. 6b) as well as for the transfer film that is deposited on the countersurface (Fig. 7b). The plucked marks shown in Fig. 6b are due to the transfer film formation and subsequent adhesion. The reorientation of the polymer chains can

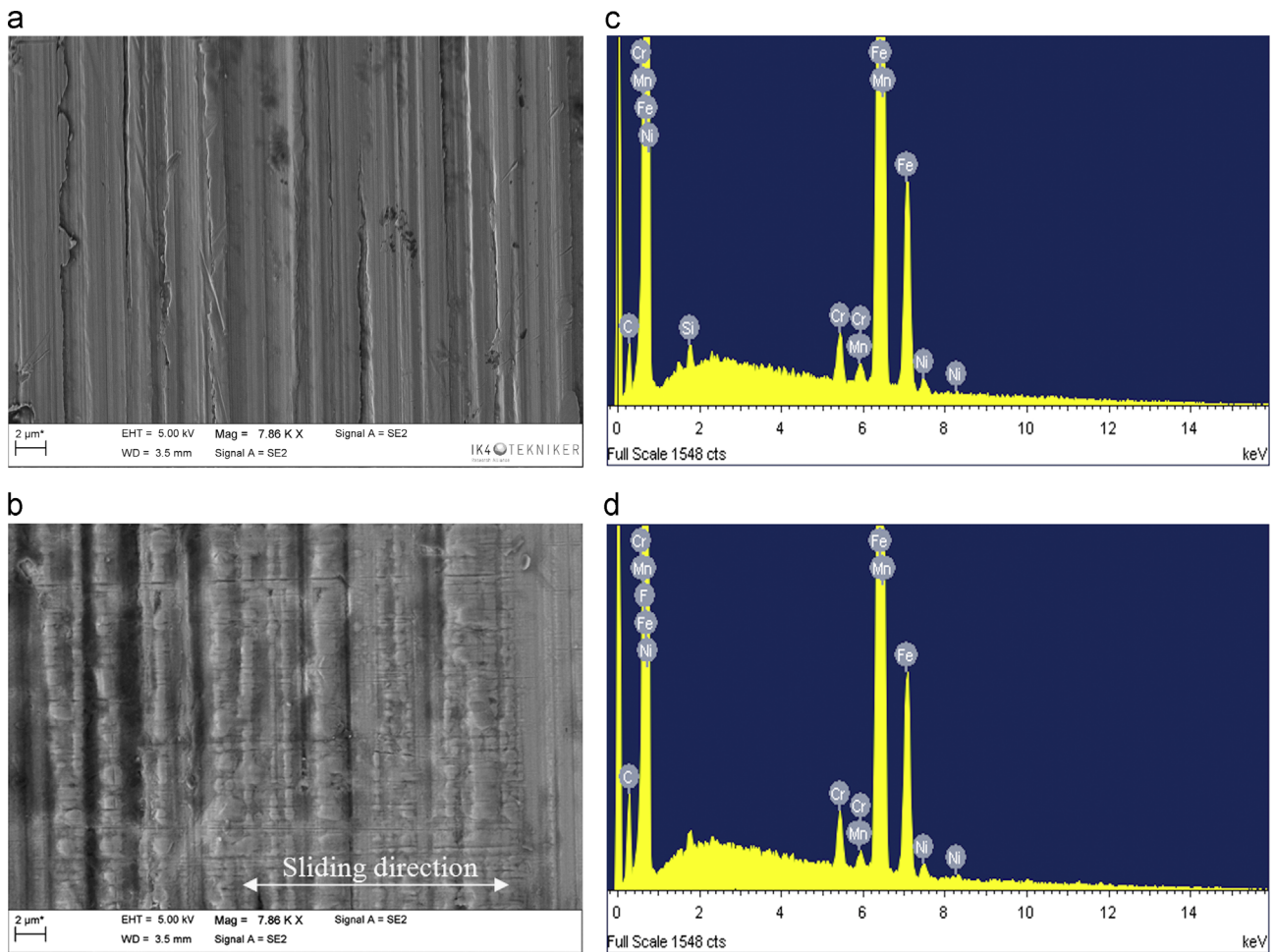


Fig. 7. SEM captions and EDS of steel contact surface before (a, c) and after (b, d) the tribological test.

be clearly appreciated at the interface between the wear scar and the non-contact surface in the same figure. A stable transfer layer promotes stable low friction and low wear.

In Fig. 7 SEM captions show a relevant change in the counter-surface due to the presence of the transfer layer: in Fig. 7d, that is, the caption of the steel surface after the test, the Fluorine peak appears in the EDS spectrum as a proof of the transfer layer formation. All the other elements of the steel maintain the same proportions found in the spectrum taken in the non-contact area of the steel sample (Fig. 7a).

5. Conclusions

The method presented in this paper allows estimating the actual contact temperature range during actual working conditions of a polymeric component sliding on a steel surface starting from laboratory scale tests. Said tests are tailored to the calculation model of Block and Jaeger in order to overcome its limitations.

This tailored experimental configuration allows considering:

- a planar stationary heat source at the contact;
- the evolution of the coefficient of friction along the time;
- the variation of the thermal properties of the materials with temperature.

The calculation method needs as inputs: the test parameters (velocity, ambient temperature, stroke opportunely chosen,

normal load), the final area of the wear scar, the coefficient of friction evolution vs time and the thermal characteristics of the polymer vs temperature. Surface finishing, material hardness and other parameters are indirectly included as per their effect on the coefficient of friction. The analytical calculation method was applied to a virgin PTFE polymer knowing all its thermal characteristics. It was demonstrated how the use of constant thermal characteristics could result in an under estimation of the frictional heating resulting, in some cases, in an unexpected failure of the component.

The calculation methods can be considered to be a useful tool to understand the real behavior of rubbing polymers in several applications like, for example, seals. When polymer composites are considered, frictional heating calculations should also be carried out when a hard phase present in the bulk material is rubbing against the countersurface as shown in [23].

Acknowledgments

The authors would like to thank their colleagues Xana Fernandez, Miren Blanco and Gemma Mendoza for carrying out the tribological tests, the thermal analysis and SEM analysis respectively. The method was set up during a comparative study for selecting the most appropriate material for a sealing system. The authors are grateful with the reviewers' contributions for improving this paper.

References

- [1] Kennedy FE. Thermal and thermomechanical effects in dry sliding. *Wear* 1984;100:453–76.
- [2] Bucher F, Knothe K, Theiler A. Normal and tangential contact problem of surface with measured roughness. *Wear* 2002;253:204–18.
- [3] Kalin M. Influence of flash temperatures on the tribological behaviour in low-speed sliding: a review. *Mater Sci Eng A* 2004;374:390–7.
- [4] Kennedy FE. Single pass rub phenomena – analysis and experiment. *J Lubr Technol* 1982;104:582–8.
- [5] Archard JF. The temperature of rubbing surfaces. *Wear* 1958–1959;2:438–55.
- [6] Conte M, Fernandez B, Igartua A. Effect of surface temperature on tribological behavior of PTFE composites. *Surface effects and contact mechanics X*. UK: WIT Press; 2011; 219–30.
- [7] Tieyuan FU, Yuchen QI, Suyun WU, Donglin C. Equilibrium heat of fusion of PTFE. *Polym Commun* 1985;4:323–31.
- [8] Wang Y, Yan F. Tribological properties of transfer films of PTFE-based composites. *Wear* 2006;261:1359–66.
- [9] Blumm J, Lindemann A, Meyer M, Strasser C. Characterization of PTFE using advanced thermal analysis techniques. *Int J Thermophys* 2010;31(10):1919–27.
- [10] Wang XQ, Chen DR, Han JC, Du SY. Crystallization behavior of PTFE. *J Appl Polym Sci* 2002;83:990–6.
- [11] Brown EN, Rae PJ, Orlor EB, Gray III GT, Dattelbaum DM. The effect of crystallinity on the fracture of PTFE. *Mater Sci Eng C* 2006;26:1338–43.
- [12] Persson BNJ. Rubber friction: role of the flash temperature. *J. Phys: Condens Matter* 2006;18:7789–823.
- [13] Sutter G, Ranc N. Flash temperature measurement during dry friction process at high sliding speed. *Wear* 2010;268:1237–42.
- [14] Kennedy FE, Frusescu D, Li J. Thin film thermocouple arrays for sliding surface temperature measurement. *Wear* 1997;207:46–54.
- [15] Tzanakis I, Hadfield M. Evaluation of flash temperatures of a composite elastomer tip seal with a dry sliding condition in contact with a high carbon steel plate. *Surface effects and contact mechanics X*. UK: WIT Press; 2011; 3–14.
- [16] Sinha SK, Briscoe BJ. *Polymer tribology*. UK: Imperial College Press; 2009.
- [17] Stachowiak GW, Batchelor AW. *Engineering tribology*. UK: Elsevier; 2005.
- [18] Bowden FP, Tabor D. *The friction and lubrication of solids*, vol. 1. UK: Clarendon Press; 1964.
- [19] H Block. Theoretical study of temperature rise at surfaces of actual contact under oiliness lubricating conditions. In: *Proceedings of the general discussion on lubrication*, London, vol. 2, 1937, p. 222–235.
- [20] Jaeger JC. Moving sources of heat and the temperature at sliding contact. In: *Proceedings of the royal society of New South Wales*, vol. 76, 1943, p. 203–224.
- [21] Conte M, Fuentes E, Fernandez X, Igartua A. Effect of fillers on tribological properties of PTFE materials. In: *Proceedings of the Ecotrib, Wien, Austria*, 2011, p. 207–212.
- [22] Conte M, Pinedo B, Igartua A. Role of crystallinity on wear behavior of PTFE composites. *Wear* 2013;307:81–6.
- [23] Tzanakis I, Conte M, Hadfield M, Stolarski TA. Experimental and analytical thermal study of PTFE composite sliding against high carbon steel as a function of the surface roughness, sliding velocity and applied load. *Wear* 2013;303:154–68.